University Abd El Hamid Ibn Badis Mostaganem
Faculty of Sciences and Technology FST
Department of Mechanical Engineering

Order N°: D 73/2019

THESIS

In partial fulfillment of the requirements for the degree of

Doctor of Philosophy

Option: **Mechanics of Materials**

Submitted by

MESBAH Moustafa

Treatment of Spinal Disorders using Flexible Constructions

Doctoral Committee:

Prof. Guechichi Hocine	**President**	University of Mostaganem
Prof. Kebdani Said	**Examiner**	University of Oran, USTO
Prof. Boualem Noureddine	**Examiner**	University of Oran, USTO
Dr. Chiali Hakim	**Invitee**	CHU Tlemcen
Dr. Bendoukha Mohammed	**Thesis advisor**	University of Mostaganem

Academic Year: 2018-2019

Acknowledgements

I know by experience that this is the hardest part of a thesis to write. I also know that a couple of months are not enough to develop the cynicism to look back and harshly criticize your work. This is probably the reason for my hesitation in writing these pages.

This thesis was developed at the Faculty of Sciences and Technology FST, Department of Mechanical Engineering under the guidance of Dr. Bendoukha Mohamed, to whom I owe gratitude for giving me the opportunity to work in such a challenging research field throughout the years. I would like to thank the president of the doctoral committee Prof. Guechichi Hocine, my examiners Prof. Kebdani Said and Prof. Boualem Noureddine and Dr. Chiali Hakim for providing insightful comments and carefully reviewing my thesis. My examiners not only improved this dissertation with their constructive criticism, but also made a huge impact on my professional development.

I am grateful to all the people who gave their contribution to this work, in particular to: Pr. Moumene Missoum, the wise man, my example, and the mentor who success at teaching me how to study the "spine" appropriately. Other than that, I think he has invented the well-known spinal devices in the world, his guidance (six months) has been the foundation of all that I have learned and done in the field of Spine biomechanics. He helped me with his expertise in the field of biomechanics, thank you for everything.

I would like to thank Professor. Joáo Manuel Tavares from the University of Porto FEUP, Dr. Barkaoui Abd el Wahed from University of Tunis El Manar ENIT and all colleagues, especially of the computational biomechanics group of the University of Tunis El Manar. Their friendship and discussions made the days interesting and enjoyable. Lastly, I would like to thank all my friends that were dragging me away from the computer from time to time and helped me to find answers at the bottom of a glass.

Finally, I am most grateful to all members of my family, for their constant support, patience and encouragement throughout my dissertation, this work is dedicated to them. My Parents, my brothers and my sister appeared to be influenced by my interest in biomechanical engineering for a while, I love you all and I will continue to do my best to be worthy of your support.

Table of contents

List of figures

Chapter 3: Biomechanical Response of Lumbosacral Segments under Physiological Functions

Chapter 6: Anisotropic Response of the Holzapfel's Constitutive Model for the Lumbar Spine Considering Degenerative Related changes

List of tables

List of notations

E	Young's modulus, MPa
ε	Strain
ν	Poisson's ratio
μ	Micron, 10^{-6}
C_{ij}	Material constants characterizing the hyperelastic strain energy equations
I_i	Invariants of the deviatoric of the left Cauchy-Green strain tensor
D_1	Material incompressibility factor
K	bulk modulus of the material
$K1$	Fiber Stiffness Parameter
$K2$	Fiber Nonlinearity Parameter
κ	Fiber Dispersion Parameter
σ	Normal Stress
J	The material constants for the annulus ground substance
V	Local volume ratio
V_0	Initial volume ratio
l	Direction cosine with respect to the x direction
m	Direction cosine with respect to the y direction
n	Direction cosine with respect to the z direction
S	Total stress on general plane
S_x	x component of total stress on a general plane
S_y	y component of total stress on a general plane
S_z	z component of total stress on a general plane
S_n	Stress normal to general plane
σ	Normal stress
τ	Shear stress

γ	Shear strain
λ_i	Extension or stretch ratio; i=1, 2, 3 for principal directions
K	Stress invariant
D	Displacement
K	Curvature of a polynomial
W	Work
U	Strain energy density
F	Force generating simple shear deformation
Δh	Variation of height

List of abbreviations

AF	Annulus Fibrosus
NP	Nucleus Pulposus
IVD [~s]	Intervertebral Disc
ALL	Anterior Longitudinal Ligament
PLL	Posterior Longitudinal Ligament
CL	Capsular Ligament
FL	Flavum Ligament
ITL	Intertransversal Ligament
ISL	Interspinous Ligament
SSL	Supraspinous Ligament
PDS	Posterior Dynamic Stabilization
DSS	Dynamic Stabilization system
Dynesys	Dynamic Neutralization System
VAS	Visual Analogue Score
ODI	Oswestry Disability Index
MIS	Minimally Invasive Surgery
LBP	Low Back Pain
L1	First Lumbar vertebra
L1/S1	Lumbosacral Spine
CT	Computational Tomography
DDD	Degenerative Disc Disease
DOF	Degree Of Freedom
FCE [~s]	Fluid Cavity Element
FEA	Finite Element Analysis
FEM	Finite Element Method
FSU [~s]	Functional Spinal Unit
IDP	Intradiscal Pressure
MRI	Magnetic Resonance Imaging

ASD	Adjacent Segment Disease (Deterioration)
DS	Degenerative Spondylolysthesis
DTO	Dynamic Transition Optima
FDA	Food and Drug Administration
PCU	Polycarbonate Urethane
PEEK	Poly Ether Ether Ketone
PET	Polyethelene
Ti	Titanium
ROM	Range of Motion
STL	Stereoletheography
UMAT	User Material; ABAQUS user subroutine
V [~e]	Vertebra
IGES	Initial Graphics Exchange Specification
CAD	Computer Aided Design
NURBS	Non-Uniform Rational Basis Spline
C3D8	ABAQUS Continuum 3D hexahedral element
C3D8H	ABAQUS Continuum 3D hexahedral Hybrid element
F3D4	ABAQUS 3D Fluid quadrilateral element
T3D2	ABAQUS 3D Truss element
S4R	ABAQUS 4 quadrilateral shell element
ALIF	Anterior Lumbar Interbody Fusion
CCE	Constraint Coupling Element
SED	Strain Energy Density

Abstract

The mechanism and surgical treatment of lumbar spine pain remain controversial. As the name implies, flexible stabilization is based on the concept of instability as a cause of activity-related. Unfortunately, spinal instability is not well defined and is poorly understood. Spinal fusion has been the cornerstone of surgical treatment for back pain, this procedure has been practiced for almost a century, and generally results in successful clinical outcomes. Although fusion works in the majority of patients, in many cases persistent back pain. Furthermore, accelerated degeneration of the adjacent segment after initial clinical success with fusion surgery is fairly common. The concept of flexible stabilization was developed as a result of fusion's failure to deliver the wanted clinical result.

The purpose of this thesis is to investigate the treatment of spinal disorders using flexible stabilization constructs. This work aims to find the best stabilization that restores the kinematics of spinal segments of normal movement without overloading the structural elements that govern specific movement using a parametric finite element FE modeling, consequently the basic key in the process of the thesis is the validation work which was carried out by development of computational analogues of the spinal morphologies based on the reconstruction computer tomography CT scan imaging by the creation of detailed Three-dimensional FE model of an intact Lumbosacral segments that mimics the real biomechanical behavior of the human spine.

Flexible rods have been introduced for use with anterior interbody cages to achieve a more successful fusion. The hybrid dynamic stabilization to fusion was introduced to provide special protection against fusion-induced adjacent segment disease including adjacent segment degeneration and adverse effects.

The description of the mechanical behavior of the healthy and degenerative conditions of the intervertebral disc were quantified by developing the mechanical properties annulus fibrosus tissue using an anisotropic constitutive continuum model of Holzapfel as well as developing a realistic description of the nucleus geometry with optimization determination of the requisite material coefficients.

Key words: lumbar spine, flexible stabilization, spinal fusion, finite element, hybrid dynamic stabilization, adjacent segment disease.

Resumé

Le mécanisme et le traitement chirurgical des douleurs rachidiennes restent controversés. Comme son nom l'indique, la stabilisation flexible est basée sur le concept d'instabilité durant l'activité. Malheureusement, l'instabilité vertébrale n'est pas bien définie et est mal comprise. La fusion spinale reste la pierre angulaire du traitement chirurgical des douleurs dorsales. Cette procédure est pratiquée depuis près d'un siècle et aboutit généralement des résultats cliniques positifs. L'accélération de la dégénérescence du segment adjacent après le succès clinique initial de la fusion est assez commune. Le concept de stabilisation flexible a été développé à la suite de l'échec de la fusion pour fournir des résultats cliniques voulus.

Le but de cette thèse est d'étudier le traitement des troubles spinaux en utilisant des constructions de stabilisation flexibles. Ce travail vise à trouver la meilleure stabilisation qui restaure la cinématique des segments vertébraux du mouvement normal sans surcharger les éléments structuraux qui gouvernent le mouvement spécifique en utilisant une modélisation paramétrique par éléments finis EF, par conséquent la clé de base dans le processus de la thèse est le travail de validation, qui a été réalisée par le développement des analogues informatiques de la morphologie de la colonne vertébrale basée sur la reconstruction d'imagerie médicale tomodensitométrique et la création d'un modèle EF tridimensionnel détaillé du segment lombo-sacré intact pour imiter le comportement biomécanique réel du rachis humaine. Des tiges flexibles ont été introduites pour une utilisation avec des cages intersomatiques antérieures pour obtenir une fusion plus réussie. La stabilisation dynamique hybride à la fusion a été introduite pour fournir une protection spéciale contre la maladie du segment adjacent induite par la fusion, y compris la dégénérescence du segment adjacent et les effets indésirables. La description du comportement mécanique des conditions saines et dégénératives du disque intervertébral a été quantifiée en développant les propriétés mécaniques de la tissue annulaire fibrose en utilisant un modèle continuum anisotrope constitutif de Holzapfel et en développant une description réaliste de la géométrie du noyau avec la détermination de l'optimisation des coefficients matériels requis.

Mots clés: rachis lombaire, stabilisation flexible, fusion spinale, éléments finis, stabilisation dynamique hybride, maladie du segment adjacent.

ملخص

آلية العلاج الجراحي لآلام العمود الفقري القطني لا تزال مثيرة للجدل. وكما يوحي الاسم، فإن الاستقرار المرن يقوم على مفهوم عدم الاستقرار بوصفه سببا من أسباب النشاط . لسوء الحظ ، عدم الاستقرار في العمود الفقري غير محدد وغير مفهوم جيدا ، حيث أن الانصهار الشوكي لا يزال حجر الزاوية في العلاج الجراحي لآلام الظهر، وقد مورس هذا الإجراء منذ ما يقرب من قرن، ويؤدي عموما إلى نتائج استشفائية ناجحة. على الرغم من أن الانصهار ناجع في غالبية المرضى، في كثير من الحالات لوحظ استمرار آلام الظهر. وعلاوة على ذلك، الإنحطاط المعجل من الجزء المجاور رغم النجاح السريري الأولي بعد جراحة الانصهار شائع إلى حد ما. وقد تم تطوير مفهوم الاستقرار المرن نتيجة فشل الانصهار في تقديم النتائج الاستشفائية المطلوبة.

والغرض من هذه الأطروحة هو التحقيق في علاج اضطرابات العمود الفقري باستخدام بناءات استقرار مرنة. يهدف هذا العمل إلى إيجاد أفضل إستقرار يعيد حركيات شرائح العمود الفقري للحركة العادية دون إثقال العناصر الهيكلية التي تحكمها حركة معينة باستخدام نظرية العناصر المنتهية في النمذجة، وبالتالي فإن المفتاح الأساسي في هذه الأطروحة هو التحقق من صحة النموذج من خلال تطوير نظائرها الحاسوبية من مورفولوجيا العمود الفقري على أساس إعادة التشكيل الحاسوبي باستخدام صور التصوير المقطعي عن طريق إنشاء مفصل لنموذج ثلاثي الأبعاد لقطاعات قطنية عجزية سليمة التي تحاكي السلوك الحيوي الحقيقي للعمود الفقري البشري.

وقد أدخلت قضبان مرنة للاستخدام مع أقفاص أمامية لتحقيق انصهار أكثر نجاحا. الهدف من إدخال الاستقرار الديناميكي الهجين إلى الانصهار هو توفير حماية خاصة ضد المرض الناجم عن الانصهار الناجم عن اضطراب الجزء المجاور والآثار السلبية .

وصف السلوك الميكانيكي للظروف الصحية والتنكسية للأقراص الفقرية تم تحديدها من خلال تطوير الخواص الميكانيكية للنسيج الليفي للحلقة باستخدام نموذج تأسيسي متواصل من هولزافيل (Holzapfel) فضلا عن وضع وصف واقعي لهندسة النواة مع تحديد أمثل لمعاملات المواد المطلوبة.

الكلمات المفتاحية: العمود الفقري القطني، الاستقرار المرن، الانصهار الشوكي، العناصر المنتهية، الاستقرار الديناميكي الهجين، اضطراب الجزء المجاور.

Introduction

Lower back pain LBP results in a significant decrease in the quality of life and affects a substantial portion of the world's population. Currently, the gold standard for surgical intervention is the arthrodesis which involves removing the lumbar intervertebral disc, which is assumed to be causing the pain. This practice has existed for almost a century, and generally results in successful clinical outcomes. However, the lack of flexibility at the fused segments may lead to adjacent segment disease ASD. As a result, Flexible or namely Dynamic stabilization technologies have been introduced as a motion preserving alternative to spinal fusion.

So far, most clinicians like to believe that some form of spinal instability, be it abnormal motion and/or abnormal load sharing is a crucial factor in the pathophysiology of mechanical lower back pain to disc degeneration or facet pain. Thus, flexible stabilization indicates control of motion and/or load sharing of the motion segment, to address instability and the resultant lumbar pain.

The study of spinal flexible implants requires minimal knowledge of the spine, at least in terms of its geometry characteristics, its mechanical properties, the pathologies and surgical procedures associated with it. A better understanding of the biomechanical environment associated with spinal disorders is needed in order to properly assess device performance.

The current dissertation outlines several studies, which evaluated the biomechanics of spinal implants. We have established our dissertation based on several specific aims.

Specific Aim 1: Develop a validated finite element model of the healthy human lumbosacral spine.

The main objective of this dissertation was to develop a better appreciation of the biomechanics of treatment of spinal disorders and evaluate the contemporary treatment strategies through finite element modeling. To reach this objective, a FE model of the healthy human lumbar spine was generated based on the reconstruction of computed tomography CT scan imaging and radiographic apparent.

In Chapter 3, The basic key in the process of validation was stated by development of computational analogues of the spinal morphologies, by the creation of sophisticated three-dimensional Finite Element model of an intact ligamentous L1-S1 motion segment, that matches the real biomechanical behavior of the human lumbosacral spine and for this purpose, the validation was carried out in all 6 DOF. It has the possibility of representing the realities with a much higher degree of fidelity. Lumbar functional spinal unit (L4-L5) are investigated using finite element method, and the effects of these relationships on the nonlinear moment-rotation predictions are interrogated. Mesh convergence was verified based on kinematic and mechanical predictions, including range of motion ROM and intradiscal pressure IDP.

This effort and the employed methodology are extended to generate a finite element model of the lumbar spine (L1-S1) in Chapter 3, with particular detail attention ascribed to the mesh refinement and validation protocols.

Specific Aim 2: Simulate the implantation of rigid and flexible (dynamic) constructions, and evaluate the changes in biomechanical behavior of the spine compared to the healthy, destabilized and stabilized states.

In Chapter 4, 5, implementation of the flexible, rigid stabilization systems into the validated finite element model is documented, and the effects of lumbar arthroplasty using conventional arthrodesis and innovative stabilization systems are assessed within the framework of the healthy and degenerative states of the lumbar intervertebral disc.

Specific Aim 3: Develop a nonlinear, anisotropic, constitutive relationship for the mechanical behavior of degenerated human annulus fibrosus AF, and implement this into the previously developed finite element model of lumbar spinal functional unit

Degenerative disc disease is a major source of low back pain. It is hypothesized to significantly alter the biomechanics of the lumbar spine both at the tissue and motion segment (multi-vertebral) levels. However, explicit correlations between the former and the latter has not been established, and this critical link is only possible through modeling the intervertebral disc tissue behavior within a constitutive framework and implementing it in a finite element model of the lumbosacral spine.

In Chapter 6, anisotropic Holzapfel's constitutive models are implemented into the validated finite element model of a lumbar functional spinal unit L4-L5 in order to simulate degenerative disc disease DDD (that is developed and validated in Chapter 3), and the effects of degeneration on local and global biomechanics of the spinal motion segments are reported.

The Laboratory of Numerical and Experimental Modeling of Mechanical Phenomena LMNEPM since couple of years has started research in biomechanical modeling. This laboratory activity was initiated by the creation of the Muscoloskeletal biomodel in 2014 by respectively developing detailed models of the lumbar spine, and subsequently thoracic and cervical spine. The advantages of these modeling are in particular a perfect reproducibility and the parameterization of the model which makes it possible to understand the behavior of the spine. The Laboratory of LMNEPM has been at the heart of the development of a personalized biomechanical finite element model, and the surgical procedure that can be associated with it.

Finally, we have endeavored to show the relevance that this type of modeling can offer the biomechanical understanding of "implant-patient" interactions.

Chapter 1:

Background

1.1 Introduction

The mechanical behavior of the human spine is characterized by remarkable diversity. On the one hand its flexibility allows a wide range of mobility. The thoracic and the lumbar part of the spine contribute up to sixty degrees to forward bending, fifty degrees to side bending and approximately the same amount to rotation. On the other hand, the spinal column can sustain internal compressive forces of a multiple of the body weight. This broad range of functionality is based on twenty-four mobile vertebrae which interact with each other in a complex system of facet joints, intervertebral discs, and ligaments. The gel like intervertebral disc transfers loads between the vertebral bodies and also absorbs energy from vibrations and impact situations. Due to its complex structure and the proximity of the spinal cord, which is surrounded by the vertebrae, surgical interventions of the spine are particularly delicate. However, such interventions may become necessary for indications such as degenerated discs, unstable segments or severe cases of spinal deformities. A bony fusion, which is also called arthrodesis, is the widely accepted standard treatment for these indications. The purpose of an arthrodesis is to mitigate or eliminate the pain that comes from the movement of degenerated discs or joints. In the case of spinal deformities, a fusion maintains the spine in the corrected position or prevents the progression of the deformity.

The first spinal fusion was performed in 1911 for the treatment of spinal tuberculosis by both Hibbs and Albee. Three years later, Hibbs performed the first spinal fusion surgery for scoliosis treatment. Yet it was only in 1929 that Chandler adopted spinal fusion for the treatment of lower lumbar back pain. The vast majority of fusions performed nowadays are for the treatment of back pain, due to its high prevalence, whereas spinal deformities account for only a small fraction.

Since then, numerous new methods and techniques have been introduced to

improve the fusion of the bones. Pedicle screws allowed for the attachment of rods to stabilize the spine posteriorly. Anterior stabilization can be advantageous in some cases, which is achieved with plates mounted to the vertebral bodies, or intervertebral cages. A review of the literature shows that there was a statistically significant increased fusion rate in instrumented surgeries, compared to noninstrumented procedures [4]. Nevertheless, the application of spinal fusion has been controversially discussed in the last three decades, especially for the treatment of degenerative diseases. This is mainly due to the fact that follow up studies generally do not report a significant improvement in the clinical results with instrumentation [4]. Regardless of which indication the spinal fusion relies on, there are other concerns: adverse effects on adjacent segments. Biomechanical studies have shown that the relative immobility of the fused segments changes the mechanical environment [7, 20]. The drastic increase in stiffness of the fused segment consequently leads to increased motion and stress concentrations in adjacent levels [13]. In a clinical study, Ghiselli et al. [24] reported that about one third out of 215 patients who underwent lumbar fusion surgery had degenerated adjacent segments ten years after surgery. Gillet et al [26] reported similar results in a follow-up study up to fifteen years after initial surgery. 41% of the patients showed signs of degeneration, 20% required corrective surgery. However, there is still a controversy whether the adverse effects are just the naturally progressing degeneration or if it is a consequence of the fusion.

Arthroplasty is an alternative to spinal fusion. Motion preserving implants for the treatment of degenerative disc disease have been available for about twenty years. The first long-term clinical results suggest that adjacent level effects are less frequent, compared to spinal fusions. Two recent studies [8, 21] with about 100 patients and a follow-up of at least ten years reported that the rate of adjacent levels requiring surgical intervention was 2.5%, and 5%, respectively. These results support the hypothesis that adjacent level effects are due to the spinal fusion and not due to the natural progression of the degeneration.

Motion preserving treatment of spinal deformities is even more challenging than for degenerative diseases, mainly because not only one segment, but a big portion of the spine is affected. The only non-fusion treatment is currently available for early-onset scoliosis which is a term used for deformations at children under the age of five. The

principle of the treatment is to use a growing rod which allows for spinal growth and corrects the curvature. Each lengthening is performed in a surgical procedure. However, many patients require a definite fusion, once they reached a certain age or size. For adolescent idiopathic scoliosis, which is the most common form of scoliosis, a fusion of a big part of the spine still is the only way to correct severe curvatures and prevent progression.

Theoretically, fusionless or mainly the flexible stabilization treatment strategies have the advantage of preserving motion, thus maintaining the functionality of the spine, and allowing for a physiologic growth of infantile and adolescent patients. Furthermore, the degeneration of adjacent levels may be reduced as this effect seems to be strongly influenced by the fusion of one or more segments. However, the development of more advanced implants and treatment strategies also requires a more detailed knowledge of the pathological and healthy mechanical properties of the spine. The mechanical behavior of a fused segment is based on static, load sharing principles. Motion preserving designs also require a profound knowledge of the kinematic and dynamic properties of the spine in order to properly characterize the in vivo performance of the implant.

This chapter outlines to the objectives of this thesis. A brief overview of the functional anatomy of the spine explains how its mechanical behavior is related to its main anatomical components and structures, i.e. ligaments, intervertebral discs and facet joints. The state-of-the-art experimental methods in spinal biomechanics are then reviewed and their advantages and disadvantages are discussed. Beside experimental data, mathematical models give important insight into the behavior of the spine. A review of numerical models shows which research questions can be addressed and which constitutive laws are used to model the different anatomical structures of the spine. Mathematical models can be solved in two ways: If the mechanical properties are given the solution can be determined, which is called direct problem. If the mechanical properties are to be computed based on experimental data, an inverse problem has to be solved. In the last section of this chapter the objectives and structure of this thesis are presented.

1.2 The Spine

This succinct presentation of the anatomy of the spine is intended primarily for

mechanics. It aims to familiarize the reader with the different clinical terms.

After a quick presentation of the reference plans for the anatomical description of the human body, we will focus on the descriptive anatomy of the healthy lumbar spine by deliberately limiting ourselves to the osseoligamentous system.

1.2.1 Reference planes

The study of the human body is based on the fundamental planes of space (Figure 1.1):

• Sagittal planes: these are vertical planes oriented in the anteroposterior direction. The median sagittal plane passes through the axis of the body and divides it into two right and left side

• The coronal (frontal) planes: The coronal plane is the frontal plane passing through the axis of the body, it defines the ventral and dorsal sides of the body.

• The axial (horizontal) planes: they are perpendicular to the two others and cross the body transversely.

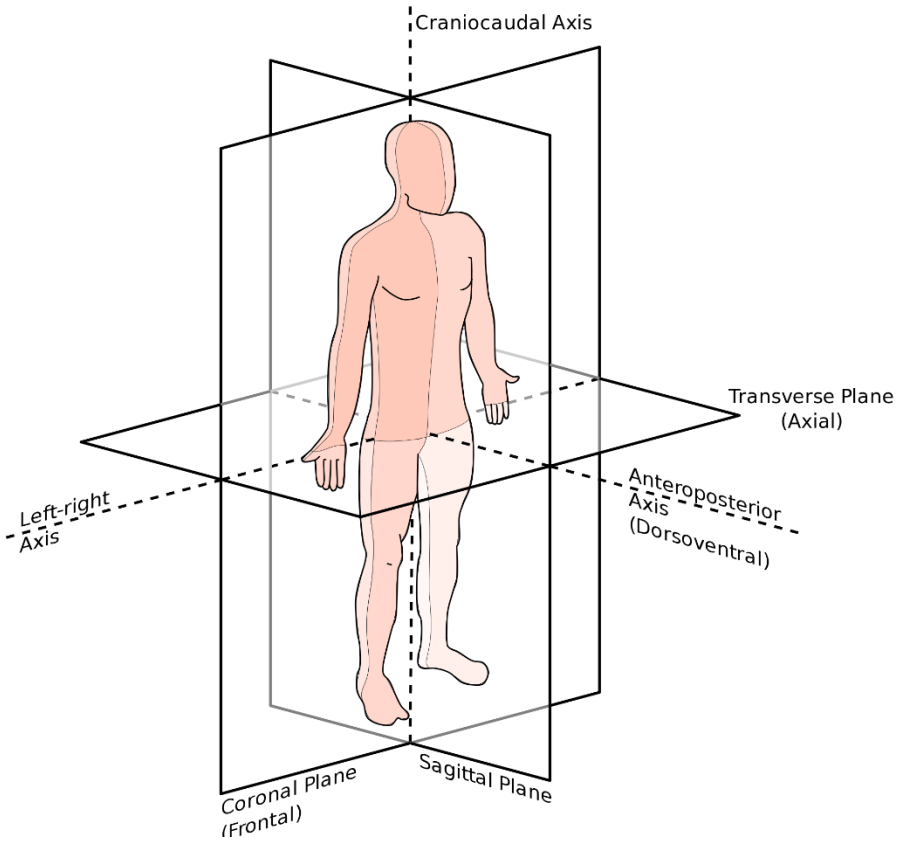

Figure 1.1: Reference planes and axis [66].

1.2.2 Descriptive Anatomy of the Spine

The spine, or vertebral column, consists of a movable column of twenty-four free bony parts and a fixed column formed of welded or fused vertebrae which are connected to each other in an elastic system, consisting of intervertebral discs and ligaments: the sacrum and the coccyx. It is the mast of fixation of many muscles essential for the posture and the locomotion and ensures the protection of the spinal marrow located in the vertebral canal. It supports the head and transmits the weight of the body to the joints of the hip. About 70 cm long in men (60 cm in women), its decrease can reach 2 cm when standing

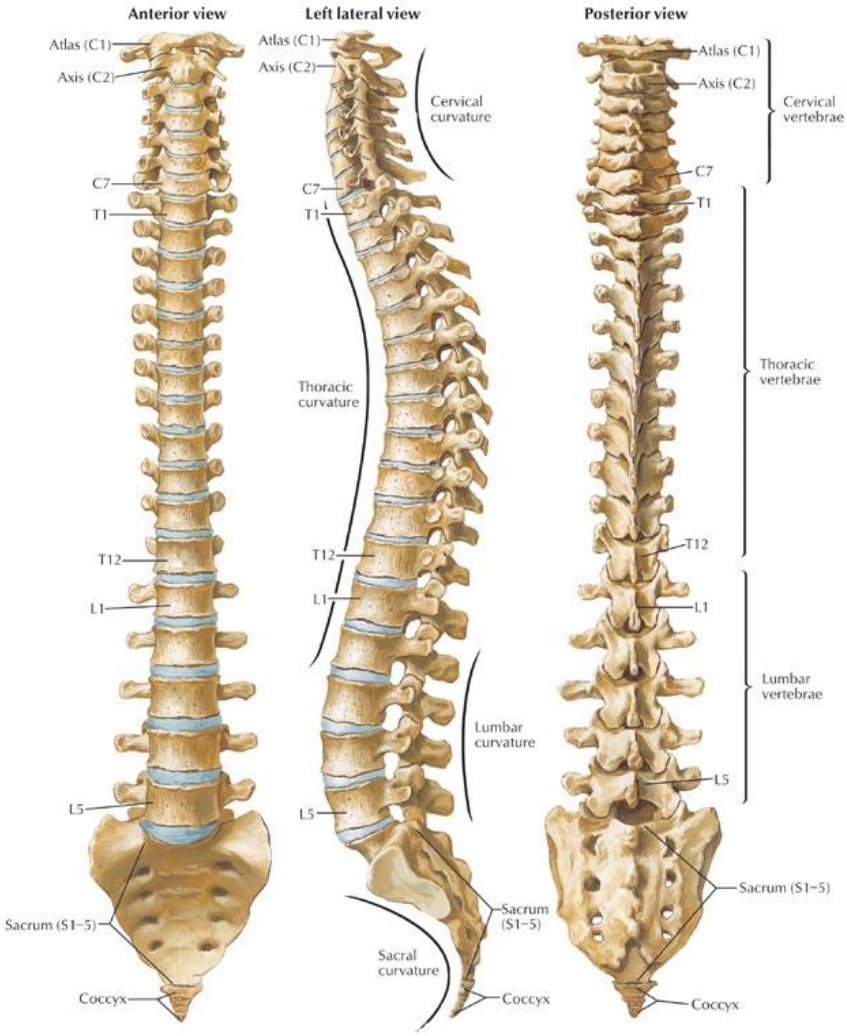

Figure 1.2: The spine [67].

The vertebrae can be divided into an anterior and a posterior part. The anterior part consists of the vertebral bodies, which are piled one upon the other, thus forming the

vertebral column. The pedicles, two lamina and seven processes make up the posterior part (Figure 1.3).

The backbone is bent in the sagittal plane. It presents two primary curvatures (concave forward), as called kyphosis, to the level of the thoracic spine and sacrum, as well as two secondary curvatures (concave behind) named lordosis to the level of the cervical spine and lumbar.

The spine can be grouped in five parts (Figure 1.2):

The cervical spine constituted of 7 vertebrae.

The dorsal spine (or thoracic) constituted of 12 vertebrae.

The spine lumbar (or lumbar) constituted of 5 vertebrae.

The sacral spine (or sacrum) and the coccyx.

1.2.2.1 Bony Vertebrae

The two major components of the vertebrae are the cortical and trabecular bone. While the former is significantly stiffer and denser, the latter has a sponge-like porous structure which produces a globally more compliant behavior. Several studies have shown that aging leads to different levels of reduction in the solid volume fraction in trabecular bone, and, in severe cases, this leads to osteoporosis. Adams et al [46]. Moreover, physiological loading is known to affect the bone remodeling process, with the major trabecular orientation coincident with the principal loading directions. Freiberg et al [49]. The orientation of the trabeculae shows a clear vertical and horizontal alignment. The pedicles and the lamina form the neutral arch, which en- closes the spinal cord. From the neural arch, the spinous process projects backwards, the two transverse processes project to the side. These three processes serve as attachment and lever arms for ligaments and muscles. With two superior and two inferior articular processes, the vertebrae interact with adjacent levels (Figure 1.4). Mechanically, the anterior vertebral column can sustain compressive forces, while the posterior parts, which are connected to each other only by ligaments, can only sustain tensile forces.

In the anterior column, a stiff cortical shell encloses a trabecular core, and this structural feature becomes especially advantageous under compressive loads. The cortical endplate distributes the load almost uniformly over the trabecular bone, providing additional support at the radial extrema. The posterior elements have an extremely

complex geometry, and the "spinal canal" encompasses the volume between these elements and the vertebral bodies (Figure 1.3). This provides a physical, protective environment for the spinal cord. A total of four facets in the inferior and superior regions form the zygapophyseal joints through articulation with superior and inferior adjacent vertebral levels.

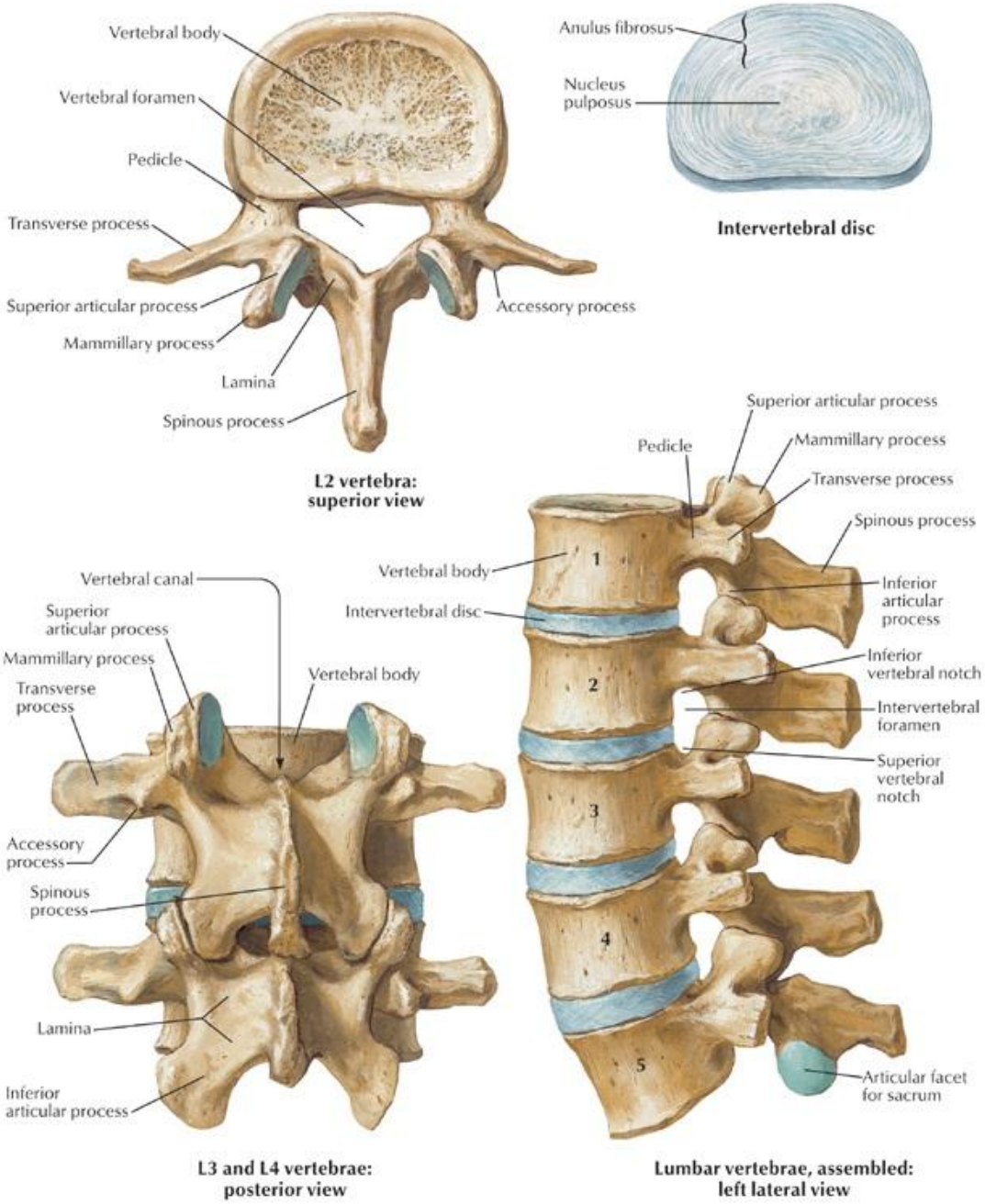

Figure 1.3: The lumbar spine anatomy [68].

Bilateral transverse processes and the pedicles at the posterior extremities serve as ligament insertion sites, transmitting force between each level and improving stability.

The reduction in the bone quality in many cases is followed by endplate fractures or critical damage on the vertebral bodies, preventing the vertebra from carrying out its primary load-carrying function. Bogduk [52]. Bone cement injection and vertebroplasty are current techniques of surgical intervention which seek to provide immediate stability to the spine.

The aforementioned types of bone tissue are known to undergo infinitesimal deformations *in vivo* during the activities of daily living. Therefore, a simplistic approach such as linear elasticity is sufficient for describing the physiological mechanical response of these tissues. Crawford et al [51]. Orthotropic and fully isotropic constitutive relationships have been proposed, and a large range of elastic moduli values are reported in the literature.

1.2.2.2 Spinal ligaments

Spinal ligaments have a significant effect on the mobility of motion segments, and, therefore, are crucial for understanding and predicting spinal biomechanics. Zander et al [56]. Similar to tendons, ligaments primarily consist of Type I collagen, elastin, PGs and water with minor amounts of other proteins and different types of collagen. Panjabi et al [17]. With the collagen fibers aligned in the usual loading direction, their mechanical behavior is highly anisotropic. Transverse isotropy is a sufficiently accurate model to describe and model this behavior. Woo et al [60].

The presence of the collagen fiber results in a highly nonlinear static tensile behavior and increases the global strength of the tissue. The mechanical properties of spinal ligaments have been quantified in numerous studies in the past, and substantial differences are observed between the responses of different ligaments. Zander et al [56] (Figure 1.4).

There are seven major spinal ligaments that connect the vertebral bodies and the posterior elements in the lumbar region: Anterior longitudinal ligament (ALL) runs through the entire spine from the sacrum to the cervical region, inserting into the anterior surfaces of the vertebral bodies and covering their associated intervertebral discs. Similarly, the posterior longitudinal ligament (PLL) extends in the same range in the

inferior – superior direction, inserting into the posterior surfaces of their associated vertebral bodies along the spinal canal (Figure 1.5).

On the posterior side of the spinal canal, the ligamentum flava (LF) connect the laminae of each vertebral body to its subsequent inferior and superior levels. Likewise, the Intraspinous ligament (ISL) inserts into spinous processes at the inferior and superior ends and supraspinous ligament (SSL) inserts into the posterior edges at each level. Capsular ligaments (CL) provide additional stability around the facets, covering the entire zygapophyseal joint. And the intratransverse ligaments intratransverse ligaments (ITL) connect the costal process of two adjacent vertebra.

Ligaments are connective tissues that are characterized by a preponderance of collagen fibres and a small content of ground substance, cells and fluid. Thus, the mechanical behaviour reflects the combined properties of an elastic solid and a viscous fluid: Ligaments are viscoelastic. At low strain rates, the viscous element has a negligible effect, so that the tissue behaves predominantly like an elastic structure.

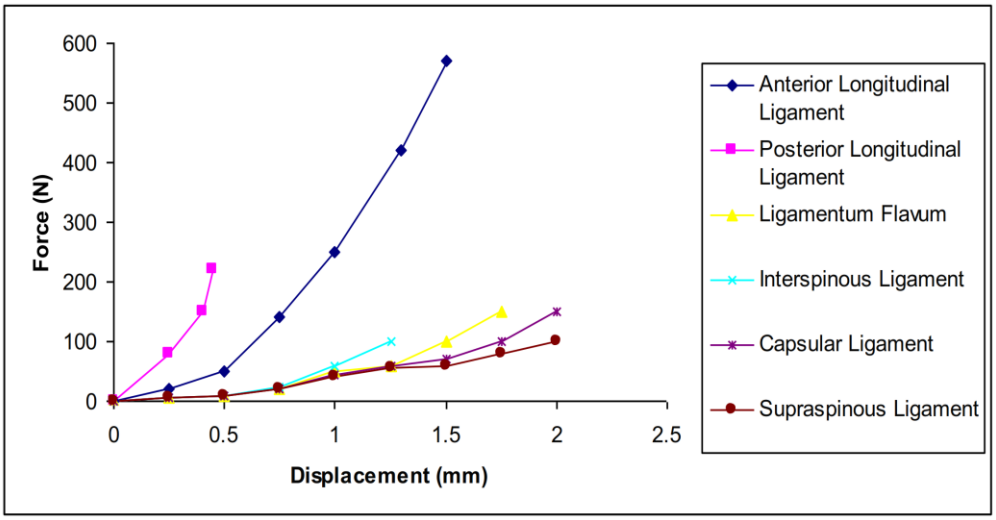

Figure 1.4: Tensile mechanical behavior of spinal ligaments. Figure reprinted from Ayturk et al [69].

The collagen fibers, arranged in parallel bundles, are responsible for the mechanical properties. The tensile strength of ligaments is therefore much bigger in the longitudinal direction than in orthogonal directions. The anterior longitudinal ligament stretches along the front side of the vertebra body (Figure 1.6). With its deep fibres it connects adjacent vertebral bodies and with its superficial fibres it bridges several segments. The collagen

fibres are firmly interwoven with the vertebral bodies, but only loosely connected to the discs. (Figure 1.7).

The posterior longitudinal ligament is situated in the vertebral channel and extends along the backside of the vertebral bodies. The ligament is thicker at the intervertebral disc space than at the vertebral bodies. The superficial layers of the ligament occupy the space between three or four segments, while the deep layers stretch between adjacent vertebrae. The ligamentum flavum extends between the vertebral arches of adjacent vertebrae. It has the highest percentage of elastic fibres of any tissue in the body. Nachemson et al [25]. In upright posture, the ligamentum flavum is under pre-tension. The intertransverse ligament extends between the transverse processes, the interspinous ligament between the spinous processes of adjacent vertebrae. The supraspinous ligament connects the apices of the spinous processes. The superficial layer of the ligament extends over three or four segments, while the deep layers stretch between adjacent vertebrae.

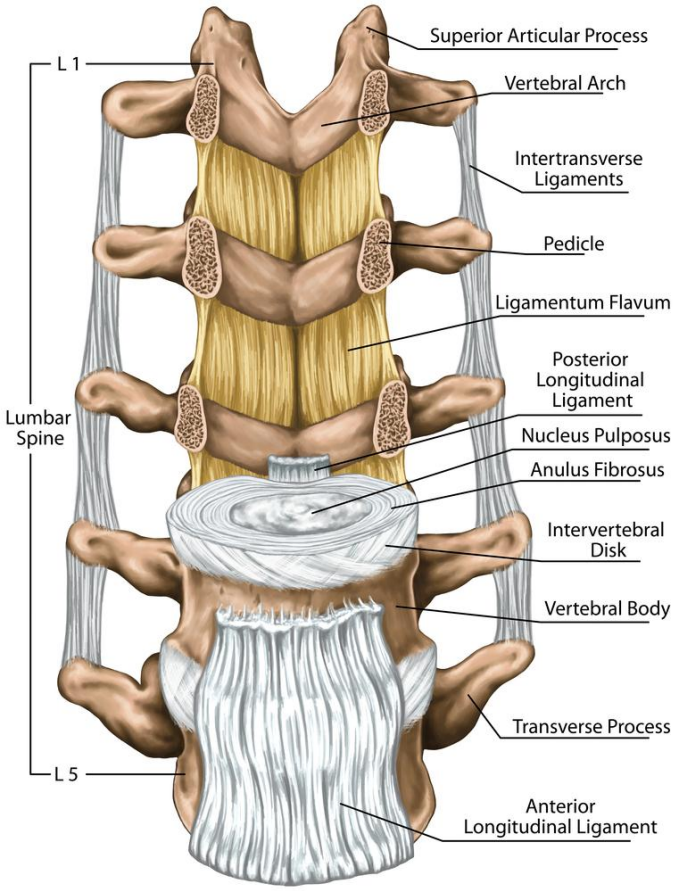

Figure 1.5: Anatomy of the spine: Ligaments of the vertebral column [70].

1.2.2.3 Intervertebral disc IVD

Each intervertebral disc is bound to the vertebral bodies which connects two vertebral bodies inferiorly and superiorly through cartilaginous endplates (Figure 1.3). while at the same time allowing them to move relative to each other. To the naked eye, two distinct structures can be distinguished: An outer ring of concentric lamellae of collagen fibres, called annulus fibrosus (Figure 1.3). The central region, called nucleus pulposus, is characterized by a high proteoglycan and thus water content. The cartilaginous endplates are interposed between the bony vertebral bodies and the intervertebral disc itself.

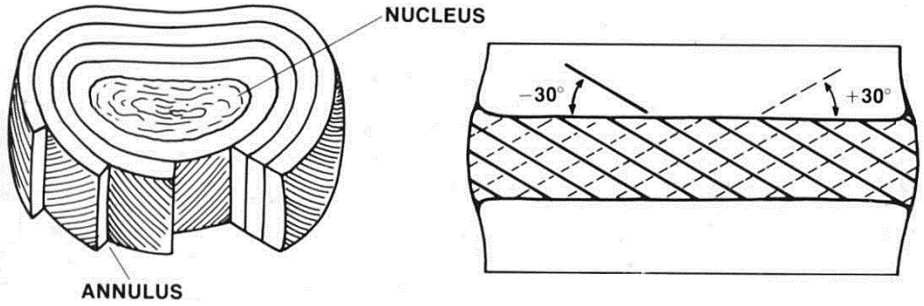

Figure 1.6: Intervertebral disc. Annular fibers and their orientation [17].

Water, collagen, and proteoglycans constitute 90%-95% of the volume of the normal disc [41]. The interplay of these components determines the mechanical behavior of the intervertebral disc. Water and proteoglycan content are highest in the nucleus and lowest in the annulus, whereas the collagen distribution is inverse. The semi-permeable endplates are the primary source for the flow of water into and out of the intervertebral disc. Proteoglycans are negatively charged and thus imbibe water until the hydrostatic pressure is in balance with the external forces. These external forces come from the stresses in the collagen fibres and the active forces applied by ligaments and muscles. If the active forces are increased, fluid is expressed and the proteoglycan concentration and hence the osmotic pressurizes. Alternatively, if the active forces are decreased, fluid is imbibed, and the osmotic pressure falls. The inflow and outflow of water is relevant only for long-term loadings situations. Malko et al [23] reported that the disc volume increased by approximately 10% during overnight bed rest and decreased by 5% after eight hours of walking. When loads to the spine are applied only on a short-term basis, the fluid flow can be disregarded. For such loading scenarios, the intervertebral disc can be considered as a hydrostatic system with membrane-like outer shell.

Nutrients are transported to the avascular discs through these hyaline cartilage tissues via diffusion. Furthermore, these tissues are innervated at the periphery. Aging and/or chemically induced degeneration produces distortion and mineralizes the endplates, which is believed to cause significant pain, as well as increase the risk of endplate fracture and collapse of the intradiscal space. Decreased permeability of the endplates is shown to change the mechanical loading environment inside the disc. Natarajan et al [55]. The elasto- static behavior of this tissue is usually accepted as linear in the non-degenerated discs. Dooris, et al [47]. Schmidt et al [57].).

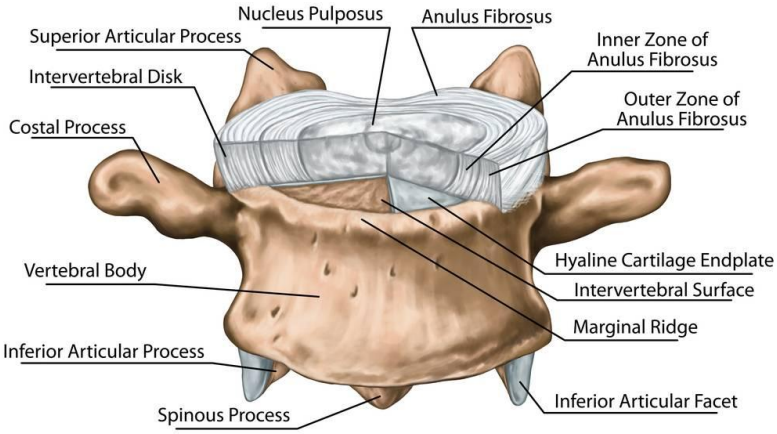

Figure 1.7: Components of the vertebrae and the intervertebral disc [70].

The core of the intradiscal space, the "nucleus pulposus", is a proteoglycan-rich viscous material. Negatively charged glycosaminoglycans (GAG), proteoglycans (PG), Type II collagen and water are the main constituents of this tissue. The random orientation of the collagen fibers demonstrates the lack of a structured organization, which consequently generates an isotropic mechanical response. Guerin et al [48]. Furthermore, the negative charges and the presence of PGs result in a high swelling pressure throughout the tissue. This pressure is substantially elevated under the application of compressive loads, and balances itself by creating circumferential "hoop" stresses in the annular lamellae. Adams et al [46].

The anisotropic behavior of the annulus can be described with a transverse isotropy model within a cylindrical coordinate system. Three-dimensional finite element modeling (FEM) approaches allow for the geometric representation of individual fibers, and consequently reinforcement in the preferred orientation. Dooris et al [47]. This approach gives satisfactory results in terms of predicting the global, structural kinetic response;

however, modeling of the tissue-level mechanics of the annulus requires a more rigorous technique. Figure 1.8.

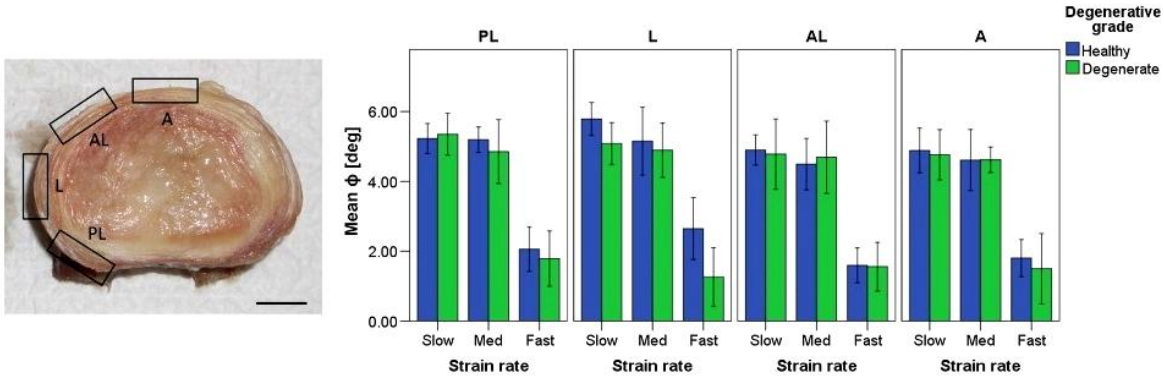

Figure 1.8: strain rates of the human lumbar annulus fibrosus specimens under tensile loading bundles. Pham et al [61].

Spencer's continuum model for orthotropic materials with multiple fiber families has been employed in previous studies to achieve adequate modeling fidelity (Spencer, 1984). The invariant-based strain energy potentials can be decomposed into individual components of physiological relevance (potentials of the proteoglycan-rich matrix, tissue incompressibility, collagen fibers, etc.) Wagner et al [58]. Guerin et al [48]. in order to simulate the nonlinear mechanical behavior of the annulus fibrosus (Figure 1.9).

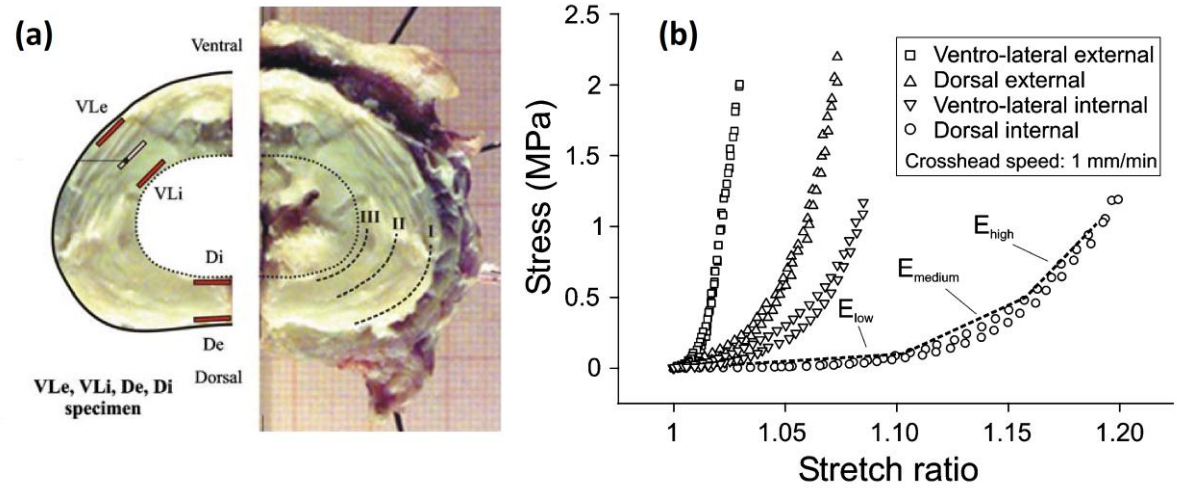

Figure 1.9: Annulus fibrosus. a) Cut in the horizontal plane with, four regions are distinguished: ventro-lateral external (VLe), ventro-lateral internal (VLi), dorsal external (De) and dorsal internal (Di), b) Stress-stretch relation of single lamellae. Figure reprinted from Holzapfel et al [17].

The fibres of the annulus anchor into the endplates where they align horizontally. In the lumbar region of the spine, the fibres are arranged in 10-20 concentric lamellae and with alternating orientation in each layer. Commonly, angles of ±30° with respect to the horizontal plane are given in the literature. However, recent studies indicate a more complex situation. Skaggs et al [37] conducted measurements on single lamellae and reported that lamellae from the posterior region have a significantly lower stiffness, than those of the anterior region. This observation is confirmed by Ebara et al [19] who conducted experiments on multi-lamellae specimens. Holzapfel et al [17] reported a significantly higher stiffness of external lamellae than of internal lamellae (Figure 1.9). The orientation of the collagenous fibers was more vertical in the posterior part compared to the anterior regions. Skaggs et al [37] made the important observation that adjacent lamellae with different fiber orientations have the same tensile modulus.

1.3 Functional Anatomy of Human Lumbar Spine

The human lumbar spine is a load bearing structure that carries and transfers the weight of the upper body to the lower extremities through the sacrum and the pelvis. Its mechanical function is not only limited to resisting multi-dimensional loads, but it also confers a certain range of mobility to the upper body via tissue deformation.

The behavior of the lumbar spine under physiologic loads and moments on this multi-joint complex yield different ranges of segmental motion (ROM) at each level (Figure 1.10). However, this load- displacement relationship is commonly nonlinear. Furthermore, relatively small loads generate large displacements due to low tension in the ligaments and the intervertebral disc, resulting in an initially compliant kinetic response known as the neutral zone. The neutral zone (NZ) is regarded as a measure of the joint laxity, and its magnitude can be significantly altered as a result of injuries to the disc such as degeneration or herniation. Mimura et al [54]. Excessive changes in the extent of the NZ have been theorized to be predictors of spinal instability, and therefore, it is an important diagnostic parameter in detecting the aforementioned injuries and diseases.

There is an increasing trend of range of motion in the inferior direction from L1 to S1; however, no significant differences are reported except between the lumbosacral level and all of the intra-lumbar levels. Guan et al [50].

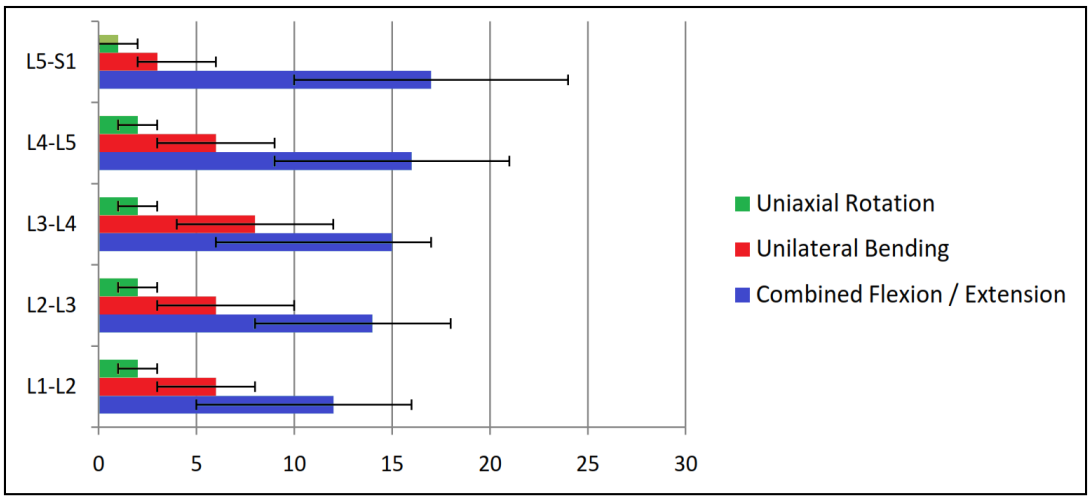

Figure 1.10: Average physiological ROM (in degrees) of lumbar motion segments in principal loading axes. Error bars indicate the normal physiologic limits. Panjabi et al [17].

1.4 Experimental methods in spinal biomechanics

The mechanical testing of load-bearing structures of the human body implicates many more difficulties than in classical engineering disciplines. In vitro tests of human spines have the advantage that experiments can be performed under well-defined and controlled conditions and thus allow the investigation of its normal function. However, the limitations of testing specimens outside their physiologic environment are difficult to quantify. When testing human spines, a crucial question to answer is how many spinal segments should be taken. A motion segment is the smallest functional unit, which consists of two vertebrae, the intervertebral disc, and the intervening soft tissue. Some ligaments, as the supraspinous ligament or the anterior and the posterior longitudinal ligaments have superficial fibres which extend across several segments and which have to be dissected. Another issue concerns the support of the specimen and how the loads should be applied. When performing measurements on a single motion segment, neither of the vertebrae is supported physiologically. Intervertebral discs and ligaments have to be kept moist to prevent changes of the mechanical properties. In order to reduce the complexity, muscles are usually completely dissected. Eventually, cadaver spines usually originate from middle aged or elderly people and thus limit the generality of the results.

On the contrary, in-vivo experiments allow measurements under physiologic conditions, and at patients with the pathology of interest. However, due to ethical

reasons the possibilities of performing invasive measurements at the spine are limited. Also, the anatomical accessibility is usually restricted and tests cannot be performed to the fatigue limit. Moreover, boundary conditions of the vertebrae in the in vivo surrounding are unknown.

1.4.1 Spinal loading simulator

In the mid 1970s, the first mathematical models of the human spine were developed to address clinical problems, as sports injuries, scoliosis, and stability of the spine. In order to have data available as input for these models, Panjabi et al [54] performed the first experiments in which the three-dimensional load-displacement behaviour of single thoracic motion segments was determined. To account for more physiologic loading scenarios, one year later, Panjabi et al [31] conducted experiments including axial pre-loading. The axial pre-load originates from the body weight above the segment and from contracting muscle forces that counter-balance the moments from the weight of the body lying anterior of the center of rotation of the vertebrae. Panjabi [28] also emphasized the necessity to examine the behaviour of the spine in three-dimensional space, as before predominantly the uniaxial behaviour of the intervertebral disc has been studied.

Later, the methodology and testing framework has been refined. Panjabi et al [29] suggested to apply pure bending moments in the main anatomical directions when testing spinal segments. This was a pragmatic decision, as physiological loading conditions are not only hard to define, but also difficult to simulate on a test frame. Pure bending moments have the advantage, that the moment loading is constant along the entire specimen. This strategy became the standard for the mechanical testing of spines. A variety of custom-made testing frames, which were called spinal loading simulators, were reported in the literature. These include systems which were based on pulleys and cables [4, 21, 40], stepper motors on a gimbal that can move with a travelling gantry. Wilke et al [42] or Steward Platforms. Stocks et al [39].

Spinal loading simulators were used to determine the mechanical properties of cadaver spines. Due to the high prevalence of low back pain, studies have been conducted predominantly on the lumbar spine. Moment-angle relations were investigated by Guan et al [17], Oxland et al [26], and Panjabi et al [32]. Experiments to

examine the influence of functional spinal structures have also been performed. Heuer et al [15, 16] consecutively removed ligaments, facet capsules, and the nucleus and measured the moment- angle relation after each step.

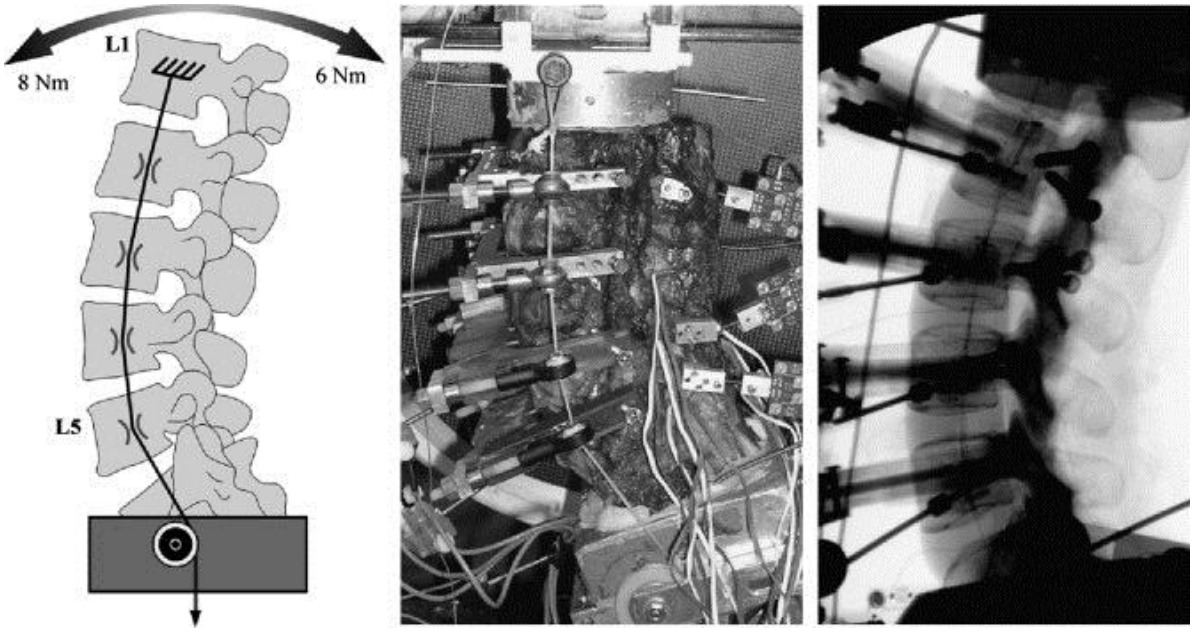

Figure 1.11: Mechanical testing of human lumbar spine, Frank et al [44].

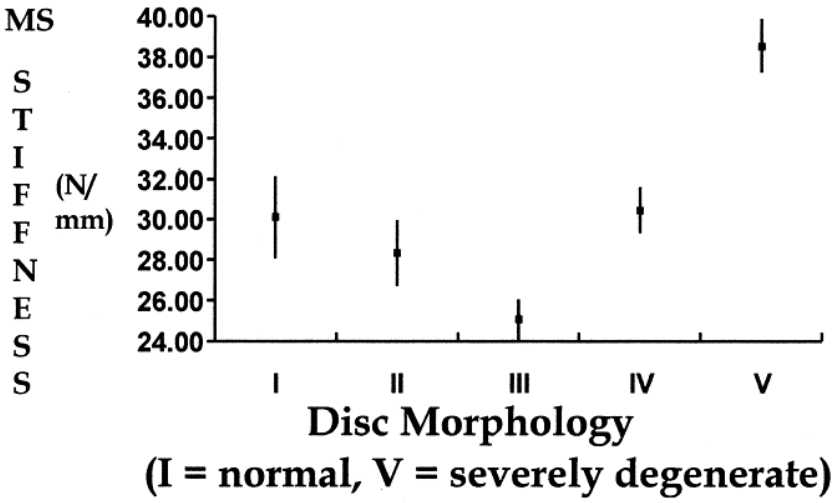

Figure 1.12: Literature review: Correlation between the measured stiffness of the motion segment and the disc morphology, Figure reprinted from Brown et al [5].

1.5 Mathematical models of the spine

Computational models supplement experimental methods when investigating the mechanics of the spine. As it was mentioned before, in vitro experiments allow to analyze the normal behavior of the spine, but the generality is limited by the availability of

cadaver specimens and the variability among them. In vivo measurements provide information of the spine in its physiologic environment, but are restricted due to the necessity of minimal invasiveness. Numerical models allow to assess internal forces, stresses and strains which cannot be measured in laboratory or in vivo experiments. However, numerical models depend on experimental data as input for constitutive laws and thus incorporate the limitations of the experimental methods. Although modern imaging technology, computing power and advances in theoretical mechanics allow for a more realistic modelling, simplifications.

1.5.1 Models considering the elastic behavior

Models that describe the elastic behaviour of soft tissue establish the vast majority. The first FE model of the human spine was developed by Belytschko et al [3]. The vertebral bodies were defined as rigid beams, while the IVDs were modelled as linear elastic beam elements and the ligaments as linear elastic truss elements. Geometric non-linearities were already accounted for, but it was assumed that the deformation of each element is small. One year later, the first model of the intervertebral disc taking into account the cross-sectional geometry was reported by the same author [2]. The disc was considered as an axisymmetric body and the annulus was modelled as an orthotropic material. A three-dimensional simulation of an entire motion segment considering symmetry about the sagittal plane, including facet articulation was reported by Shirazi-Adl et al [36], the annulus was modelled as a composite material of collagenous fibres embedded in a matrix of ground substance. Few studies did not only take into account non-linear geometry, but also used non-linear stress-strain relations for fibres and ligaments. Embedding discrete truss elements in the ground substance is still a frequently used method for modelling the annulus fibrosus [36, 63, 64].

The development of a general, anisotropic continuum theory allowed to overcome the grid dependency of embedded truss elements. The continuum mechanical approach offers another crucial advantage: The tissue properties can be determined directly from experiments. In contrast to the discrete modelling, the behaviour of the individual constituents, i.e. ground substance and fibers, have to be determined explicitly. For a long time, information on collagen fibrils could only be determined from complete tissues. Only recently, force-displacement curves from isolated, single collagen fibrils

were determined with atomic force microscopy. Graham et al [13].

The basic concepts of the continuum theory of fiber reinforced composites were established by Spencer et al [38]. These fundamental principles were the basis for the definition of non-linear stress-strain relations considering the laws of thermodynamics. For most material definitions to conduct quasi-static simulations, the reversibility of an elastic deformation, or in other words, no increase of entropy is assumed. This postulates the existence of a potential, which is a measure for the energy stored in the deformation and thus is called strain energy density SED function. An elastic material that can be defined by a strain energy function, is called hyperelastic material or Green-elastic material. The assumption of hyperelasticity is frequently used for the definition of non-linear elastic materials, as the stress state can be determined directly by deriving the strain energy function with respect to the deformation. Ayturk et al [62].

The first anisotropic, hyperelastic model based on a continuum theory for the annulus fibrosus was proposed by Klisch and Lotz [18]. The authors conducted simultaneous regressions based on four experimental data sets to determine the nine constants of their proposed exponential strain energy function. The specimens used for testing consisted of multiple lamellae and were harvested from different regions of the annulus fibrosus. Eberlein et al [9] proposed an exponential strain energy function with four parameters, which is reduced to three parameters when incompressibility is assumed. Experiments with single annulus lamellae were conducted for the determination of the material parameters.

Recently, eight FE models were employed in study included five lumbar vertebra These FE models simulated the intact lumbar spine under static loading conditions. Dreischarf et al [65]

1.5.2 Models considering the viscoelastic behavior

It is well known that collagenous soft tissues exhibit both elastic and viscous, i.e. time-dependant behavior. Viscoelasticity is characterized by creep and stress relaxation, dependence of strain rate, and hysteresis in a loading cycle. The shear stresses in a viscous fluid are proportional to the velocity gradient or the strain rate, respectively. Therefore, when testing the quasi-static mechanical properties of ligaments, slow loading rates are applied. The reported rates to apply forces in tensile tests vary from 1 mm/min

(Chazal et al [6]) to 10 mm/s (Yoganandan et al [43]). Pioletti et al [35] conducted experiments with anterior cruciate ligaments from bovine calves. Up to strain rates of approximately 5% identical stress-strain curves were obtained. A distinct dependency of the stress-strain curve was only noticeable for higher strain rates. Consequently, models, which include viscoelastic soft tissue properties aim to simulate the dynamic behaviour of the human spine. Injuries of the cervical spine may be severe because they have the potential to damage the spinal cord. Numerous models addressed this issue, commonly using an elastic constitutive law for the ligaments and the annulus fibrosus. Panzer et al [33] recently reported a model of the entire cervical spine which includes strain rate dependent properties for the ligaments to investigate the behaviour in frontal car crash scenarios.

1.5.3 Biphasic material behaviour

The fact that the annulus is less hydrated than the nucleus was the basis for the separation of fluid and solid phase in the models employing elastic and viscoelastic constitutive laws. For the description of the kinematic behaviour of motion segments or to determine stresses and strains in the soft tissue such models are sufficient. However, this approach does not allow to simulate the flow of the interstitial fluid through the endplates. Poroelastic (or biphasic) models describe soft tissue as saturated porous media where fluid can move through the voids until an equilibrium is reached.

Early poroelastic models employed an isotropic permeability and were used to examine the behaviour of the intervertebral disc under compressive loadings. As the permeability decreases with increasing compression, Argoubi and Shirazi-Adl [1] implemented a strain-dependent formulation to investigate its influence on the creep behaviour. Poroelastic models were also used to investigate the metabolism of the intervertebral disc. The disc is an avascular structure and thus receives its metabolites via diffusion transfer. These means of diffusion can be concentration gradients or convective transfer. The convective transfer of nutrients is connected to the fluid transfer through the adjacent vertebral endplates. Small molecules such as glucose and oxygen are transported to the disc mainly by diffusion [40]. Ferguson et al [10] used a poroelastic model of the intervertebral disc assuming an isotropic permeability and linear elastic behaviour of the solid phase to investigate whether the transport of large molecules is enhanced by fluid flow.

1.5.5 Direct and inverse problems

Commonly, in engineering simulations the solution for a given mathematical model is determined with given material properties. This approach is known as direct method. Solving an inverse problem, the material parameters for a given mathematical model are sought using a given set of experimental data. A simple example is the determination of the material constant in linear elasticity theory. Creating a homogenous uniaxial stress state in a tensile bar, the Young's Modulus can be computed with a simple linear regression. In case of large deformations, a homogenous distribution of stress and strain cannot be assumed any more due to the contraction of the cross section. In such cases, the least squares function describing some kind of deformation, has to be solved with the finite element method which allows to compute the displacement field knowing the boundary conditions.

Most numerical models in spine biomechanics were solved employing the direct method. The material parameters for ligaments, annulus fibrous, cartilage or bone were taken from in-vitro experiments. Patient-specific material properties of spinal segments were evaluated using a parameter identification of constitutive models. Studies have been reported, solving this inverse problem for scoliotic spines using radiographs in an upright and bent or elongated position. Ghista et al [11] used a two-dimensional mathematical representation of the spine, while Petit et al [34] and recently Lafon et al [19] used more detailed three-dimensional models. An important result of these studies is that published mechanical properties for straight spines cannot adequately reproduce the bent position, while individually adapted parameters resulted in considerable improvement. However, the optimization was based only on the displacement of the vertebrae, the forces applied to obtain this displacement were not taken into account.

Reference:

[1] Argoubi M, Shirazi-Adl A, Oct 1996. Poroelastic creep response analysis of a lumbar motion segment in compression. J Biomech 29 (10), 1331–1339.
[2] Belytschko T, Kulak R.F, Schultz A.B, Galante J.O. May 1974. Finite element stress analysis of an intervertebral disc. J Biomech 7 (3), 277–285.
[3] Belytschko T.B, Andriacchi T.P, Schultz A.B, Galante J.O. Jul 1973. Analog studies of forces in the human spine: computational techniques. J Biomech 6 (4), 361–371.
[4] Bono C.M, Lee C.K, Feb 2004. Critical analysis of trends in fusion for degenerative disc disease over the past 20 years: influence of technique on fusion rate and clinical outcome. Spine (Phila Pa 1976) 29 (4), 455–63; discussion Z5.

[5] Brown M.D, Holmes D.C, Heiner A.D, Wehman K.F. May 2002. Intraoperative measurement of lumbar spine motion segment stiffness. Spine (Phila Pa 1976) 27 (9), 954 – 958.
[6] Chazal J, Tanguy A, Bourges M, Gaurel G, Escande G, Guillot M, Vanneuville G. 1985. Biomechanical properties of spinal ligaments and a histological study of the supraspinal ligament in traction. J Biomech 18 (3), 167–176.
[7] Cunningham B.W, Gordon J.D, Dmitriev A.E, Hu N, McAfee P.C. Oct 2003.
Biomechanical evaluation of total disc replacement arthroplasty: an in vitro human cadaveric model. Spine (Phila Pa 1976) 28 (20), S110–S117.
[8] David T, Mar 2007. Long-term results of one-level lumbar arthroplasty: minimum 10-year follow-up of the charite artificial disc in 106 patients. Spine (Phila Pa 1976) 32 (6), 661–666.
[9] Eberlein R, Holzapfel G. A, Schulze C, 2001. An anisotropic model for annulus tissue and enhanced finite element analyses of intact lumbar disc bodies. Comput Method Biomech
4, 209–229.
[10] Ferguson S.J, Ito K, Nolte L.P, Feb 2004. Fluid flow and convective transport of solutes within the intervertebral disc. J Biomech 37 (2), 213–221.
[11] Ghista D.N, Viviani G. R, Subbaraj K, Lozada P.J, Srinivasan T.M, Barnes G, 1988.
Biomechanical basis of optimal scoliosis surgical correction. J Biomech 21 (2), 77–88.
[12] Gillet P, Aug 2003. The fate of the adjacent motion segments after lumbar fusion. J Spinal Disord Tech 16 (4), 338–345.
[13] Graham J.S, Vomund A.N, Phillips C.L, Grandbois M. Oct 2004. Structural changes in human type i collagen fibrils investigated by force spectroscopy. Exp Cell Res 299 (2),
335–342.
[14] Guan Y, Yoganandan N, Moore J, Pintar F. A, Zhang J, Maiman D. J, Laud P, 2007.Moment-rotation responses of the human lumbosacral spinal column. J Biomech 40 (9),
1975–1980.
[15] Heuer F, Schmidt H, Claes L, Wilke H.J, 2007. Stepwise reduction of functional spinal structures increases vertebral translation and intradiscal pressure. J Biomech 40 (4), 795–803.
[16] Heuer F, Schmidt H, Klezl Z, Claes L, Wilke H.-J. 2007. Stepwise reduction of func- tional spinal structures increase range of motion and change lordosis angle. J Biomech 40 (2), 271–
280.
[17] Holzapfel G.A, Schulze-Bauer C.A.J, Feigl G, Regitnig P, Mar 2005. Single lamellar mechanics of the human lumbar anulus fibrosus. Biomech Model Mechanobiol 3 (3), 125–140.
[18] Klisch S.M, Lotz J.C, Oct 1999. Application of a fiber-reinforced continuum theory to multiple deformations of the annulus fibrosus. J Biomech 32 (10), 1027–1036.
[19] Lafon Y, Lafage V, Steib J.-P, Dubousset J, Skalli W, Jan 2010. In vivo distribution of spinal intervertebral stiffness based on clinical flexibility tests. Spine (Phila Pa 1976) 35 (2),
186–193.
[20] Lee C. K, Langrana N. A, Sep 1984. Lumbosacral spinal fusion. a biomechanical study.
Spine (Phila Pa 1976) 9 (6), 574–581.
[21] Lemaire J.P, Carrier H, Ali E.H. S, Skalli W, Lavaste F, 2005. Clinical and radiolog- ical outcomes with the chartie artificial disc. J Spinal Disord Tech 18, 353–359.
[22] Maletsky L.P, Sun J, Morton N.A. 2007. Accuracy of an optical active-marker system to track the relative motion of rigid bodies. J Biomech 40 (3), 682–685.
[23] Malko J.A, Hutton W.C, Fajman W.A, Apr 2002. An in vivo mri study of the changes in volume (and fluid content) of the lumbar intervertebral disc after overnight bed rest and during an 8-hour walking protocol. J Spinal Disord Tech 15 (2), 157–163.

[24] Markert B, Ehlers W, Karajan N, 2005. A general polyconvex strain-energy function for fiber-reinforced materials. Proc. Appl. math. Mech. 5, 245–246.
[25] Nachemson A.L, Evans J.H, Aug 1968. Some mechanical properties of the third human lumbar interlaminar ligament (ligamentum flavum). J Biomech 1 (3), 211–220.
[26] Oxland T.R, Lin R.M, Panjabi M.M, Jul 1992. Three-dimensional mechanical proper- ties of the thoracolumbar junction. J Orthop Res 10 (4), 573–580.
[27] Panjabi M, Henderson G, Abjornson C, Yue J, May 2007. Multidirectional testing of one- and two-level prodisc-l versus simulated fusions. Spine (Phila Pa 1976) 32 (12), 1311–1319.
[28] Panjabi M.M, Jan 1977. Experimental determination of spinal motion segment behavior. Orthop Clin North Am 8 (1), 169–180.
[29] Panjabi M.M, Oct 1988. Biomechanical evaluation of spinal fixation devices: I. a concep- tual framework. Spine (Phila Pa 1976) 13 (10), 1129–1134.
[30] Panjabi M.M, Brand R.A, White A.A, 1976. Three-dimensional flexibility and stiffness properties of the human thoracic spine. J Biomech 9 (4), 185–192.
[31] Panjabi M.M, Krag M. H, White A. A, Southwick W. O, Jan 1977. Effects of preload on load displacement curves of the lumbar spine. Orthop Clin North Am 8 (1), 181–192.
[32] Panjabi M. M, Oxland T. R, Yamamoto I, Crisco J. J, Mar 1994. Mechanical behavior of the human lumbar and lumbosacral spine as shown by three-dimensional load-displacement curves. J Bone Joint Surg Am 76 (3), 413–424.
[33] Panzer M. B, Fice J. B, Cronin D.S. Jun 2011. Cervical spine response in frontal crash. Med Eng Phys.
[34] Petit Y, Aubin C.E, Labelle H, Jan 2004. Patient-specific mechanical properties of a flexible multi-body model of the scoliotic spine. Med Biol Eng Comput 42 (1), 55–60.
[35] Pioletti, D.P., Rakotomanana, L.R., Leyvraz, P.F., Mar 1999. Strain rate effect on the mechanical behavior of the anterior cruciate ligament-bone complex. Med Eng Phys 21 (2), 95–100.
[36] Shirazi-Adl A, 1994b. Biomechanics of the lumbar spine in sagittal/lateral moments. Spine 19, 2407–14. [37] Skaggs D. L, Weidenbaum M, Iatridis J. C, Ratcliffe A, Mow V. C, Jun 1994. Regional variation in tensile properties and biochemical composition of the human lumbar anulus fibrosus. Spine (Phila Pa 1976) 19 (12), 1310–1319.
[38] Spencer A. 1984. Continuum theory of the mechanics of fibre-reinforced composites. Springer Verlag.
[39] Stokes I. A, Gardner-Morse M, Churchill D, Laible J. P, Apr 2002. Measurement of a spinal motion segment stiffness matrix. J Biomech 35 (4), 517–521.
[40] Urban J.P, Holm S, Maroudas A, Nachemson A. Oct 1982. Nutrition of the interverte- bral disc: effect of fluid flow on solute transport. Clin Orthop Relat Res (170), 296–302.
[41] Urban J.P, McMullin J.F, Feb 1988. Swelling pressure of the lumbar intervertebral discs: influence of age, spinal level, composition, and degeneration. Spine (Phila Pa 1976) 13 (2), 179–187.
[42] Wilke H.J, Claes L, Schmitt H, Wolf S, 1994. A universal spine tester for in vitro experiments with muscle force simulation. Eur Spine J 3 (2), 91–97.
[43] Yoganandan N, Kumaresan S, Pintar F. A, Dec 2000. Geometric and mechanical proper- ties of human cervical spine ligaments. J Biomech Eng 122 (6), 623–629.
[44] Frank M.P, Michael N.T, Leonard I.V, Robert M.H, Gerard C, Susan M.R, David M.R, Jorge A.O, Patwardhan A.G, 2009. Effect of the Total Facet Arthroplasty System after complete laminectomy-facetectomy on the biomechanics of implanted and adjacent segments. The Spine

Journal 9 (2009) 96–102
[46] Adams M, Bogduk N, Burton K, & Dolan, P. (2002). The Biomechanics of Back Pain. London: Churchill Livingstone.
[47] Dooris A, Goel V, Grosland N, Gilbertson L, & Wilder D. (2001). Load sharing between anterior and posterior elements in a lumbar motion segment implanted with an artificial disc. Spine, E122-E129.
[48] Guerin H, & Elliott D. (2006). Degeneration affects the fiber reorientation of human annulus fibrosus under tensile load. Journal of Biomechanics, 1410-1418.
[49] Freiberg. (1902). Wolff's law and the functional pathogenesis of deformity. The American Journal of Medical Sciences, 956-972.
[50] Guan Y, Yoganandan N, Moore J, Pintar F, Zhang J, Maiman D et al. (2007). Moment-rotation responses of the human lumbosacral spinal column. Journal of Biomechanics, 1975-80.
[51] Crawford R, Rosenberg W, & Keaveny T. (2003). Quantitative computed tomography based finite element models of the human lumbar vertebral body: effect of element size on stiffness, damage, and fracture strength predictions. Journal of Biomechanical Engineering,434.8
[52] Bogduk N. (1999). Clinical Anatomy of the Lumbar Spine and Sacrum. London: Churchill Livingstone.
[53] Guerin H & D Elliott. (2007). Quantifying the contributions of structure to annulus fibrosus mechanical function using a nonlinear, anisotropic, hyperelastic model. Journal of Orthopaedic Research, 508-516.
[54] Mimura M, Panjabi M, Oxland T, Crisco J, Yamamoto I & Vasavada A. (1994). Disc degeneration affects the multidirectional flexibility of the lumbar spine. Spine, 1371-80.
[55] Natarajan R, Williams J, & Andersson, G. (2006). Modeling changes in intervertebral disc mechanics with degeneration. Journal of Bone and Joint Surgery Supplement 2, 36-40.
[56] Zander T, Rohlmann A & Bergmann, G. (2004). Influence of ligament stiffness on the mechanical behavior of a functional spinal unit. Journal of Biomechanics, 1107-1111.
[57] Schmidt H, H. F. (2009). Dependency of disc degeneration on shear and tensile strains between annular fiber layers for complex loads. Med Eng Phys. Theory of the Mechanics of Fibre-Reinforced Composites (pp. 1-32). New York: Springer Verlag.
[58] Wagner D, & Lotz J. (2004). Theoretical model and experimental results for the nonlinear elastic behavior of human annulus fibrosus. Journal of Orthopaedic Research, 901-909.
[59] Spencer A.J.M., Theory of invariants, in Continuum Physics, Vol.1 Eringen, A.C., Ed., Academic Press, New York (1971) 239253 (1971) 239253
[60] Woo S, Lee T, Abramowitch S & Gilbert T. (2005). Structure and function of ligaments and tendons. In H. R. Mow VC, Basic Orthopaedic Biomechanics and Mechano-biology (pp. 301-342). Philadelphia: Lippincott Williams & Wilkins.
[61] Pham D.T, Shapter J.G, Costi J.J. Tensile behaviour of individual fibre bundles in the human lumbar anulus fibrosus, Journal of Biomechanics (2017),
doi: https://doi.org/10.1016/j.jbiomech. 2017.11.016
[62] Ayturk U.M, Puttlitz C.M. 2011. Parametric convergence sensitivity and validation of a finite element model of the human lumbar spine. Computer methods in biomechanics and biomedical engineering 14, 695–705.
[63] Little J.P, Adam C.J, 2013. Geometric sensitivity of patient specific finite element models of the spine to variability in user-selected anatomical landmarks. Computer methods in biomechanics and biomedical engineering
[64] Park W.M, Kim K, Kim Y.H, 2013. Effects of degenerated intervertebral discs

on intersegmental rotations, intradiscal pressures, and facet joint forces of the whole lumbar spine. Computers in biology and medicine 43, 1234–40.
[65] Dreischarf M, Zander T, Shirazi-Adl A, Puttlitz C.M, Adam C.J, Chen. C.S, Goel V.K, Kiapour
A, Kim. Y.H, Labus K.M, Little J.P, Park W.M, Wang Y.H, Wilke H.J, Rohlmann A, Schmidt. H. Journal of Biomechanics 2014 Jun 3; 47(8):1757-66.
[66] https://commons.wikimedia.org
[67] The spine. Google Sites
[68] http://www.backpain-guide.com
[69] Ayturk U.M, 2010. "Alterations in Lumbar Spine Mechanics Due to Degenerative Disc Disease," Ph.D. thesis, Colorado State University, Fort Collins, Colorado.

Chapter 2:

Treatment of Spinal Disorders Using Flexible Stabilization Constructions

2.1 Degenerative Disc Disease

The characteristic effects of the degenerative disease and aging on the intervertebral disc are very similar. Consequently, biochemical degradation and reduction in the mechanical properties of the intervertebral discs are common problems in the elderly population due to their tendencies to make traumatic injuries more likely to happen during daily physical activities (Figure 2.1). In vitro experimentation has demonstrated that excessive loading of the disc is likely to fail the vertebral endplate first rather than the disc itself in a healthy disc can only be generated under the combined application of excessive bending and compressive loads. Adams et al [1].

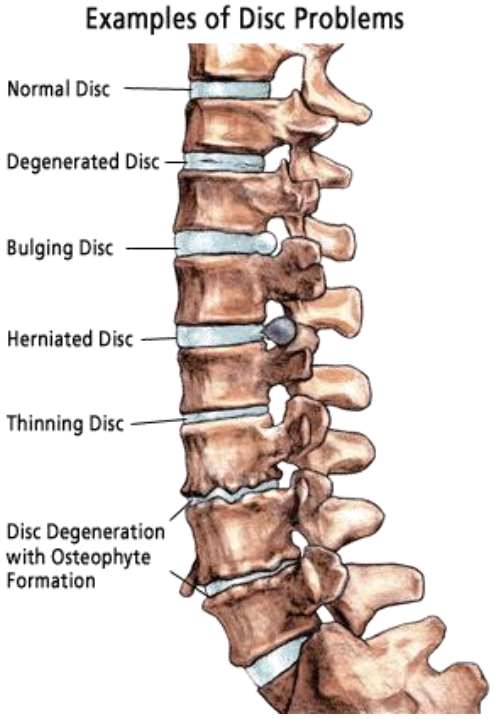

Figure 2.1: Common intervertebral disc related issues [45].

However, during the early stages of degeneration, herniation is more likely to occur

due to the significant reduction in the strength of the annulus fibrosus.

In such cases, annular tissue is strained radially in the postero-lateral direction, penetrating into the spinal canal and putting pressure on the spinal cord and nerve roots (Figure 2.1). This resultant "nerve pinching" mechanism is a major source of low back pain, and in many cases, can only be treated operatively. The current gold standard in surgical treatment of the aforementioned problem is fusion, wherein the injured disc tissue is completely removed and two adjacent vertebral bodies are fused to each other using instrumentation. It has been postulated that replacing the nucleus with a hydrogel substance can restore the intradiscal pressure, provided that the damage to the annulus is not too severe. However, the use of artificial discs, which are essentially metal-polymer-metal joint constructs, is becoming more common due their ability to preserve the intact state of mobility (as compared to fusion).

2.1.1 Pathology of Disc Degeneration

The underlying mechanics of lumbar disc degeneration disease is still not entirely clear. Yet, with aging, the biochemical composition of the disc is known to change. Classification of disc degeneration assessment is clinically achieved in the literature by assigning grades depending on the severity of the disease. The "Thompson Scale" is a commonly used grading scheme by clinicians and researchers, and it groups the progression of the morphological changes in the disc into six stages (Figure 2.2).

The intervertebral disc is the largest avascular tissue in the human body. Therefore, minor disruptions or injuries to the individual components of the tissue might become rather severe in the long-term due to the difficulties in healing. While fissures and tears in the annular lamellae are common during the late stages of degeneration, reductions in mechanical strength of the annulus can lead to excessive bulging and even herniation at earlier time points in the degeneration cascade. A progressive reduction in disc height can be observed, in addition to the formation of osteophytes and loss of integrity of the bony endplate. Goel et al [6]. Overall, the degenerative changes in the morphology and mechanics of the disc are significant and often inter-related, and are described in more detail in the following sub-sections.

2.1.2 Changes in the Morphology of the Intervertebral Disc

Degeneration has been postulated to initiate within the nucleus pulposus tissue.

Water comprises 90 % of the weight of the healthy nucleus pulposus in children, and its content decreases to 70% in adulthood. Antoniu et al [4]. Reduction of hydration initiates inside the nucleus, and subsequently, dehydration begins to affect the remainder of the intervertebral disc. Degenerated nucleus pulposus is shown to include increased levels of matrix- metalloproteinases (MMPs), which stimulate the breakdown of PGs. Furthermore, the total content of Type II collagen is significantly decreased, while there is an increase in the level of Type I collagen content. Andersson et al [3]. With these biochemical changes and the increased resemblance of a solid tissue (rather than a fluid-filled structure due to the reduced water content), the nucleus starts to become a more fibrotic structure. Indeed, in the later stages of degeneration, the annulus and nucleus become histologically indistinguishable.

An immediate loss of functionality and progressive calcification of the cartilaginous endplates accompanies these changes in the nucleus. Blood vessels and nerve endings are observed to grow from the vertebral bodies to inside the disc, since there is limited or no osmotic transportation through the endplates (Bernick et al [5]). Cracks and fissures are also common along the surface of the bony endplates.

In addition to increased cross-linking among the collagen fibers, the water content in the annulus is decreased. These microstructural changes in the annulus have a definitive mechanical outcome. Due to the loss of water content and the breakdown of the PGs, the hydrostatic pressurization in the nucleus is lost, and consequently the in situ circumferential tension in the annular lamellae disappears. Meakin et al [8]. The lack of tension in the annulus tissue increases the catabolic effect of MMPs significantly. Lotz et al [10], leading to a further reduction in the PG content (and thus hydration). Moreover, under in vivo compressive loads, this lack of pre-existing tension causes the individual layers to buckle and delaminate, rather than radially bulge. In fact, in the later stages of degeneration, the disintegration of the annular lamellae with rupture and buckling of the collagen fiber bundles have been observed by Iatridis et al [7]. Furthermore, due to this increased axial deformation, the intradiscal space becomes narrower.

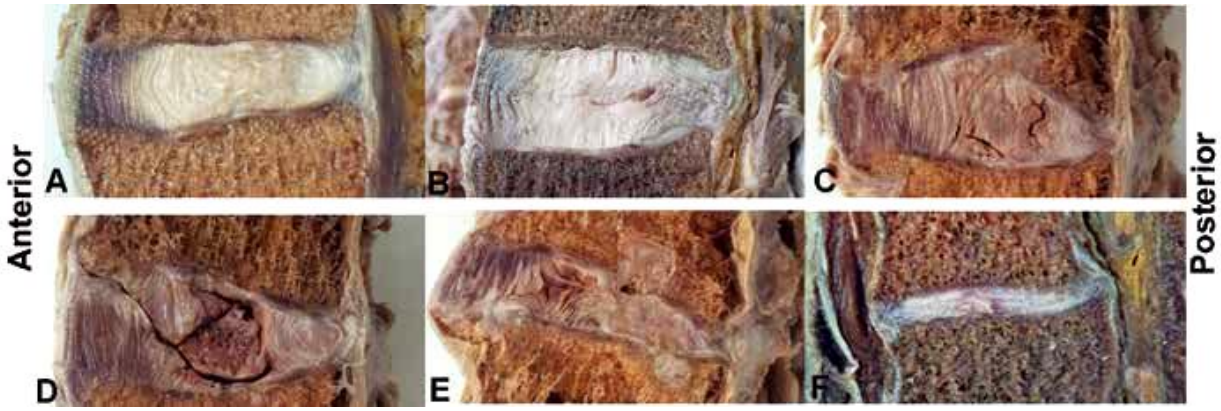

Figure 2.2: Lumbar intervertebral discs fixed in 4% formalin in sagittal section [28].

Note the different macroscopic appearances found in the aging and degeneration process, evaluated according to Thompson's macroscopic degeneration scale16. (A) Thompson I: NP of gelatinous appearance and AF with organized lamellae; (B) Thompson II: NP with whitened fibrous tissue and mucinous material between the lamellae of the AF, note small fissure in the NP; (C) Thompson III: Loss of AF/NP distinction, focal defects in the VP, see dehydration of NP and longitudinal and vertical fissure; (D) Thompson IV: Fissures in the NP and parallel to the VP, with presence of focal sclerosis at this point; (E) Thompson V: Diffuse sclerosis and Schmorl's nodes; (F) Thompson 5: total sclerosis and flattening of the disc. [28]

Osteophyte formation often accompanies disc degeneration around the rim of the endplate. It has been hypothesized that this is actually a remodeling phenomenon wherein these changes increase the cross-sectional area of the endplate and distribute the loads to a broader area. Adams et al [1]. However, these mineralized tissues do not display a consistent pattern and usually encompass random geometry. Recently published data suggest that these mineralized deposits contribute to the global resistance of the functional spinal unit primarily under bending loads. Al-Rawahi et al [2]. Furthermore, osteoarthritic involvement in the zygapophyseal joints usually follows disc degeneration due to severe changes in the load-sharing relationship between the anterior and posterior spinal columns. Niosi, et al [11].

2.2 Spinal disorders

Despite the scientific advances, chronic low back pain remains a major socio-economic problem of public health. Low back pain, often referred to as "back pain", is the

most expensive benign condition affecting the working population of industrialized countries. Low back pain has been defined by the International Association for the Study of Pain (IASP) as the perception of pain from the lumbar or sacral area of the spine or the combination of both [1]. This definition does not take into account the cause of the pain nor does it suggest that the source of the pain is located in the lumbar spine or sacrum. Low back pain is therefore defined solely from the location of painful places for the patient.

The difficulty for the clinician, in order to be able to best treat the patient, is to determine the exact origin of the pain. The pain can be projected which means that it is felt in an area innervated by nerves that are not the cause of the pain. This implies that pain can be felt in both remote and contiguous areas of pain [1].
Radicular pain (radiculalgia) is projected pain. They are not caused solely by mechanical compression, but occur as a result of irritation of a spinal nerve or its roots, an inflammatory process caused by NP tissues [1]

2.2.1 Degenerative pathologies

The "normal" functioning of the FU depends largely on the integrity of its components and their coordinated interaction. Any modification of any of these components causes a disruption of their interaction that causes dysfunction, ultimately leading to lower back pain, deformities and neurological disorders. Sukthankar et al [43]. From a clinical point of view, the changes related to degeneration of the lumbar spine are expressed by various pathologies called "degenerative". The most common pathologies are presented below: disc herniation, degenerative spondylolisthesis, osteoarthritis, lumbar stenosis and instability. The common symptom of all these pathologies is the pain felt by the patient, called lumbago or radiculalgia depending on its location.

2.2.2 Herniated disc

The herniated disc corresponds to a leak of the nucleus (NP) of an IVD towards the spinal canal by rupture of its fibrous ring (AF) (Figure 2.3). This results in nerve root compression that can be intermittent or permanent. The hernia can be protruded or excluded. Herniated disc is the most common cause of radicular pain. The most affected lumbar levels are L4-L5 and L5-S1. The main symptom of lumbar disc herniation is root pain in the leg with or without sensorimotor deficiency. However, herniated discs do not

always produce symptoms, they are frequently encountered in asymptomatic people. MRI is the imaging method of choice for the diagnosis of this pathology. Surgical treatment of disc herniation involves removing a portion of the disc (discectomy). It is sometimes supplemented by laminectomy and decompression (see section 2.3.2).

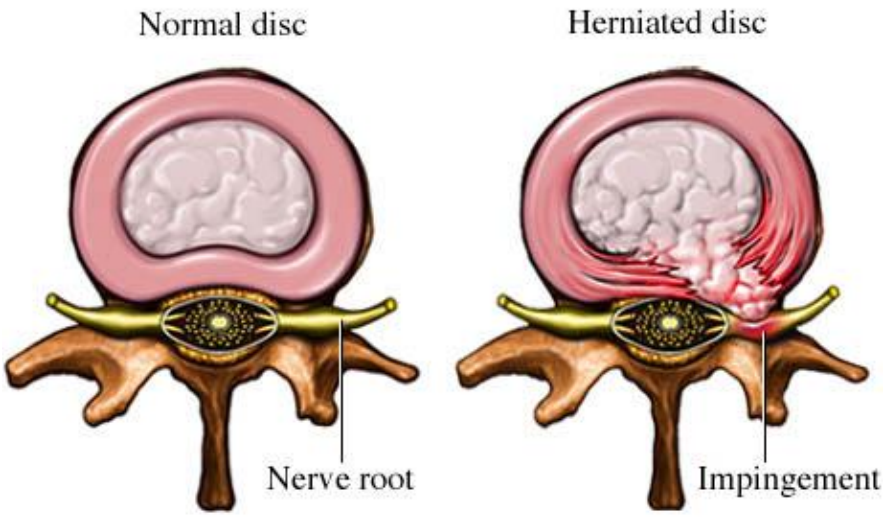

Figure 2.3: Normal and Herniated disc [46].

2.2.3 Degenerative spondylolisthesis

The term "degenerative spondylolisthesis" (DS) was introduced by Newman in 1963. It is defined as a postero-anterior (forward) sliding of a vertebra with respect to the underlying vertebra (Figure 2.4). Without isthmic lysis, ie without rupture of the posterior arch. This pathology, more common in women (four women for one man) occurs mainly after 40 years. Pedram et al [44]. Lumbar DS is therefore one of the causes of lumbar canal stenosis, it can be responsible for lombo radiculalgia and its treatment is often surgical. The characteristic symptoms are low back pain in the form of cramps or burning (more than 90% of cases) associated with radiculalgia (40% to 50% of cases) [44]. The slippage usually does not exceed 30% of the width of the vertebral body. The sagittalization of the facet joints is characteristic of this pathology, favoring the sliding of the vertebra forward (Figure 2.4) [44].

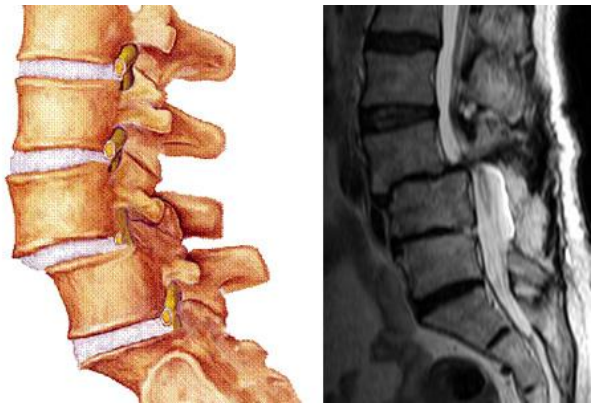

Figure 2.4: X-ray shows the spondylolisthesis [47].

2.2.4 Arthrosis of the joints

Osteoarthritis is the chronic wear of the cartilage of a joint, accompanied by an imbalance between the production and the degradation of the bone cells. In the UF, osteoarthritis is localized in the zygapophyseal joints. The phenomenon tends to self-amplify and lead to the painful limitation of joint mobility. Lumbar osteoarthritis is most often the result of an abnormal posture (hyperlordosis or scoliosis) or a poor repetitive position when practicing a sport or during a professional activity. It can also be linked to the degeneration of the IVD, which induces an overload of the articular facets, favoring the phenomenon. The production of osteophytes4, related to articular osteoarthritis, possibly to hypertrophy of the yellow ligament and to a disc protrusion, can in some cases compress the nerve roots (stenosis).

2.2.5 Lumbar stenosis or narrow lumbar canal

The decrease in vertebral canal space is a condition called narrow lumbar canal or lumbar stenosis (Figure 2.5). The main symptom associated with lumbar stenosis is referred to as neurogenic claudication. It is a painful sensation that appears after a walk or prolonged standing. In severe cases the patient can hardly walk a few meters. Generally, the pain disappears in the flexion position.

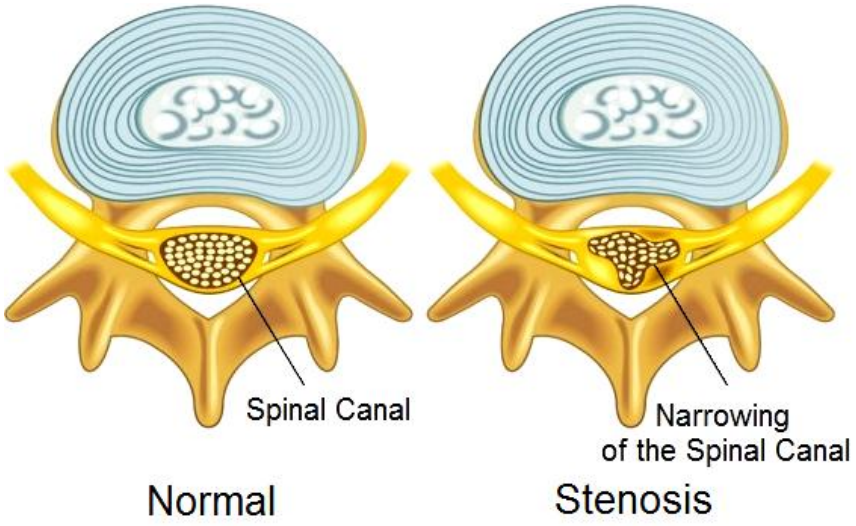

Figure 2.5: Stenosis [48].

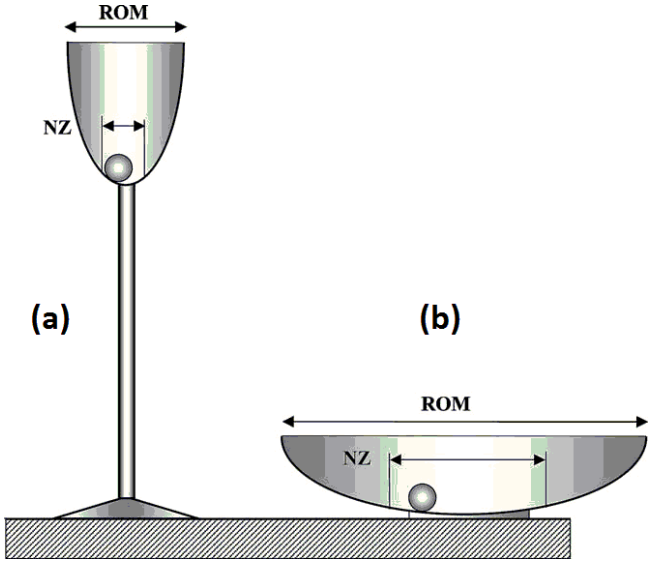

Figure 2.6: Different stabilities. Using the analogy bowl to represent the load–displacement curve of the spine of a ball-in (a) a deep glass and (b) a shallow soup plate represents a more and a less stable spine respectively, NZ: Neutral Zone, Panjabi [49].

2.3 Treatment of spinal disorders

2.3.1 Conservative Treatment Options

• **Physical therapy and exercise:** Physical therapy is a long-term pain management technique that aims to enable the patient to control pain effectively and function normally, without undergoing a surgical procedure. This attempts to improve

flexibility in the neck, arms and legs through stretching exercises. The therapist may also include additional strengthening exercises in the program. Under supervision, physical therapy may take three or more months and eventually the patient becomes independent and performs activities independently.

• **Neck traction:** This is a technique in which a force is applied to a part of the body to reduce muscle spasms by stretching soft tissues, and in some cases separating facet joint surfaces or bony structures [30]. Neck traction must be constant so that the muscles may tire and the strain falls on the joints. Forces between 20-50 pounds are commonly used to achieve inter vertebral separation.

• **Chiropractic manipulation:** This is a precise procedure applied to the joints of the neck, usually applied by hand. Chiropractors claim that neck adjustment improves the mobility of the spine and restores the range of motion. It can also increase movement of the adjoining muscles [31]. Patients report an improved ability to turn and tilt the head and a reduction of pain, soreness and stiffness.

• **Osteopathic manipulation:** Osteopathic manipulation claim to restore normal joint motion and can be helpful in reducing pain from a cervical herniated disc [32]. The restrictions of nerve passages are said to be released, the movement of cerebrospinal fluid through the spinal cord is said to be optimized, and misaligned bones are said to be restore to their normal position. This therapy is used to treat mental stress, neck and back pain, migraines, TMJ syndrome and chronic pain conditions such as fibromyalgia.

• **Activity modification:** Some activities may tend to exacerbate the herniated disc pain and it is recommended to avoid these activities to prevent nerve root irritation. Such activities may include heavy lifting, activities causing increased vibration and compression to the cervical spine such as boating, snowmobile riding, and overhead activities that require prolonged neck extension and/or rotation.

• **Medications:** The primary mechanism of action in NSAIDs is a reduction of cyclooxygenase activity which leads to decreased prostaglandin synthesis. Prostaglandins are active mediators during the inflammatory cascade. A reduction in their local concentration could therefore explain the combined anti-inflammatory and analgesic properties of NSAIDs.

• **Injections:** Epidural steroid injections are delivered directly at the source of pain. Since the vast majority of pain stems from chemical inflammation, an epidural steroid injection serves to control the local inflammation by flushing out the inflammatory proteins and chemicals from the local area that may contribute to and exacerbate pain [33]. Triamcinolone acetonide, Dexamethasone, and Methylprednisolone acetate are commonly used steroids used to treat low back pain.

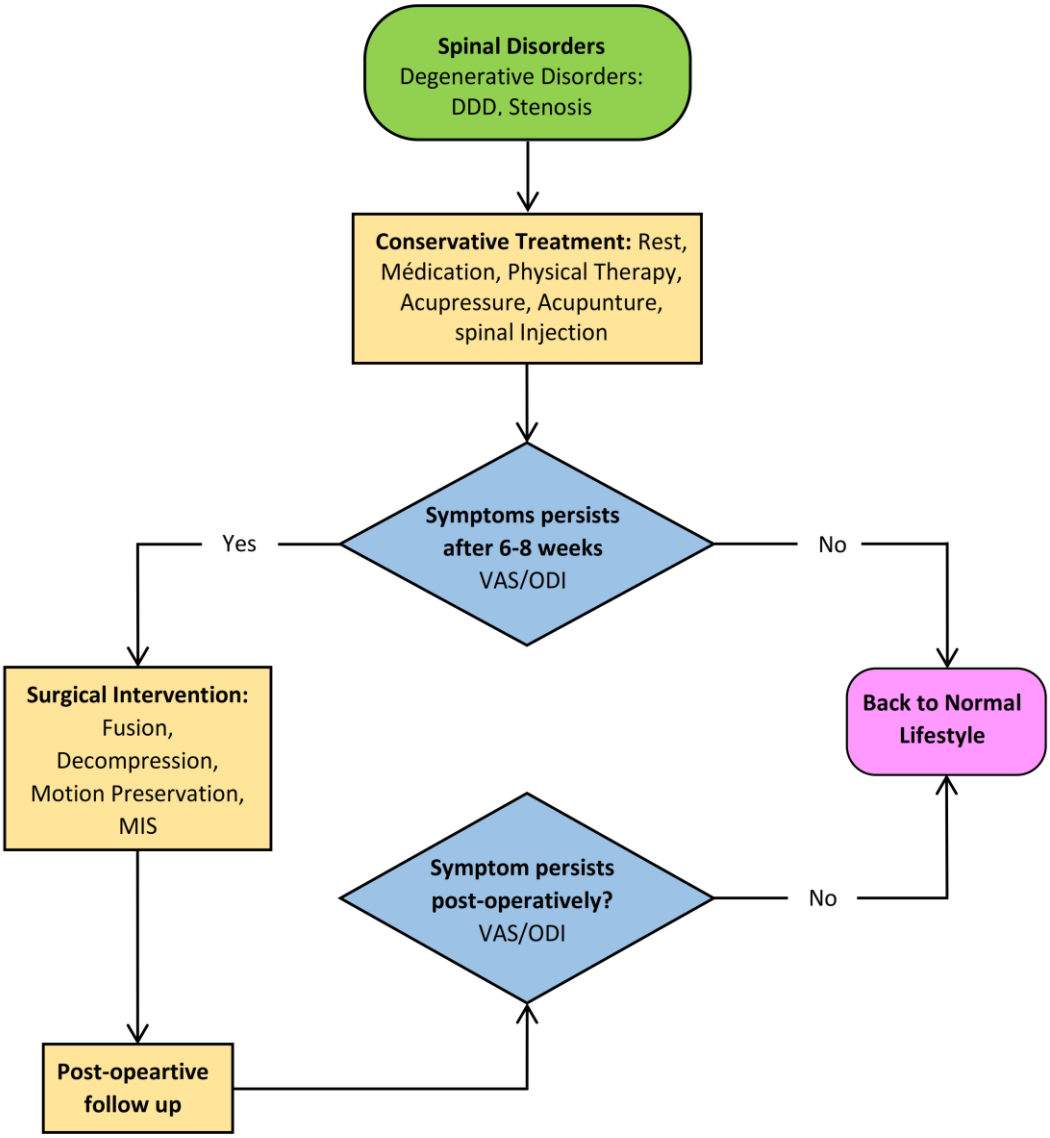

Figure 2.7: A simplified treatment option flow chart for spinal ailments.

VAS: Visual Analogue Score

ODI: Oswestry Disability Index

MIS: Minimally Invasive Surgery

When conservative treatment fails to alleviate pain, surgical intervention may be the only remaining option to regain the original lifestyle. Non-surgical treatment may prove unsuccessful in the treatment of degenerative disc disease (DDD), particularly when spondylosis or spondylolisthesis is present. Thus, the aim of a surgery is to alleviate pain and restore a normal lifestyle. A simplistic algorithm to elucidate the treatment options has been depicted in Figure 2.7.

The range of spinal ailments that are treated using instrumented spinal surgery is vast. The aim of the next section is to provide an overview of the existing surgical options that are being utilized for the treatment of degenerative condition.

2.3.2 Surgical Intervention

The goals of surgical intervention are to remove the diseased or injured tissue and to restore stability and function in the spinal unit.

2.3.2.1 Spinal fusion or arthrodesis

Fusion has remained the gold standard with respect to surgical intervention of disc-related issues in the lumbar spine for the last few decades. Following the removal of the disc tissue, the intradiscal space is filled with bone graft and the injured level and its adjacent segments are reinforced with instrumentation (Figure 2.8).

In an attempt to overcome these shortcomings, the use of flexible stabilization systems has been proposed as an alternative to the traditional fusion techniques. These posterior spring- rod mechanisms shift the center of rotation posteriorly and are generally intended to unload the anterior column. However, dynamic stabilization is a relatively new concept, and its efficacy still remains unknown since the long-term follow-up results are yet to be reported. The main clinical problem addressed in spinal fusion is the restoration of stability in a clinically unstable spine. As the name suggests, the bony segments of the spine are fused with the goals of correcting the deformity, pain reduction and restoration of stability. Spinal fusion may be accomplished with or without the use of spinal instrumentation. External instrumentation can be used as an alignment and load sharing device until a bony fusion is achieved [34]. This instrumentation has evolved over a time and is used in combination with external braces and bone grafts to improve both the rate and degree of bone consolidation.

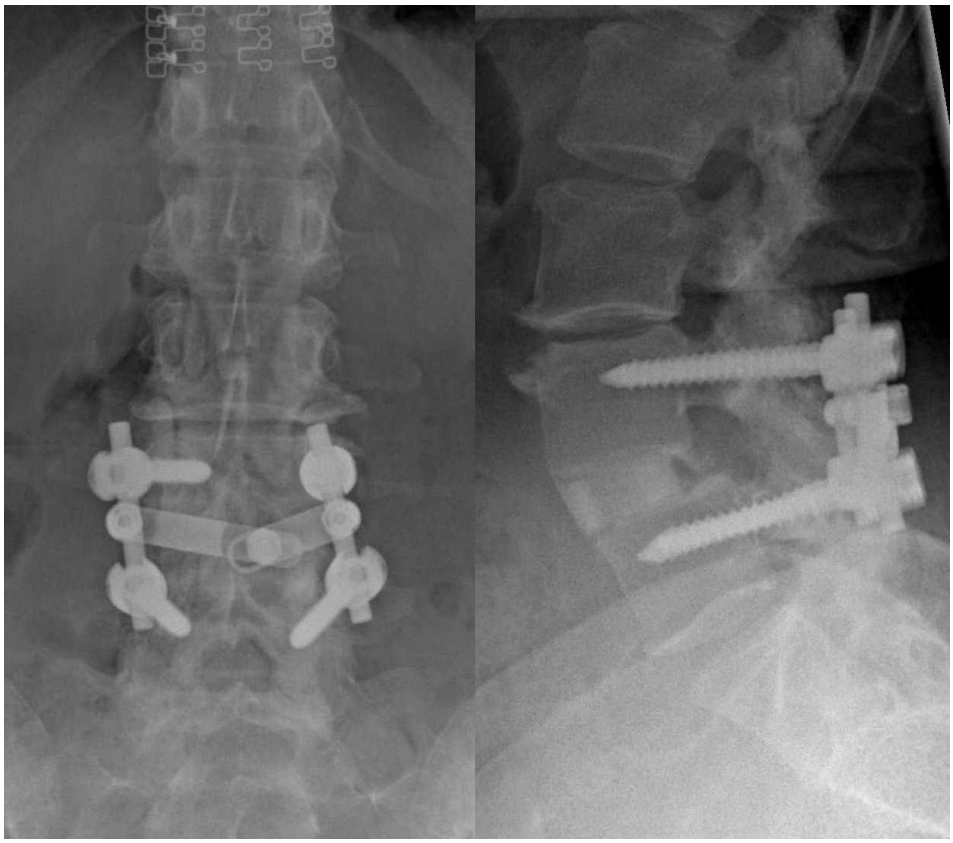

Figure 2.8: Fusion with posterior application of rods and pedicle screws to L4-L5 [50]

Harrington was the first to utilize hooks and rods to correct spinal deformity and instability and is considered to be a pioneer of posterior fixation devices for fusion [34]. Sublaminar wires were also introduced for fixation procedures [34]. However, wires were associated with further complications and did not prove clinically successful. Pedicle screws with rod and plate systems came next. These systems were founded on the fact that the pedicles have an advantage in terms of force application as compared to the facets and laminae [34]. Apart from pedicle screw-based systems interbody cages have also become popular as an effective fusion device. Interbody cages are metallic (e.g. titanium) or polymeric (e.g. polyetheretherketone PEEK) devices with an empty central region that is packed with bone graft material and then placed in the intervertebral space. These devices have an open design to allow direct bone growth through the cage fromone vertebral body into the next [35].

A common surgical approach for these devices is the ALIF (anterior lumbar interbody fusion) procedure. Yet, some cages can be inserted using a posterior approach (PLIF). Traditionally, anterior interbody fusions utilized autologous bone,

harvested intra-operatively from the patient's iliac crest. Apart from graft site morbidity, there was a high incidence of non-union with these procedures. Threaded cylindrical cages designed in the late 1990s improved the success rate of these procedures by providing a more rigid fixation within the disc space.

2.3.2.1 Challenges and drawbacks associated with fusion procedure

Although fusion was first performed over 100 years ago and still remains the gold standard of treatment for DDD, accelerated adjacent level degeneration, morbidities after spinal fusion and increased cost due to long postoperative rehabilitation still remains a concern [36]. In spite of being a successful procedure, fusion surgeries lead to decreased mobility at the surgical level thus causing the patient to cease certain activities.

Additionally, fusion has shown drawbacks such as pain at the bone harvesting site and adjacent level degeneration (ALD). After initial pain relief, pain is likely to return due to spinal stenosis, facet hypertrophy, osteophyte formation, posterior muscular debilitation or disc degeneration at levels adjacent to the fusion site. It is however unclear whether adjacent segment degeneration is an outcome of the iatrogenic reasons or if it is.

A progression of the natural history of the underlying degenerative disease [37]. Adjacent level disease (ALD) is a condition characterized by arthrosis of the caudal and/or cranial vertebral joint next to the fused unit. The reduced motion at the fused segments leads to an increased motion at the adjacent level. In a study by Katsurra et al. [38]. The rate of ALD was found to be around 50% at the end of 10 years. A reoperation rate of 6% in addition to 36% rate of clinical deterioration was confirmed by Goffin et al [39] at the end of 8 yrs. In a study by Lee et al [29] hypertrophic degenerative arthritis of the facet joints was observed at the adjacent level.

Additionally, incidence of stenosis, degenerative spondylolisthesis and disc degenerative conditions were observed in 18 patients after a period of 8.5 yrs. An in vitro study by Chow et al [40] proved increased segmental motion and intradiscal pressure for adjacent vertebras. In another clinical study by Wai et al [41] approximately 70% of the patients showed evidence of degeneration, while almost 30% of the patients had advanced degenerative symptoms localized to the adjacent level. Wittenberg et al [42] concluded that long implants may give rise to strain at the adjacent level causing

early degeneration and destabilization; therefore, short segment fixation is preferred in spite of its inherent shortcomings. Reduced motion, ALD and donor site pain due to fusion have paved the way towards the quest for alternative measures. Along these lines, many non-fusion techniques are being investigated and some have emerged in recent times that are capable of replacing the conventional fusion techniques. The classification in the field of spinal instrumentation is summarized in the flow chart (Figure 2.9).

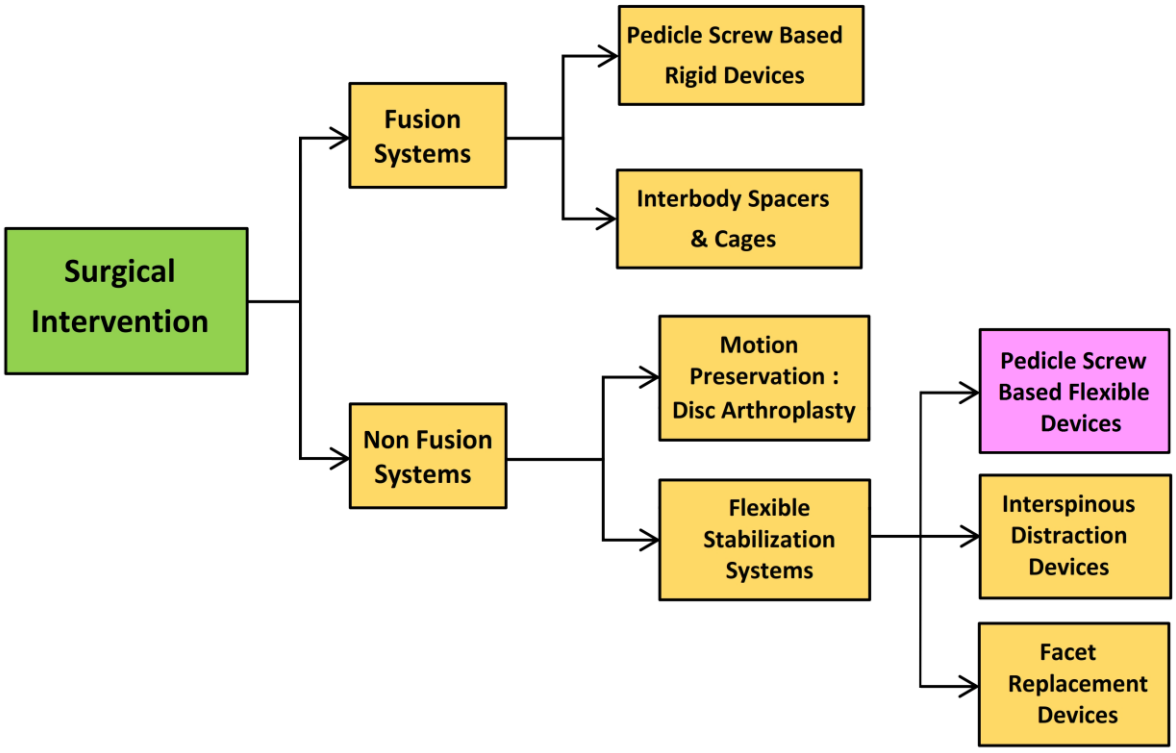

Figure 2.9: Classification of spinal instrumentation systems

2.4 Posterior Pedicle Fixation-Based Flexible Stabilization Devices

2.4.1 Graf Ligament

In 1992, Graf described the use of the Graf ligamentoplasty system to treat low back pain without fusion [13]. According to his theory, abnormal rotary motion was the primary source of mechanical low back pain. He later improved the Graf ligamentoplasty system by inserting titanium pedicle screw anchors into the vertebra, both superior and inferior to the symptomatic level, and using a braided polypropylene. Graf ligamentoplasties also produce a significant increase in lateral canal stenosis, especially when patients exhibited preexisting degenerative changes in the facet joints or in the infoldings of the ligamentum

flavum, owing to the marked lordosis of the segment instrumented. Early clinical failures were associated with this surgical complication [14]. Graf ligaments transfer the load from the anterior aspect of the disc to the posterior annulus, thereby increasing the disc pressure in this region. This may explain the late failure of the Graf ligament, which accelerates disc degeneration by overloading the posterior part of the disc [12].

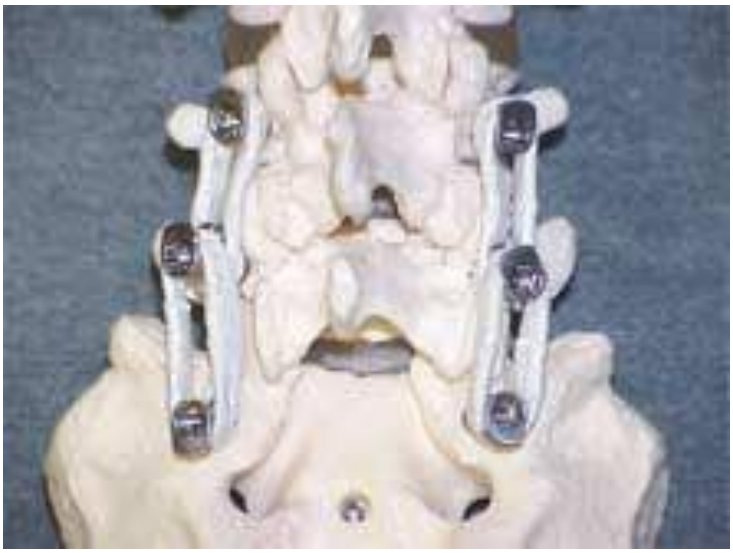

Figure 2.10: Graf ligamentoplasty system [51].

Recent randomized evaluations reported better clinical outcomes in patients that underwent Graf ligament placements versus fusions. If the patient is experiencing spondylolisthesis or flexion instability, then a Graf ligamentoplasty is a good choice. However, if the patient complains of scoliosis or lateral listhesis, then the Graf ligamentoplasty is not a good choice and could lead to a higher likelihood of reoperation.

2.4.2 Dynamic Neutralization System (Dynesys)

The dynamic neutralization system (Dynesys) was developed by Stoll et al. 2002 [15]. This system consists of titanium alloy (protasul 100) pedicle screws, polyester (sulene-PET) cords, and polycarbonate urethane (sulene-PCU) spacers (Figure 2.5). The PET cord resists tensile forces and provides resistance to spine flexion, similar to the concept used in Graf ligamentoplasties. However, the Dynesys PCU spacers resist compression during extension and thereby prevent foraminal narrowing by maintaining foraminal height and decreasing load to the posterior annulus [16,17]. Dynesys treatment is indicated for patients with degenerative diseases in the lumbar motion segment, instability, and in combination with functional or structural spinal canal stenosis. Contraindications for this system are spinal

fractures, infections, lytic/isthmic spondylolisthesis, degenerative spondylolisthesis, facetectomy, and stabilization of the thoracic and cervical spine.

Figure 2.11: Dynesys device applied on a spinal model [52].

2.4.3 Bioflex Spring Rod Pedicle Screw System

The Bioflex system (Bio-Spine Inc.) is a pedicle screw-based system that is composed of rod-shaped Nitinol with one or two loops to confer stability in flexion, extension, and lateral bending (Figure 2.6). Nitinol is an alloy of titanium Ti and nickel Ni, also called the "memory metal" due to its ability to return to its original shape after deformation. In a study conducted by Kim et al., 103 patients treated with the Bioflex system were observed preoperatively and postoperatively for range of motion (ROM) changes. The patients were divided into two groups: dynamic stabilization with or without posterior lumbar interbody fusion (PLIF) (Group1) and rigid fixation (PLIF+ Bioflex system only) (Group 2). The changes in the ROM in looped segments that were treated with PLIF were significantly reduced, but the changes in the ROM in looped segments without PLIF were not significant. The authors concluded that the Nitinol Bioflex dynamic stabilization system achieved stabilization while simultaneously permitting physiological movement which in turn decreases the degeneration of adjacent segments [18].

In a study conducted by Kim et al [18] 12 patients were treated with the Bioflex system to examine functional motion one or more years after Bioflex system placement.

Six patients were treated with a L3-4-5 construct, and another six patients were treated with a L4-5-S1 construct. The followup period varied from 12 to 33 months; standing neutral lateral flexion, extension, and postero-anterior radiographs

Figure 2.12: The Bioflex system [53].

2.4.4 Dynamic Stabilization System (DSS).

The DSS system was developed by Sengupta et al [19] as an improvement of the FASS system. Biomechanical studies show that the FASS system produces too much loading during flexion which leads to early device failures. The DSS system has two designs that have been tested in the laboratory. The DSS-I consists of a titanium spring, made of a 3 mm cross-section diameter of spring-grade titanium wire (Figure 2.7). The DSS-II system consists of an elliptical coil spring, made from 4 mm spring-grade Ti rods.

Figure 2.13: Dynamic Stabilization System DSS [54].

2.4.5 NFlex dynamic stabilization system

NFlex (N. spine, Inc., San Diego, CA) is a dynamic stabilization system [21] (Figure 2.8). It is composed of two parts: polyaxial rigid screw and titanium and polycarbonate urethane rod. NFlex is first implanted in 2006.

Figure 2.14: NFlex dynamic stabilization system [55]

A multicenter study was performed related to NFlex dynamic stabilization system [22]. In this retrospective study 72 consecutive patients who have degenerative diseases of the spine underwent surgery with NFlex dynamic system. Mean followup was 25.6 months. VAS and Oswestry disability index of the patients were improved obviously after operations. Just three implant-related complications were observed. This study showed that NFlex dynamic system seems to improve pain and functional scores and may be considered a good alternative to rigid fusion [22].

2.4.6 Accuflex rod system

Accuflex rod system (Globus Medical Inc.) is a semirigid rod which has been situated between rigid rods. Accuflex system obtained FDA clearance in 2005 as a single-level tool to stabilize lumbar interbody fusion [20]. A clinical study was done related to Accuflex rod system. This study reported that Accuflex semirigid system showed clinical benefits and ceased the degenerative process in 83% of the patients although high incidence of implant failure (22.22%) was observed [23].

2.4.7 CD Horizon legacy peek rod

CD Horizon legacy peek rod (Medtronic, Safamor Danek, Memphis, TN) has been introduced to the market as a semi- rigid alternative to titanium rods (Figure 2.9). FDA clearance has been got in June 2005. In a biomechanical study, Gornet reported that peek rod system provided intervertebral stability comparable to currently marketed titanium lumbar fusion constructs [24]. Ormond et al studied retrospective 42 case series from 2007 to 2009 for degenerative lumbar disease and performed them posterior lumbar fusion using PEEK rods [25].

Figure 2.15: The CD-Horizon Legacy PEEK rod [56].

2.4.8 Stabilimax NZ Pedicle-Based Posterior Dynamic System

The Stabilimax NZ (Applied Spine Technologies, New Haven, CT) is a pedicle-based posterior dynamic system which was developed and designed to specifically address pathological alterations in the neutral zone by Panjabi [26,27] (Figure 2.11). Its indications include moderate to severe degenerative lumbar spinal stenosis and discogenic low back pain. The Stabilimax NZ is composed of a system of ball and socket joints to decrease the load on the pedicle screw and double connecting springs [20, 26, 27]. They observed that 8 of 42 patients with PEEK rods underwent reoperation. Reoperations included adjacent

segment degeneration (5/8) and nonunion with cage migration (3/5). In conclusion authors reported that PEEK rods demonstrated similar fusion and reoperation rate in comparison with other instrumentation modalities.

Figure 2.16: The Stabilimax NZ [57].

Reference

[1] Adams M, Bogduk N, Burton K, & P. Dolan, (2002). The Biomechanics of Back Pain. London: Churchill Livingstone.

[2] Al-Rawahi M, Luo J, Pollintine P, Dolan P & Adams, M. (2010). Mechanical Function of Vertebral Body Osteophytes, as Revealed by Experiments on Cadaveric Spines. Spine, In Press.

[3] Andersson G. (1998). What are the age-related changes in the spine? Baillieres Clin Rheumatol , 161-173.

[4] Antoniu J, Steffen T, Nelson F. (1996). The Human Intervertebral Disc: Evidence for Changes in the Biosynthesis and Denaturation of the Extracellular Matrix with Growth, Maturation, Ageing, and Degeneration. J Clin Invest, 996-1003.

[5] Bernick S & Cailliet R, (1982). Vertebral Endplate Changes with Aging of Human Vertebrae. Spine, 97-102.

[6] Goel V, Sairyo K, Vishnubhotla S, Biyani A & Ebraheim N. (2006). Spine Disorders: Implications for Bioengineers. In E. A. Kurtz SM, SPINE Technology Handbook (pp. 145-182). London, UK: Elsevier.

[7] Iatridis J, Gwynn I. (2004). Mechanisms for Mechanical Damage in the Intervertebral Disc Annulus Fibrosus. J Biomech , 1165-1175.

[8] Meakin J, Redpath T, Hukins D. (2001). The Effect of Partial Removal of the Nucleus Pulposus from the Intervertebral Disc on the Response of the Human Annulus Fibrosus to Compression. Clinical Biomechanics, 121-128.

[9] Kruyt M, van Gaalen S, Oner F, Verbout A, de Bruijn J, Dhert W. (2004). Bone tissue engineering and spinal fusion: the potential of hybrid constructs by combining osteoprogenitor cells and scaffolds. Biomaterials, 1463-1473.

[10] Lotz J, Hadi T, Bratton C, Reiser K, Hsieh A. (2008). Anulus fibrosus tension inhibits degenerative structural changes in lamellar collagen. Eur Spine J , 1149-1159.
[11] Niosi C, Oxland T. (2004). Degenerative mechanics of the lumbar spine. Spine J, 202S-208S.
[12] Sengupta D.K. "Dynamic stabilization devices in the treat- ment of low back pain," Neurology India, vol. 53, no. 4, pp. 466–474, 2005.
[13] Graf H, "Evaluation of the therapeutic effect of the graf stabilisation system," in Proceedings of the 2nd Annual Meeting of the European Spine Society, Rome, Italy, 1991.
[14] Grevitt M.P, Gardner A.D. H, Spilsbury J et al. "The Graf stabilisation system: early results in 50 patients," European Spine Journal, vol. 4, no. 3, pp. 169–175, 1995.
[15] Stoll T.M, Dubois G, & Schwarzenbach O, "The dynamic neutralization system for the spine: a multi-center study of a novel non-fusion system," European Spine Journal, vol. 11, supplement 2, pp. S170–S178, 2002.
[16] Delamarter R.B, Maxwell J, Davis R, Sherman J, & Welch W. "Nonfusion application of the Dynesys system in the lumbar spine: early results from IDE multicenter trial," Spine Journal, vol. 6, supplement 1, article S77, no. 5, 2006.
[17] Schnake K.J, Schaeren S & Jeanneret B. "Dynamic stabilization in addition to decompression for lumbar spinal stenosis with degenerative spondylolisthesis," Spine, vol. 31, no. 4, pp. 442–449, 2006.
[18] Kim Y.S, Zhang H.Y, Moon B.J et al, "Nitinol spring rod dynamic stabilization system and Nitinol memory loops in surgical treatment for lumbar disc disorders: short-term follow up," Neurosurgical Focus, vol. 22, no. 1, article E10, 2007.
[19] Sengupta D.K, Herkowitz H.N, Hochschuler S, & R.C. Mullholland, "Load sharing characteristics of two novel soft stabilization devices in the lumbar motion segments-a biomechanical study in cadaver spine," in Proceedings of the Spine Arthroplasty Society Congress, 2003.
[20] Bono C.M, Kadaba M, & Vaccaro A.R. "Posterior pedicle fixation-based dynamic stabilization devices for the treatment of degenerative diseases of the lumbar spine," Journal of Spinal Disorders and Techniques, vol. 22, no. 5, pp. 376–383, 2009.
[21] Buttner-Janz K. "Classification of spine arthroplasty devices," in Motion Preservation Surgery of the Spine, J.J. Yu, R. Bertagnoli, P. C. McAfee, and H. S. An, Eds., pp. 21–35, Saunders Elsevier Press, Philadelphia, Pa, USA, 2008.
[22] Coe J.D, Kitchel S.H, Meisel H. J, Wingo C.H, Lee S. E, & Jahng T.-A. "NFlex dynamic stabilization system: two- year clinical outcomes of multi-center study," Journal of Korean Neurosurgical Society, vol. 51, no. 6, pp. 343–349, 2012.
[23] Reyes-Sànchez A, Zàrate-Kalfòpulos B, Ramìrez-Mora I, Rosales-Olivarez L. M, Alpizar-Aguirre A, and Sànchez-Bringas G. "Posterior dynamic stabilization of the lumbar spine with the Accuflex rod system as a stand-alone device: experience in 20 patients with 2-year follow-up," European Spine Journal, vol. 19, no. 12, pp. 2164–2170, 2010.
[24] Gornet M.F, Chan F.W, Coleman J.C et al. "Biomechanical assessment of a PEEK rod system for semi-rigid fixation of lum- bar fusion constructs," Journal of Biomechanical Engineering, vol. 133, no. 8, Article ID 081009, 2011.
[25] Ormond D.R, Albert Jr L & Das K. "Polyetheretherketone (PEEK) rods in lumbar spine degenerative disease: a case series," Journal of Spinal Disorders & Techniques, 2012.
[26] Yue J.J, Malcolmon G, and Timm J. P, "The stabilimax NZ posterior lumbar dynamic stabilization system," in Motion Preservation Surgery of the Spine, J. J. Yu, R. Bertagnoli, P.

C. McAfee, and H. S. An, Eds., pp. 476–482, Saunders Elsevier Press, Philadelphia, Pa, USA, 2008.
[27] Yue J.J, Timm J.P, Panjabi M.M, Jaramillo-de la Torre J. "Clinical application of the Panjabi neutral zone hypothesis: the Stabilimax NZ posterior lumbar dynamic stabilization system," Neurosurgical focus, vol. 22, no. 1, p. E12, 2007. The treatment of neurogenic intermittent claudication: two-year follow-up results," Spine, vol. 30, no. 12, pp. 1351–1358, 2005.
[28] Baptista J. S, R. B. V, Fontes E, Liberti A. "Aging and degeneration of the intervertebral disc: review of basic science" Coluna/Columna vol.14 no.2 São Paulo Apr./June 2015. http://dx.doi.org/10.1590/S1808-185120151402141963.
[29] Ghiselli G, Wang JC, Bhatia NN, Hsu WK, Dawson EG. Adjacent segment degeneration in the lumbar spine. J Bone Joint Surg Am, 2004. 86-A(7): p. 1497-503.
[30] Care S.H, Neck Traction. 2011 [cited 2010 12/16/10]; Available from: http://www.neckpaintraction.com/.
[31] M.C Staff. Chiropractic Adjustment. 2010 [cited 2010 12/10/10]; Available from: http://www.mayoclinic.com/health/chiropractic-adjustment/MY01107.
[32] AACOM. What Is Osteopathic Medicine. [cited 12/10/10; Available from: http://www.aacom.org/about/osteomed/pages/default.aspx.
[33] M. Richard Staehler, How Epidural Steroid Injections Work. 1999 2007; Available from: http://www.spine-health.com/treatment/injections/how-epidural-steroid-injections-work.
[34] Goel V.K, and Gilbertson L.G, Basic science of spinal instrumentation. Clin Orthop Relat Res, 1997(335): p. 10-31.
[35] Peter F, Ullrich J. Interbody Cages for Spine Fusion. http://www.spine-health.com/treatment/spinal -fusion/interbody-cages-spine-fusion. 188
[36] Hilibrand A.S, and Robbins M. Adjacent segment degeneration and adjacent segment disease: the consequences of spinal fusion? The spine journal: official journal of the North American Spine Society, 2004. 4(6 Suppl): p. 190S-194S.
[37] Park P, Garton H.J, Gala V.C, Hoff J.T, McGillicuddy J.E. Adjacent segment disease after lumbar or lumbosacral fusion: review of the literature. Spine, 2004. 29(17): p. 1938-44.
[38] Katsuura A, Hukuda S, Saruhashi Y, Mori K, Kyphotic malalignment after anterior cervical fusion is one of the factors promoting the degenerative process in adjacent intervertebral levels. European spine journal: official publication of the European Spine Society, the European Spinal Deformity Society, and the European Section of the Cervical Spine Research Society, 2001. 10(4): p. 320-4.
[39] Goffin J, Van Calenbergh F, van Loon J, Casey A, Kehr P, Liebig K, Lind B, Logroscino C, Sgrambiglia R, Pointillart V, Intermediate follow-up after treatment of degenerative disc disease with the Bryan Cervical Disc Prosthesis: single-level and bi-level. Spine, 2003. 28(24): p. 2673-8.
[40] Chow D.H, Luk K.D, Evans J.H, Leong J.C, Effects of short anterior lumbar interbody fusion on biomechanics of neighboring unfused segments. Spine, 1996. 21(5): p. 549-55.
[41] Wai E.K, Santos E.R, R.A. Morcom, R.D. Fraser, Magnetic resonance imaging 20 years after anterior lumbar interbody fusion. Spine, 2006. 31(17): p. 1952-6.
[42] Wittenberg R.H, Shea M, Edwards W.T, Swartz D.E, White A.A, 3rd, Hayes W.C, et al, A biomechanical study of the fatigue characteristics of thoracolumbar fixation implants in a calf spine model. Spine, 1992. 17(6 Suppl): p. S121-8.

[43] Sukthankar A, Nerlich AG, Paesold G. Age-Related Changes of the Spine. Spinal Disorders: Fundamentals of Diagnosis and Treatment. Spinger, 91-122, 2008.
[44] Pedram M, Dupuy R, Vital JM. Spondylolisthésis lombaire dégénératif. Encyclopédie Médico Chirurgicale, Appareil locomoteur, Elsevier, 15-835-B-10, 2003.
[45] http://www.sandiego- spine.com/subject.php?pn=lumbar-disc- disease-035.
[46] https://img.webmd.com/dtmcms/live/webmd/consumer_assets/site_images/media/medical/hw/
[47] http://www.spineinfo.co.uk/wp-content/uploads/
[48] https://www.spineuniverse.com/conditions/spinal-stenosis/surgery-spinal-stenosis
[49] Panjabi M.M. Clinical spinal instability and low back pain. Journal of Electromyography and Kinesiology 13 (2003) 371–379.
[50] https://static.spineuniverse.com/sites/default/files/images/2010/08/12/.
[51] https://www.spine-health.com/figure-7-graf-ligament
[52] Kashkoush A, Agarwal N, Paschel E, Goldschmidt E, Gerszten PC. Evaluation of a Hybrid Dynamic Stabilization and Fusion System in the Lumbar Spine: A 10 Year Experience. Cureus. 2016 Jun 10;8(6):e637. doi: 10.7759/cureus.637
[53] http://www.buykorea.org/product-details/bioflex-spring-rod-system--3004522.html
[54] http://globalpatientnetwork.com/devices/DSS.html
[55] Kaner, Tuncay, and Ali Fahir Ozer. Dynamic stabilization for challenging lumbar degenerative diseases of the spine: a review of the literature. Advances in Orthopedics, 2013.
[56] http://www.thespinemarketgroup.com/cd-horizon-peek-rods/
[57] Panjabi M.M, Timm J.P. Development of Stabilimax NZ From Biomechanical Principles. SAS Journal, Volume 1, Issue 1, March 2007, Pages 2-7

Chapter 3:

Biomechanical Response of Lumbosacral Segments under Physiological Functions

3.1 Introduction

The purpose of this study is to establish an accurate computational FE model to simulate the biomechanical response of human lumbar spine under physiological functions. Its success at simulation is not guaranteed but must be proven by suitable validation to ensure the accuracy in any function. The model is considered as successfully validated if, in limited number of situations, its predicted behavior comes close to the experimental results. It is then assumed that the model may now be exercised to predict behavior of the structure in other situations by knowledge of regular spinal movements [19, 34]. The lumbar region is a recurrent site of spinal disorders [12, 40]. Clinical studies have testified that abnormal intervertebral motions occur in some patients who have low-back pain and the utmost proportion (about 90%) of spinal disorders is located in the lumbar spine segment. Luoma et al [15]. While, in absence of pathological disease, regular daily activities, lifting stationary work postures, heavy physical work and vibrations are factors that contribute to low back disorders [22, 36]

Usually, orthopedic treatment is essentially based on the experience of the surgeon who predicts the best solution for each patient. Using mathematical models and computer simulations could hypothetically be a key tool that supports clinical decisions in order to predict the presence and evolution of spine pathologies, for preoperative planning and implant design. [30,36,43]. The present work is focused on the analysis of the lumbar spine with the aim of studying the influence and the roles that the different components of the spine play on its biomechanical response, in particular the presence of an injury in the intervertebral disc (IVD).

In order to understand the whole lumbosacral segments response under physiological conditions, the complete three-dimensional elastic physical properties of the

lumbar spine were precisely documented, then, (L1–S1) rachis FE model was built and their mechanical responses under static loading were predicted. [34, 39].

Pure moments of flexion-extension, inlateral axial torque, and inlateral lateral bending were applied, and three-dimensional intervertebral motions were determined. The motions were presented in the form of a set of six load-displacement curves, quantifying the intervertebral rotations and translations. The current model should preserve the anatomical details required to simulate the biomechanical response, including tissue material properties appropriate for treatment of spinal disorders, and be validated in relevant loading scenarios.

3.2 Medical, image-based bone reconstruction

The biological or medical imaging signifies the creation of anatomical images of human body parts and function. In the biomedical field, imaging conventionally indicates CT (computed tomography) or MRI (magnetic resonance imaging) techniques are favorites for the most, bioengineers and medical physicians, active in biomedical modeling, due to their ability to prove high inherent image contrast between bone and soft tissue.

CT is capable of generating 2D images of various body structures, based on their ability to endure the emitted X-rays. As bone has a unique spectrum of X-ray permeability within the human body, it shades white in a CT slice. Figure 3.1, thus allowing its relatively unimpeded segmentation of the bone from soft tissue, since no other body part exhibits overlapping CT numbers. Winder et al [1]. This results in a 2D outline of the scanned bone and the 3D data set, is generated from consecutive measurements. Contemporary CT units facilitate slice, spacing in the magnitude of 0.5 mm, or even lower. Schmutz et al [2], and overlaying these slices, allows the tridimensional reconstruction of virtually any skeletal characteristic within the human body. Such models range from smaller parts like the mandible to high mobility joints 19-21 and complex anatomical structures as the entire spine. Lafage et al [3].

MRI scanning is based on atoms magnetization rather than ionizing radiation used by CT. This is mainly useful when trying to capture tissue with many hydrogen nuclei and little density contrast thus providing high accuracy even for soft tissue images. The

basic concept in reconstructing 3D geometries, through MRI, is similar to the one of CT. Chirani et al [4].

Following two distinctive steps, thresholding of the desired spectrums, to determine the bone contour within every scan and overlaying of those to constitute the 3D geometry. The slice spacing however is slightly distanced when compared to CT imaging techniques, as conventional MRI units fail to capture images less than 1mm apart. Drapikowski et al [5]. CT and MRI scanning protocols follow data acquisition in accordance to DICOM (Digital Imaging and Communications in Medicine). DICOM is the standard communication protocol for structuring and encoding medical reports of Riesmeier et al [6] used by commercial image manipulation software Mimics 17.0, required for converting multiple 2D images into a 3D one. As the aforementioned multislice-imaging capabilities of most medical section are insufficient to reconstruct an isotropic data set of the examined anatomy, interpolation of the image information is required to ensure accurate representation. Although this process does not result in higher resolution of the reconstructed geometry, it leads to smoother representation allowing the distinct removal of the remaining soft tissue in close proximity to the bone.

The segmentation of bone and soft tissue is a process of significant importance as it represents the final step in acquiring the desired bone geometry. There exist a variety of segmentation methods of Messmar et al [7] based on purely automated methodologies reconstructing *.stl files (stereolithographie: triangle surface models) of the bone contour through Mimics 17.0

An exact three-dimensional nonlinear finite element model of L1-S1 has been developed. The primary information was obtained from CT images of a 43-year-old male. These images were arranged in a sequential cross-section at 0.5 mm intervals and imported into Mimics 17.0 (Materialise Mimics ver. 17.0), in *.dcm file format. An image processing step was undertaken to develop bone boundaries, by defining a brightness threshold for detecting bony tissue from surrounding soft tissue. The defined borders for each vertebra were combined together and used to create the outer area of bony tissue. Then, a smoothing procedure was performed on the volume boundaries by replacing each node at a slightly different location. This procedure helps in refining the geometry without any reduction in node (or element) numbers. Subsequently, the surface areas of

new volumes of each vertebra were exported to finite element software in IGES file format (Figure 3.1).

There exists however, a consensus throughout literature that highly accurate models require semi-automated segmentation, supported by manual correction of the threshold results by experienced operators. Such multi threshold segmentation techniques calculate the mean grey-scale within the image and employ sensitive edge detection filters. Rathnayaka et al [8], to distinguish the apparent tissue types.

After the representation of the model's outer surfaces, cortical and cancellous bone properties have to be assigned. This can be directly achieved within the Mimics 17.0 through accurate distinction of the two types based on their CT spectrum or by considering both, the inner and outer cortex of the cortical bone, or by creation of outer shell using Abaqus mesh tools. Herein lies the main disadvantage of MRI when attempting to reconstruct skeletal models, as bone cannot generate a magnetic resonance signal, due to its severely short transverse relaxation times. Therefore, the bone is indirectly approximated through the signal generated from the surrounding soft tissue which in most cases leads to accurate results, requires however extreme caution and experience in cases where interposing soft tissue is present.

However, in cases, extensive bone areas have to be scanned MRI exhibits another significant disadvantage. Scanning of a region of 20 cm in length, requires approximately 25 minutes with MRI, whereas just a few seconds would be sufficient in CT. This severely affects the measurement accuracy of un-sedated patients and therefore requires a further step during the reconstruction process. A variety of motion compensation techniques and software have been developed to sustain this. Pipe et al [9]. This disadvantage of MRI does however compensate for the less invasive character of the methodology (radiation wise) when compared to CT, the long exposure of patients during extensive scanning, renders this technique in some cases (i.e. young children) ethically unjustifiably by Brenner et al [10]

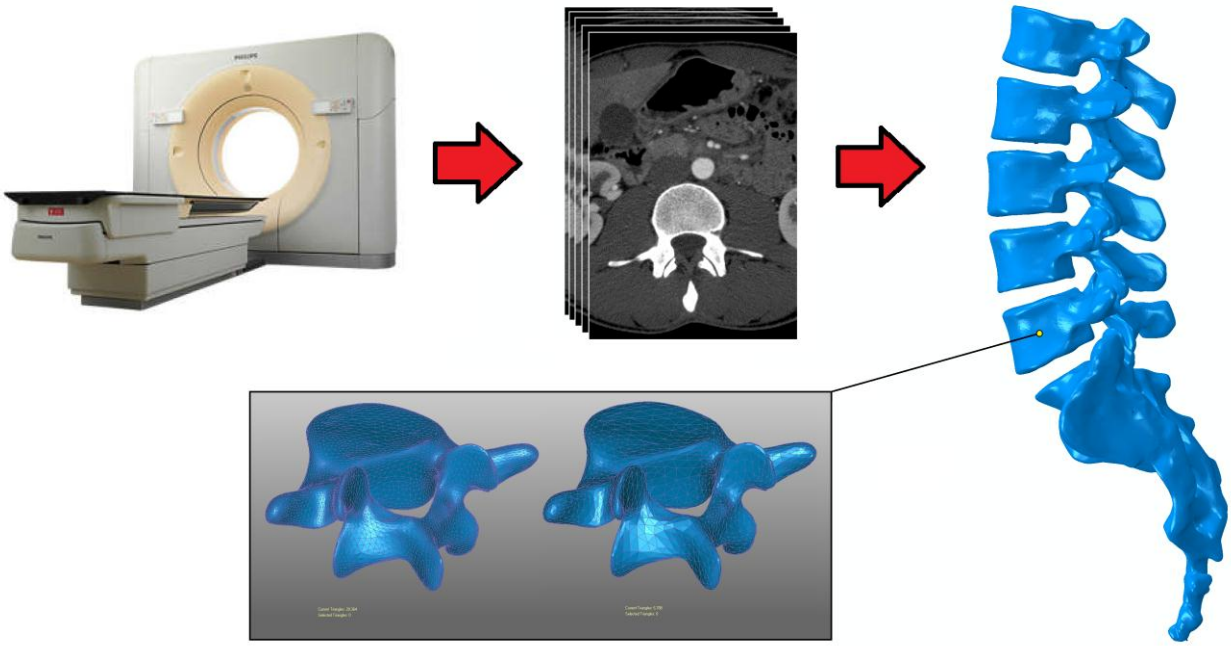

Figure 3.1: Medical imaging-based reconstruction of a vertebral column based on volumetric mesh. Smoothed and decimated polygons of the L5.

3.3 CT scanning and 3D mesh model reconstruction

The main steps include post-processing of a triangulated vertebra surface mesh generated from segmented 3D imaging data, extraction of spline from the triangulated surface mesh, construction of spline surfaces from the triangulated surface mesh, and finally creating solid, splines from the spline surfaces. The workflow is outlined below.

A real-life case was selected to enable finite element modeling of the lumbosacral spine. A 43-year-old male patient undergoing back pain treatment was scanned with 0.5 mm slice thickness, 0.5 mm slice increment, and acquiring a total of images. The DICOM images were imported into Mimics 17.0 for image processing and 3D model reconstruction (other biomedical platforms such as Amira have similar functions).

FE Analyses were performed using a 3-Dimensional nonlinear model of the spine arraying from L1 to S1, created following multiple processes (Figure 3.6). The global geometry was derived from a CT scan based on the reconstitution of the L1-S1 FSU Data, then translated to patch *.iges model then to a simplified solid model using Power surfacing (Solidworks 2013). (Figure 3.1) This geometrical simplification allowed the full optimization of an accurate three-dimensional model. The geometry of the vertebra and

the intervertebral disc was approximated to match the realistic model of normal cadaveric lumbar segments.

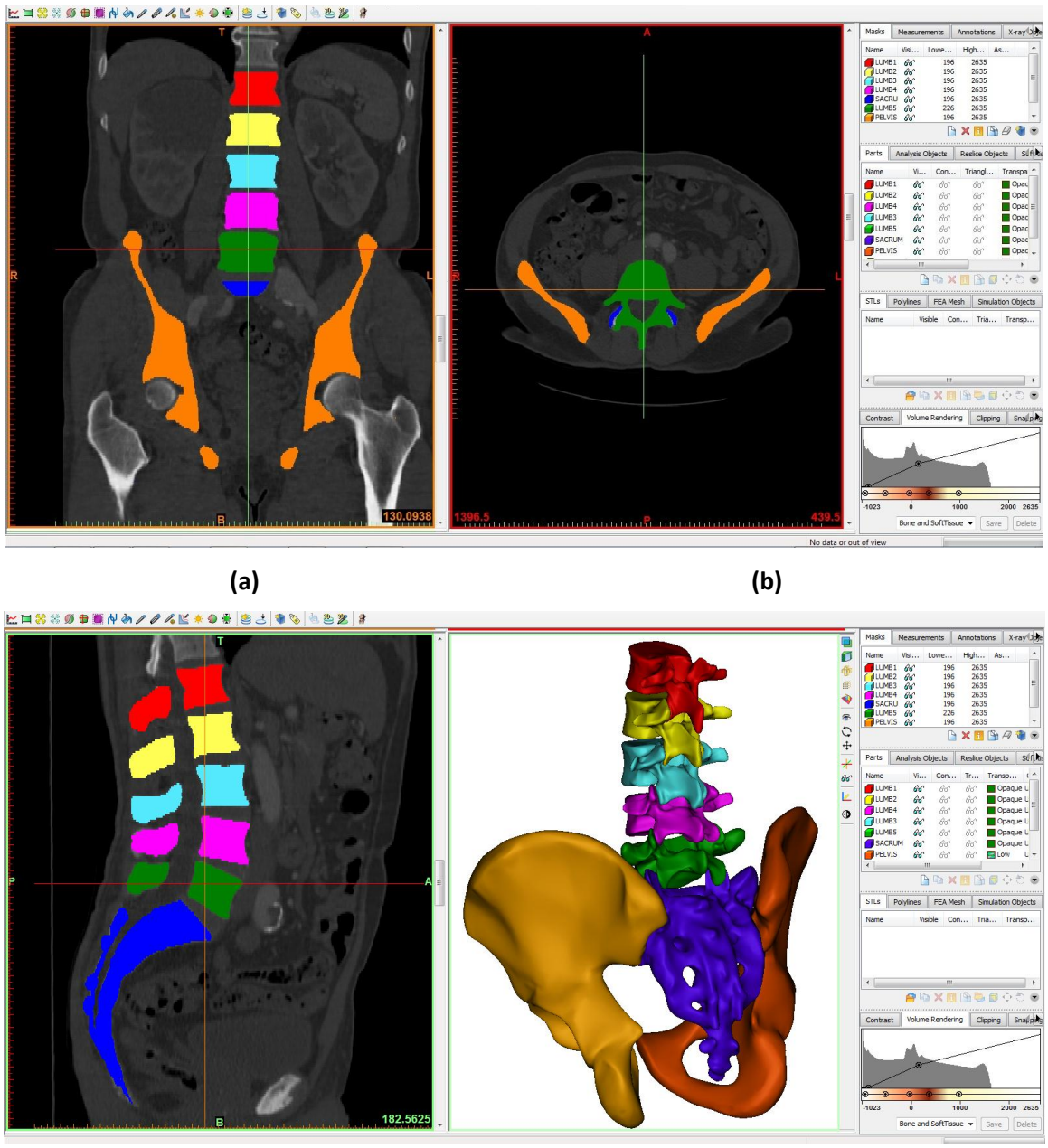

Figure 3.2: 3D model of lumbar spine reconstructed from CT images.

The vertebrae were separated from whole tissues by extracting regions of interest using segmented masks. (a) coronal plane, (b) transverse plane, (c) sagittal plane, (d) 3D view.

Figure 3.3 shows the reconstructed lumbosacral spine bone created using CT images. The procedure involved three steps: thresholding, region growing, and 3D calculation. On the

images, the masks of hard tissues (bone) vertebra were not connected, so the mask of (Cortical + Spongy (trabecular bone) could be separated easily from the spinal structure by region growing with seed in vertebra. The accuracy of the model is related to the quality of the image and the scanning slice interval, but is also affected by the manually determined parameters for the HU threshold value recommended by the software for different tissues; for example, the range for bone is 226 – 2635, and for muscle within 5 – 135. However, these are not always applicable in individual cases. The 3D model can then be exported as an STL file and used for 3D printing, parametric surface design, or FEM modeling.

3.3.1. FEM modeling based on triangular mesh

A reconstructed rough triangular mesh consists of a group of linked triangles, and is an approximation of the real surface of a part by many planar facets. It is thus extremely useful to describe parts that have complicated geometry. However, as the triangular mesh only includes surface information, it needs to be transferred into the volume mesh required in FEM simulation.

3.3.2 Triangulated Surface Mesh Post-Processing

The triangulated surface mesh generated from segmented imaging data may contain geometric features and degeneracies that prohibit downstream processes. These items include duplicate vertices, duplicate edges and faces, non-manifold vertices and edges, holes and opening ends (missing end caps), and so on. These features are especially detrimental to the sensitivity of the centerline-producing algorithm. A mesh healing and repairing step is carried out semi-manually using Geomagic. Like any geometry cleaning operation, care must be taken not to distort, smooth or remove important characteristics and attributes found in the raw data. This is largely carried out visually at the discretion of the user.

3.3.3 Mesh preprocessing and volume mesh creation

3-matic, a meshing tool of Materialise, or Abaqus plugin “convert triangulation to tertrahedron” can be used to create the volume mesh from the surface triangular mesh, the hollow of the surface model with the triangular mesh is filled with the volume element, the internal structure of the bone marrow cavities filled with volume element, thereby representing the actual structure of bone geometry.

(a) Triangular mesh model including 14, 758 triangles, from the cut model certain internal structures can be seen, (b) tetrahedron mesh model including 76,877 elements, where the hollow model is filled by volume elements.

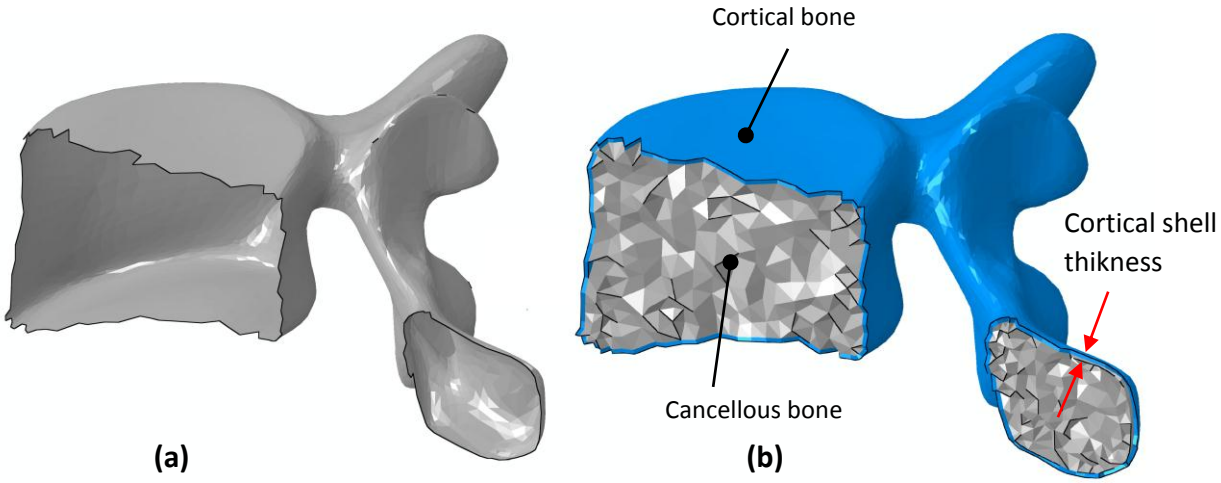

Figure 3.3: Volumetric mesh created from triangular mesh

(a) Triangular mesh (b) volumetric mesh + cortical shell insertion.

Mesh processing can also be used for mesh model preprocessing; for example, Geomagic, in which the mesh can be fixed, smoothed, and easily reduced. If the triangular mesh passes a quality check without errors, it can then be used to create a volume mesh with a 4 nodes tetrahedron element. The volume mesh can be created directly in 3-matic, or in Abaqus, via the mesh edit tool. The file pattern for data exchange between the two platforms is the input file of Abaqus, which is named *.inp. Figure 3.3 shows the change in the model when the volume mesh is created from the triangular mesh. The number of elements has increased by almost five times that of the triangular mesh, and thus the volume mesh can be directly used in FEM calculations with the homogenous material properties.

3.3.4 FEM modeling based on parametric surface

Parametric surface is the most popular geometrical tool used to describe 3D models in all commercial CAD platforms. Although the parametric surface of a bone model is very difficult to create because of the complicated geometrical structure of bone, it remains the main data source used in FE modeling for biomechanical analysis. However, in order to obtain a high-quality parametric surface model of a bone and increase the

capability in FEM meshing, a number of necessary operations are required to simplify and approximate the surface in the triangular

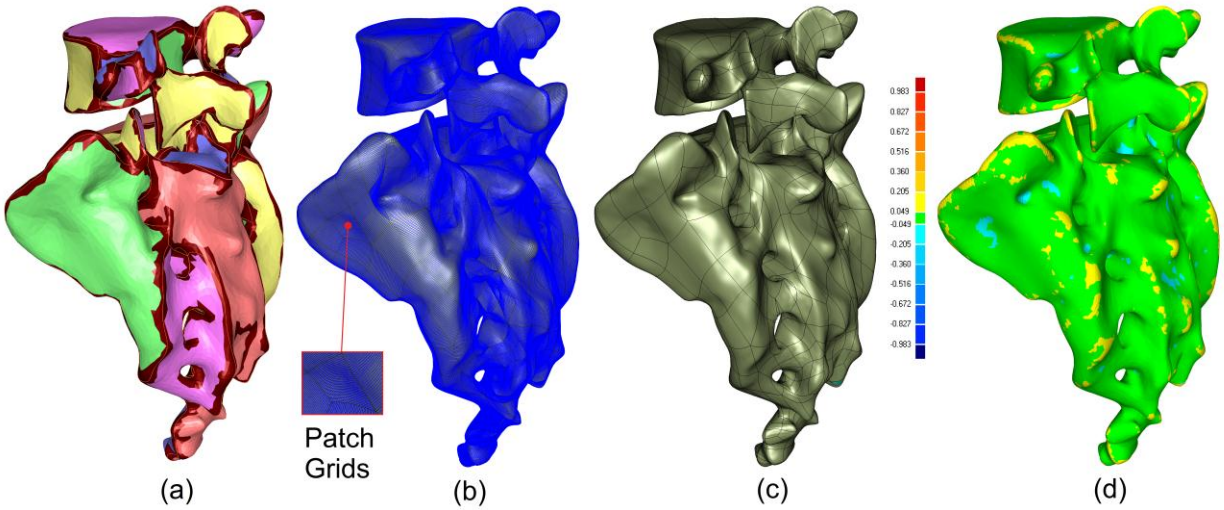

Figure 3.4: Parametric surface model creation.

(a) Curvature estimated based on triangular mesh (24,350 triangles) to create feature curves and separate initial patches using different colors, (b) For each patch, interpolation grids created for fitting, which will determine the control points of each parametric surface, (c) Surface model created by fitting of triangular mesh, (d) Parametric surface model compared to original triangular mesh model and deviation obtained. Mesh model, and these introduce extra errors in the model and decrease model accuracy. Therefore, the balance between surface quality (including accuracy) and modeling efficiency during parametric surface creation is a crucial issue.

3.3.5 Patch creation for triangular mesh

As the basis for parametric surface fitting, the triangular mesh only includes discrete information. Although a fully automatic method for a parametric surface represents model construction based on the triangular mesh in Geomagic, it is not robust enough for the mandibular bone with its complicated geometry. Therefore, manual operation is required, but this is tedious and time-consuming.

Figure 3.4, 3.5 shows the procedure of NURBS surface creation from triangular mesh. To create four-side patches for parametric surface fitting, the curvature is estimated automatically on the triangular mesh and the features of acute borders can then be detected. These curve borders can be used as the primary curves when dividing the

triangular mesh directly into serial patches. However, certain errors may exist, as shown in Figure 3.7 (b), which then result in intersected, disordered, or singular triangular patches. In addition, if there are too many patches, the calculation time is increased, and thus the number of patches can be decreased using a manual setting.

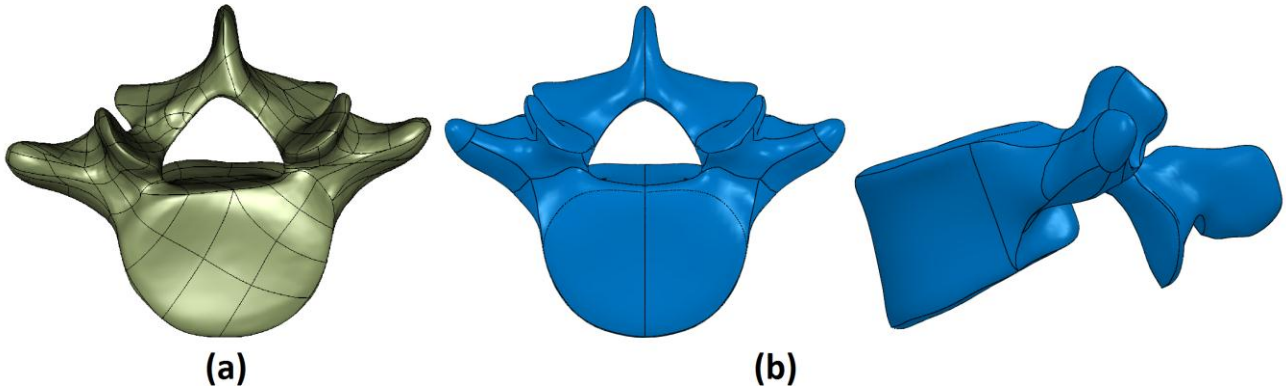

Figure 3.5: Parametric surface model creation. (a) Automatic patch generation (290 patchs) (b) Mosta simplified parametric surface generation (30 patchs).

To improve the quality of patches, it is possible to perform manual operations such as patch optimization, point moving, adding or removing, and swapping sides. Then each patch can be used to create a 4-sided parametric surface, and all the linked surfaces can be joined with G1 continuity crossing the borders. Based on the interpolation points extracted from the related triangles, parametric surfaces can be approximated using boundary continuity constraints to obtain the whole surface model. Geomagic provides an error analysis tool for comparing the parametric surface model with the original triangular mesh model, and a color-coded deviation image can then be acquired.

As shown in Figure 3.5, the surface model has high accuracy compared to of the triangular mesh model.

3.3.6 Solid model creation and re-meshing

The parametric surface model can be saved as an IGES file (*.igs), which can then be imported into almost all CAD platforms, such as Solidworks 13.0 (Figure 3.5). These surface patches can then be stitched to form a completely solid model. The solid model is evidently uniform without any internal structures, which is different from the volume model constructed from the triangular mesh model. However, with powerful design tools

within CAD platforms, some of the required parts with complicated geometries can be designed, such as implants, fixation plates, screws, or individualized grafts.

The solid model can be exported via several types of file, such as a parasolid file (*.x_t), Step file (*.stp) or other files defined by CAD software; these can then be imported and recognized by Abaqus 14.1. The meshing tools in Abaqus can be used to create the FEM mesh on the solid model, but using these tools, the geometrical problems in model are very hard to be fixed, which often results in failure of the meshing work.

3.3.7 Topological Comparison of Biomodels

Topological comparisons were performed in Geomagic 14 software between reconstructed 3D digital models and STL data of anatomical models. The 3D topological differences are examined as the shortest distance from the test model to any point on the reference model. The magnitude of 3D deviations (positive and negative values of maximum distances) is represented as in colored contour plots as illustrated in Figure 3.4. The diagnosis map between reference and test models is shown. Figure 3.6.

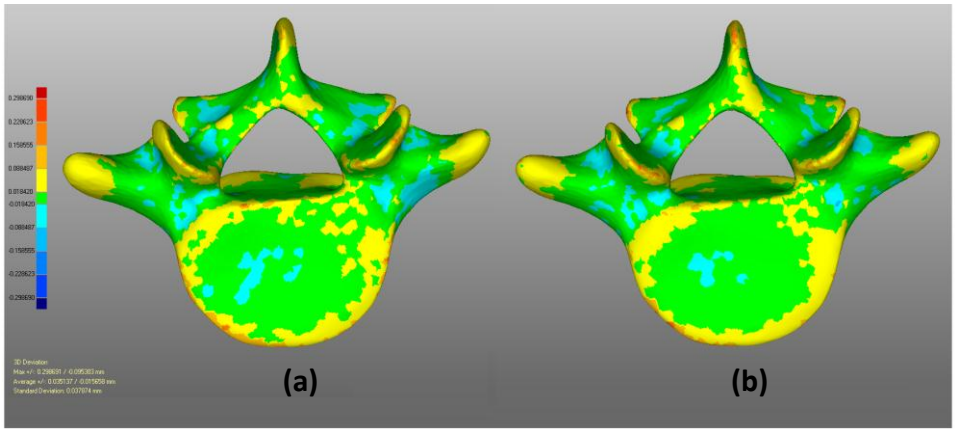

Figure 3.6: The magnitude of 3D deviation of vertebra performed with Geomagic relaxing (a) Prime model (b) Smoothed model (1 iteration).

3.4 Finite element model formulation

The main procedure is employing hierarchical approaches to develop a biomedically validated computational model of the lumbar spine to investigate the spinal disorders and diseases [29,34]. An Osseo-ligamentous FE model of the L1-S1 levels was built and validated through comparison to literature data. An extended description of the model and its adaptation for the present study are outlined below in this study. The

developed lumbar spine FE model was created based on anatomically accurate geometries and was modeled based on epidemiology for injuries and disease due to the literature [26, 29, 34]. FE Analyses were performed using a 3-Dimensional nonlinear model of the spine arraying from L1 to S1, created following multiple processes (Figure 3.8).

The global geometry was derived from a CT scan based on the reconstitution of the L5-S1 FSU Data taken from male cadaver what did not have any trauma or pathology that effect bone quality and integrity of vertebral bodies, then translated to patch iges model then to a simplified solid model using Power surfacing (Soliworks 2013). (Figure 3.7).

The geometry of the vertebra and the intervertebral disc was approximated to match the realistic model of normal cadaveric lumbar segments. The model of a Lumbar Spine was developed using Ansys revision 15.0 (Ansys Inc., Houston, PA, USA). However, fully automated hexahedral mesh generation is not available for complex geometric entities such as the human lumbar spine. Utilizing hexahedral elements to effectively model the complexly shaped lumbar spine is not trivial and requires a substantial amount of work to subdivide the geometry in preparation for mesh generation. This meshing is desirable for FE analysis due to the nature of their shape function and ability to handle large deformations without creating numerical instabilities.

Concerning the parametric meshing, the developed spinal mesh was symmetrically modeled across the midsagittal plane as adopted by Moumene et al [30], the mesh density and geometry was defined to represent the key passive anatomical features: cortical and cancellous bone; endplates; posterior elements of the vertebrae; annulus fibrosis and nucleus pulposus; articular cartilage; synovial fluid of the facet joint [44,49]. 8-node solid element (C3D8) were used to define the cancellous bone and posterior elements of the vertebrae and articular cartilage of the facet joints, the cortical bone and endplates of the vertebrae and elsewhere using hexahedral element based on hybrid formulation for hyperelastic structure for the Annulus Pulposus (AP). Cortical bone and endplates of the vertebrae modeled using 8-node brick elements with 0.635 mm thickness. [25, 30]. Abaqus 14.1 was used to formulate the FE model.

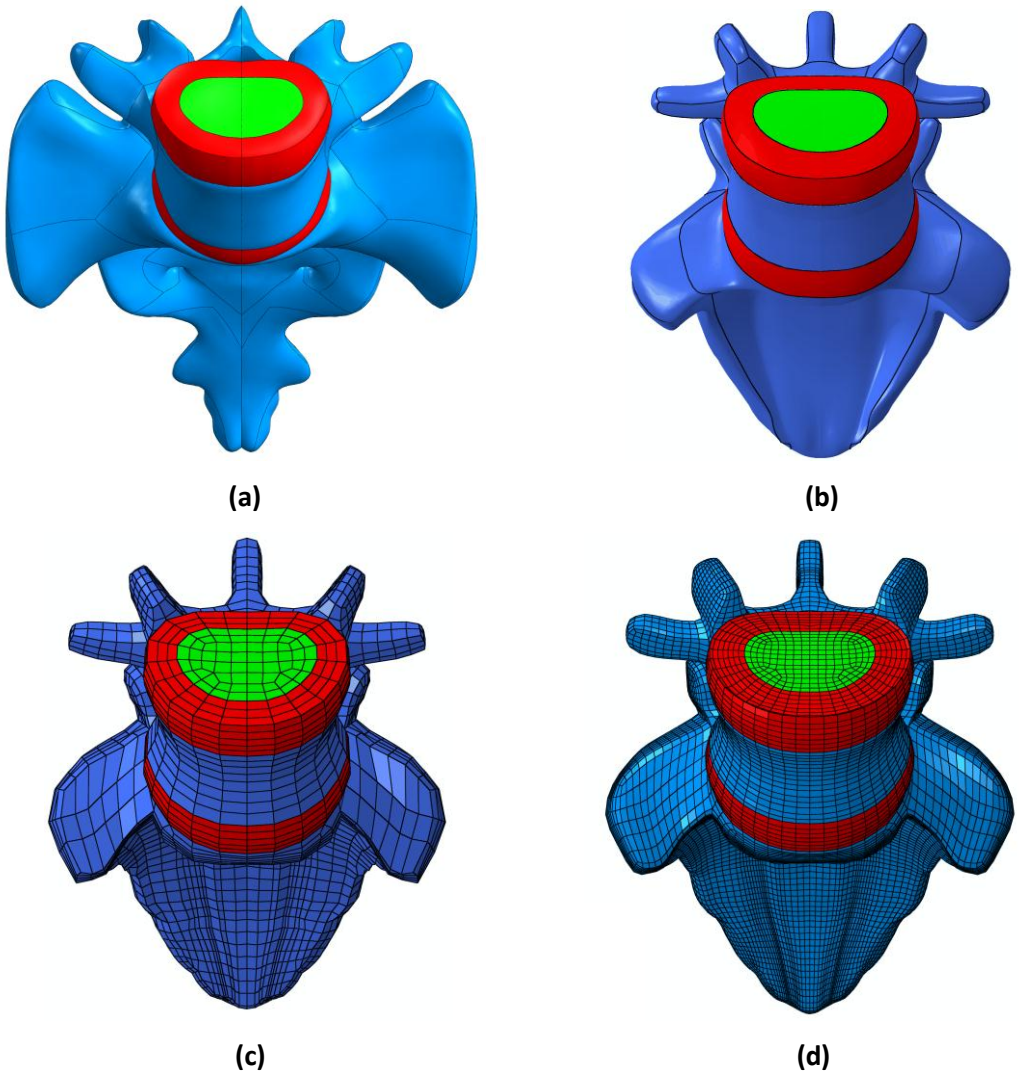

Figure 3.7: Finite element model formulation (a) Realistic L5-S Geometric Model, (b) Simplified Power Surfacing Geometric Model, (c) Generated Meshed Model using Ansys, (d) Refined smoothed FE Model

Thus, the utmost critical component of the spine in both its mobility and load bearing ability is, consequently the intervertebral disc (IVD) and its FE formulations have an excessive significance.

The Annulus Fibrosus (AF) was simulated as a typical composite-like ground structure including a solid matrix with embedded bands of reinforced collagenous fibers in concentric rings, defined as 3D Truss tension-only behavior cable elements (T3D2) (Figure 3.8), around the nucleus pulpous [21,30]. The collagenous Fibers lamellae elements were arranged in 7 layers in a crisscross fashion by connecting diagonally the

corner nodes of the inner and outer faces of the annulus elements to mimic the slant wisely realistic fibers. Moumene et al [30].

The Nucleus Pulposus (NP) was assumed as incompressible body, it was modeled as fluid filled cavity using hydrostatic fluid elements [31, 34]. Whither; the minimum intradiscal pressure was limited to zero which is 0.1 MPa relative to atmospheric pressure. Rohlmann et al [44]. Hydrostatic fluid elements overlaid the boundaries of the nucleus pulposus. They share the nodes at the cavity boundary with the elements of annulus fibrous and the endplates. Paige et al [34]. The nucleus lumped standard 8-node brick elements assumed to occupy 43% of the whole volume of the disc. Baroud et al [11].

Facet joints. Overall, it is accepted in the clinical studies that articular facets are two of the three joints that transmit the load from one vertebra to the next. It has been assessed that they transmit from 18% to 36% of the load shared upon from the spinal posture [32, 52]. The zegapopheseal joints was simulated by a cartilaginous layer, and assumed to be multi-linear elastic in compression using 3D contact surfaces-to-surface finite sliding penalty tangential connection with softened contact in the normal direction by a thin cartilage material of 0.4 mm in thickness. [30,53] which exponentially increases the contact stresses, transmitting only compressive loads through spinal column with an initial gap of 0.2 mm [32, 45]. The cartilage of the facet joint was modeled by 8-node solid elements overlaid with 8-node thin shell elements to mimic the meniscuses function in the lumbar zygapophyseal joints which behave linearly [44, 45, 49].

The basic sought is the use of real transverse and longitudinal angles morphologies; whereas, the present study conducts each and every articular facets of vertebral column from L1 to S1 as a critical articulation, totally chosen in accordance to previous observations from Masharawi et al [28], Panjabi et al [38] using Hypermesh 13.0 (Altair Engineering.Inc). (Figure 3.8). The facet joints work as typical contact structures governed by unilateral conditions, limiting and preventing excessive the spinal movements, extension, lateral bending, axial torsion and translation between adjacent vertebrae and resist forces acting perpendicular to the vertical articular surfaces, thus stabilize the lumbar spine in compression, almost in the plane of the disc. White et al [52].

Ligaments. The strength characteristics of the various ligaments differ from ligament to ligament as well as from region to region. The effectiveness of a ligament is determined

by its intrinsic morphology. [32, 45, 55]. As the load increases, the solid (component) becomes ‘‘fully engaged’’ and enters the elastic zone. For small displacements, the size of the deformation is proportional to the deforming force. The relation is linear. And the solid develops a permanent set or deformation that does not change when the stress is removed [51,52].

All of the seven major ligaments in the lumbar spine, including anterior Longitudinal Ligament ALL; Posterior Longitudinal Ligament PLL; Intertransverse Ligament ITL; Ligamentum Flavum LF; Capsular Ligament CL; Supraspinous Ligament SSL; and Interspinous Ligament ISL were modeled as three-dimensional, two node truss elements (T3D2) and assigned nonlinear hypoelastic behavior [17,22,45]. Hypoelastic material designations allow simulation of naturally changing ligament with different axial stiffness at a different level as a function of axial strain stiffness, initially low stiffness at low strains which create a toe region followed by increasing stiffness at higher strains. The ligament attachment points were chosen to mimic observed anatomic attachment locations as closely as possible. The material properties for various spinal elements were adopted from literature and summarized elsewhere (Table 3.1).

The 3D geometry of L1, L2, L3 and L4 was adapted from the model of L5 vertebrae by replication and 3-dimensional anatomy which had been formed and morphologised using Hypermesh 13.0. This Procedure generates the mesh of L1–L5 vertebra and then positioned such that the angle between the vertebrae was mimic the curvature of cadaveric spinal lumbar lordosis [23]. The intervertebral discs were created between vertebrae using the adjacent superior and inferior surfaces of the vertebral bodies. To model the lumbar spine, we discretize 16558 eight node brick elements, corresponding to a total of 20595 nodes and 4416 truss element (T3D2) (Figure 3.8).

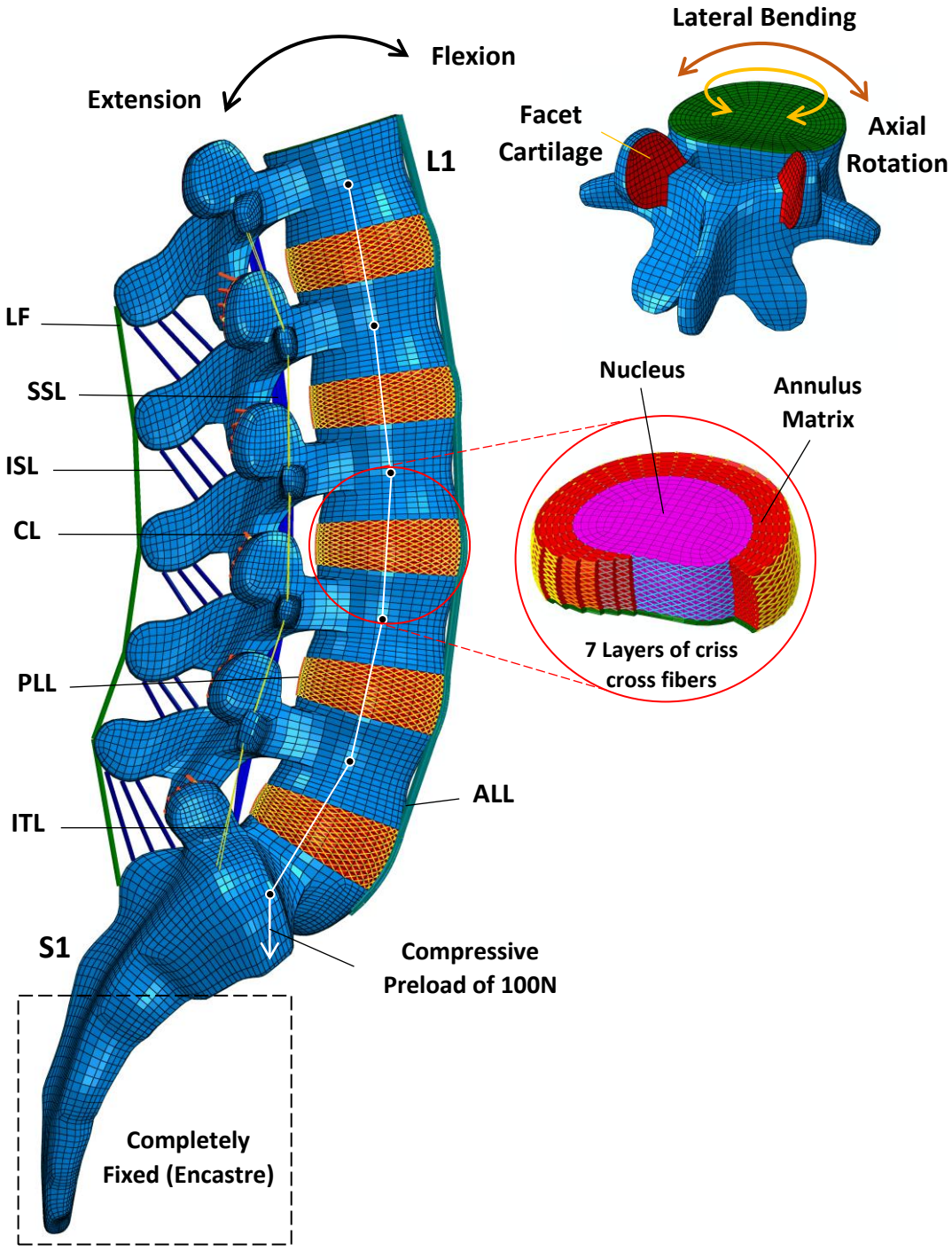

Figure 3.8: Finite element model of the lumbosacral spine

3.5 Finite Element Model Formulation Workflow chart

The FE model development followed the workflow chart described in Figure 3.9 The meshed model files were exported from Hypermesh to Abaqus solver. Post-processing was performed using Abaqus CAE /Post. The algorithms proposed in the present study is implemented into Abaqus as a User Material UMAT code embedded in a

Python and Intel Fortran Compiler environment to simulate the biomechanical behavior of the lumbar spine components. This numerical approach consists on hyperelastic constitutive model of Mooney-Rivlin model of the Annulus Pulposus (AN) and a constitutive model of the hypoelastic material of the seven major Ligaments, which were implemented in Abaqus via (UMAT) subroutines and Python Scripts (Appendix A, B and C). This module was used to define the strength of the material, using a first order equation. The material parameters of the hypoelastic constitutive model were calculated by three-dimensional truss strain invariants. It was found that only one material parameter varies linearly. The new numerical approach was able to predict the load-displacement plot.

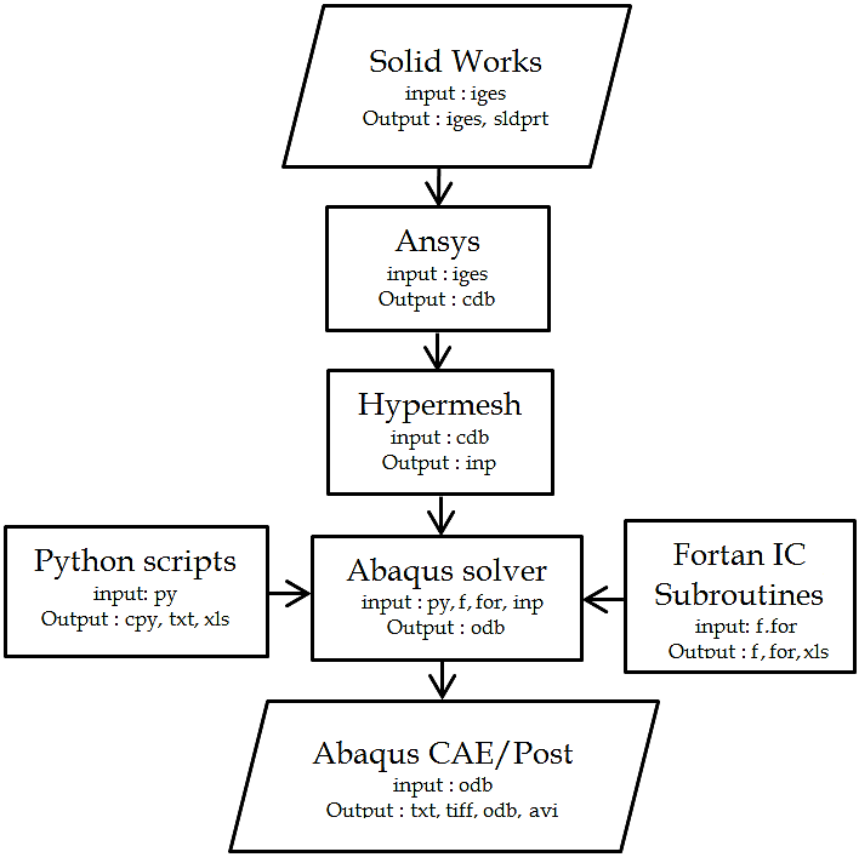

Figure 3.9: Finite Element Model Formulation Workflow Chart

3.6 The intervertebral disc (IVD) Model Validation

The symmetric FE model of the human lumbar disc is developed to investigate the optimized properties required to mimic the intact by matching model predictions to experimental results. This model was checked for sensitivity to the input parameter values

and found to give reasonable behavior. The model has incorporated increasing detail to represent an individual disc rather than discs as a whole. This modeling attempts to represent reality by simplifying the system.

Table 3.1: Details of the element types and material properties used in the FE model

Anatomical structures	**Elastic modulus (MPa)**		**Element type**	**Constitutive relation**	**Poisson's ratio**	**References**
Cortical bone	12,000		C3D8		0.3	[22,24,39,53]
Cancellous bone	100		C3D8		0.2	[22,30,47,53]
Posterior element	3,500		C3D8	Isotropic, elastic	0.25	[22,24,47,49]
Endplate	24		C3D8		0.4	[20, 32]
Facet Cartilage	11		C3D8		0.4	[15, 32, 47]
Nucleus pulposus			F3D4	Incompressible fluid filled cavity Formulation		[21, 21, 44]
Annulus ground			C3D8H	Isotropic, hyperelastic formulation Mooney Rivlin C_{01} = 0.56, C_{10} =0 .14		[22, 49]
Facet contact			Contact element	Nonlinear soft contact		[44,45]
Annulus fibers					**Cross-sectional Area (mm^2)**	
Layer 1	550		T3D2		0.72	
Layer 2	485		T3D2	Isotropic,	0.56	[11 ,48]
Layer 3	420		T3D2	elastic	0.45	
Layer 4	360		T3D2		0.34	
Ligaments						
ALL	7.8 (<12%)	20 (>12%)	T3D2		63.7	
PLL	10 (<11%)	20 (>11%)	T3D2		20	
LF	15 (<6.2%)	19 (>6.2%)	T3D2		40	
CL	7.5 (<25%)	33 (>25%)	T3D2	Hypoelastic	30	[17, 22, 30,45]
ITL	10 (<18%)	59 (>18%)	T3D2		1.8	
ISL	10 (<14%)	12 (>14%)	T3D2		30	
SSL	8 (<20%)	15 (>20%)	T3D2		40	

Nucleus Pulposus (NP) exhibits a gelatinous core and the Annulus Fibrosus (AF) was considered as an encompassing structure consisting of isotropic Crisscross reinforced fibers lamellae, therein describes the mutually coupled behavior of both solid deformation

and viscoelastic characteristics of fluid flow [21,45]. The Nucleus Pulposus and the annulus fibrosus of the intervertebral disc provide substantial tensile stiffness to axial stress, this aptitude decreases with initiative degenerative domain [33, 48].

As well as Nucleus Pulposus; the annulus ground also absorbs the hydrostatic pressure that results from mechanical loading of the spine. In fact, the annulus plays the great role in the biomechanics of the intervertebral discs [21, 33, 42].

3.7 Hyperelastic Model for the Annulus Ground Matrix

The hyperelastic response of the annulus ground substance was modeled using the isotropic hyperelastic Mooney–Rivlin (C_{10}, C_{01}) formulation based on the following reduced polynomial strain energy function (W):

$$W = C_{10}(I_1 - 3) + C_{01}(I_2 - 3) + (J - 1)^2/D_1 \quad (\mathbf{3.1})$$

where

C_{10}, C_{01} material constants characterizing the deviatoric deformation of the material

I_1, I_2 first/second invariants of the deviatoric of the left Cauchy-Green strain tensor

$D_1 = 2/K$ material incompressibility factor with K initial bulk modulus of the material

$J = V/V_0$ local volume ratio, the material constants for the annulus ground substance C_{10} and C_{01} were defined using the following approximation for Young's modulus E [26, 36]:

$E = 6(C_{10} + C_{01})$ Where $C_{10} = 4\,C_{01}$ and $K = E / 3(1-2\nu)$ by taking $\nu \cong 0.45$.

Values of 0.56 and 0.14 for the annulus were used for C_{10} and C_{01}, respectively. These values correspond to a Young's modulus of 4.2 MPa [42].

The behavior of the annular fibers was described by a linear tension only truss element, which was obtained from previous reports [17, 22, 30]. The cross-section stiffness of collagenous fibers was varied subsequently through the thickness of the annulus from inner to outer lamellae [47, 48], varied from 23% at the outer fiber layer to 5% at the inner layer [54], the maximum value is presumed near the outer annulus to approximate the Young's modulus of the ground substance in order to fulfill the required results. Table 3.1. [45, 47].

Various forms for the equations are governing the behavior of these materials and these are described in the following section. In order to entirely understand these equations, it is necessary to understand the laws for the state of stress in a structure.

3.7.1 Hyperelasticity Theories and Continuum Mechanics

A description of the laws of continuum mechanics relating to the hyperelastic strain energy equation is provided in the following sections.

3.7.1.1 Stress and Strain [54, 55]

In order to understand these variables it is necessary to understand the nature of the state of stress and strain on a general plane within a material (Figure 3.10).

The orientation of this general plane may be expressed in terms of direction cosines, ***l***, ***m***, and ***n*** (Equation 3.2). In this equation $\boldsymbol{x}_{OP}$, $\boldsymbol{y}_{OP}$ and $\boldsymbol{z}_{OP}$ are the vector co-ordinates of a vector between the origin of the co-ordinate system ***O***, and a point on the general plane ***P***.

$$l = \cos(\alpha) = \frac{x_{OP}}{r}, \quad m = \cos(\beta) = \frac{y_{OP}}{r}, \quad n = \cos(\gamma) = \frac{z_{OP}}{r} \tag{3.2}$$

Because the direction cosines aren't mutually exclusive a relationship is defined for them

$$l^2 + m^2 + n^2 = 1 \tag{3.3}$$

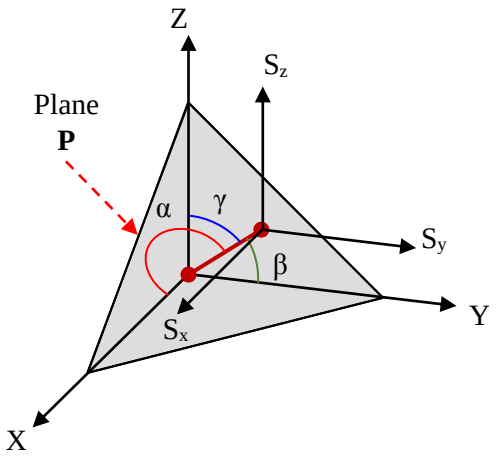

Figure 3.10: General plane showing the angles and the stress in that plane resolved in rectangular coordinates

Let *S* be the total stress on a general plane, *P*. If this stress is resolved in the rectangular co-ordinate system (Figure 3.6), it may be expressed as shown in Equation 3.4.

$$S = (S_x^2 + S_y^2 + S_z^2)^{\frac{1}{2}} \tag{3.4}$$

If the equilibrium of forces in each of the 3 directions is considered, expressions for the individual stress components in three orthogonal directions, S_x, S_y, and S_z, are determined (Equation 3.5).

$$S_x = \sigma_{xx} \cdot l + \tau_{xy} \cdot m + \tau_{xz} \cdot n$$

$$S_y = \tau_{yx} \cdot l + \sigma_{yy} \cdot m + \tau_{yz} \cdot n \quad \textbf{(3.5)}$$

$$S_z = \tau_{zx} \cdot l + \tau_{zy} \cdot m + \sigma_{zz} \cdot n$$

Where, σ = a stress normal to a plane, τ = a shear stress on a plane.

The subscripts on the normal and shear stresses in Equation 3.5 are interpreted as follows:

- The first subscript is the direction of the normal to the plane in which the stress acts
- The second subscript is the direction in which the stress acts. The *x, y* and *z* planes are normal to the *x, y* and *z* axes, respectively.
- The stress in a direction normal to the general plane may be determined by resolving the stress components in Equation 3.5 in the normal direction to give Equation 3.6. In this equation S_n is the stress normal to the general plane.

$$S_n = \sigma_{xx} \cdot l^2 + \sigma_{yy} \cdot m^2 + \sigma_{zz} \cdot n^2 + 2 \cdot \tau_{xy} \cdot l \cdot m + 2 \cdot \tau_{yz} \cdot m \cdot n + 2 \cdot \tau_{zx} \cdot n \cdot l \quad \textbf{(3.6)}$$

This is essentially the equation for transformation of stresses between co-ordinate systems of varied orientation.

There are 3 planes within the stressed system which are mutually perpendicular and on which there is a zero shear stress acting. The normal stresses acting on these 3 planes are called principal stresses. The first stress is a maximum, σ_1, the second is an intermediate value, σ_2, and the third is a minimum value, σ_3.

The principal stresses may be determined using the knowledge that in order for a normal stress to be a maximum on a plane, then the derivative with respect to the direction cosines of the expression for the normal stress (Equation 3.6) must be zero. Finding this derivative gives the expression for the principal stress σ_p in terms of the x, y and z stress components and the direction cosines stated in Equation 3.7.

$$\frac{S_x}{l} = \frac{S_y}{m} = \frac{S_z}{n} = \sigma_p, \quad S_x = \sigma_p \cdot l, \quad S_y = \sigma_p \cdot m, \quad S_z = \sigma_p \cdot n \quad \textbf{(3.7)}$$

This expression is then substituted into Equation 3.5 to obtain a system of equations which may be solved to determine the direction cosines for the plane in which the principal stresses act (Equation 3.8).

$$\begin{aligned}\left(\sigma_{xx}-\sigma_p\right)\cdot l+\tau_{xy}\cdot m+\tau_{xz}\cdot n=0\\ \tau_{yx}\cdot l+\left(\sigma_{yy}-\sigma_p\right)\cdot m+\tau_{yz}\cdot n=0\\ \tau_{zx}\cdot l+\tau_{zy}\cdot m+\left(\sigma_{zz}-\sigma_p\right)\cdot n=0\end{aligned} \quad \textbf{(3.8)}$$

In order to find a nontrivial solution for the system of equations outlined in Equation 3.8 the determinant of the stress matrix must be zero (Equation 3.9).

$$\begin{vmatrix}\sigma_{xx}-\sigma_p & \tau_{xy} & \tau_{xz}\\ \tau_{yx} & \sigma_{yy}-\sigma_p & \tau_{yz}\\ \tau_{zx} & \tau_{zy} & \sigma_{zz}-\sigma_p\end{vmatrix}=0 \quad \textbf{(3.9)}$$

If this determinant is expanded, the result is a cubic equation which may be solved to determine the principal stresses in terms of the stress invariants, $K_{i=1,2,3}$

$$\sigma_p^3-K_1\cdot\sigma_p^2+K_2\cdot\sigma_p-K_3=0 \quad \textbf{(3.10)}$$

Where

$$K_1=\sigma_{xx}+\sigma_{yy}+\sigma_{zz}$$

$$K_2=\sigma_{xx}\cdot\sigma_{yy}+\sigma_{yy}\cdot\sigma_{zz}+\sigma_{zz}\cdot\sigma_{xx}-\tau_{xy}^2-\tau_{yz}^2-\tau_{xz}^2$$

$$K_3=\begin{vmatrix}\sigma_{xx} & \tau_{xy} & \tau_{xz}\\ \tau_{yx} & \sigma_{yy} & \tau_{yz}\\ \tau_{zx} & \tau_{zy} & \sigma_{zz}\end{vmatrix}$$

$$=\sigma_{xx}\cdot\sigma_{yy}\cdot\sigma_{zz}+2\cdot\tau_{xy}\cdot\tau_{yz}\cdot\tau_{zx}-\sigma_{xx}\cdot\tau_{yz}^2-\sigma_{yy}\cdot\tau_{zx}^2-\sigma_{zz}\cdot\tau_{xy}^2 \quad \textbf{(3.11)}$$

3.7.1.2 Stress components and the strain energy equation, *W*

Strain energy in a body will be independent of the orientation of the structure. Therefore, in finding an expression for strain energy, it is desirable to express this quantity in terms of strain parameters which have no dependence on the body's orientation. Accordingly, the strain energy W may be expressed as a function of the strain invariants

$$W = f\left(I_1, I_2, I_3\right) \tag{3.12}$$

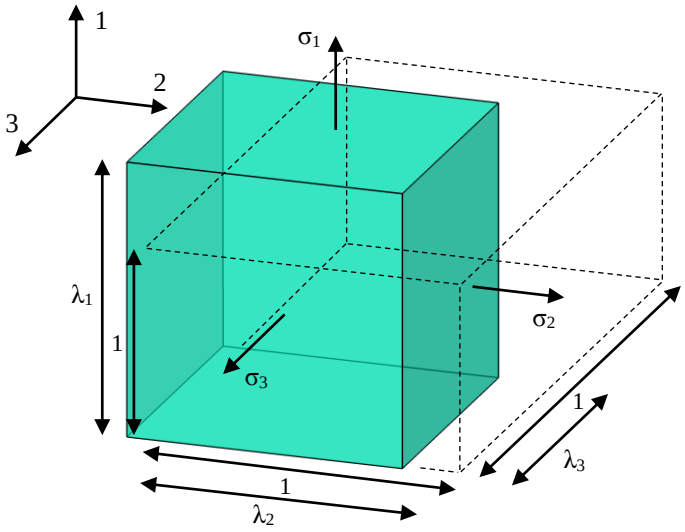

Figure 3.11: Cube of unit length subjected to pure deformation to give side lengths of λ_1, λ_2 and λ_3.

Consider the application of a stress to a unit cube such that the final structure experiences pure deformation and no shear. This deformation results in final edge lengths of λ_1, λ_2 and λ_3. Because there is no shear, these edge lengths are the principal extensions. For this deformation, the strain invariants will not include any terms for shear

$$\begin{aligned} I_1 &= \lambda_{xx}^2 + \lambda_{yy}^2 + \lambda_{zz}^2 \\ I_2 &= \lambda_{xx}^2 \cdot \lambda_{yy}^2 + \lambda_{yy}^2 \cdot \lambda_{zz}^2 + \lambda_{zz}^2 \cdot \lambda_{xx}^2 \\ I_3 &= \lambda_{xx}^2 \cdot \lambda_{yy}^2 \cdot \lambda_{zz}^2 \end{aligned} \tag{3.13}$$

The force acting in direction 1 in Figure 3.10, F_1, is defined in terms of the stress acting in this direction, σ_1 and the area of the face on which this stress acts.

$$F_1 = \sigma_1 \cdot \lambda_2 \cdot \lambda_3 \tag{3.14}$$

The displacement caused by this force, F_1 is $d\lambda_1$. Work is performed when a force acts over some displacement, therefore, it may be seen that the above force, F_1, does work (Equation 3.18).

$$W_1 = \sigma_1 \cdot \lambda_2 \cdot \lambda_3 \cdot d\lambda_1 \quad \textbf{(3.15)}$$

W_1 Work performed by force, F_1

It is relevant to find a similar expression for the state of stress in an incompressible material. In order to do this, it is necessary to consider the effect a hydrostatic pressure will have on the material. Since incompressible materials do not generate a change in volume under load, the 3rd strain invariant, I_3, will be equivalent to **1** (Equation 3.16). Expressions for the strain invariants for incompressible materials may be generated using the unity of I_3 (Equation 3.21).

$$I_1 = \lambda_1^2 + \lambda_2^2 + \lambda_3^2$$
$$I_2 = 1/\lambda_1^2 + 1/\lambda_2^2 + 1/\lambda_3^2 \quad \textbf{(3.16)}$$
$$I_3 = 1$$

Where the variables I_1, I_2 and I_3 are the principal extension ratios.

Hydrostatic stresses will result in no change in the strain energy. This may be seen by manipulation of Equation 3.19 when the stress components are set to σ_H and the relationship $\lambda_1 \cdot \lambda_2 \cdot \lambda_3 = 1$ is included. Therefore, the expression for the stress components in an incompressible material will be similar to Equation 3.21 with an additional term for hydrostatic pressure (Equation 3.17)

$$\sigma_1 = \frac{1}{\lambda_2 \cdot \lambda_3} \cdot \frac{\partial W}{\partial \lambda_1} + p \quad \textbf{(3.17)}$$

$p =$ hydrostatic Pressure

If the hydrostatic pressure term was not included in Equation 3.17, then it would not accurately predict the stresses present when only a hydrostatic pressure was applied.

In this instance, the ∂W term would not predict any stress and the presence of the hydrostatic pressure would not be evident.

On the basis of Equation 3.17 expressions for the 3 stress components may be derived for an incompressible material.

$$\sigma_1 = 2 \cdot \lambda_1^2 \cdot \frac{\partial W}{\partial I_1} - \frac{2}{\lambda_1^2} \cdot \frac{\partial W}{\partial I_2} + p$$

$$\sigma_2 = 2 \cdot \lambda_2^2 \cdot \frac{\partial W}{\partial I_1} - \frac{2}{\lambda_2^2} \cdot \frac{\partial W}{\partial I_2} + p \qquad \textbf{(3.18)}$$

$$\sigma_3 = 2 \cdot \lambda_3^2 \cdot \frac{\partial W}{\partial I_1} - \frac{2}{\lambda_3^2} \cdot \frac{\partial W}{\partial I_2} + p$$

The strain energy equation, *W*, is a function of the strain invariants and satisfies the condition that $W = 0$ when, $\lambda_1 = \lambda_2 = \lambda_3 = 1$

2.7.2 Forms and Applications of the Strain Energy Equation

Mooney (1940) stated that the primary problem in elastic theory was to find a strain energy equation which accurately described the material in question. He notes that if the material is subjected to small strains and is isotropic and homogeneous, then an expression for the strain energy of the material may be derived on the basis of the elastic modulus and rigidity modulus. However, in the case of rubber, the strains observed are too large for the materials mechanical behavior to be accurately modelled using classic small strain theory. Mooney (1940) noted the necessity for the development of a relationship which could suitably describe the nonlinear, elastic, large strain behavior of rubbers.

Mooney (1940) observed that under uniaxial loading, the mechanical response of rubber is nonlinear, while under shear loading, the mechanical response follows Hooke's law. Also, rubbers behave as near incompressible materials. On the basis of these criteria, Mooney (1940) developed two strain energy equations to describe rubber mechanics. The first equation assumed that the material was linear in shear and incompressible (Equation 3.19) and the second equation assumed the material was nonlinear in shear and incompressible. However, the second equation was later discounted as incorrectly representing the behavior of rubbers (Rivlin, 1984). An additional assumption associated with the Mooney equation that assumed linear shear behavior was that the material was isotropic. Mooney Strain Energy Equation is defined by

$$W(\lambda_1, \lambda_2, \lambda_3) = C_{10}\left(\lambda_1^2 + \lambda_2^2 + \lambda_3^2 - 3\right) + C_{01}\left(1/\lambda_1^2 + 1/\lambda_2^2 + 1/\lambda_3^2 - 3\right) \qquad \textbf{(3.19)}$$

The expression in Equation 3.19 was later altered by Rivlin (1984) to incorporate the

strain invariants (Equation 3.20).

$$I_1 = \lambda_1^2 + \lambda_2^2 + \lambda_3^2$$

$$I_2 = 1/\lambda_1^2 + 1/\lambda_2^2 + 1/\lambda_3^2 \quad \textbf{(3.20)}$$

$$I_3 = \lambda_1^2 \cdot \lambda_2^2 \cdot \lambda_3^2$$

This equation was then referred to as the Mooney-Rivlin Mooney-Rivlin strain energy equation (3.21) where the expressions for I_1 and I_2 were substituted into Equation 3.20. For incompressible materials, I_3 is equivalent to 1.

$$W = C_{10}(I_1 - 3) + C_{01}(I_2 - 3) \quad \textbf{(3.21)}$$

Several researchers have used hyperelastic material formulations to represent the material behaviour of biological tissues.

Nucleus Pulposus. The nucleus Hyperelasticy was introduced as incompressible fluid-filled cavity material. Its elastic response was modeled using material discretization of fluid cavity with the same nodes and connectivity, by F3D4 fluid elements to allow the cavity surface-endplate connection [24, 31, 34, 44]**.** An initial hydrostatic pressure of 0.1 MPa was prompted in the fluid filled cavity in the nucleus pulposus to simulate unloaded motion segments [34].

3.6.1 Loading and Boundary Conditions.

The IVD model comprises the intervertebral disc and the adjacent vertebral bodies. The lower vertebral body was rigidly fixed. Pure unconstrained axial compressive loads were applied to the upper vertebral body in stepwise fashion increasing from 0 to 3000 N, to the reference point which coupled all points on upper surface of the disc as it has been recommended [51,52]. The resulting vertical displacement (i.e.,a reduction in height Δh) and the intradiscal pressure at the center of the disc were estimated using Pressure Point NP. Theoretically speaking, we used the concept of nucleus pulposus pressure measurement; by means of in vitro experiments on vertebra-disc-vertebra preparations whither, we found that the incompressible fluid pressure within the nucleus is directly related to the axial compression applied to the disc (Figure 3.12)

3.8 Validation

3.8.1 Loading and Boundary conditions

To ensure the accuracy of the complete assembled FE model, the disc behavior was additionally compared with measurements based on a previously performed cadaveric study [22, 24, 37, 41, 51, 52] for the intradiscal pressure and vertical displacement data under axial compression.

3.8.2 Results

The finite element model predicted an increase in hydrostatic stress in the middle regions of the annulus by nearly four-fold. The intradiscal pressure IDP is considered to be very significant component to approximate internal stress behavior of the intervertebral disc, the IDP in the nucleus was determined as gauge pressure defined by a reference point inside the incompressible fluid cavity. The In vitro measurements of the nucleus pressure in human intervertebral discs have shown proportion between IDP pressure and applied Load on the superior surface of the disc to be almost 1.4. Ranu et al [42].

Under a physiologic compressive load of 400 N, the predicted vertical displacement of 0.41 mm showed a good agreement with the experimentally determined in vitro data of 0.50 mm [42]. These predictions are within the measured range of experimental values. The generated results provided a linear behavior between the applied compressive load up to the point of bony fracture and the intradiscal pressure (Figure 3.12), the IVD model predictions were also in good agreement with the presented experimental results. [42]. When the spinal segment was subjected to the bony fracture loading of 3000 N, the model predicted an intradiscal pressure of 2.98 MPa. As shown in Figure 3.12; the vertical displacement as a function of the applied compressive load. Both, the numerical and the in vitro experimental curve present overall a similar nonlinear curve. The stiffening behavior of the disc is evident and this is primarily due the tensile stiffness of the annulus collagenous fibers.

3.9 The L4-L5 Model Validation

3.9.1 L4-L5 Indiscal pressure IDP and Facet Joint Force FJF validation

As recommended in [20], the model is subject to combined load of compression with flexion, extension, bending or torsion. The loading modes are detailed in Table 3.2.

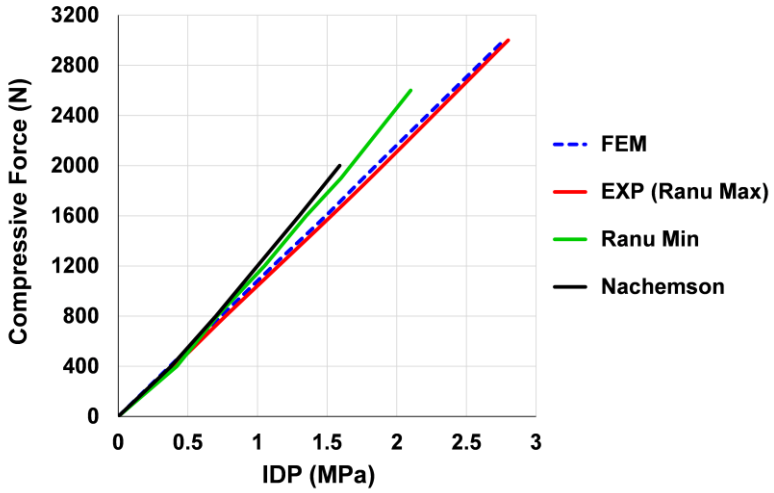

Figure 3.12: Intradiscal pressure against the applied compressive force compared with in vitro models.

The IDP and the FJF are assessed and compared to those obtained by [13, 35, 41]. The IDP is closed to in vivo IDP the flexion and the extension. Wilke et al [51]. What about lateral bending and axial rotation, the predicted IDP is cute close to in vivo IDP. Figure 3.12 shows respectively for the intact segment model that Low value of IDP is predicted for extension (0.34 MPa, in vitro 0.6 MPa), Lateral Bending (0.59 MPa, in vitro 0.6 MPa) and axial torsion moment (0.63 MPa, in vitro 0.65 MPa), whither, the nucleus pressure did not strongly increase compared with the same load applied in a flexion (1.2 MPa, in vitro 1.6 MPa).

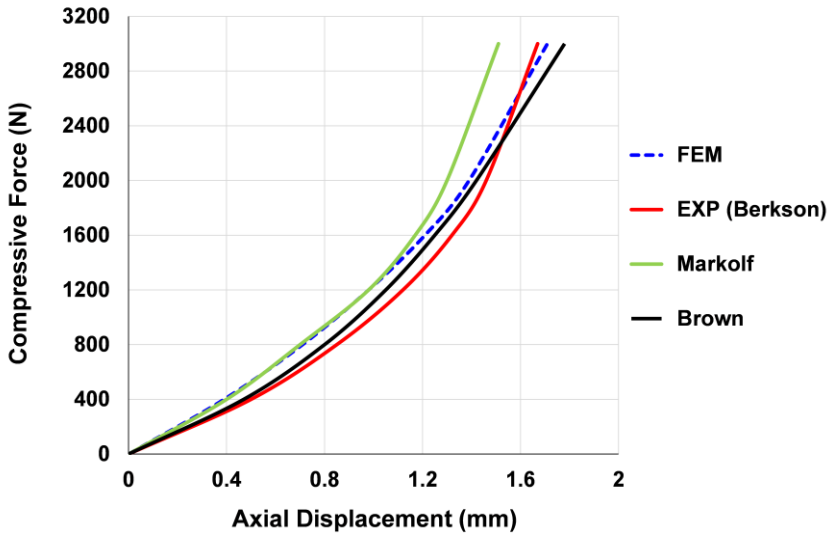

Figure 3.13: Vertical displacement against the applied compressive force compared with in vitro models.

Table 3.2: Loading modes using for the different motions

Motion	Compressive follower load (N)	Pure Moment (Nm)	References
Flexion	1175	7.5	[33]
Extension	500	7.5	[33]
Lateral bending	700	7.8	[8]
Axial rotation	720	5.5	[9]

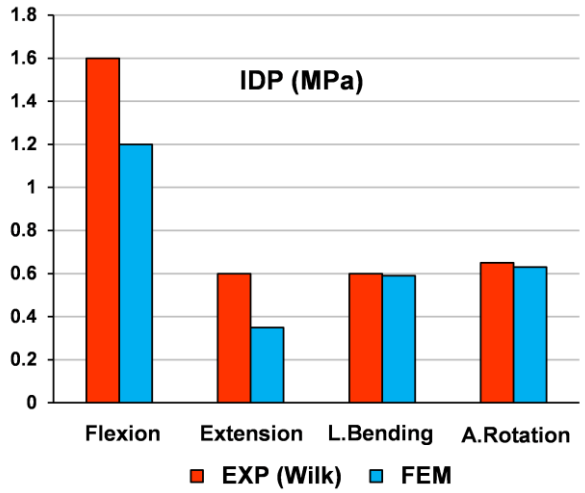

Figure 3.14: Intradiscal pressure of L4-L5 IVD under Combined load Conditions.

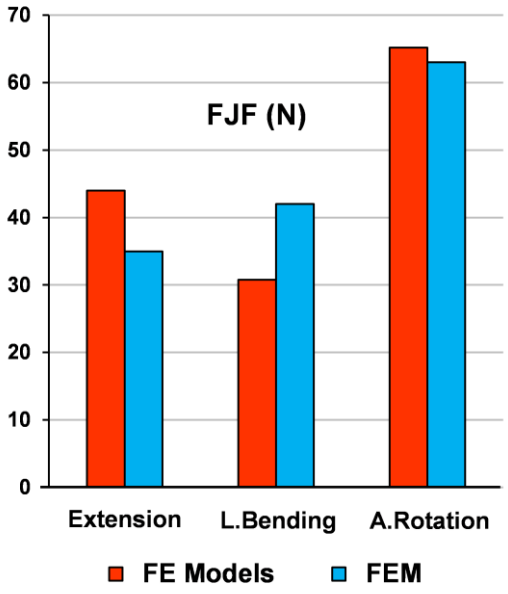

Figure 3.15: Facet Joint Force FJF of L4-L5 FSU

Concerning the FJF, in flexion, the facet joint of the intended segment is unloaded (Magnitude of 0 N). The FJF was highest axial rotation (65N), followed by inlateral bending (35 N) then extension (22 N), they are mainly close to the median values of the

FJF of FE model [30] (Figure 3.15).

3.9.2 Loading and Boundary Conditions.

The lower portion of the L5 vertebral body and its inferior facets were rigidly fixed. The load was applied to the center of the vertebra through a reference node constrained to the vertebral nodes using Abaqus Coupling Constraints elements (CCE). A three-dimensional coordinate system fixed in space has been placed at this reference node (Figure 3.16). The L4-L5 Functional Spinal Unit (FSU) move in six different directions (six degrees of freedom (DOF)). In other words, six translations (±Tx, ±Ty, ±Tz) and six rotations (±Rx, ±Ry, ±R). Thus, the response of the intact functional spinal unit was measured in twelve cases:

1- Application of six external forces of 150 N: compression-tension (± Fy), anterior/posterior shear (± Fz), and left/right shear (± Fx).

2- Application of six moments of 7.5 Nm: flexion, extension (± Mx), left/right rotations (±My), and left/right bending (± Mz). Similar testing was conducted after the IVD was injured by (a) Annular injury by removing part of the annulus on the right side

(b) Remove the nucleus from the window created by the first injury.

The FE model was tested for its accuracy in predicting mechanical response to external loads measured three-dimensionally to provide valid representation of the actual behavior of the lumbar spine. Among all the cadaveric model results available in the literature, the in vitro experimental results of Panjabi et al [26] were chosen to validate the finite element model of the L4-L5, as this work includes the response of the lumbar motion segment to all physiologic loading components. The resulting translations and rotations in the same direction as the applied load were estimated at the center of the upper vertebral body (Figure 3.16).

3.9.3 Model Validation

The numerical diagrams match Panjabi experimental data [26] (Figure 3.17). For the intact model, under a moment of 7.5 Nm, flexion showed with 3.8°, followed by lateral bending with 3.66°, extension with 2.1°, and axial rotation with 1°.

3.9.4 Results

The resultant of maximum primary motion (the motion in the same direction as the

applied load F-T, M-R) under various loading conditions obtained from the FE model were compared with experiments data and shown in Figure 3.17.

As hypothesized, the FE model showed that the motion segment is additionally rigid under a torsional load (± My) than in lateral bending (± Mz) and flexion-extension (± Mx) cases. The orientation of the facet joints was varied in a parametric way in order to obtain the influence on the motion response derived from [38,48]. The behavior of the disc is more pronounced in compression and distraction load cases. Similarly, to the experimental data, the the FE model shows that the model behavior, and in specific the disc, flexiblity in distraction (+Fy) is more evident than in compression (-Fy) case. The results demonstrate the good agreement of FE model with the experimental data in all 6 DOF.

The overall mechanic function of the L4-L5 FSU is affected by injuries, Detailed Schematics of the two injuries and the resulting motions of the intact and injured spines are shown in Figure 3.17. As can be seen, the L4-L5 FSU schematics findings show independently that there are significant changes in the spinal behavior after both the annular and nucleus injuries than the intact motion. The magnitude of the ROM changes is more apparent after the removal of the nucleus than when the annulus defect is created by annular injury. The disc is the main load-bearing component of the spinal column. It can lead to altered sharing of the load between the disc and the zegapophyseal joints. Annulus injury with nucleus removal produced greater changes than the annulus injury alone for both of rotations and displacements. The maximum absolute changes were seen in flexion and left lateral bending. On whether, it was the axial rotation that showed the greatest effect of the disc injury. As hypothesized; the facets restrict the range of axial rotation, with great contact stresses occurring in the joint surfaces. [45, 52].

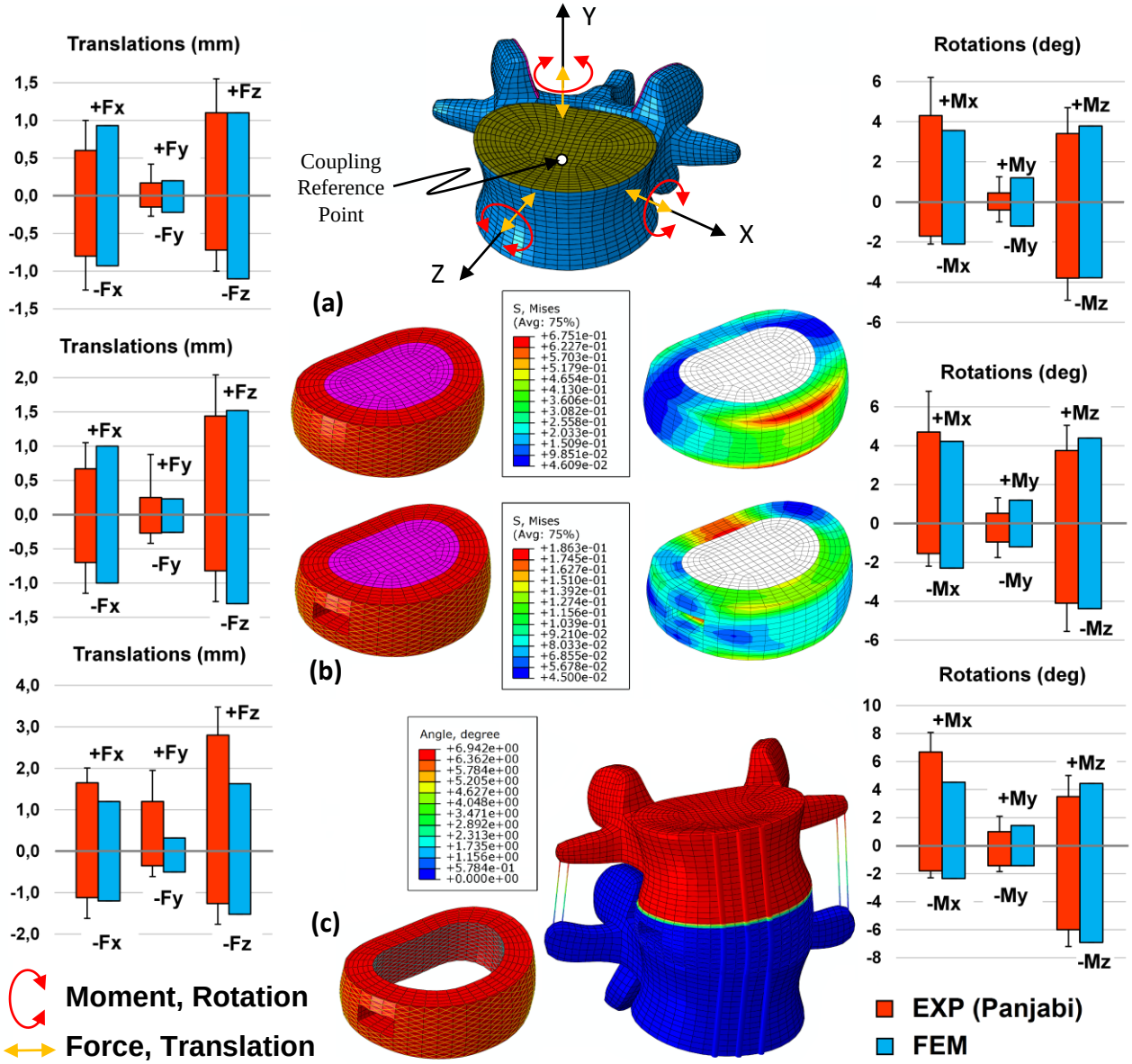

Figure 3.16: FE model validation based on cadaveric in Vitro data: (a) Intact, (b) Annular injury, (c) Nucleus Removal

3.10 L1-S1 motion segment validation

3.10.1 Loading and Boundary Conditions

A well-defined Hybrid protocol was used to study the lumbosacral spine behavior. This key issue analysis reestablishes to principle applied loading on the motion segments of pure momentum increasing incrementally from zero to 10 N.m (2.5, 5, 7.5, 10 N.m). Compressive follower preload of 100 N was applied in all modalities to the intact lumbar spine model in the follower load path direction, settled as suggested thereby allowing the axial load to follow the motion of the spine [50]. The Follower load was applied to the

center of the vertebra through a Reference Node Constrained to the vertebral body nodes using Coupling Constraints Elements (CCE) (Figure 3.16). The resulting FE model was positioned in static Momentum Loads to match the experiment. Homogeneous Dirichlet boundary conditions were applied to all bottom side nodes, not involved in the motion procedure. The interpedicular displacement was predicted for the intact model in all directions comparing with that of previous experimental studies [37]. Introduce the generated lumbar spine model not only allows personalized biomechanical analysis, but it also offers detailed geometric data to simplify simulation to mimic the realistic Lumbar spine. Knowledge of the normal motions of whole lumbar spine and lumbosacral joint is important for evaluating clinical pathologic conditions.

3.10.2 Methods.

Load-displacement curves of experimental data were collected for a full lumbar (L1-S1) specimen in 4 rotations: flexion/extension, right lateral bending, and Right axial rotation conducted by Panjabi et al [37] compared with each of the five levels from L1 vertebrae to the sacrum S1 due to the application of physiological conditions. The main motion was defined as the rotation in the direction of the applied moment is plotted and compared with that of experiment. +RX flexion, -RX extension, -RY right rotation, +RZ right lateral bending

3.10.3 Results.

The results display a greater no-linearity of the spine response. Under load combination, the ROM of most of the dedicated FSU level, respectively from L1 to S1 are within the range of in vitro measurements as shown in Figure 3.17, except a reduction of the predicted ROM in flexion, where the mobility is smaller than what is expected (L2-L3, L4-L5, L5-S1), taking into account in vitro conditions.

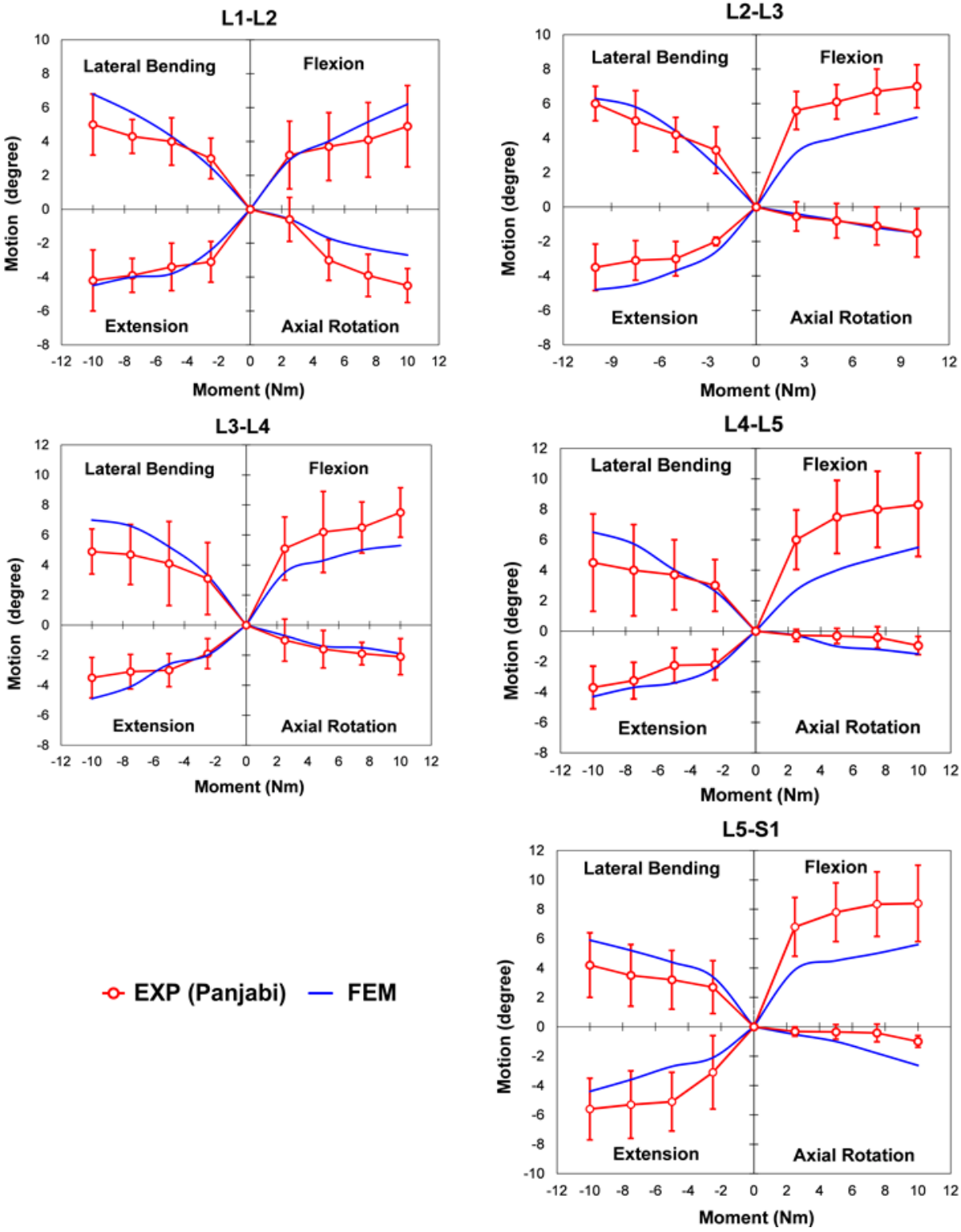

Figure 3.17: Comparison between predicted intervertebral rotations results in different spinal levels for the loading cases: flexion, extension, lateral bending, and axial rotation.

In lateral bending and in axial rotation, the movement amplitudes are close to those found in the literature measurements as shown in Figure 3.17. In particular, in extension

such as for the other movements, ROM are within the range of movements performed by the experimental ones especially for L1-L2, L2-L3, L3-L4 segments. Except for the segment L5-S1 which performs a little lower extension than in vitro measure, at L1-L2 level for extension in which we obtain a value of 4.2° against the experimental value of 4°. The numerical model in extension for the L4-L5 segment shows a deviation of 0.5° against the calculated experimental values.

The curves are similar with slightly higher rotation angles for the model in Axial Rotation for L4-L5 and L5-S1. The segment L2-L3, L4-L5 shows the best results with an error of 0.1° and for the L3-L4 segment with a deviation of 0.2 between the FE model and experimental. The maximum flexion moment ROM of the segments L1-L2 is higher than for the other segments, the maximum rotation value has little variation between upper (-6.1° for L1-L2 level) and lower (-5.8° for L4-L5) segments. The FE models is obtained at L2-L3 level a deviation of 0.2° in the lateral bending and represent a deviation of 0.8° for the Axial Rotation of L5-S1.

3.11 Discussion.

Validation of any new finite element model should be observed the correlation between FE predictions and in vitro data for nucleus pressures, vertical displacement of the IVD and primary rotations at each spinal level to demonstrate the ability of the model to correctly reproduce key aspects of in vitro response of the lumbar spine. The Rotations-Displacement curves from the generated FE model shows good accuracy to the experimental kinematics measurements.

This FE model of a human L1-S1 motion segment was used to explore the effect of removal structures injuries on overall motion segment response of a spinal FSU. The excellent agreement at the level of the individual motion segments demonstrates that the model not only predicts kinematics well across L4-L5 FSU, but that the ROM configuration of the model also matches the experiment well for the overall L1-S1 endpoints. The loading applied to the model was formulated to simulate the observed physiological functions. The finite element modeling has long been used in biomechanical studies for research concerning clinical pathologies of the lumbar spine as well as for predicting the biomechanical characteristics. The lumbar spine model was developed to investigate the disc behavior and the whole L1-S1 functions under physiological

conditions. The focus of this study was validation of the meshing, and FE model generation procedure, with the latter step comprising construction and of the lumbar model L1-S1. This model generation steps require a substantial time commitment.

The geometric assumptions made in development of the model were intended to allow an anatomically detailed representation of the Posterior-Anterior column. The computational results presented in this study represent an attempt to explore the role of passive spinal structures in generating rotations displacements accompanying primary spinal motions. We presented a finite element model for a healthy osseoligamentous lumbosacral spine with all intact ligaments and a hydrostatic nucleus pulposus.

(1) The structure of the vertebral body was assumed as isotropic with homogenous properties of the IVD, and the mechanical properties such as the non-linear behavior of the spinal ligaments.

(2) The loading conditions were not truly physiological, because of the lack of the mechanical effects of muscular contraction forces which change with upper trunk position [15], [29]. Although the finite element model of this study had assumptions and limitations, the results were comparable to previous publications. A follower load of 100 N, which delivers realistic pressure values for standing, is not sufficient for simulating flexion ROM; subsequently it does not consider the global muscle force required for stabilizing the flexing-bending upper body [45]. The model can also be used for probabilistic and sensitivity studies related to implant position and implant size. It is understood that this loading does not accurately characterize in the in vitro conditions

3.12 Limitations of the FE Analysis.

As with all finite element model research, there are some inherent limitations to the models used: To realize a better resolution and results, it might be essential to refine the mesh which steer more anatomic details, require significant sensitivity analysis with more elements and nodes, including more degrees of freedom. These additions would have inconveniently increased the computation time and necessitate expense of computation power. The geometry of the IVD was based on realistic 3d model reconstituted from slice imaging scans but with limited accuracy. The variation in geometric parameters, such as disc height, cross-sectional area of the intervertebral disc, size and position of the nucleus, fiber orientation, or the number of fiber layers, can affect the mechanical behavior of the intervertebral disc and the whole lumbar functions. [22, 24].

The procedure that join FE models with different geometries might lead to remarkable different results and the modification in geometries and conditions of soft tissues in the finite element model introduced in previous biomechanical studies may alter the reported ROM.

3.13 Conclusion.

We have presented a FE model of the lumbar spine and have described how the model has been constructed based on the anatomical and computational features of the spine segments in the sake of computational efficiency. The intact model has been validated in good correlation with the literature where simulations have been achieved for physiological ROM (Figure 3.17). This study presents a first step in the validation process of the FE model for individual human lumbar spine. Out of a number of model features analyzed computationally, reasonable approximations of the experimental data are provided by this model.

Future work will focus on better understanding the sensitivity of FE predictions to variations in material properties associated with factors such as degeneration and the use of an optimization method based on differential evolution to calibrate the FE model the whole lumbar spine.

The approach for selecting such material properties involves calibrating the model by choosing the properties that produce the best compatibility with the in vivo and in vitro mechanical response of the lumbar spine. Whether, these approximations will be expressed terms of a FE model for the intact L1-S1 finite element formulation, and the developed model could be considered as a valuable tool for the investigation of mechanical analysis of the lumbar segment in the perspective promote of pre and postoperative clinical analysis.

References.

[1] Winder J, Bibb R. (2005) Medical Rapid Prototyping Technologies: State of the Art and Current Limitations for Application in Oral and Maxillofacial Surgery, Journal of Oral and Maxillofacial Surgery. 63(7): 1006-1015.

[2] Schmutz B, Wullschleger ME, Schuetz MA (2007) The effect of CT slice spacing on the geometry of 3D models, Proceedings 6th Australasian biomechanics conference, The University of Auckland, Auckland, New Zealand.

[3] Lafage V, Dubousset J, Lavaste F, Skalli W (2004) 3D finite element simulation of Cotrel–Dubousset correction, Computer Aided Surgery. 9(1/2): 17–25.

[4] Chirani R.A, Jacq J.J, Meriot F, Roux C (2004) Temporomandibular joint: a methodology of

magnetic resonance imaging 3-D reconstruction, Oral Surgery, Oral Medicine, Oral Pathology, Oral Radiology & Endodontics. 97(6): 756-761.
[5] Drapikowski P (2008) Surface modeling-uncertainty estimation and visualization, Computerized Medical Imaging and Graphics. 32 (2): 134–139
[6] Riesmeier J, Eichelberg M, Kleber K, Oosterwijk H, von Gehlen S, Grönemeyer D.H.W, Jensch P (2001) DICOM Structured Reporting—a prototype implementation, International Congress Series (Computer Assisted Radiology and Surgery). 1230:795-800.
[7] Messmer P, Matthews F, Jacob A.L, Kikinis R, Regazzoni P, Noser H (2007) A CT database for research, development and education: concept and potential, J. Digit Imaging. 20(1):17–22.
[8] Rathnayaka K, Sahama T, Schuetz M.A, Schmutz B (2010) Effects of CT image segmentation methods on the accuracy of long bone 3D reconstructions, Med. Eng. Phys. 33(2): 226–233.
[9] Pipe JG (1999) Motion correction with PROPELLER MRI: application to head motion and free-breathing cardiac imaging, Magnet Reson Med. 42(5): 963–969.
[10] Brenner D.J, Doll R, Goodhead D.T, Hall E.J, Land C.E et al. (2003) Cancer risks attributable to low doses of ionizing radiation: assessing what we really know, Proc. Natl. Acad. Sci. USA. 100: 13761–13766.
[11] Baroud G, Nemes J, Heini, P, Steffen, T. (2003). Load shift of the intervertebral disc after a vertebroplasty: a finite element study, European Spine Jourbal, 12(4), 421-426.
[12] Berkeston M, Schultz A.B. Mechanical properties of human lumbar spine motion segments: II. Response in compression and shear; influence of gross morphology. J Biomech Eng1979; 101: 53–7.
[13] Bogduk N. (2005), Clinical Anatomy of the Lumbar Spine and Sacrum, Elsevier, Churchill Livingstone, Edinburgh, London, New York, Oxford, Philadelphia, St Luis, Sidney, Toronto.
[14] Brown T, Hansen R.J, Yorra A.J: Some mechanical tests on the lumbosacral spine with particular reference to intervertebral discs; a preliminary report. J Bone Joint Surg Am 1957, 39:1135–1164.
[15] Cao K.D, Grimm M.J, Yang K.H. Load sharing within a human lumbar vertebral body using the finite element method. Spine 2001 ; 26 : E253–60.
[16] Delerba F. 2001, "Modélisation Géométrique et Mécanique Tridimensionnelle du Rachis Thoracique et Lombaire en Configuration de Choc Automobile," Ph.D. thesis, Ecole Nationale Supérieure d'Arts et Métiers, Paris.
[17] Denoziere, G, Ku, D.N. (2006). Biomechanical comparison between fusion of two vertebrae and implantation of an artificial intervertebral disc, Journal of Biomechanics, 39(4), 766-775.
[8] Dreischarf M, Rohlmann A, Bergmann G, Zander T. Optimised in vitro applicable loads for the simulation of lateral bending in the lumbar spine. Med Eng Phys 2012, http://dx.doi.org/10.1016/j.medengphy.2012.04.002.
[19] Dreischarf M, Rohlmann A, Bergmann G, Zander T. Optimised loads for the simulation of axial rotation in the lumbar spine. J Biomech 2011;44(12):2323–7.
[20] Dreischarf M, Zander T, A. Shirazi-Adl, C. Puttlitz, C. Adam, C. Chen, V. Goel, A. Kiapour, Y. Kim, Labus K et al, "Comparison of eight published static finite element models of the intact lumbar spine: Predictive power of models improves when combined together,"Journal of biomechanics, vol.47, no. 8, pp. 1757–1766, 2014.
[21] Eberlein R, Holzapfel G.A, Schulze-Bauer C.A.J. An anisotropic model for annulus tissue and enhanced finite element analyses of intact lumbar disc bodies. Computer Methods in Biomechanics and Biomedical Engineering 2001;4(3):209–29

[22] Goel V.K, Monroe B.T, Gilbertson L.G, Brinckmann P. (1995a). Interlaminar shear stresses and laminae separation in the disc. Finite element analysis of the L3-L4 motion segment subjected to axial compressive loads. Spine, 20(6), 689-698.
[23] Heuer F, Schmidt H, Klezl Z, Claes L, Wilke H.J. „Stepwise reduction of functional spinal structures increase range of motion and change lordosis angle", J Biomech 40, 271- 280, 2007
[24] Lu YM, Hutton WC, Gharpuray VM: Do bending, twisting, and diurnal fluid changes in the disc affect the propensity to prolapse? A viscoelastic finite element model. Spine Nov 1996, 21(22):2570–2579.
[25] Luoma K, Riihimaki H, Luukkonen R. et al. (2000). Low Back Pain in Relation to Lumbar Disc Degeneration. Spine, Vol. 25, No. 4, pp. 487-492
[26] MARC. Theory and user's manual. MacNeal–Schwender Corporation, 2001. vol. Version 2001.
[27] Markolf, K. L. Deformation of the thoracolumbar intervertebral joints in response to external loads. J. Bone Joint Surg. 54-A:511–533, 1972
[28] Masharawi Y, Rothschild B, Dar G, Peleg S, Robinson D, Been E, Hershkovitz I, (2004) Facet Orientation in the Thoracolumbar Spine, Three-dimensional Anatomic and Biomechanical Analysis, SPINE 29: 1755–1763
[29] Moramarco V, Palomar A.P, Pappalettere C, Doblaré, M. (2010). An accurate validation of a computational model of human lumbosacral segment, Journal of Biomechanics, 43(2), 334-342.
[30] Moumene M, Geisler FH (2007) Comparison of biomechanical function at ideal and varied surgical placement for two lumbar artificial disc implant designs: mobile-core versus fixed-core. Spine 32:1840–1851. doi:10.1097/BRS.0b013e31811ec29c
[31] Nachemson A.L: Lumbar Intradiscal Pressure: experimental studies on post-mortem material. Acta Orthopaedica Scandinavica 1960, 43. :1–104.
[32] Natarajan R.N, Andersson G.B. The influence of lumbar disc height and cross-sectional area on the mechanical response of the disc to physiologic loading. Spine 1999; 24:1873–81.
[33] Ohshima H, Tsuji H, Hirano N, Ishihara H, Katoh Y, Yamada H. Water diffusion pathway, swelling pressure, and biomechanical properties of the intervertebral disc during compression load. Spine 1989; 14:1234–44.
[34] Paige Little J. 2004, Finite element modeling of annular lesions in the lumbar intervertebral disc. (Doctoral Thesis).
[35] Panjabi M.M, Greenstein G, Duranceau J, Nolte L.P. "Three-dimensional quantitative morphology of lumbar spinal ligaments", J Spinal Disord 4, 54-62, 1991
[36] Panjabi M.M, Krag M.H, Chung.TQ. Effects of disc injury on mechanical behavior of the human spine. Spine 1984; 9:707–13.
[37] Panjabi M.M, Oxland T.R, Yamamoto I, Crisco J.J. Mechanical behavior of the human lumbar and lumbosacral spine as shown by three-dimensional load-displacement curves, J. Bone Joint. Surg., Series A, 1994, 76, 413–424.
[38] Panjabi MM, Oxland T, Takata K, Goel V, Duranceau J, Krag M. (1993) Articular facets of the human spine. Quantitative three-dimensional anatomy. S0pine 18:1298–1310.
[39] Park W.M, Kim K, Kim H.Y, Computers in Biology and Medicine 43 (2013) 1234–1240, Effects of degenerated intervertebral discs on intersegmental rotations, intradiscal pressures, and facet joint forces of the whole lumbar spine
[40] Patwardhan A.G et al. A Follower Load Increases the Load-Carrying Capacity of the Lumbar Spine in Compression. Spine, 24(10), 1003 (1999)

[41] Ranu H.S, Denton R.A, King A.I: Pressure distribution under an intervertebral disc–an experimental study. J Biomech 1979, 12:807–812.
[42] Ranu H.S. Measurement of pressures in the nucleus and within the annulus of the human spinal disc: due to extreme loading. Proc Inst Mech Eng H 1990; 204:141–6
[43] Rohlmann A, Zander T, Rao M, Bergmann G. Realistic loading conditions for upper body bending. J Biomech 2009;42(7):884–90.
[34] Rohlmann A, Zander T, Schmidt H, Wilke H-J, Bergmann G (2006) Analysis of the influence of disc degeneration on the mechanical behavior of a lumbar motion segment using the finite element method. J Biomech 39:2484–2490. doi: 10.1016/j.jbiomech.2005.07.026 Fluid
[45] Sharma M, Langrana N.A, Rodríguez J.Role of ligaments and facets in lumbar spinal stability.Spine.1995;20:887-900.
[46] Sheehan JM, CI Shaffrey, JA Jane. Degenerative lumbar stenosis: The neurosurgical perspective.Clin Orthop 2001; 384:61-74
[47] Shirazi-Adl A, Ahmed A.M, Shrivastava SC (1986)
Mechanical response of a lumbar motion segment in axial torque alone and combined with compression. Spine 11:914–927
[48] Skaggs D.L, Weidenbaum M, Regional variation in tensile properties and biomechanics composition of the human lumbar annulus fibrous, Spine, 1994, Vol. 9, pp. 120-134.
[49] Schmidt H, Heuer F, Simon U, Kettler A, Rohlmann A, Claes L. et al, Application of a new calibration method for a three-dimensional finite element model of a human lumbar annulus fibrosus, Clin. Biomech. 2006, 21, 337–344.
[50] Tyndyk M.A, Barron V, Mchugh P.E, O'MAHONEY D, Generation of a finite element model of the thoracolumbar spine, Acta Bioeng. Biomech. 2007, 9, 35–46.
[51] Wilke H, Neef P, Hinz B, Seidel H, Claes L. 2001. Intradiscal pressure together with anthropometric data – a data set for the validation of models. Clin. Biomech. (Bristol, Avon) 16 (Suppl 1), S111–S126.
[52] White A.A, Panjabi M. Clinical Biomechanics of the Spine. 2nd ed. Philadelphia: Lippincott; 1990.
[53] Zhong Z.C, Wei S.H, Wang J.P, Feng C.K, Chen C.S, Yu C.H. (2006). Finite element analysis of the lumbar spine with a new cage using a topology optimization method, Medical Engineering and Physics, 28(1), 90-98.
[54] Williams, J.G. (1973). Stress analysis of polymers. London, Longman group.
[55] Ugural A.C. and Fenster S.K. (1995). Advanced Strength and Applied Elasticity. New Jersey, Prentice Hall PTR.

Chapter 4:

Comparative Analysis of Hybrid Flexible Stabilization and Fusion for Degenerative Disease of the Lumbosacral Spine: Finite Element Analysis

4.1 Introduction.

Lumbar fusion is considered as the "gold standard" surgical treatment indicated for a wide range of well-recognized painful conditions [1, 10, 22]. Which aimed to alleviate and treat the pain from disc/facet loading in the instable degenerated levels, probably cause of the abnormal load share and stresses in lumbar spine. Moumene et al [11], Rahm et al [18], while the surgical intervention is based on the topping off fusion stabilization, we used a validated Finite Element (FE) model to determine the biomechanical basis exists for believing that the reduced stiffness and increased axial motion conferred by arthrodesis would be optimized using dynamic instrumentation based on mobile and fixed screw implants to alter the stresses in adjacent-level discs. [11, 17]. Conventionally, the Posterior Dynamic stabilization (PDS) constructs has been promoted to be used as a total fixation system. Lee et al [8] or a joined to spinal fusion (topping off or bottoming off fusion) of various rigid or semi rigid fixators assumed to diminish the load on adjacent disc and the facet joint [5,9,14]. It will be used in treating multi-level spinal degeneration requiring surgical procedure by strengthening their arthrodesis (fusion) at one or more levels and neutral stabilization (non-fusion) at an adjacent level for common pathological condition to limit stress prophylactically at the level above or below the fusion.

The Dynesys Transition Optima™ (DTO) (Zimmer-Biomet Spine, Denver, CO) (Figure 4.2, 4.3) is a novel hybrid dynamic stabilization and rigid fusion system. Potentially using as an alternative to multilevel lumbar fusion while hypothetically decreases the risk of adjacent segment disease. Few clinical studies have described the clinical experience with hybrid system [4,6,13,14,27] with an initial experience using DTO on 24-patient. Oktenoglu et al [13]. Kashkoush et al have represented a long-term clinical cohort

evaluation of 10 years on 66-patients using a unique hybrid lumbar stabilization to fusion system (Figure 4.2, 4.4). They found that DTO is a safe and proficient techniques that allows the linking of arthrodesis with dynamic stabilization at adjacent levels in the lumbar spine compared to conventional arthrodesis systems with no failure and no screw loosening. [4,6,8]

The clinical apparent hypothesized that the hybrid DTO systems supports the efficacy, safety of DTO system and leads to good outcomes to preserve the adjacent segments, these clinical studies hypothesized that the hybrid systems supports the performance of DTO system and leads to good outcomes to preserve the adjacent segments, nevertheless this technique remains a controversial area in spine surgery. Marion et al [9].

The residual Range of motion ROM of the topping off semirigid fusion constructed with Poly Ether Ether Ketone PEEK with discectomy compared to Dynesys. We are currently performing FE and lumped parameter analyses of different treatments for Degenerative Disc Disease DDD, looking at bi-level spinal implantation. Little is documented about the effect of hybrid devices on the mechanical behavior of the lumbar spine. The ROM at the operated and adjacent levels, stress distribution at the vertebral pedicles and the interpedicular displacement with respect to changes of bone/screw quality were investigated.

4.2 Materials and Methods.

The L2-S1 spine model was extracted from the previously validated nonlinear finite element (FE) model L1-S1 [28], and computationally established to simulate instability by discectomy and quantify implant stability as a function of implant/bone quality. The mesh was developed using ANSYS 15.0 (Swanson Analysis System) and Hypermesh 13.0 (Altair Engineering.Inc). Then subjected to combined compression load to flexion, extension moment of 7.5 Nm, the axial compressive load of 400 N was applied as a follower load to follow the motion of the spine (Patwardan et al [15]). The utmost component geometry of the spine was originally taken from Computer Tomography CT images. The detailed bony anatomy of the spine: vertebrae, endplates, bone processes, and facet joints were defined using 8-node Hex element [5, 11, 27, 28]. These data were treated by Abaqus 14.1 using custom preprocessor to generate three-dimensional

formulations using parametric descriptions for each bony structure. However, the intervertebral disc (IVD) is the major source of Low Back Pain (LBP) Figure 4.1, 4.5.

The Figure 4.1 illustrates the decomposed components built in previous section. Generally; the IVD composed three highly specialized structures the Annulus Fibrosis (AF), The Nucleus Pulposus (NP), and the cartilage endplate that form the interface with the adjacent vertebral bodies. The Nucleus pulposus NP occupies 30~50% volume of the IVD according to Chen et al [1] and the annulus has several layers. It can be easily done in Abaqus. For saving time from creating several IVDs, the annulus fiber layers are simplified to the inner and the outer laminates. The IVD boundary curve is already done in previous validation process [28].

The seven major ligaments, including anterior Longitudinal Ligament ALL; Posterior Longitudinal Ligament PLL; Intertransverse Ligament ITL; Ligamentum Flavum LF; Capsular Ligament CL; Supraspinous Ligament SSL; and Interspinous Ligament ISL were modeled as three-dimensional, 2 node truss elements (T3D2) and allocated nonlinear hypoelastic behavior [5,11,3]. A UMAT subroutinne (Appendix F, H, I, J) was used to simulate nonlinear Hypoelastic behavior of 2 node truss elements (Figure 4.5). This Hypoelastic formulation allows simulation of changing ligament characteristics with different axial stiffness reversibly at a different level as a function of axial strain stiffness. The strain in the ligaments depends only on the stress applied to it not on the rate of loading, or even the history of loading.

Strains and rotations are assumed to be small. Consequently, deformation is characterized using the infinitesimal strain tensor ε_{ij}^{el}. It is usually more convenient to use these fundamental independent scalar invariants to define the strain tensor [29]:

$$I_1 = \varepsilon_{kk}^{el}\ , \qquad I_2 = \frac{1}{2}(\varepsilon_{ij}^{el}\varepsilon_{ij}^{el} - \varepsilon_{kk}^{el}\varepsilon_{pp}^{el} : 3)\ , \qquad I_3 = \det(\varepsilon_{ij}^{el}) = \frac{1}{6}(\in_{ijk} \in_{lmn} \varepsilon_{li}^{el}\varepsilon_{mj}^{el}\varepsilon_{nk}^{el}) \qquad \textbf{(4.1)}$$

Where: I_1 is a measure of the volume change associated with the strain, I_2 is a measure of the shearing caused by the strain, I_3 hasn't a good physical interpretation. The rate of change of stress is defined as a tangent modulus matrix multiplying the rate of change of the elastic strain:

$$d\sigma = D^{el} : \varepsilon^{el} \qquad \textbf{(4.2)}$$

Where: $d\sigma$ is the rate of change of the stress, D^{el} is the tangent elasticity matrix, and $d\varepsilon^{el}$ is the rate of change of the elastic strain. The entries in D^{el} are provided by giving, Young's modulus, E, and Poisson's ratio, v, as functions of the three strain invariants [30].

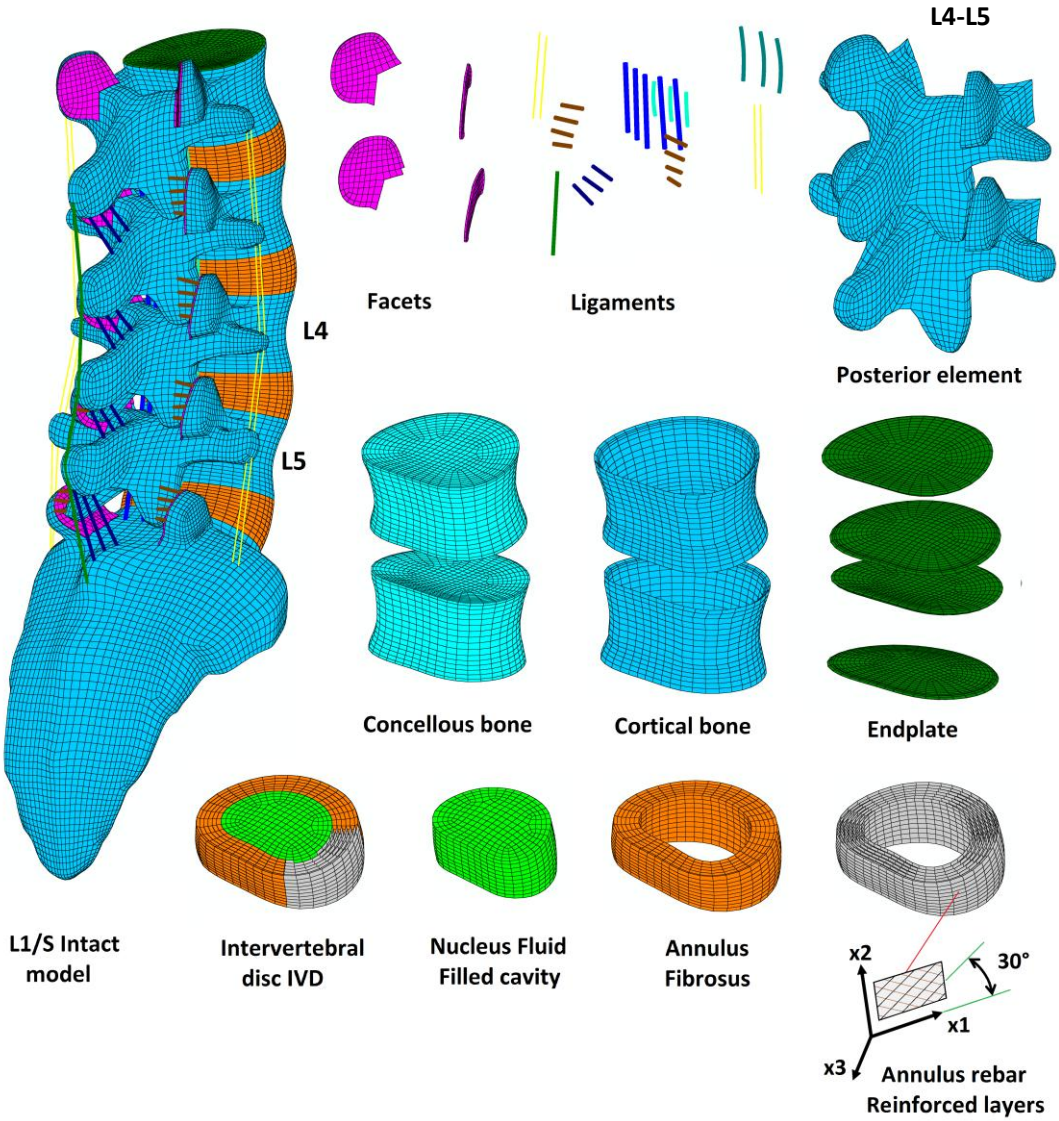

Figure 4.1: Decomposed illustration of FE model in the lumbosacral spine L2-S1

$$I_1 = trace(\varepsilon^{el}), \qquad I_2 = \frac{3}{4}(\varepsilon^{el} : \varepsilon^{el} - I_1^2) \ , \qquad I_3 = \det(\varepsilon^{el}) \qquad \textbf{(4.3)}$$

According to our ligament model, it is assumed that I_1=0; that is, the material is assumed to be incompressible, the ligament was treated as a truss uniaxial stress case which implies that

$$I_1 = 0, \qquad I_2 = \frac{3}{4}(\varepsilon_{11}^{el})^2, \qquad I_3 = \frac{1}{4}(\varepsilon_{11}^{el})^3 \tag{4.4}$$

The cross-section areas of ligaments are separated into several trusses (Figure 4.1) for avoiding the constraint of stress. The entire model consists of approximately 115000 C3D8 element and 128000 nodes and 465516 DOF.

The annulus rebar reinforced layer is meshed in isotropic quads, and each quad shell element has its local orientation axes. The isotropic mesh benefits all first axes parallel with the endplate, facilitate defining the material orientation. The collagenous Fibers lamellae were defined as fiber-reinforced concentric rings including embedded bands of reinforced collagenous fibers defined as rebar element surrounded the nucleus pulpous (Schmidt et al [20]). These Fibers elements were oriented at approximately (±30) into one layer.

Table 4.1 Material properties used in the FE model of lumbosacral spine L1-S1 and the implants

Bony structures	**Young's modulus E (MPa)**	**Poisson's ratio υ**	**Reference**
Concellous bone	100	0.2	
Cortical bone	12,000	0.3	[5,13,27]
Posterior Process	3,500	0.25	
Cartilaginous End plate	23.8	0. 4	[23,20]
Facet cartilage	11	0.4	
Facet contact	Nonlinear soft contact		[19, 20]
Annulus Ground	incompressible fluid		[14,19]
Nucleus Pulposus	4.2	0.45	[5,13]
Annulus fibers	175	0.3	[13]

Major Ligaments	**E (MPa)**	**Strain transition**	**Cross-Sectional Area (mm^2)**	
ALL	7.8 - 20	12%	63.7	
PLL	10 - 20	11%	20	
LF	15 - 19	6.2%	40	[3,5,11]
CL	7.5 - 33	25%	30	
ITL	10 - 59	18%	1.8	
ISL	10 - 12	14%	40	
SSL	8 - 15	20%	30	

The Nucleus Pulposus (NP) was modeled as hydrostatic fluid elements [14, 19]. The facet joints simulated by a cartilaginous layer extruded in Abaqus along the vectors normal to

the inferior face of the superior articular process to the central of thickness of 0.4 mm were modeled to be multi-linear elastic in compression (Moumene et al [11]) by surfaces-to surface contact with softened contact in the normal direction with a coefficient of 0.1 [19, 20] An initial typically gap of 0.2 mm was specified as reported [3, 11].

Table 4.2 Material properties used in the implants

Implants component	E (MPa)	Poisson's ratio	Pretension (N)	
Pedicular screws (all	110.000	0.3	-	[24]
PEEK rods	3,500	0.4	-	[26]
PCU Spacers (all models)	62.5	0.4	-	[24]
300 N Pretention Cord	1500	0.4	300	[24]

4.3 Implant Placements.

Hybrid Stabilization or namely Modular Stabilization system design would restore the kinematics of the normal motion segment without overloading the structural elements that govern the specific motion. Recently, flexible rods have been introduced, to be used supplemented with bone grafts and/or interbody cages in order to achieve a more successful fusion [26, 27]. The hybrid stabilization offers particular protection against included fusion-induced adjacent segment disease ASD and the adverse effects, with a reduction of 25 % of stresses the intact spine (Figure 4.2, 4.3). The instable post-operative segments were modeled in three different configurations of the model by:

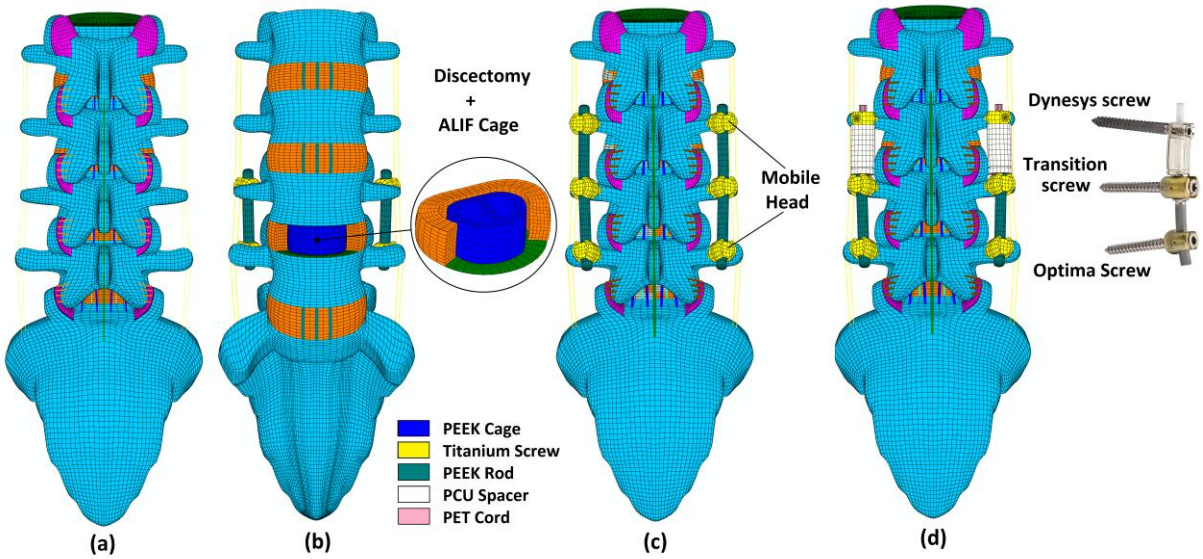

Figure 4.2: FE model of the lumbosacral spine after posterior of hybrid surgery: (a) Intact, (b) Fusion, (c) PEEK+ Fusion P-F, (d) Dynesys + Fusion (DTO) D-F

1. Fusion model (Figure 4.2, b): two 5.5-mm PEEK rods and one PEEK spacer were added through placing them along the L3-L4 segments without distraction. All pedicle screws were rigidly fixed to the vertebrae.

2. The topping off fusion assembly was simulated using pedicle screw-based instrumentation with Supra adjacent level PEEK Rods P-F (Figure 4.2, c) and Dynesys D-F showed in Figure 4.2, d.

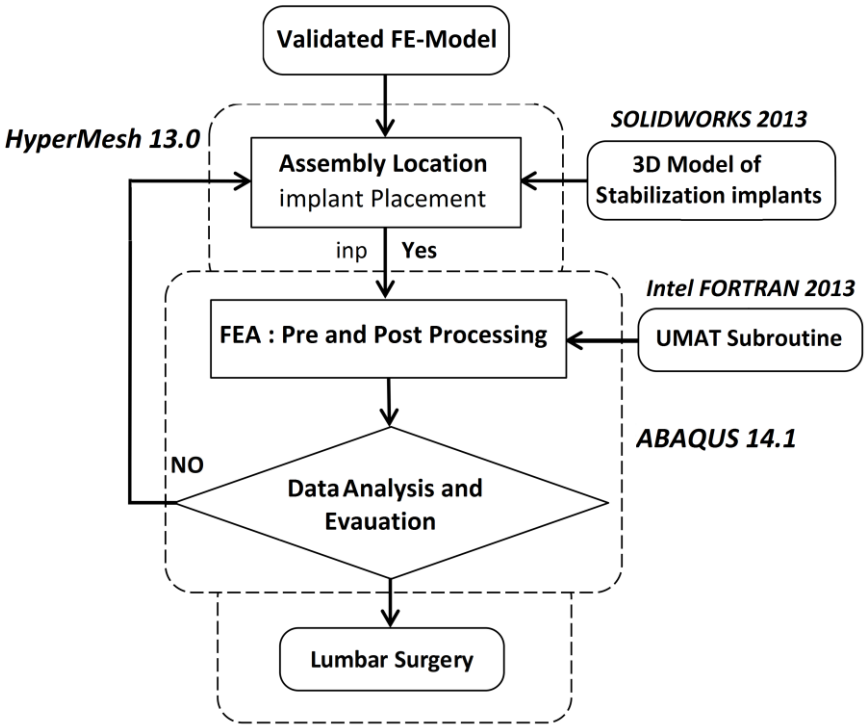

Figure 4.3: Whole process of FE model Formulation and analysis Workflow

The novel implant for the Dynesys + Fusion (DTO) model consisted of six titanium alloy screws (diameter: 6.4 mm, length: 45 mm) and using PEEK rod instead of Ti rod Moreover, two PCU spacers (Diameter: 12 mm, Length: 30 mm) and 300 N pretention PET cord, which contacted the screw in Dynesys model. Shih et al [24]. The intact model was modified to simulate the instability caused by a discectomy, which modeled by removing some part of the annulus from the anterior side of the disc, the procedure involves surgically removing disc material, the size of a window approximately the same width as the interbody cage; removing the anterior longitudinal ligament; and removing the nucleus and a space in the annulus entirety (a separately discectomy).

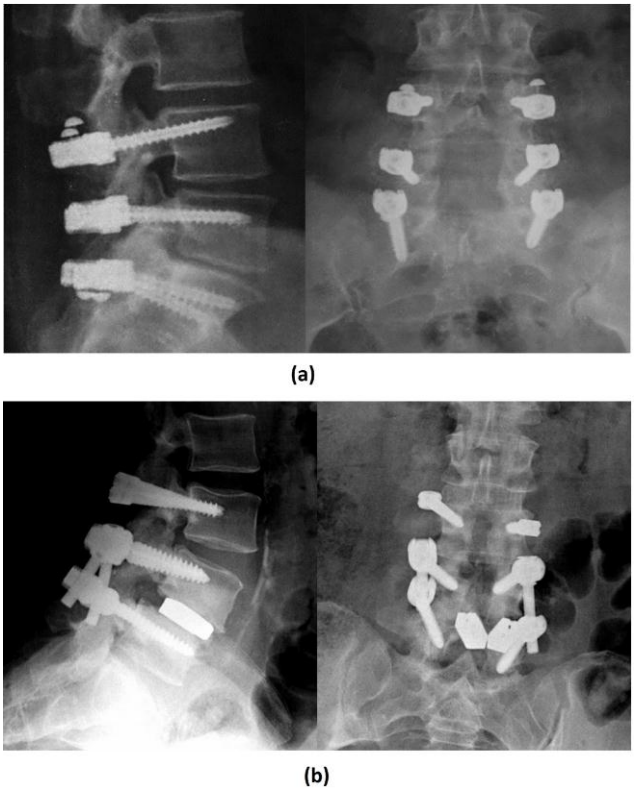

Figure 4.4: Post-operative posterior digital radiographs of the lumbosacral spines with posterior hybrid surgery (a) PEEK+ Fusion, (b) Dynesys + Fusion (DTO)

The FE model allowed mimicking the surgical approach by removing elements and subsequently placing the cage within the disc space, and the ideal location of the implant placement will be the between the cage and the vertebral end-plates were solved by node-to-node contact using a friction coefficient of 0.5. Tsuang et al [26]. One that produces natural physiological spinal motions Figure 4.5. The cage was simulated in the fused level attempting to restore the lumbar lordosis during surgery.

4.4 Results.

4.4.1 Intersegmental rotation:

The results indicate that the free (unfused) intervertebral level is subjected to additional stresses and acquires increasing motions overtime (Figure 4.5, 4.6). There have been several biomechanical studies attempting to document changes in spine due to simulated fusion. Hypermotion in flexion was predicted after fusion by 10~16% in L2-L3 and L3-L4 and about 43~55% in L2-L3 and L3-L4 in extension. The reduction of ROM following hybrid instrumentation is shown in Figure 4.5. Following discectomy, L3-L4

extension ROM decreased by 63% for P-F and 57% for D-F. Stabilizing these segments with D-F controlled that ROM to 70% versus that of an intact segment.

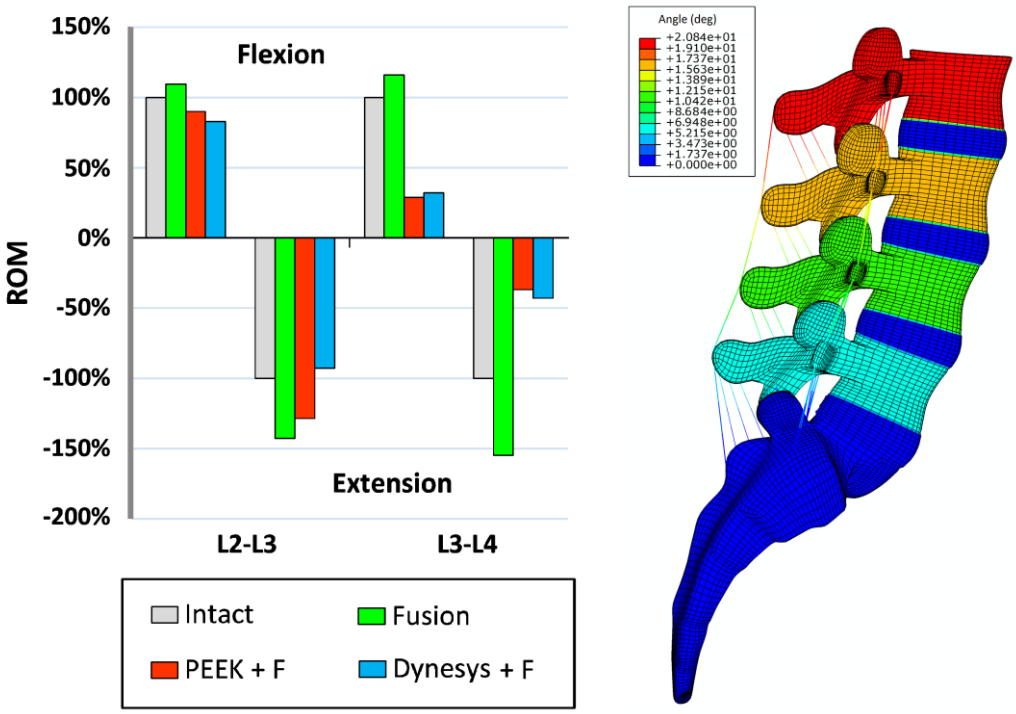

Figure 4.5: ROM (deg) at the level of fusion, topping off fusion and adjacent level as compared to the intact Spinal

Adding PEEK and Dynesys systems is sufficient to stabilize the corresponding L3-L4 ROM while preserving more than 32~28% of its intact flexion. D-F allows displacement while eliminating screw loads, a major source of the screw toggling and loosening.

In contrast, the Dynesys and PEEK systems reduce the ROM and increase screw loading. The PEEK rod, due to its bending flexibility, reduces the ROM but increases the screws axial forces bending loads. At the fused segment (L3-L4), all implants had the same stabilizing effect by reducing the angular motion by 86% compared to the intact spine. The fusion induced increased motion at the adjacent segment (L3-L4) while the P-F reduced potentially the motion.

4.4.2 The stresses of different surgical constructs

As it is predicted; the hybrid systems are highly stressed, while the rest of the structure's motion is preserved (Figure 4.9). Principal stresses in the intervertebral disc specify that, the nucleus pulposus is always induced in compression; with fusion the tensions were higher at the periphery of the Annulus for both flexion and extension, as predicted that the decrease of stresses was accompanied by an increase of shear strain.

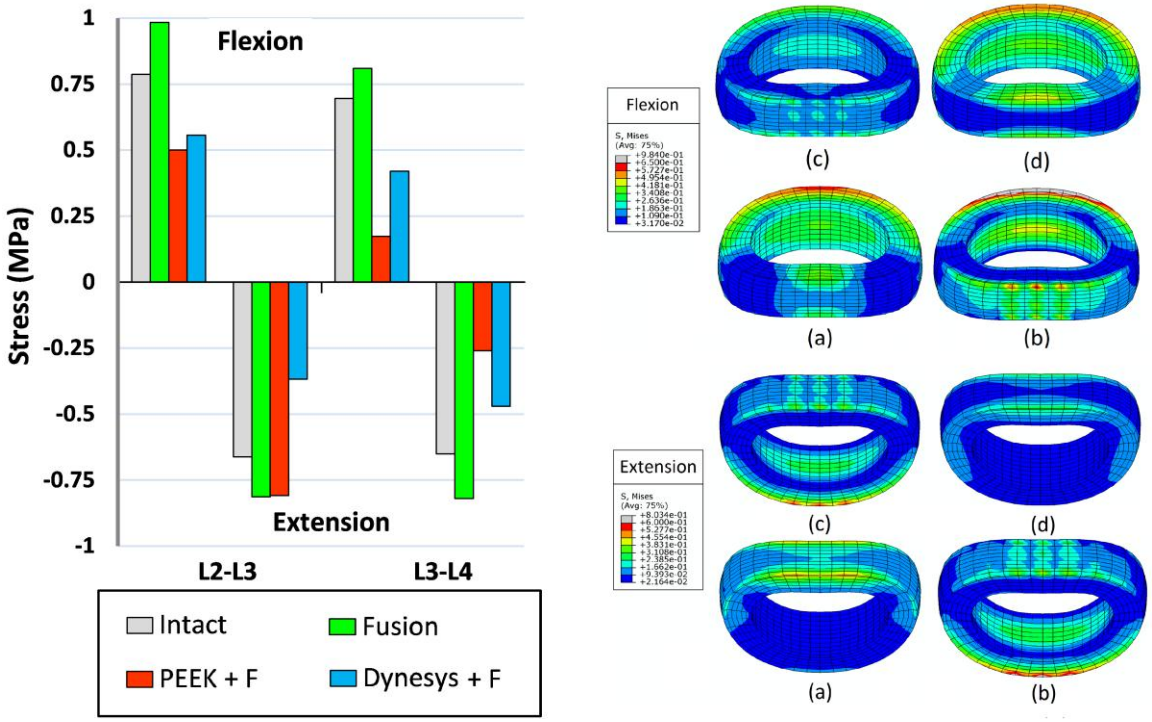

Figure 4.6: Von Mises Stress distribution of the Annulus of L3-L4 level after: (a) Intact, (b) Fusion, (c) PEEK + Fusion, (d) Dynesys + Fusion

4.4.3 The itradiscal pressure

At adjacent level L2-L3 in intact model is higher four times than the P-F for flexion (about 380 KPa) (Figure 4.7). In contrast, it is affected by D-F implant which is slightly lower (365 KPa). The pressure reduction in extension is even more pronounced for hybrid solution, however fusion IDP increases to a level of about 8.5% compared to the healthy model. In contrast, hybrid implant decreases the pressure in the adjacent disc L2-L3 about 79~86%.

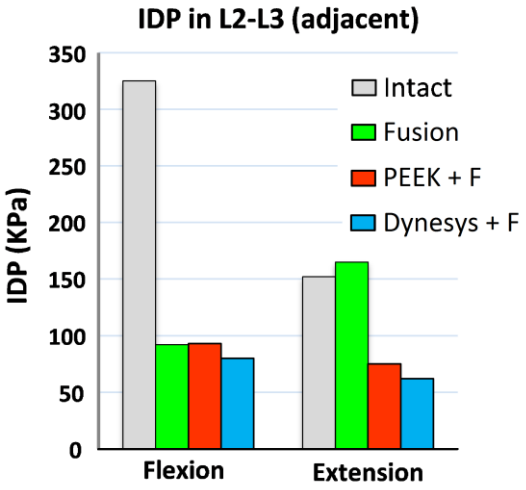

Figure 4.7: Intervertebral disc IDP (KPa) at the L2-L3 level observed in the intact, Fusion, PEEK + Fusion, Dynesys + fusion under flexion and extension

4.4.4 Comparisons of the Stress and Axial forces of different surgical constructs

Loads in the semi-rigid fixator P-F are all higher than in the dynamic one D-F, the forces are calculated for flexion-Extension (up to 58 ~50 N), however the Fusion had minor effect on axial implant forces (26~37 N). Compressive force in the implant is predicted also slightly high 44~56 (Figure 4.8).

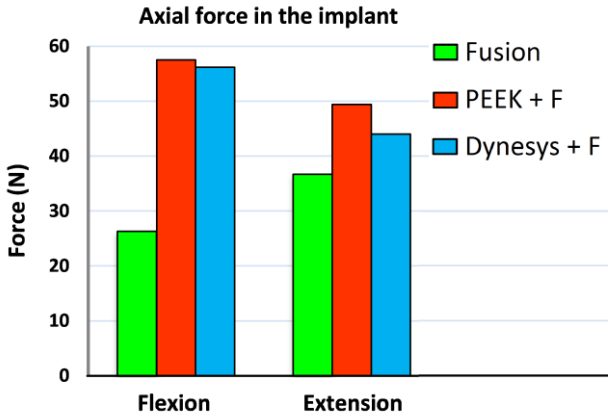

Figure 4.8: Axial force in the implant for different scenarios

The value of the largest maximal Von Mises stress on rods during all states of motion was the largest in the D-F fixation model. The value of the largest maximal Von Mises stress of the pedicle screws was 1640 MPa and rods during nearly all states of motion was smallest in the P-F fixation model. Therefore, this stress distribution may reduce the possibility of broken or loosened screws. Flexion, extension, lateral bending,

and axial rotation tests were conducted to measure the loading forces on the screws. In the current study, we found that P-F at the adjacent level may result in a stiffer construct and less Von Mises stress on pedicle screws compared with fusion fixation.

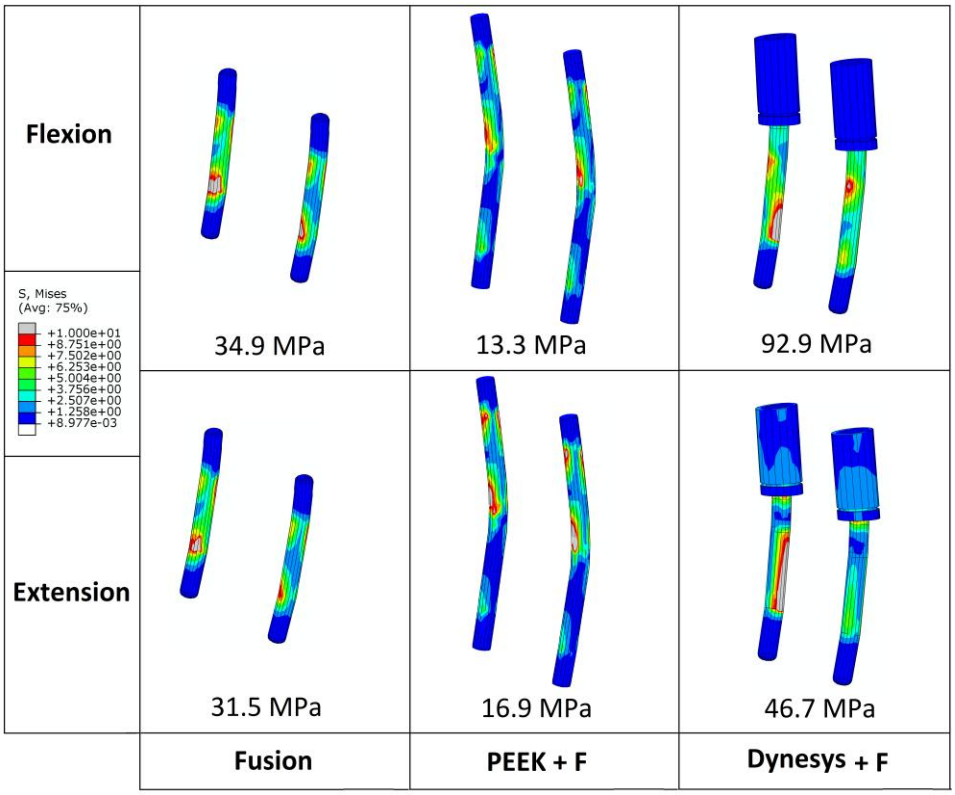

Figure 4.9: Stress nephogram of the flexible rods

4.4.5 The cage-endplate stresses of different surgical constructs

The maximal Von Mises stresses of all constructs were predicted at the endplate interface with flexion, and most of the maximal stresses of the facet joints were detected with D-F in flexion (3.32 MPa) in the anterior side 50% higher than the Fusion, a mildly higher stress of the posterior region detected in extension (0.964 MPa) for D-F and decreased about 10% for P-F. The cage was highly stressed (flexion 54 MPa ~ extension 35 MPa) (Figure 4.10) and the stresses of the facet decreased from 7.7 MPa (D-F) and 6.47 MPa (Fusion) to 3 MPa (P-F).

Of all the structures, the most significant changes in the maximum stress occurred on the inferior and the superior endplate of L5 vertebra. There were two main reasons that caused the risky increase in the stress on the endplates. Even though the pointed edges of the cages avoided the significant moments between endplates and cages, this used design

resulted in peak stress concentration. Then, the PEEK material is stiffer to be used as a graft material. So, the phenomenon of stress shielding on ALIF cages was severe used in D-F. Figure 4.10.

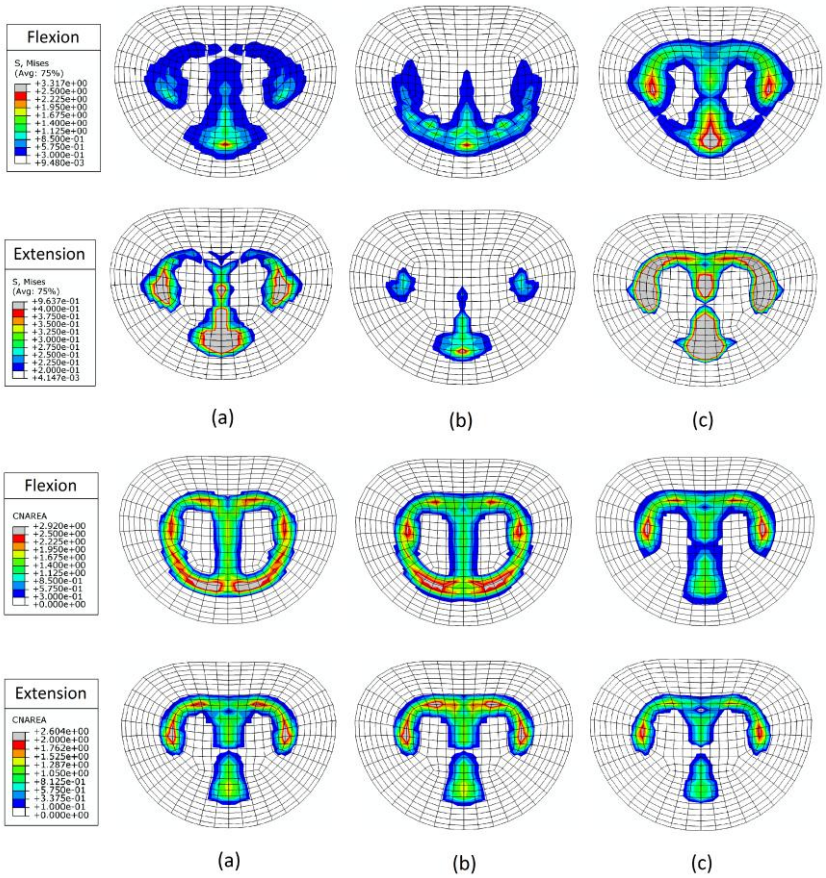

Figure 4.10: Stress and contact area nephograms on cage-endplate interface of L4-L5 level after: (a) Fusion, (b) PEEK + Fusion, (c) Dynesys + Fusion

The majority of the load was transferred onto the cages more than the posterior hardware as the rods. Thus, the ALIF with cages caused tremendous increase in the stress on the endplates. Excessive stresses on the vertebrae endplates may cause osteolysis of the endplate and subsidence of the fused level. Consequently, in order the surgical model using ALIF cages protect the endplate, the surgical model using should reduce the stresses concentration on the endplates.

From the showed results of stresses on the rods and the endplates, the P-F model was better than the other two models. Therefore, this surgical method was recommended for the patients who had already suffered from the ASD and osteoporosis conditions. This endorsement was because that the two main risks confronted in the ALIF procedure were

the further ASD and the subsidence or damage of endplate (after using the interbody cages, which would eventually result in the failure of fusion surgery. Compared to the two models using cages, the P-F model could successfully subside such risk phenomenon. Stress distribution on the vertebra-ALIF cage interface signifies vertical compression force wielded on the bony

Endplate. The D-F model exerted the highest stress on the L4 endplate compared to the other models (Figure 4.9). This might be due to the stress not being fully shielded by the intervertebral construction and being redistributed by the cage and transmitted onto the L4 endplate. Relatively, the stress was shielded by the screws in all models and thus less stress was distributed on the endplate.

In the P-F model, because of its relatively high ROM control, the distributed stress on the endplate was more than in the other two models. The D-F model had higher vertical load on the L4 endplate than the other counterparts. The prevalence of ALIF cage subsidence may increase higher vertebral stress. On the other hand, unshielded vertical load may be beneficial for implant consolidation according to Wolff's law.

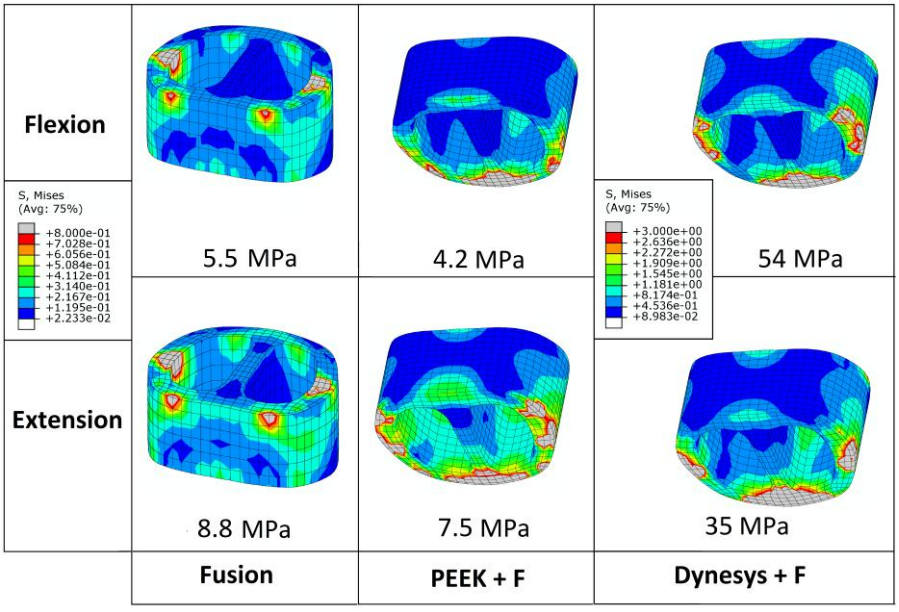

Figure 4.11: Von Mises stress distribution at the interbody cage for the three models of lumbar stabilization

The comparative predictions showed that the smallest stresses on ALIF cages and endplates were found in the P-F model, but the forces on the implants were found greatest

in this model, so it may be inferior to the other two surgical models. The P-F model showed a similar considerable stress on the bony endplate. The Fusion model showed an increased in the percentage change of adjacent discs and medium stresses on the endplates.

Our FE study certain limitations. Firstly, The NP was modeled with a fluid filled cavity without considering its continuum structure, muscle forces and loads were not simulated in the current study. The muscle contractions may carry complicated external forces that have significant influences on the biomechanical viewpoint [9]. The above factors will be considered in our further study. Although there were certain simplifications in our FE model, the FE model was well validated previously.

Consequently, the L1-S1 model modified in this study is reasonable and can be used as an effective tool to assess the effects of three stabilization systems on the lumbosacral spine. In all the placement cases, there was no incidence of abnormal high stress concentration that could lead to the implant failure.

4.5 Discussion.

The treatment outcome using hybrid constructs was relatively satisfactory. Chou et al [2]. A PDS topping off semi-rigid fusion system was optimized with a stiffness equivalent to that of an intact spinal segment is sufficient to stabilize the spine while preserving 60% of its intact ROM, consequently, reducing the load on its structural element. Dynesys and PEEK rods reduced most of segment ROM, as well as strengthening as fusion devices. Semi-rigid Fusion P-F alters the kinematics in the adjacent segment by redistributing the range of motion and leads to increase tension in the disc's fibers. The results showed that the adjunct PDS combined with lumbar spinal fusion D-F was able to decrease the adjacent level motion while efficiently providing stability at the operated level as compared to lumbar fusion. Stress levels around the adjacent level appeared to be far inferior to the surrounding bone strengths (Figure 4.6). However, concerns for high stress level at the interpedicular process still remain especially in extension. In conclusion, the adjunct device combined with lumbar spinal fusion may be able to contribute to reducing degeneration process at the adjacent levels while effectively providing stability to the operated level. However, potential failure of stressed pedicles and processes need to be addressed. The preservation of segmental motion obtained in

non-fusion technology created the concept of symptomatic same level degeneration, as opposed to what is seen in a solid fusion. The flexible implant is assumed to reduce inter-segmental rotation at implant level, decreases intradiscal pressure in adjacent segments for flexion-extension, and decreases facet joint forces at implant level. The inter-segmental rotation at implant level is insignificantly increased for flexion.

Fusion surgery of the spine is accomplished by stimulating bone to grow between two or more adjacent spinal segments to prevent future motion. The instrumentation used in flexible stabilization is designed to control the amount of motion between adjacent vertebrae, but it does not completely eliminate this movement, preventing degenerative changes in the adjacent segments, and reducing instrument failures such screw toggling and loosening. Flexible stabilization for fusion technology support for better physiological bone fusion without shielding the stress. As such, the system is adaptable to the various stages of disc degeneration from early degenerative stage of intervertebral disc to ultimate stage of disc degeneration requiring a fusion. This level of flexibility not only offers spine surgeons more options in the treatment of lumbar disc diseases, but also allows selective segmental stabilization during the surgical procedure to improve treating multiple disc diseases

4.6 Significance.

The current FE investigation suggested that substitution of the superior level fusion with the adjunct PDS devices in multi-level fusion procedures may be able to offer similar biomechanical outcome and stability while reducing likelihood of ASD and the feasibility of a PDS adjunct combined to fusion implant system that provides increased load sharing with the construct addressing the Lumbar stenosis, facet pain and the disc degeneration. This avoids the PDS material stress shielding compared to non-dynamic design iterations. Non-fusion techniques are newly innovated compared to fusion, as an option in the surgical treatment for low back pain. As new techniques, long term prospective studies must be designed to achieve their effectiveness.

Reference:

[1] Chen H, Charles Y.P, Bogorin I, Steib J.P. Influence of 2 different dynamic stabilization systems on sagittal spinopelvic alignment. Journal of spinal disorders & techniques.2011; 24(1):37-43.

[2] Chou W.Y, Hsu C.J, Chang W.N, Wong C.Y. Adjacent segment degeneration after lumbar spinal posterolateral fusion with instrumentation in elderly patients. Arch Orthop Trauma Surg 2002; 122:39-43.
[3] Denoziere G, Ku D.N. (2006). Biomechanical comparison between fusion of two vertebrae and implantation of an artificial intervertebral disc, Journal of Biomechanics, 39(4), 766-775.
[4] Formica M, Cavagnaro L, Basso M, Zanirato A, Felli L, Formica C: Is it possible to preserve lumbar lordosis after hybrid stabilization? Preliminary results of a novel rigid-dynamic stabilization system in degenerative lumbar pathologies. Eur Spine J. 2015, 24:849–54.10.1007/s00586-015-4264-8
[5] Goel V.K, Monroe B.T, Gilbertson L.G, Brinckmann P. (1995a). Interlaminar shear stresses and laminae separation in the disc. Finite element analysis of the L3-L4 motion segment subjected to axial compressive loads. Spine, 20(6), 689-698.
[6] Kashkoush A, Agarwal N, Paschel E, Goldschmidt E, Gerszten P.C. Evaluation of a Hybrid Dynamic Stabilization and Fusion System in the Lumbar Spine: A 10 Year Experience. Cureus. 2016 Jun 10;8(6):e637. doi: 10.7759/cureus.637
[7] Kumar M.N, Baklanov A, Chopin D. Correlation between sagittal plane changes and adjacent segment degeneration following lumbar spine fusion. Eur Spine J 2001;10:314-9.
[8] Lee S.E, Jahng T.A, Kim HJ: Hybrid surgery combined with dynamic stabilization system and fusion for the multilevel degenerative disease of the lumbosacral spine. Int J Spine Surg. 2015, 9:45. 10.14444/2045
[9] Marion P.h, Barrios C, Rouch P, Charles Y.P , Steib J.P , Skalli W. Clinical Outcomes and Complications After Pedicle-anchored Dynamic or Hybrid Lumbar Spine Stabilization: A Systematic Literature Review.J Spinal Disord Tech 2015 Oct;28(8):E439-48
[10] Maserati M.B, Tormenti M.J, Panczykowski D.M, Bonfield C.M, Gerszten P.C. The use of a hybrid dynamic stabilization and fusion system in the lumbar spine: preliminary experience. Neurosurgical focus. 2010;28(6):E2.
[11] Moumene M, Geisler F.H (2007) Comparison of biomechanical function at ideal and varied surgical placement for two lumbar artificial disc implant designs: mobile-core versus fixed-core. Spine 32:1840–1851. doi:10.1097/BRS.0b013e31811ec29c
[12] Ohshima H, Tsuji H, Hirano N, Ishihara H, Katoh Y, Yamada H. Water diffusion pathway, swelling pressure, and biomechanical properties of the intervertebral disc during compression load. Spine 1989;14:1234–44.
[13] Oktenoglu T, Erbulut D.U, Kiapour A, Ozer A.F, Lazoglu I, Kaner T, Goel V.K . Pedicle screw-based posterior dynamic stabilisation of the lumbar spine: in vitro cadaver investigation and a finite element study. Computer Methods in Biomechanics and Biomedical Engineering. 2014;:1 doi :10.1080/10255842.2014.890187
[14] Paige Little J. 2004, Finite element modeling of anular lesions in the lumbar intervertebral disc. (Doctoral Thesis).
[15] Patwardhan A.G, et al. A Follower Load Increases the Load-Carrying Capacity of the Lumbar Spine in Compression. Spine, 24(10), 1003 (1999).
[16] Phillips FM, Slosar PJ, Youssef JA, Andersson G, Papatheofanis F. Lumbar spine fusion for chronic low back pain due to degenerative disc disease: a systematic review. Spine (Phila Pa 1976). 2013; 38(7):409–422. doi:10.1097/BRS.0b013e3182877f11
[17] Prasath M, Fernando T, Robb W.C, Tara F.B, Robert FM, Hybrid dynamic stabilization: a biomechanical assessment of adjacent and supra adjacent levels of the lumbar spine Laboratory investigation, Journal of Neurosurgery: Spine ,2012. DOI: 10.3171/2012.6.SPINE111054.

[18] Rahm M.D, Hall B.B. Adjacent-segment degeneration
after lumbar fusion with instrumentation: a retrospective study. J Spinal Disord 1996;9:392-400.
[19] Rohlmann A, Zander T, Schmidt H, Wilke H-J, Bergmann G (2006) Analysis of the influence of disc degeneration on the mechanical behaviour of a lumbar motion segment using the finite element method. J Biomech 39:2484–2490. doi: 10.1016/j.jbiomech.2005.07.026
[20] Schmidt H, Heuer F, Simon U, Kettler A, Rohlmann A, Claes L. et al. Application of a new calibration method for a three-dimensional finite element model of a human lumbar annulus fibrosus, Clin. Biomech., 2006, 21, 337–344.
[21] Sears W.R, Sergides I.G, Kazemi N, Smith M, White G.J, Osburg B. Incidence and prevalence of surgery at segments adjacent to a previous posterior lumbar arthrodesis. Spine J. 2011; 11(1):11–20. doi:10.1016/j.spinee.2010.09.026
[22] Sengupta D.K, Webb J.K, Mulholland R.C. Can soft stabilization in the lumbar spine unload the disc and retain mobility? A biomechanical study with fulcrum assisted soft stabilization on cadaver spine. ISSLS Annual Meeting; 2001 Jun 19-22; Edinburgh, Scotland.
[23] Sharma M, Langrana N.A, Rodríguez J. Role of ligaments and facets in lumbar spinal stability.Spine. 1995; 20:887-900.
[24] Shih S.L, Liu C.L, Huang L.Y, Huang C.H, C.S Chen. Effects of cord pretension and stiffness of the Dynesys system spacer on the biomechanics of spinal decompression- a finite element study. BMC Musculoskelet Disord 2013 19; 14:191. Epub 2013 Jun 19.
[25] St-Pierre G.H, Jack A, Siddiqui M.M, Henderson R.L, Nataraj A: Nonfusion does not prevent adjacent segment disease: Dynesys long-term outcomes with minimum five-year follow-up. Spine (Phila Pa 1976). 2015, 41:265-73.
[26] Tsuang Y.H, Chiang Y.F, Hung C.Y, Wei H.W, Huang C.H, Cheng C.K. Comparison of cage application modality in posterior lumbar interbody fusion with posterior instrumentation - A finite element study. Medical Engineering & Physics 31 (2009) 565–570
[27] Zhong Z.C, Wei S.H, Wang J.P, Feng C.K, Chen C.S, Yu C.H. (2006). Finite element analysis of the lumbar spine with a new cage using a topology optimization method, Medical Engineering and Physics, 28(1), 90-98.
[28] Bendoukha M, Mosbah M: Biomechanical Evaluation of Lumbosacral Segments Response under Physiological Functions: Finite Element Analysis, Építő anyag – Journal of Silicate Based and Composite Materials,Vol. 69, No. 3 (2017), 122–126. p. https://doi.org/10.14382/epitoanyag-jsbcm.2017.22
[29] Bower A.F, Applied Mechanics of Solids .Chapter 3: Constitutive laws, 3.3 Hypoelasticity http://solidmechanics.org/Text/Chapter3_3/Chapter3_3.php
[30] Abaqus Analysis 6.10 User's Manualhttps://www.sharcnet.ca/Software/Abaqus610/ Documentation/ docs/ v6.10/books/usb/default.htm?startat=pt05ch19s04abm06.html

Chapter 5:

Biomechanical Analysis of Adjacent Segment Level Following Hybrid Dynamic Stabilization Topping off Fusion of the Lumbar Spine

5.1 Introduction

Advantages of the hybrid approach include reducing the risk of excessive disc stress when compared with a wider posterior lumbar fusion, as well as avoiding the potential complications associated with rigid fusion, such as the great damage during hyper-motion in the adjacent segment that may lead to degeneration in patients. Topping off fusion also offers a theoretically lower risk of adjacent segment destabilization [17, 29].

Advances in instrumentation systems have allowed the development of minimally invasive techniques that now commonly used as an adjunct approach, however, only some of clinical reports have evaluated the hybrid technique. These studies report satisfactory stability [7, 11, 20]. Nonetheless, controversy remains, as some investigators believe hybrid fixation provides inadequate stability that may lead to higher rates of instrumentation failure and pseudoarthrosis. St. Pierre et al [44]. Defining the best method for posterior stabilization procedures remains unknown. Previous biomechanical studies have shown increased construct stiffness with combined PDS to fusion constructs fixation can assure higher fusion rates compared with conventional fusion alone [29,40]., with reported fusion rates between 90% and 100% in these reports.

Assessment of the COR location is an essential diagnose to evaluate objectively the mechanical abnormalities of the spine which can be detected after degenerative conditions [8]. Determining the CORs is a tool to evaluation of fusion techniques by adjusting the ICR location for stabilization systems attempting to get the COR location closer to that of the healthy motion segment. Any inconsistency in the kinematics between a dynamic stabilization system and the motion segment would lead to differences of the load-

Distribution in the spinal segment. Sengupta et al [41]. This could change the strain degrees and could also induce the stress shielding according to Wolff's law.

A lot of experimental studies investigated the COR [1, 5, 8, 21, 26, 36, 39] In this study we developed a finite element (FE) model which will quantify the motion pattern and stress–strain distribution in the Lumbar segments. Qiu et al [30]. The field of spine fusion surgery remains extremely dynamic with changes in preoperative care constantly affecting patient care. A big collection of flexible stabilization systems is currently in advanced phase of development and clinical investigation in order to address the arthrodesis related limitations. Kumar et al [12].

This project aimed to describe the three-dimensional characteristics of the COR preoperative and postoperative spine using hybrid constructs. Therefore, the hypothesis of the present study was that isolated simulation of degeneration changes in the disc in the L4-L5 lumbar spine segment with normal facetectomy which would cause significant shift in the COR. We therefore proposed the hypothesis that different stabilization system concepts lead to substantial differences in the location of the CORs. We furthermore hypothesized that the different implant designs lead to a similar range of motion ROM.

5.2 Methods and boundary conditions.

5.2.1 Implanted models Formulation.

Based on the available knowledge and the biomechanical analysis; the instable post-operative segments were modeled in four different configurations of the model by adding PEEK, Ti rods, NFlex, and Dynesys by placing them along the L3-L4 level topping off fusion based on 5.5-mm Ti and PEEK rod without distraction. All pedicle screws were rigidly fixed to the vertebrae. While a 6mm Ti rod of NFlex was used. The intact model was modified to simulate the instability caused by degenerated disc and bilateral facetectomy by removing the facets portion and the capsular ligaments to model bilateral facetectomy. All models were loaded by using the hybrid protocol in flexion, extension, lateral bending. A 7.5 Nm moment was applied to all modalities while under a follower compressive follower load of 400 N. The interpedicular displacement was predicted for the intact and for the destabilized models before and after instrumentation systems in all directions. Some FE models' studies compute pressures within adjacent discs but did not study the effects of dynamic instrumentation [38, 47].

5.2.2 Contact definitions.

The surfaces of the facet joints were simulated by a cartilaginous layer with a coefficient of friction of 0.2, which was assumed to be multi-linear elastic in compression. Sharma et al [42]. The orientation and curvature of the facet joints were modeled to fulfill reported by Masharawi et al [16] and Panjabi et al [22]. The following interfaces: pedicle screw/vertebral body and pedicle screw/rod were fixed using Rigid fixation was simulated using tie constraint. The pedicle screws were placed based on surgical approaches.

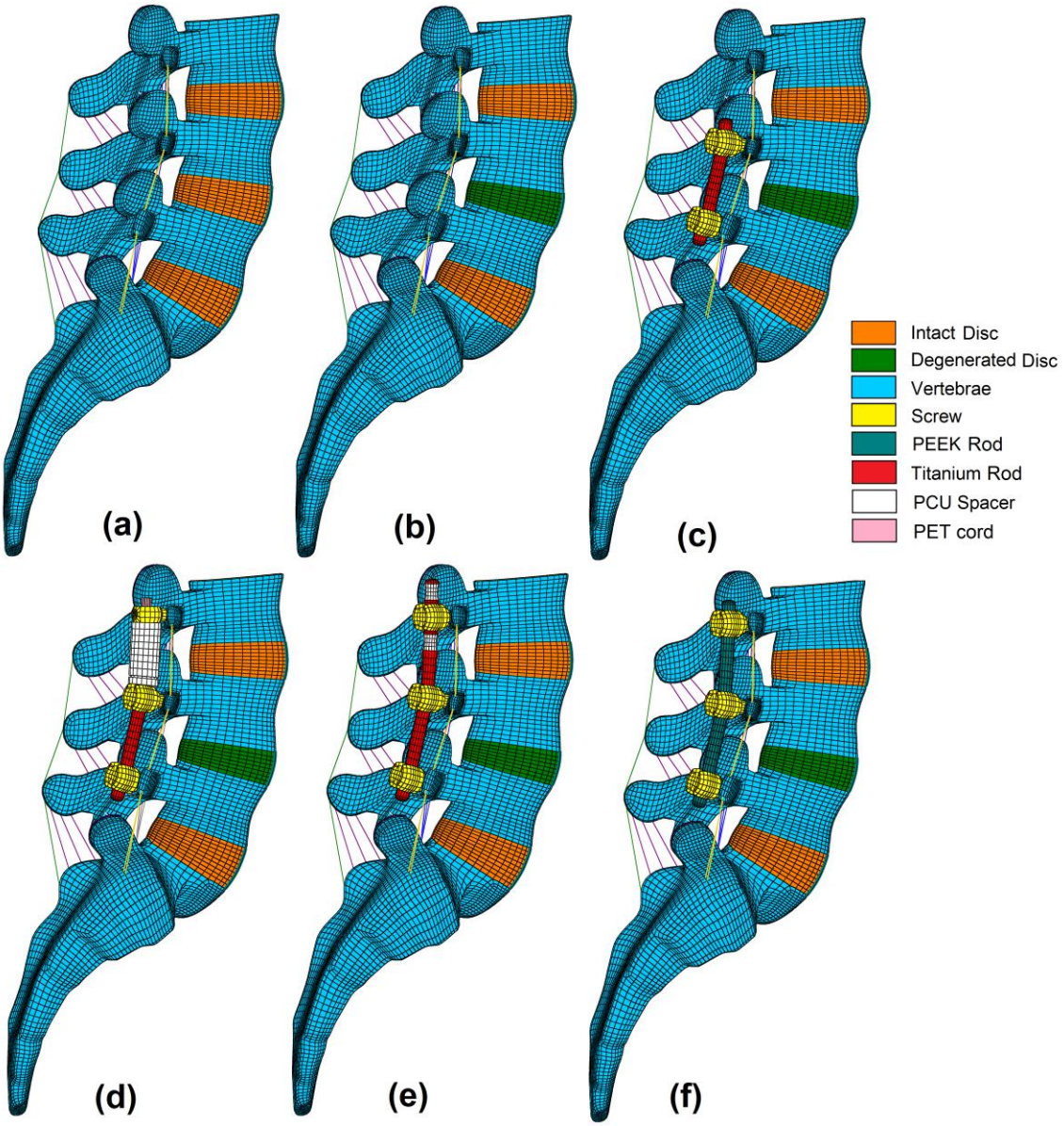

Figure 5.1: FE model of L3-S1 FSUs in different scenarios: (a) Intact, (b) Degenerated, (c) Fusion, (d) Dynesys (DTO), (e) NFlex, (f) PEEK

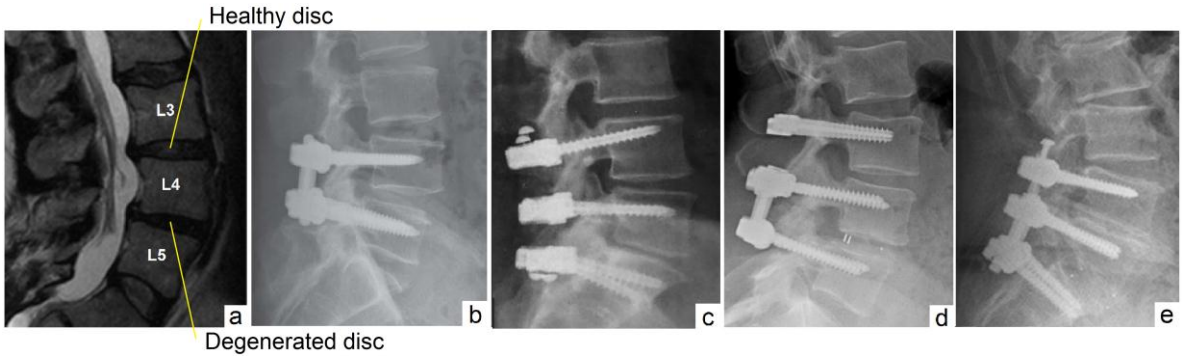

Figure 5.2: Posterior digital radiographs and of the lumbosacral spines with posterior hybrid surgery (a) MRI of Lumbosacral spine, (b) Ti Fusion, (c) Bilevel PEEK, (d) Dynesys + Fusion (DTO) (e) NFlex + Fusion [11,48,49,50]

5.2.3 Methods of detection of COR locations:

Identifying the center of rotation **(COR)** has been gradually used as an efficient tool to investigate the changing of pre and post-operative spinal kinematics. The primordial method used to determine the COR locations was based on features detection of planar radiographic images of motions. A validated 3D FE model of the L3-S1 segments (Figure 5.1) with two levels of disc conditions **(Healthy, Degenerated)** was used. All the bony structures were modeled by using hexahedral. The annulus fibers were defined as reinforced rebar where the orientation of the annulus fibers was 30° and -30° at the anterior.

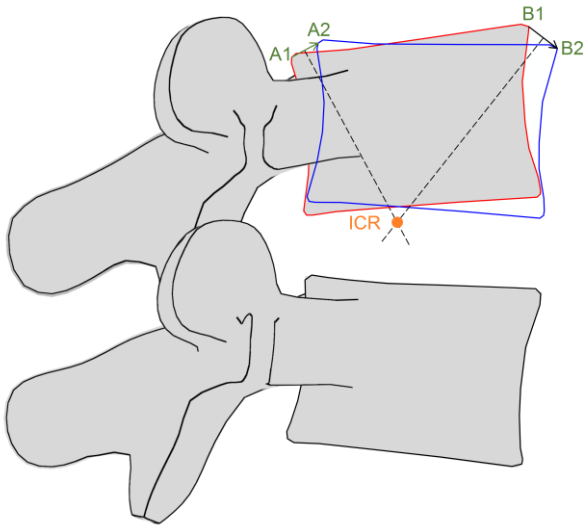

Figure 5.3: Determining the instantenous centre of rotation ICR from one position to another (1-2)

The seven ligaments were modeled with hypoelastic T3D2 elements using UMAT subroutines and python codes (Appendix F, H, J). The nucleus pulposus composed 43% of the whole volume of the disc. The model consisted of 1575 link elements and 115644 solid elements in total. Disc degeneration was simulated by changing disc height (20 and 40% loss for degenerated level, respectively). Rohlmann et al [34].

Table 5.1: Material properties used in finite element model of lumbar spine components

Bony structures		E (MPa)	Poisson's ratio υ	Reference
Cortical bone		12,000	0.3	[9]
Cancellous bone		100	0.2	
Posterior bone		3,500	0.25	[20], [47]
Cartilaginous End plate		24	0.24	
Facet cartilage		11	0.4	[37], [41]
Annulus Ground	Healthy	Incompressible fluid filled cavity		[34], [25]
	Degenerated	Compressible fluid filled cavity		
Nucleus Pulposus	Healthy	4.2	0.45	[9]
	Degenerated	6	0.45	
Facet contact		Nonlinear soft contact		[17], [34]

Table 5.2: Material properties of the seven major ligaments

Annulus fibers	E (MPa)		Cross-sectional Area (mm^2)	Reference
ALL	7.8 (<12%)	20 (>12%)	63.7	[4], [9], [17]
PLL	10 (<11%)	20 (>11%)	20	
LF	15 (<6.2%)	19(>6.2%)	40	
CL	7.5 (<25%)	33 (>25%)	30	
ITL	10 (<18%)	59 (>18%)	1.8	
ISL	10 (<14%)	12 (>14%)	40	
SSL	8 (<20%)	15 (>20%)	30	

Table 5.3: Mechanical properties of the stabilization devices components [43, 46]

Component	E (MPa)	Poisson's ratio υ	Preload
Ti	110.000	0.3	-
PEEK	3,500	0.3	-
PCU	50	0.3	-
Pretention Cord	1500	0.4	300

A pure bending moment of 7.5 Nm with an axial compression preload of 400 N was applied simulating upper body weight without muscle forces in both two planes of

motion. The CoRs were evaluated by using the Reuleaux method [33] (the point generated by the intersection of the perpendicular bisectors of displacement vectors of two nodes of the inferior endplate of the vertebrae based Based on the initial and final states of the vertebral body). Facet joint forces, annulus stresses and strain were calculated. The spine Functional Spinal Units FSUs joints move predominantly in one plane for primary motions (e.g. Flexion, Extension, Lateral bending) in which case the motion can be approximated and analyzed by graphical methods. The COR may be located inside and outside of the boundaries of the rotating body (Vertebrae – IVD – Vertebrae). The position of the COR may be remodeled (Figure 5.3). The lower sacrum body was rigidly fixed.

5.3 Results.

5.3.1 Change in Center of Rotation Analysis:

The COR for the overall motion during flexion-extension is shown for the Spine L3-S1 FSUs during flexion-extension, it was observed that the COR of the intact FSU was posterior compared to the other sectioned configurations while the Nflex solution is similar to in real COR. The COR translates from the center of the disc anteriorly and posteriorly, respectively. The fusion affects the orientation of the vectors, so the grouping of the COR becomes more spread out and translates ventral side. The PEEK system displays that the COR progresses from the center of the disc toward the posterior side of flexion-extension. These patterns remain consistent until the intact and degenerated levels for fused and adjacent segments, where there is a substantial decrease in the amount of range of motion. In the intact and degenerated mode, the COR was located close to the superior endplate of the vertebra in sagittal motion, close to the real COR at the endplate periphery of the vertebra. The maximum change in the position of the centrode due to degeneration was below 4 mm in sagittal plane. (Figure 5. 4)

The locations of the CORs of L3 through L5 were slightly superior and posterior to the geometric center of the respective inferior vertebra. The L5 COR was near the superior endplate of S1, while no significant differences in average location COR were identified with respect to Pearcy et al [26] predictions. The CORs During flexion-Extension were predicted in the mid-height of the vertebrae for the fused level The COR was found to be in the center of the superior endplate for fusion and bottom level. With

Dynesys, and NFlex the CORs moved toward the anterior direction by contrary to the PEEK solution. Figure 5.4

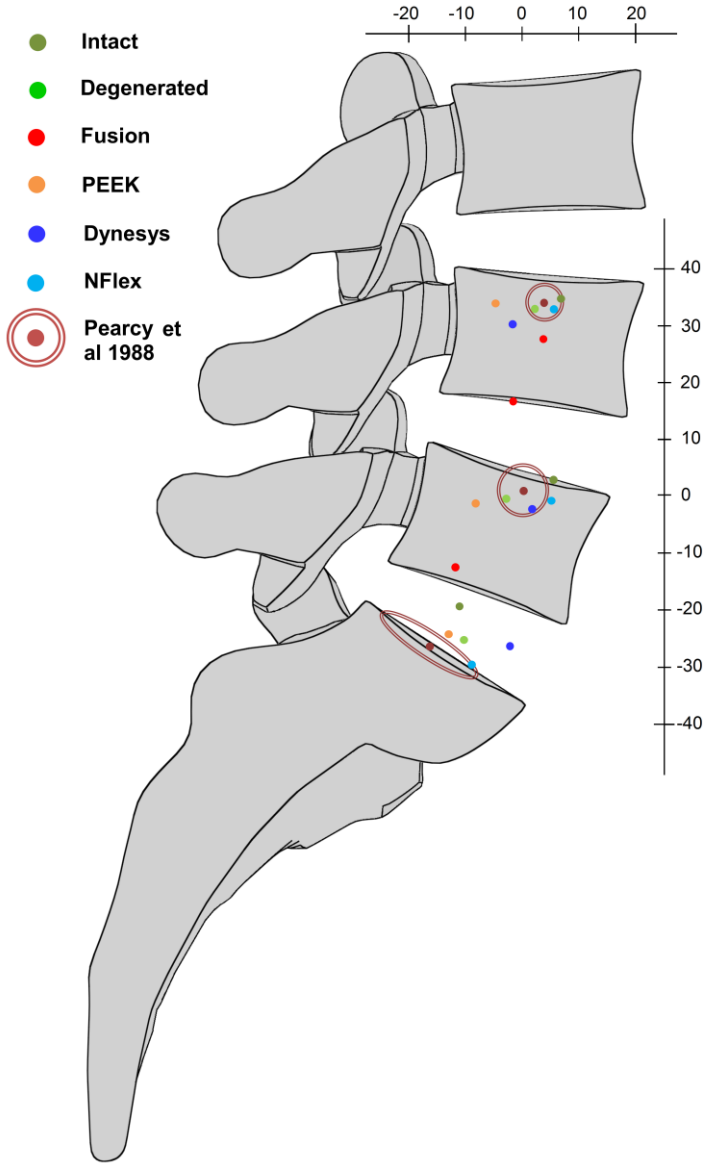

Figure 5.4: Change in COR for all configurations (mm).

5.3.2 Strain distributions:

Overall, Principal shear strains in the intervertebral disc specify that, the nucleus pulposus is always induced in compression.

With fusion the tensions were higher at the periphery of the Annulus for both extension and lateral bending. The strain decreased with disc degeneration but there was a significant change with further degeneration in extension for fusion. No change occurred

in flexion in the degeneration level or all hybrid stabilization. Annulus strains decreased constantly with disc degeneration. Figure 5.3.

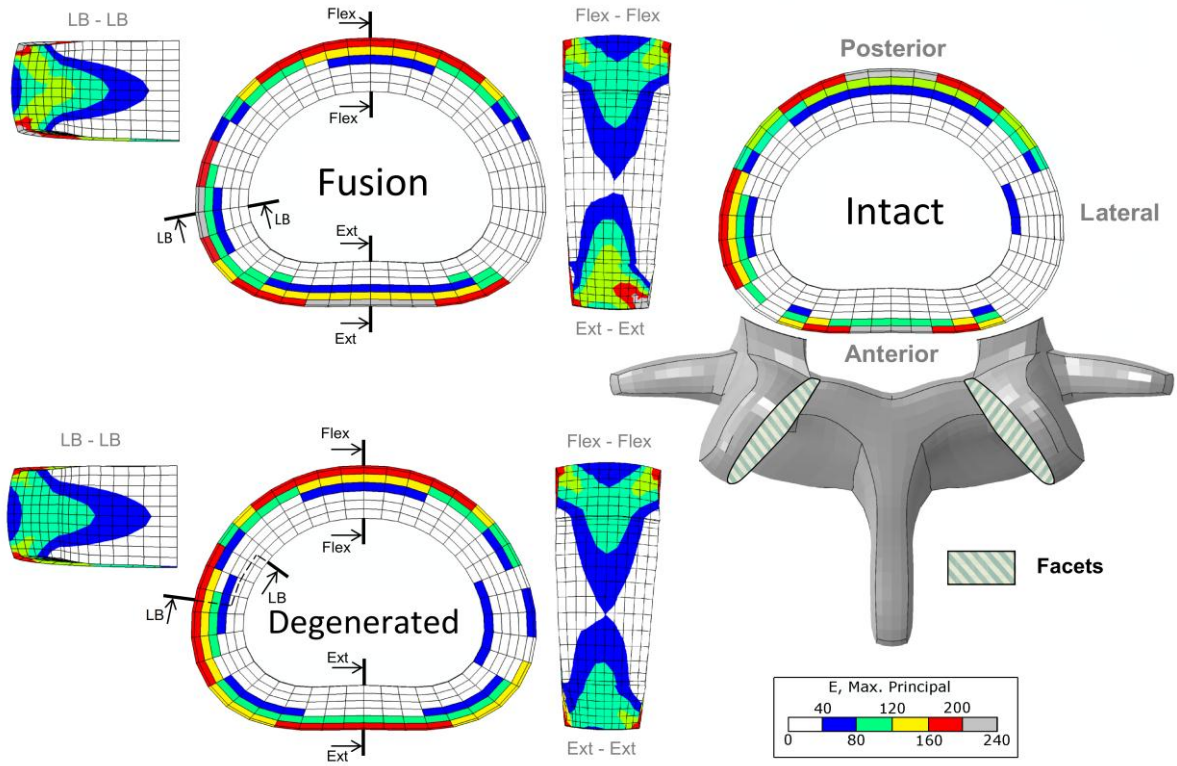

Figure 5.5: Predicted maximum strain distribution (10^{-3}) in the disc for Intact, Degenerated and Fusion modes (Flexion – Extension – Lateral Bending)

5.3.3 Bending stiffness.

For Flexion/extension the stiffness was drastically increased for all reconstruction techniques compared with the intact condition (Figure. 5.6). At the level of fusion, rotation stiffness was increased by greater than 67~87% of intact stiffness for unilateral and 43~74% of degenerated condition. There were significant differences observed within the hybrid construction and fusion fixation tested. Figure 5.6. Displays the bending stiffness values for each model. The deletion of nucleus compressibility increased the stiffness. The lateral bending revealed no ROM differences at the superior adjacent level between any of the simulated fusion constructs and the intact condition (Figure 5.7, 5.9), but there were differences noted between fusion and posterior hybrid constructs. In lateral bending, more than 61% of intact ROM remained after fusion fixation, compared with less than 17% of intact ROM after Nflex fixation. ROMs achieved with Dynesys and PEEK posterior fixations compared with intact ROM were less than 21% and 26%,

respectively. Therefore, the unfused intervertebral level is subjected to additional stresses and acquires increasing bending stiffness overtime (Figure 5.5, 5.7). There have been several biomechanical studies attempting to document changes in spine biomechanics due to successful fusion procedures. Highly strains and stresses in flexion, lateral bending was predicted after fusion. The reduction of ROM following hybrid instrumentation is shown in Figure 5.6, whereas bending stiffness was ranged from 0.98 N.m/deg for lateral bending at intact mode to 5.57 N.m/deg for the Nflex stabilization.

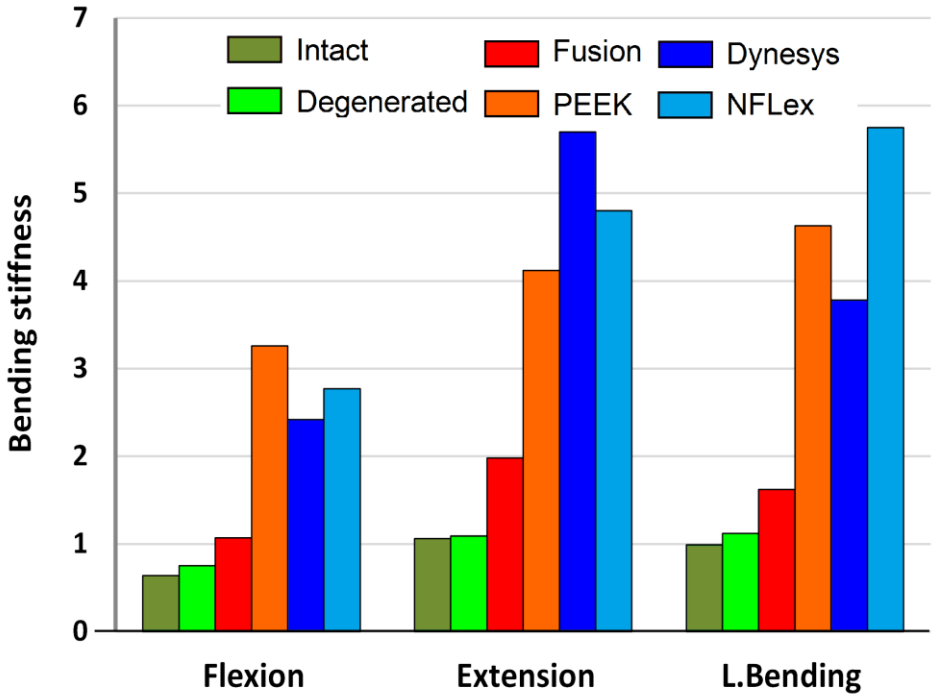

Figure 5.6: Bending stiffness (N.m/deg) for all configurations

5.3.4 Maximum Annulus Stress.

In lateral bending, maximum stiffness had a steady trend initially and reached a maximum during NFlex solution comparing to Dynesys, which was similar to that of other systems (Figure 5.5). Likewise, in extension, maximum annulus stress was higher than in for degenerated and fusion modes. (Figure 5.8).

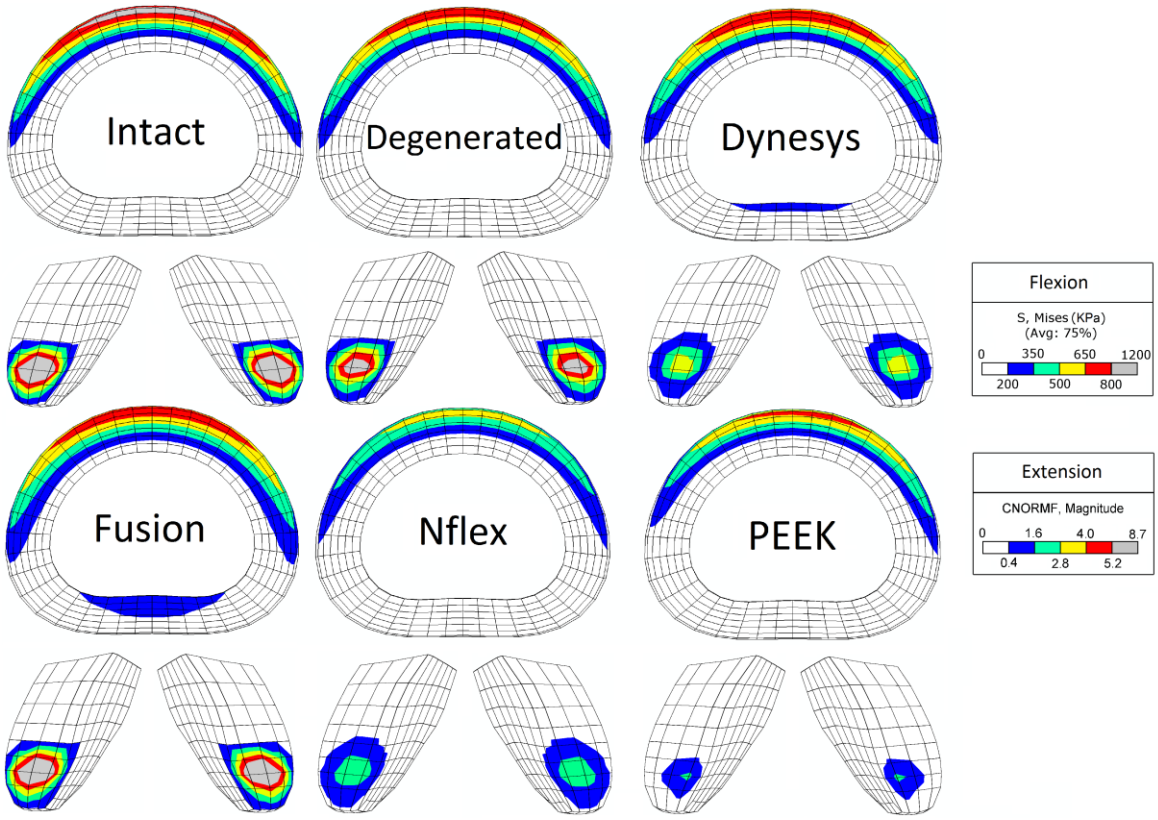

Figure 5.7: Predicted maximum stress and facet joint forces distribution for all configurations: Flexion-Extension

5.3.5 Facet joint force

Facet joints Forces increased non-linearly; i.e. they generated a progressive slope resulting in 50 N at 7.5 Nm extension moment for the fusion mode.

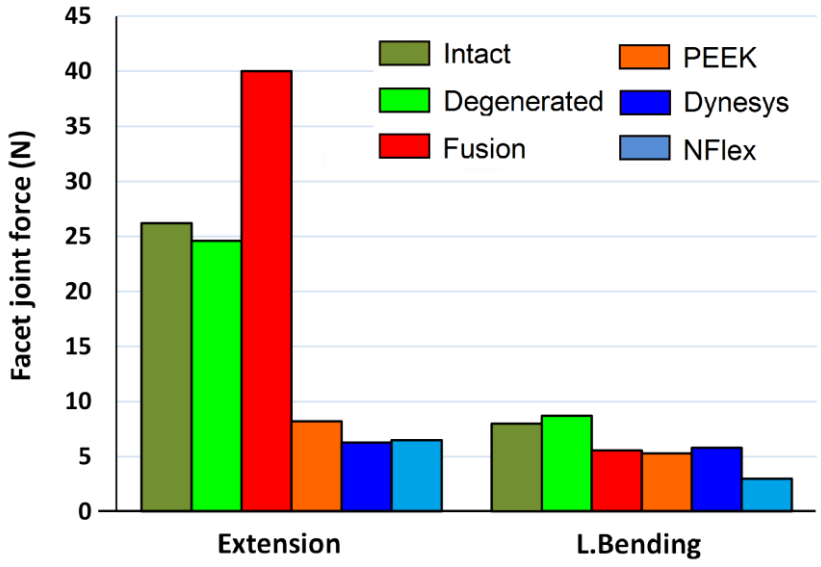

Figure 5.8: Facet joint loads of L3-L4 level after Hybrid stabilization

Forces of the facet joint were summarized for a resultant force value **(FJF).**

This force was calculated as a vector summation direction obtained from each contact element. The maximal facets force of all constructs was predicted at the endplate interface with Extension, and most of the maximal stresses of the facet joints were detected in fusion (40N), mildly lower forces detected in PEEK (6.3N). The facet joints stayed unloaded for flexion, because the opposing facet surfaces displaced apart from each other. In extension, the facets joint forces were also determined to be higher for fusion and be similarly alleviated for hybrid solutions (Figure 5.7). With decreasing stresses and facet forces; the PEEK COR moved posteriorly with a distance of 8 mm.

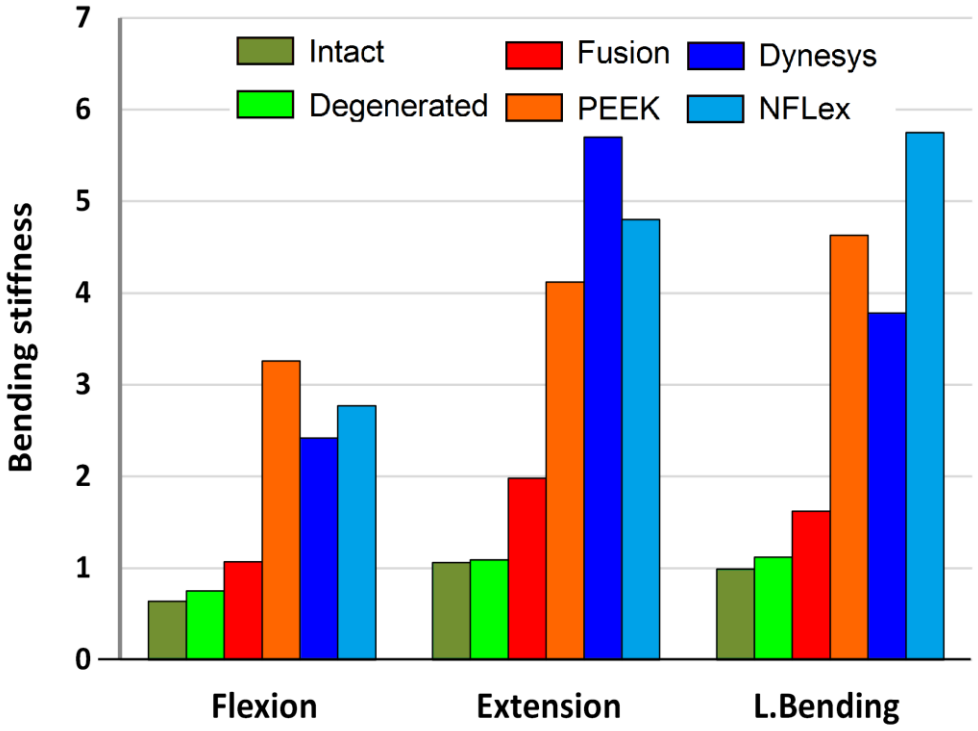

Figure 5.9: Von Mises Stress distribution of the Annulus of L3-L4 level after Hybrid stabilization.

5.4 Discussion

The average CORs presented by Pearcy and Bogduk [26] are currently the most widely used dataset for representing spinal joints as spherical joints in rigid body dynamics simulations. However, some detection methods provide uncertain values [28, 32]. Mean CORs from the current study were comparatively more inferior and anterior compared to Pearcy and Bogduk [26] but were closer to experimental values. Xia et al [45]. In general, with no fixation the location of the CORs remained within the experimental region, dependently to the direction of load. While the stresses and the facet

joints were only slightly loaded for hybrid stabilization and highly loaded for fused stabilization. For all modes, the facet joints remained unloaded for flexion, these higher stresses magnitudes and facet forces affected the migration of the CORs to migrate anteriorly comparing to in vitro data, especially after PEEK and Dynesys stabilization (DTO) for the adjacent level, which resulted in CORs outside of the region.

As expected, the highest facet loads occurred, after fusion when the COR was located outside of the intervertebral disc. Our calculations may be due to the less accurate Reulaux method, 1876 for in vitro studies [33]. We believe that the CORs locations identification in the current study are more precise than determined by previous in vitro studies. Because our FE-model was found to be in excellent agreement with prior in vitro predictions [10, 23]. The current study showed that extension and lateral bending generated the maximum strains postero-laterally and not anteriorly. While motions or different stiffness regions within the disc lead to the relocation of the most strained disc regions.

The followed methodology in this project has some assumptions and limitations. We haven't focused on the geometry of spinal segments. The geometry of the IVD, facets joints surfaces affect the magnitude of the generated contact forces and influenced annulus stresses. Thus, the variation in bone structures, ligament and fiber orientation, nucleus geometry or position and disc height affect the range of motion and the stress distribution the disc and the facets. Noailly et al [18]. Which lead to more changes in the COR, but they should have similar characteristics. Therefore, the applied follower load assumed to be a load condition that could have an influence on the COR during rotation.

Assuming more precisely visco- and poro-elastic material properties dispose the IVD to be stiffer which leads to an influence on the COR location. Without considering coupled motions. Because, coupled flexion, extension, and lateral bending motion can be assumed to be ignored. High accuracy of in defining the CORs is needed because of small movements, which occur when the spine is treated to fusion in order to avoid measurement errors would already produce large deviations, as previously discussed. PDS topping off fusion is an increasingly popular technique for the treatment of degenerative conditions of the lumbar spine. This procedure is traditionally supplemented with bilateral posterior stabilization using pedicle screws and rods. Although PDS topping

semi-rigid fusion augmentation has been proposed as an alternative to PDS topping rigid fusion procedures. This study comprehensively investigated the changes in stiffness, annulus stresses, and facet loads with respect to imposed COR locations in the lower lumbar spine. This comparative analysis suggested that the CORs locations of the spine were strongly correlated with stresses, strain and facets forces.

5.5 Summary

This study characterized the lumbar intervertebral CORs based on high-accuracy skeletal kinematic data in vivo postoperative hybrid surgery. The COR of the intact model was within the range of in vivo data. Pearcy et al [26]. The COR for 75% facetectomy shifted up towards the inferior endplate of the upper vertebra. In the implanted models with graded facetectomies, the COR moved towards the posterior region of the motion segment (Figure 5.4). Defining the COR alone might not be a reliable tool to detect degenerative conditions. The changes in the COR could be used to confirm the clinical evaluations.

The change in the COR location varied the path of the motion and thus the stress distribution within the disc, the stretch of each ligament, and the moment arm, that is, the distance to the COR, of each ligament. Hence, at any COR location, the movement of the spinal segment caused a new composition of load distribution among the elements of the segment. The long-term complications of this technique remain a controversial area of spine surgery because of constructs loosening or breakage. Marion et al [14].

References

[1] Bogduk N, Amevo B, Pearcy M. 1995. A biological basis for instantaneous centres of rotation of the vertebral column. Proc. Inst. Mech. Eng. [H] 209, 177–183.

[2] Chen H, Charles YP, Bogorin I, Steib JP. Influence of 2 different dynamic stabilization systems on sagittal spinopelvic alignment. Journal of spinal disorders & techniques.2011; 24(1):37-43.

[3] Cossette J.W, Farfan H.F, Robertson G.H, Wells R.V, 1971. The instantaneous center of rotation of the third lumbar intervertebral joint. J. Biomech. 4, 149–153.

[4] Denoziere G, Ku D.N. (2006). Biomechanical comparison between fusion of two vertebrae and implantation of an artificial intervertebral disc, Journal of Biomechanics, 39(4), 766-775.

[5] Dimnet J, Fischer L.P, Gonon G, Carret J.P, 1978. Radiographic studies of lateral flexion in the lumbar spine. J. Biomech. 11, 143–150.

[6] Farfan H.F, Cossette J.W, Robertson G.H, Wells R.V, Kraus H, 1970. The effects of torsion on the lumbar intervertebral joints: the role of torsion in the production of disc degeneration. J. Bone Joint Surg. Am. 52, 468–497.

[7] Formica M, Cavagnaro L, Basso M, Zanirato A, Felli L, Formica C: Is it possible to preserve lumbar lordosis after hybrid stabilization? Preliminary results of a novel rigid-dynamic stabilization system in degenerative lumbar pathologies. Eur Spine J. 2015, 24:849–54.10.1007/s00586-015-4264-8

[8] Gertzbein S.D, Holtby R, Tile M, Kapasouri A, Chan K.W, Cruickshank B, 1984. Determination of a locus of instantaneous centers of rotation of the lumbar disc by moire fringes. A new technique. Spine 9, 409–413.

[9] Goel V.K, Monroe B.T, Gilbertson L.G, Brinckmann P. (1995a). Interlaminar shear stresses and laminae separation in the disc. Finite element analysis of the L3-L4 motion segment subjected to axial compressive loads. Spine, 20(6), 689-698.

[10] Heuer F, Schmidt H, Claes L, Wilke H.J, 2007a. Stepwise reduction of functional spinal structures increase vertebral translation and intradiscal pressure. J Biomech. 40, 795–803.

[11] Kashkoush A, Agarwal N, Paschel E, Goldschmidt E, Gerszten P.C. Evaluation of a Hybrid Dynamic Stabilization and Fusion System in the Lumbar Spine: A 10 Year Experience. Cureus. 2016 Jun 10;8(6):e637. doi: 10.7759/cureus.637

[12] Kumar M.N, Baklanov A, Chopin D. Correlation between sagittal plane changes and adjacent segment degeneration following lumbar spine fusion. Eur Spine J 2001;10:314-9.

[13] Lee S.E, Jahng T.A, Kim H.J: Hybrid surgery combined with dynamic stabilization system and fusion for the multilevel degenerative disease of the lumbosacral spine. Int J Spine Surg. 2015, 9:45. 10.14444/2045

[14] Marion P.h, Barrios C, Rouch P, Charles Y.P , Steib J.P , Skalli W. Clinical Outcomes and Complications After Pedicle-anchored Dynamic or Hybrid Lumbar Spine Stabilization: A Systematic Literature Review.J Spinal Disord Tech 2015 Oct;28(8):E439-48.

[15] Maserati M.B, Tormenti M.J, Panczykowski D.M, Bonfield C.M, Gerszten P.C. The use of a hybrid dynamic stabilization and fusion system in the lumbar spine: preliminary experience. Neurosurgical focus. 2010;28(6):E2.

[16] Masharawi Y, Rothschild B, Dar G, Peleg S, Robinson D, Been E, Hershkovitz I, 2004. Facet orientation in the thoracolumbar spine: three-dimensional anatomic and biomechanical analysis. Spine 29, 1755–1763.

[17] Moumene M, Geisler F.H (2007) Comparison of biomechanical function at ideal and varied surgical placement for two lumbar artificial disc implant designs: mobile-core versus fixed-core. Spine 32:1840–1851. doi:10.1097/BRS.0b013e31811ec29c

[18] Noailly J, Wilke H.J, Planell J.A, Lacroix D. 2007. How does the geometry affect the internal biomechanics of a lumbar spine bi-segment finite element model? Consequences on the validation process. J. Biomech. 40, 2414–2425.

[19] Ohshima H, Tsuji H, Hirano N, Ishihara H, Katoh Y, Yamada H. Water diffusion pathway, swelling pressure, and biomechanical properties of the intervertebral disc during compression load. Spine 1989;14:1234–44.

[20] Oktenoglu T, Erbulut D.U, Kiapour A, Ozer A.F, Lazoglu I, Kaner T, Goel V.K. Pedicle screw-based posterior dynamic stabilisation of the lumbar spine: in vitro cadaver investigation and a finite element study. Computer Methods in Biomechanics and Biomedical Engineering. 2014;:1 doi :10.1080/10255842.2014.890187

[21] Panjabi M.M, Goel V.K, Walter S.D, Schick S, 1982. Errors in the center and angle of rotation of a joint: an experimental study. J. Biomech. Eng. 104, 232–237.

[22] Panjabi M.M, Oxland T.R, Takata K, Goel V, Duranceau J, Krag, M., 1993. Articular facets of the human spine. Quantitative three-dimensional anatomy. Spine 18, 1298–1310.

[23] Panjabi M.M, Oxland T.R, Yamamoto I, Crisco J.J, 1994. Mechanical behaviour of the human lumbar and lumbosacral spine as shown by three-dimensional load–displacement curves. J Bone Joint Surg. Am.
Vol. 76, 413–424.
[24] Patwardhan A.G, et al, A Follower Load Increases the Load-Carrying Capacity of the Lumbar Spine in Compression. Spine, 24(10), 1003 (1999).
[25] Paige Little J. 2004, Finite element modeling of anular lesions in the lumbar intervertebral disc. (Doctoral Thesis).
[26] Pearcy M.J., Bogduk N., 1988. Instantaneous axes of rotation of the lumbar intervertebral joints. Spine 13, 1033–1041.
[27] Phillips F.M, Slosar P.J, Youssef J.A, Andersson G, Papatheofanis F. Lumbar spine fusion for chronic low back pain due to degenerative disc disease: a systematic review. Spine (Phila Pa 1976). 2013; 38(7):409–422. doi:10.1097/BRS.0b013e3182877f11
[28] Powell P.L, Roy R.R, Kanim P, et al. Predictability of skeletal muscle tension from architectural determinations in guinea pig hindlimbs. J Appl Physiol. 1984;57:1715–1721
[29] Prasath M, Fernando T, Robb WC, Tara F.B, Robert F.M, Hybrid dynamic stabilization: a biomechanical assessment of adjacent and supra adjacent levels of the lumbar spine Laboratory investigation, Journal of Neurosurgery: Spine ,2012. DOI: 10.3171/2012.6.SPINE111054.
[30] Qiu T.X, Teo E.C, Lee K.K, Ng, H.W., Yang, K., 2003. Validation of T10–T11 finite element model and determination of instantaneous axes of rotations in three anatomical planes. Spine 28, 2694–2699.
[31] Rahm M.D, Hall B.B. Adjacent-segment degeneration after lumbar fusion with instrumentation: a retrospective study. J Spinal Disord 1996;9:392-400.
[32] Reitman C.A, Mauro K.M, Nguyen L, Ziegler J.M, et al. Intervertebral motion between flexion and extension in asymptomatic individuals. Spine. 2004;29(24):2832–2843.
[33] Reuleaux F, 1876. The Kinematics of Machinery: Outline of a Theory of Machines. Macmillan, London.
[34] Rohlmann A, Zander T, Schmidt H, Wilke H-J, Bergmann G (2006) Analysis of the influence of disc degeneration on the mechanical behaviour of a lumbar motion segment using the finite element method. J Biomech 39:2484–2490. doi: 10.1016/j.jbiomech.2005.07.026
[35] Rolander S.D, 1966. Motion of the lumbar spine with special reference to the stabilizing effect on posterior fusion. Acta Orthop. Scand., 90–95.
[36] Rousseau M.A, Bradford D.S, Hadi T.M, Pedersen K.L, Lotz, J.C., 2006. The instant axis of rotation influences facet forces at L5/S1 during flexion/extension and lateral bending. Eur.Spine J.15, 299–307.
[37] Schmidt H, Heuer F, Drumm J, Klezl Z, Claes L, Wilke H.J. 2007a. Application of a calibration method provides more realistic results for a finite element model of a lumbar spinal segment. Clin. Biomech.
[38] Schmidt H, Heuer F., Simon U., Kettler A., Rohlmann A., Claes L. et al., Application of a new calibration method for a three-dimensional finite element model of a human lumbar annulus fibrosus, Clin. Biomech., 2006, 21, 337–344.
[39] Schneider G, Pearcy, M.J, Bogduk N, 2005. Abnormal motion in spondylolytic spondylolisthesis. Spine 30, 1159–1164.
[40] Sears W.R, Sergides I.G, Kazemi N, Smith M, White G.J, Osburg B. Incidence and prevalence of surgery at segments adjacent to a previous posterior lumbar arthrodesis. Spine J. 2011; 11(1):11–20. doi:10.1016/j.spinee.2010.09.026

[41] Sengupta D.K, Webb J.K, Mulholland R.C. Can soft stabilization in the lumbar spine unload the disc and retain mobility? A biomechanical study with fulcrum assisted soft stabilization on cadaver spine. ISSLS Annual Meeting; 2001 Jun 19-22; Edinburgh, Scotland.
[42] Sharma M, Langrana N.A, Rodríguez J.Role of ligaments and facets in lumbar spinal stability.Spine. 1995;20:887-900.
[43] Shih S.L , Liu C.L, Huang L.Y, Huang C.H, Chen C.S . Effects of cord pretension and stiffness of the Dynesys system spacer on the biomechanics of spinal decompression- a finite element study. BMC Musculoskelet Disord 2013 19;14:191. Epub 2013 Jun 19.
[44] St-Pierre G.H, Jack A, Siddiqui M.M, Henderson R.L, Nataraj A: Nonfusion does not prevent adjacent segment disease: Dynesys long-term outcomes with minimum five-year follow-up. Spine (Phila Pa 1976). 2015, 41:265-73.
[45] Xia Q.T, Tan K.W, Lee, V.S. and Teo, E.C. 2006. Investigation of thoracolumbar T12-L1 burst fracture mechanism using finite element method. Medical Engineering & Physics, 28: 656-664.
[46] Y.H Tsuang, Y.F Chiang, C.Y Hung, H.W Wei, C.H Huang, C.K Cheng. Comparison of cage application modality in posterior lumbar interbody fusion with posterior instrumentation—A finite element study. Medical Engineering & Physics 31 (2009) 565–570
[47] Zhong Z.C, Wei S.H, Wang J.P, Feng C.K, Chen C.S, Yu C.H. (2006). Finite element analysis of the lumbar spine with a new cage using a topology optimization method, Medical Engineering and Physics, 28(1), 90-98.
[48] Lee SE, Jahng TA, Kim H.J. Hybrid Surgery Combined with Dynamic Stabilization System and Fusion for the Multilevel Degenerative Disease of the Lumbosacral Spine. International Journal of Spine Surgery. 28 August 2015. Volume 9 Article 25 doi: 10.14444/2045
[49] Ou C.Y, Lee T.C, Lee T.H, Huang Y.H. Impact of body mass index on adjacent segment disease after lumbar fusion for degenerative spine disease. Neurosurgery. 2015 Apr; 76(4):396-401; discussion 401-2; quiz 402. doi: 10.1227/NEU.0000000000000627.
[50] Michael A, Andreas F.M, George T, Spiros K, Spiros G.P. Posterior Spinal Fusion Using Pedicle Screws. Orthopedics. 2013; 36(7):e951-e957. https://doi.org/10.3928/01477447-20130624-28.

Chapter 6:

Anisotropic Response of the Holzapfel's Constitutive Model for the Lumbar Spine Considering Degenerative Conditions

6.1 Introduction

The disc degeneration is characterized by changes in the morphology and biochemistry of the IVD. Adams et al [16]. These biologic changes of disc degeneration are associated with back pain and other spinal disorders, such as disc herniation, spondylolisthesis, facet arthropathy, and stenosis. FE method is able to simulate a variety of clinical situations in a more way, and has been acting a fully matching partnership based on experimental approaches for spine biomechanics research as reported. Urban et al [12]. The FE models are widely used to provide an assessment of spine with spinal instrumentation and assist in the design, development and optimization of that spinal instrumentation. Advanced to other methods, these FE models can predict the changes of stresses and strains in the IVD, vertebrae and ligaments and very comprehensive ROM data [8,19]. Our main objective is to review the most recent computational studies in the application of FE models that report the issue of research better understanding of low back pain and eventually treat the spinal disorders. Little experiments were performed on intact motion segments (Miller 1986, Lin 1978, Hirsch & Nachemson 1954) and some on FSUs without posterior elements [2, 10, 13]. In the compression load case, the data from Brown 1957 is slightly lower than the generated values and the other experimental data. Some FE models simulate the effects of degeneration. Adams et al [16], by simply removing some elements from the annulus fibrosus. Where others [18, 18, 19] disclose the influence of geometrical, mechanical, or poromechanical parameters on IVD behavior without showing change in mechanical properties of degenerated IVD. More recently, recent poroelastic finite element model of the lumbar spine developed to assess spinal response during physiological functions and behavior of degenerative disc [15, 16].

6.2 Methods and materials

A three-dimensional finite element (FE) model of the L4-5 FSU segment (Figure 6.2) was used by modifying the mechanical properties of the intervertebral disc constituents. Chazal et al [3]. All the bony structures including cortical and trabecular bone, whereas facet cartilage layers, annulus ground substance, nucleus pulposus and cartilage endplates were modeled by using solid hexahedral elements. The nucleus pulposus composed 43% of the whole volume of the disc. The symmetric FE model of the human lumbar disc is developed to investigate the optimized properties required to mimic the intact by matching model predictions to experimental results. Facet joints simulated by a cartilaginous layer extruded in Abaqus along the vectors normal to the inferior face of the superior articular process to the central of thickness of 0.4 mm were modeled to be multi-linear elastic in compression [18] by surfaces-to surface contact with softened contact in the normal direction. An initial typically gap of 0.2 mm was specified as reported by Bendoukha et al [21].

Table 6.1: Material properties used in FE Model

Part	Structure	Young's modulus E (MPa)	Poisson's ratio υ	Element type	Reference
Vertebrae	Trabecular bone	100	0.2	C3D8	[8, 14]
	Cortical bone	12,000	0.3		[8]
	Posterior element	3,500	0.25		[8, 14]
	Cartilaginous End plate	23.8	0. 4		[20]
	Facet cartilage	11	0.4		[5, 20]
	Facet contact	Nonlinear soft contact		Contact	[21,22]

Part	Structure	C_{10}	C_{20}	K1	K2	kappa	Element type	Reference
Annulus Fibrosus	Healthy	1.5715	9.2044	12.2	39.7	0.113	C3D8	[22]
	Degenerated	1	8.6	18.56	82.31	0.226		
Nucleus Pulposus	Healthy	Incompressible fluid					F3D4	[6, 19, 21]
	Degenerated	Compressible fluid						
Ligaments		Nonlinear stress-strain curve					S4R	[7, 8, 21]

The seven major ligaments, including anterior Longitudinal Ligament ALL; Posterior Longitudinal Ligament PLL; Intertransverse Ligament ITL; Ligamentum Flavum LF; Capsular Ligament CL; Supraspinous Ligament SSL; and Interspinous Ligament ISL were modeled as three dimensional, 4 node Quadrilateral elements (T3D2) and allocated were as piecewise linear functions in stress-strain relationship [7, 8] as shown in Table 6.1 This formulation allows simulation of changing ligament

characteristics with different stress at a different level as a function of stress-strain. The entire model consists of approximately 424 S4R shell elements and 33360 hexahedral elements C3D8

The intervertebral disc (IVD). The intervertebral disc was modeled using two separate structure (Figure 6.2, 6.5):

Nucleus Pulposus (NP) exhibits a gelatinous core and, therein describes the mutually coupled behavior of both solid deformation and viscoelastic characteristics of fluid flow. Eberlein et al [7]. An initial hydrostatic pressure of 0.1 MPa was prompted in the fluid filled cavity in the nucleus pulposus to simulate unloaded motion segments. Markolf et al [17]. The healthy nucleus pulposus was modeled as incompressible fluid while the degenerated nucleus was defined as compressible fluid. Hirsch et al [10]

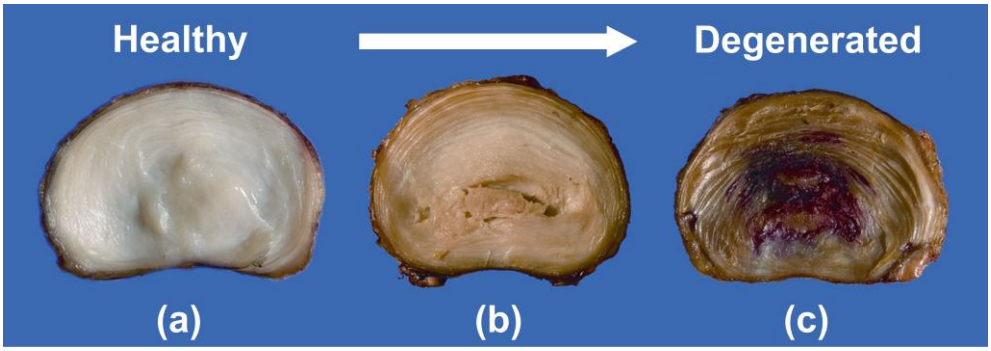

Figure 6.1: degeneration of the intervertebral disc: (a) Healthy intervertebral discs;(b) moderate degeneration; (c) severe degeneration. Illien et al [22].

The annulus fibrosus (AF) was modeled as an anisotropic continuum structure, with deformation tensor [8], and the material coefficients C_{10}, C_{20} *(Material incompressibility factor* D_1*)*, k_1, k_2 and κ were based on biaxial tension tests performed on healthy and degenerated annuli fibrosis. Heuer et al [9]. The progression of degeneration was simulated using three model variants:

$$W_{matrix} = C_{10}\,(I_1 - 3) + C_{20}\,(I_1 - 3)^2 \qquad (1)$$

$$W_{fibers} = \frac{k_1}{k_2} \sum_{\alpha=4,6} \left(e^{k_2[(1-\kappa)(I_1-3)+\kappa(I_\alpha-1)]^2} - 1\right) \qquad (2)$$

The human healthy and degenerated intervertebral disc.were modeled using three structures:

(a) Healthy intervertebral disc (grade I) defined by healthy annulus and healthy nucleus;

(b) Moderate degeneration disc (grade III) defined by healthy annulus and degenerated nucleus;

(c) Severe degeneration disc (grade IV) defined by degenerated annulus and degenerated nucleus. The grading is based on the Thompson degeneration scale Figure 6.1.

6.3 Model formulation

The algorithms proposed in the present study is implemented into Abaqus as a User Material UMAT code embedded in a Python and Intel Fortran Compiler environment to simulate the biomechanical behavior of annulus

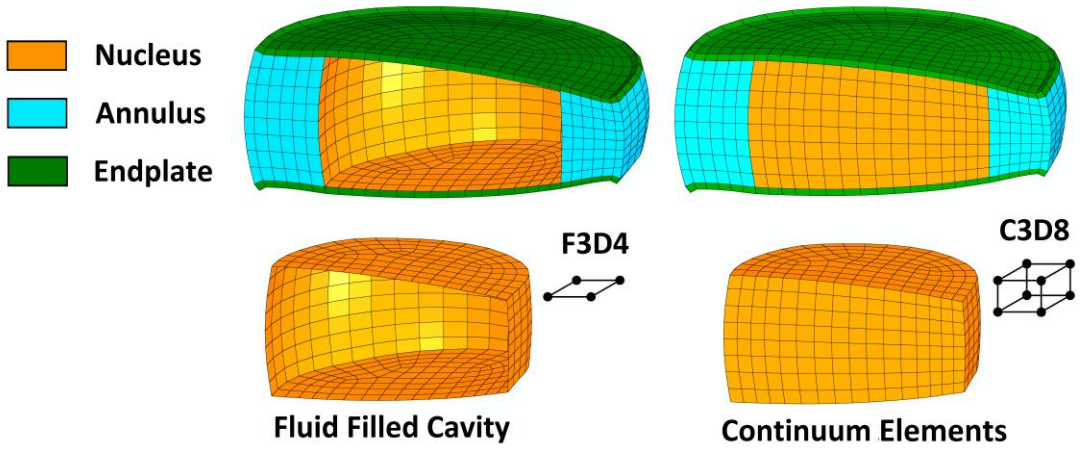

Figure 6.2: Finite Element Model formulation.

This numerical approach consists on Holzapfel's hyperelastic constitutive models of the AN and a constitutive model of the seven major Ligaments, which were implemented in Abaqus via (UMAT) subroutines (Appendix 4). The coefficients employed in all three conditions are listed in Table 6.1. While the material properties and in situ nuclear pressure were altered, osteophytes, local tears or similar macroscopic abnormalities were not modeled. Rather than attempting to simulate these defects of an independent individual and random nature, the focus was kept on the effects of measured changes in tissue mechanical behavior

6.4 Loading and Boundary Conditions

The IVD model comprises the intervertebral disc and the adjacent vertebral bodies. The lower vertebral body was rigidly fixed. Pure unconstrained axial compressive of

2000 N was applied to the upper vertebral body to the reference point which coupled all points on upper surface of the disc. The resulting stress-strain distribution at the center of the disc were estimated and the intradiscal Pressure IDP was predicted using the cavity point. Theoretically speaking, we used the concept of nucleus pulposus pressure measurement; by means of in vitro experiments on vertebra-disc-vertebra preparation whither, we found that the incompressible fluid pressure within the nucleus is directly related to the axial compression applied to the disc.

The lower portion of the L5 vertebral body and its inferior facets were rigidly fixed. The load was applied through a reference node constrained to the upper surface of the L4 vertebrae using Abaqus Coupling Constraints elements (CCE). The L4-L5 Functional Spinal Unit move in six different directions (six degrees of freedom (DOF)). A pure bending moment was incrementally increased 0, 1, 2.5, 5, 7.5, 10 Nm and applied to the model in all three planes of motion.

6.5 Results

6.5.1 ROM results.

The finite element model predicted an increase in hydrostatic stress in the middle regions of the annulus by nearly the seventh fold. The intradiscal pressure IDP is considered to be very significant component to approximate internal stress behavior of the intervertebral disc. The in vitro measurements of the nucleus pressure in human intervertebral discs have shown proportion between IDP pressure and applied Load on the superior surface motion (ROM) in all loading directions except for lateral bending comparing to experimental. The greatest changes between Healthy and Moderate and Severe models were predicted in axial rotation by 30 % and 36 %. In lateral bending, a 27% increase in ROM was predicted in the Severe scenario (with respect to the Healthy condition), while the change in the Moderate scenario was approximately 32% (Figure 6.4)

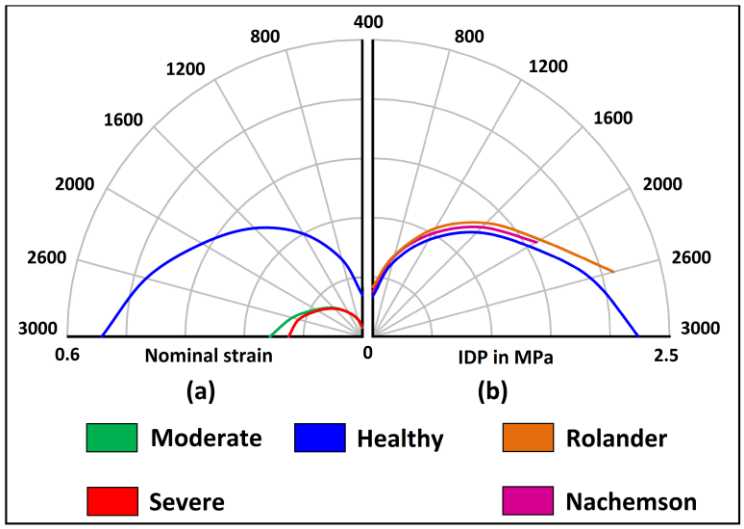

Figure 6.3: (a) Comparison of intradiscal pressure (IDP) of the Healthy model with experimental results (b) Comparison of nominal strain against the Load (N) of Healthy, Moderate and Severe models

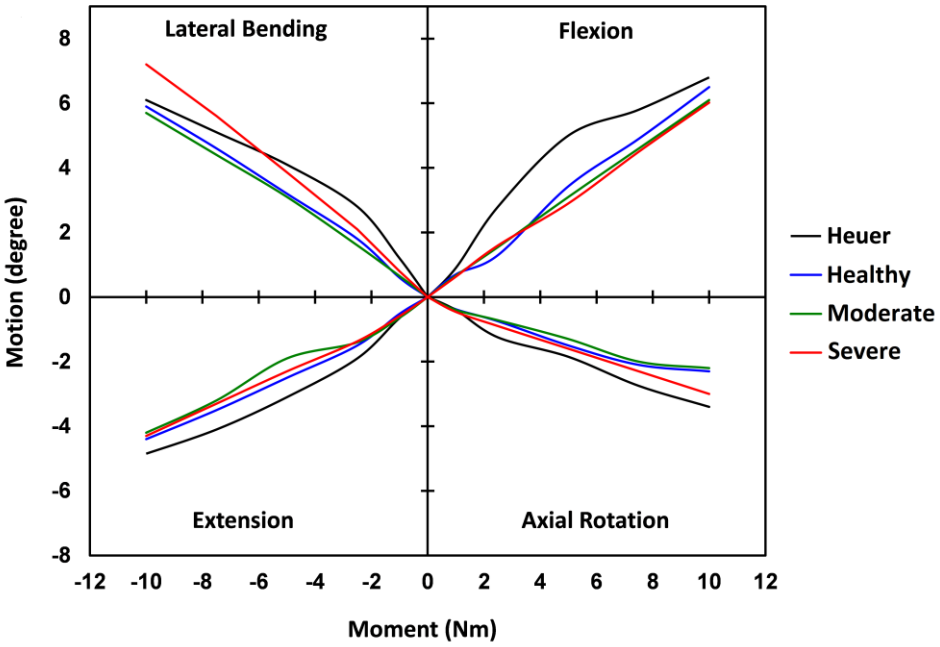

Figure 6.4: ROM of L4-5 FSU

6.5.2 Stress and strain results

The analysis of the stress results allowed us to prove the most loaded region. As a most critical region of spinal diseases, the presence of disc degeneration under physiological load steer to the alteration of the spine comportment and the pain function. The results for the body functions (Figure 6.5, 6.6) indicate that the superior values of the

stresses were situated at posterior region which reaches stress of 2.9 MPa for healthy disc and 2.4 MPa for the degenerated disc; as expected, the results highlight that the riskiest load condition corresponds to posterior side. For the degenerated nucleus the results presented in Moderate degeneration a decreased stress according to strain decreasing comparing to Healthy IVD.

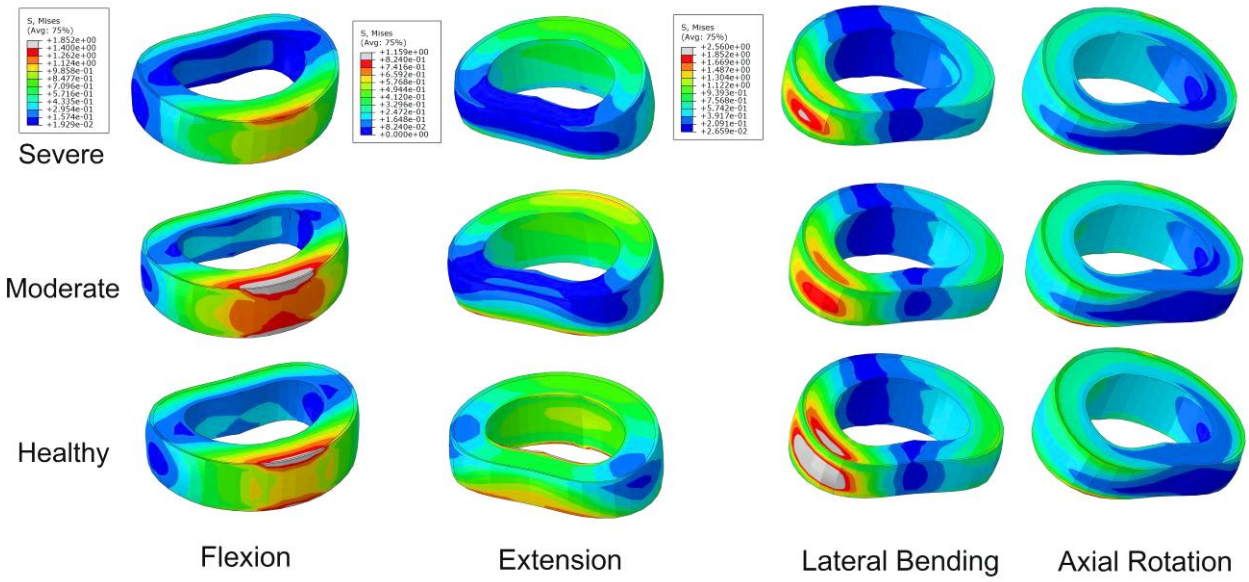

Figure 6.5: Von-Mises Stress distribution obtained from FE Models: Healthy, Moderate and Severe

Furthermore, the magnitude of stress predictions was reduced in the anterior region of the disc while they increased in the posterior region as the simulated degeneration progressed. In all cases, the highest stresses were concentrated in the posterior region of the disc in extension loading. The highest strains were concentrated in the posterolateral region of the disc in lateral bending loading as degeneration progressed (Healthy-Moderate-Severe). The compressive strain prediction in the annulus increased in anterior extremities in extension and in the posterior extremities in flexion Figure 6.6, 6.7

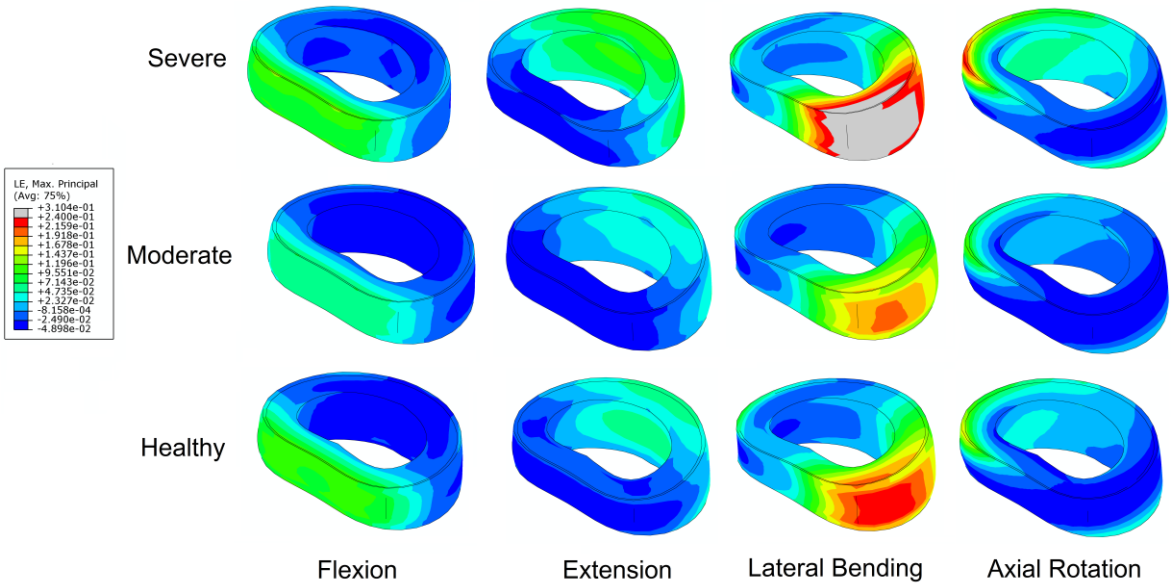

Figure 6.6: Strain magnitude distribution obtained from FE Models: Healthy, Moderate and Severe

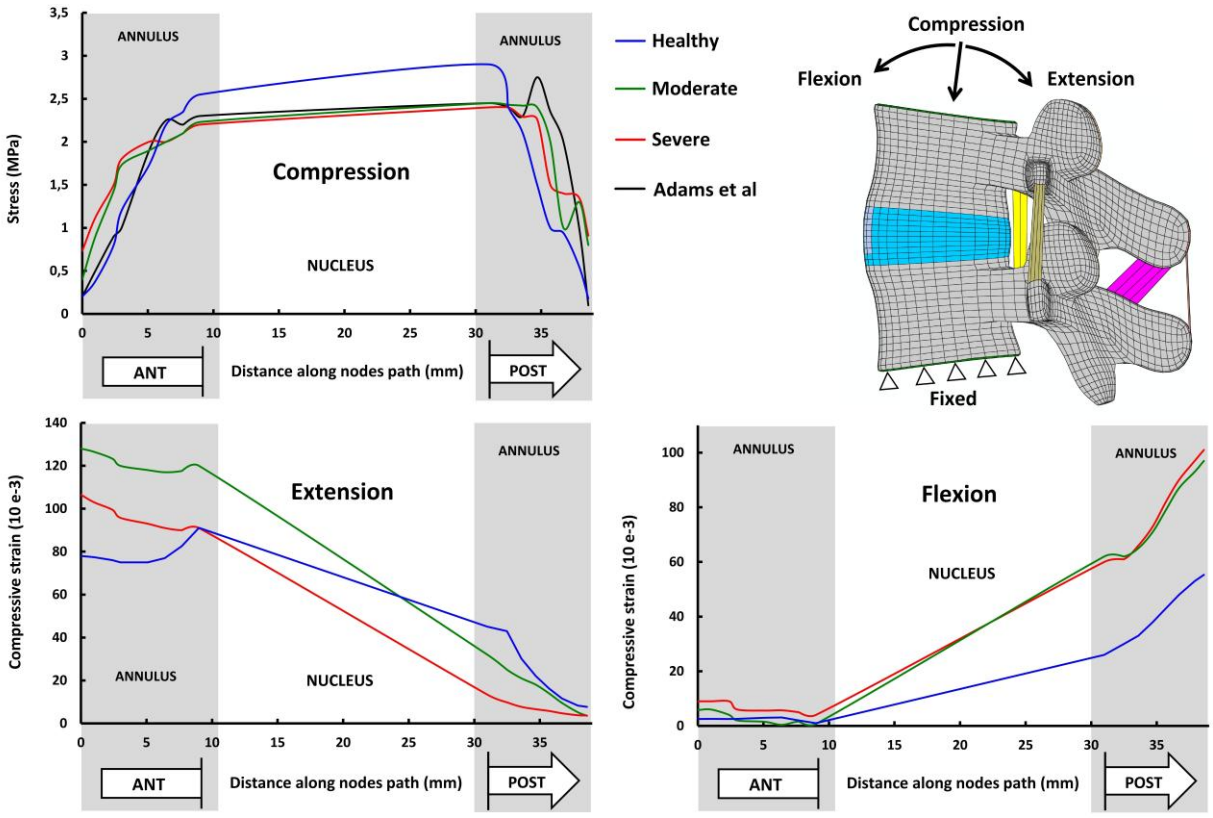

Figure 6.7: Axial stress distribution and compressive strain predictions obtained from FE Models in the mid-height plane of the IVD from posterior to anterior midline under Compression (2000N), Flexion and Extension (10 Nm).

Among all ligaments, the supraspinous ligament and capsular ligament were identified as the major load bearing tissues. The highest ligament strain was generated in lateral banding and flexion loading (Figure 6.7)

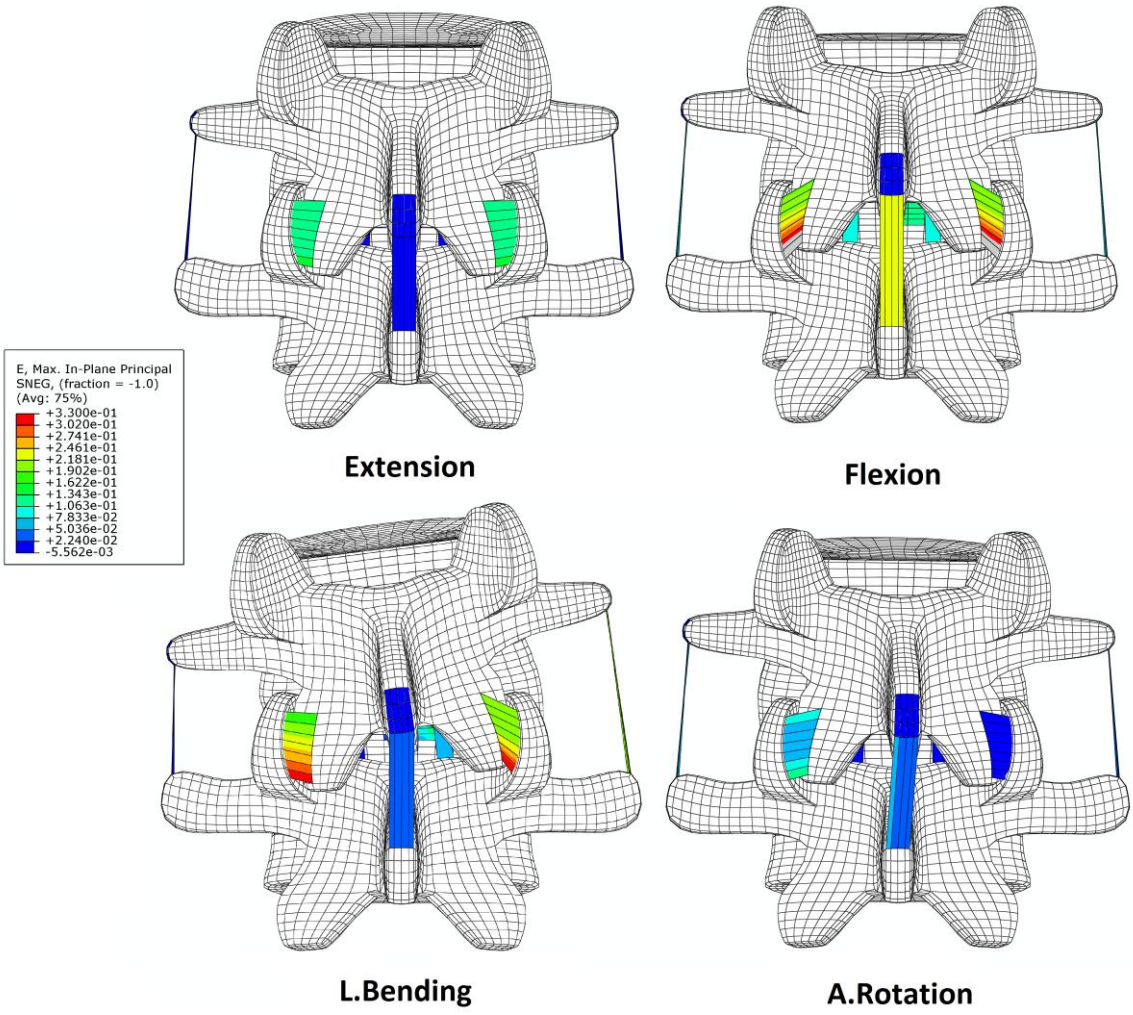

Figure 6.8: Total strain Energy predictions for the ligaments under all loading scenarios (10 Nm) for Healthy IVD.

6.6 Discussion

The aim of this work was to construct an accurate FE model to characterize the mechanical behavior of healthy and degenerated IVD. This model takes into account the IVD nature and also the clear preferential orientation of the collagen fibers in the annulus. The reduction in nonlinearity behavior with degeneration could suggest a diminished compaction effect of the degenerate tissues at large deformations which could be related to structural changes in annulus. The obtained results are also in agreement with the experimental behavior [9, 18]. Experimental results, in fact, showed an increase of the elastic modulus in the toe part, thus there is a big role of fibers therefore when the fibers

act there is no additional stiffening. In this analysis it has been obtained that the degeneration of one FSU affects the biomechanics of this FSU; in particular an increase of the ROM in extension, partial decrease in flexion and lateral bending has been noticed.

6.7 Conclusions

In conclusion, the developed FE model is capable of generating the mechanical behavior of normal and degenerated NP tissue with a favorable approximation. But on the degeneration of the other segments is a very complex procedure which should be identified in the degeneration of the AF tissue with accurate mechanical properties. Furthermore, the current work provides a qualitative analysis of the influence of single level disc degeneration on the mechanics of the segments under flexion/extension, lateral bending and axial rotation moments. It has been seen that degeneration modified the degree of motion and loading of the degenerated level. These changes could increase the risk of progression of degeneration to the nearest segments of the spine. The results obtained with the FE model seem to be in good agreement with in-vitro data as showed in Figures 6.2, 6.3, 6.4. Additionally, nonlinear analytical functions used in the IVD ligaments facet joint may be used as input data to perform more accurate computational simulations of the full lumbosacral spine.

References

[1] Berkeston M, Schultz A.B. Mechanical properties of human lumbar spine motion segments: II. Response in compression and shear; influence of gross morphology. J Biomech Eng 1979; 101:53–7.

[2] Brown T, Hansen R.J, Yorra A.J. Some mechanical tests on the lumbosacral spine with particular reference to intervertebral discs; a preliminary report. J Bone Joint Surg Am 1957, 39:1135–1164.

[3] Chazal J, Tanguy A, Bourges M, Gaurel G, Escande G, Guillot M, "Biomechanical properties of spinal ligaments and a histological study of the supraspinal ligament in traction,"J Biomech 18, 167-176, 1985.

[4] Chen S.H, Chiang M.C, Lin J.F, Lin S.C, Hung C.H. "Biomechanical comparison of three stand-alone lumbar cages--a three-dimensional finite element analysis. BMC Musculoskelet Disord. 1186/1471-2474-14-281,2013.

[5] Denoziere, G., Ku, D.N. (2006). Biomechanical comparison between fusion of two vertebrae and implantation of an artificial intervertebral disc, Journal of Biomechanics, 39(4), 766-775.

[6] Dreischarf M, Zander T, Shirazi-Adl A, Puttlitz C, Adam C, Chen C, Goel V, Kiapour A, Kim Y, Labus K et al. "Comparison of eight published static finite element models of the intact lumbar spine: Predictive power of models improves when combined together,"Journal of biomechanics, vol.47, no. 8, pp. 1757–1766, 2014.

[7] Eberlein R, Holzapfel G.A, Schulze-Bauer C.A.J. An anisotropic model for annulus tissue and

enhanced finite element analyses of intact lumbar disc bodies. Computer Methods in Biomechanics and Biomedical Engineering 2001;4(3):209–29
[8] Goel V.K, Monroe B.T, Gilbertson L.G., Brinckmann P. (1995a). Interlaminar shear stresses and laminae separation in the disc. Finite element analysis of the L3-L4 motion segment subjected to axial compressive loads. Spine, 20(6), 689-698.
[9] Heuer F, Schmidt H, Klezl Z, Claes L, Wilke H.J. Stepwise reduction of functional spinal structures increase range of motion and change lordosis angle", J Biomech 40, 271- 280, 2007
[10] Hirsch C, Nachemson A, 1954. New Observations on the mechanical behavior of lumbar discs. 610 Acta Orthopaedica Scandinavica 23 (4), 254–283.
[11] Stokes I.A, Iatridis J.C. "Mechanical conditions that accelerate intervertebral disc degeneration: overload versus immobilization," Spine, vol.29, no.23, pp.2724–2732, 2004.
[12] Urban J.P, Maroudas A, Bayliss M.T, Dillon J, "Swelling pressures of proteoglycans at the concentrations found in cartilaginous tissues," Biorheology, vol.16, no.6, pp.447–464,1979.
[13] Lin H.S, Liu, Y.K, Adams, K.H, 1978. Mechanical response of the lumbar intervertebral joint 627 under physiological (complex) loading. The
Journal of Bone and Joint Surgery 60A (1), 41-55.
[14] Lu Y.M, Hutton W.C, Gharpuray V.M: Do bending, twisting, and diurnal fluid changes in the disc affect the propensity to prolapse? A viscoelastic finite element model. Spine Nov 1996, 21(22):2570–2579.
[15] Luoma K, Riihimaki H, Luukkonen R. et al. (2000). Low Back Pain in Relation to Lumbar Disc Degeneration. Spine, Vol. 25, No. 4, pp. 487-492
[16] Adams M.A and Roughley P.J, "What is intervertebral disc degeneration, and what causes it?" Spine, vol.31, no.18, pp. 2151–2161, 2006.
[17] Markolf K. L, Deformation of the thoracolumbar intervertebral joints in response to external loads. J. Bone Joint Surg. 54-A: 511–533, 1972
[18] Miller J.A, Schultz A.B, Warwick D.N, Spencer D.L. 1986. Mechanical properties of 642 lumbar spine motion segments under large loads. Journal of Biomechanics 19 (1), 79-84.
[19] Natarajan R.N, Andersson G.B. The influence of lumbar disc height and cross-sectional area on the mechanical response of the disc to physiologic loading. Spine 1999; 24:1873–81.
[20] Rohlmann A, Zander T, Schmidt H, Wilke H-J, Bergmann G (2006) Analysis of the influence of disc degeneration on the mechanical behavior of a lumbar motion segment using the finite element method. J Biomech 39:2484–2490. doi: 10.1016/j.jbiomech.2005.07.026 Fluid
[21] Bendoukha M, Mosbah M. Biomechanical Evaluation of Lumbosacral Segments Response under Physiological Functions: Finite Element Analysis
Építőanyag – Journal of Silicate Based and Composite Materials, Vol. 69, No. 3 (2017), 122–126. p. https://doi.org/10.14382/epitoanyag-jsbcm.2017.21
[22] Illien-Jünger S, Walter B.A, Mayer J.E, Hecht A.C, Iatridis J.C. (2014) Intervertebral Disc Culture Models and Their Applications to Study Pathogenesis and Repair. In: Shapiro I., Risbud M. (eds) The Intervertebral Disc. Springer, Vienna. https://doi.org/10.1007/978-3-7091-1535-0_22

Conclusions

The biomechanical behavior of the intervertebral disc and lumbar spinal segments were investigated in this study. The employed methodology was primarily based on finite element modeling of the human lumbosacral spine (L1-S1) with the simulation of single-level disc degeneration and multi-level posterior pedicle-based stabilization, in order to assess the acute biomechanical effects of surgical treatment.

All the chapters indicate that the annulus fibrosus is of critical importance in the functioning of lumbar spinal segments in their healthy, diseased and treated conditions. Furthermore, its significance is largely due to the presence of the highly organized collagen fiber network embedded in its ground substance. Specifically, the kinematic and mechanical data (local energy and stress and strain predictions in particular) presented in Chapters 4 - 6 support our initial hypothesis by demonstrating critical changes in the load-sharing mechanism within the intervertebral disc. According to our finite element studies, it appears that the stiffness of the fused segment is increased with posterior instrumentation, and a longer segment fusion, and all influence the adjacent segment adversely. As expected, the rigid fusion increased the toughness but reducing the stiffness of the bony structure. However, without the additional stiffness from the rigid instrumentation, it may reduce the adverse influence to the adjacent segment. Most clinical studies show a beneficial effect of instrumentation to achieve fusion by stabilizing the segment, but as reported in this dissertation, the rigid instrumentation continues to exert unwanted stiffness to the fusion mass. One option to alleviate this continued adverse effect by using hybrid fixation so that the implants lose their rigidity once fusion has been achieved. The other option may be to use softer or namely flexible implants.

In chapter3, the results predicted for the pure-moment or hybrid (moment + follower load) loading scenarios were in good agreement with in vivo and in vivo kinematic measurements during the validation process of the FE Model; however more complex loading cases that incorporate lumbar muscular activity would yield valuable data in the assessment of implants performance. These efforts should be part of future stabilization

systems modeling work.

In chapter 4, the proposed (DTO + PEEK) design has the potential to address posterior joint degeneration which is the main contradiction of available arthroplasty. Moreover, this new design broadens the indications for disc replacement to low back pain patient's due posterior joint degeneration, like spinal stenosis.

Further biomechanical studies were done on components of the posterior dynamic stabilization system (PDS) to find a proper configuration for standalone PDS for application in treatment of lumbar spine disorders like stenosis and spondylolisthesis. The proposed flexible configurations were able to provide the spinal segment with a constrained range of motion and stability while maintaining lower stresses at pedicle screws compared to traditional rigid fixator. Unlike some available semi-rigid stabilization constructs, the flexible devices were shown to have more restricted flexibility in axial plane while preserving a favorable kinematics in other planes of motions.

Hybrid surgery dynamic topping of fusion DTO and PEEK construct is also considered as a treatment option within the aforementioned finite element framework. The model predictions indicated that single and two- level stabilization system preserve motion at the treated levels, while linearizing the kinematic response and increasing the facet force transmission at the adjacent level. The data reflect that the successful surgical outcome is most likely obtained when maximum preservation using hybrid surgery. The flexible instrumentation was associated with a reduction in compressive stresses compared to the fusion construct in the adjacent-level disc and showed high substantial axial force in the implant while fusion instrumentation increased the motion for both flexion and extension.

In chapter 5, There was a posterior shift of the COR with Flexible devices, a posterior tilt with PEEK system, and an anterior tilt with Dynesys and very similar to intact for the NFlex This study shows how the non-fusion devices can alter the quality of the intervertebral motion, which may be an important determinant of any stress to the device–bone junction or within the device itself, which may predict the fatigue failure, which is one of the worst concerns for long-term survival of all non-fusion devices

In chapter 4, the simulations showed that the flexible device would be strong enough to

support fusion, yet they are much softer than the conventional stainless steel and titanium rods used for posterior instrumentation. It may therefore be reasonable to expect that these flexible stabilization devices may be more effective in achieving more biological fusion mass, which may be softer yet tough to hold the motion segment stabilized without adding unwanted stiffness to the fusion mass. In order to validate clinical Evidence for a Softer Implant, our study assessed the efficacy of semirigid fixation with circumferential fusion to achieve fusion without the stress-shielding effect of rigid fixation. Although the Dynesys Dynamic Stabilization System DTO, NFlex, Viper PEEK system have been the most frequently used dynamic stabilization device approved by the FDA as a fusion device. There are as yet no reports as to their influence on the incidence of ASD.

Finally, Chapter 6 outlined the behavior conducted on healthy and degenerated annulus fibrosus tissue. Degenerative changes increased the mobility of the motion segment in all loading scenarios except for lateral bending. The kinematic and biomechanical changes were greatest in extension loading, and these findings mirror the common clinical findings of herniation and annular failure.

Most clinical studies indicate that rigid instrumentation facilitates fusion in a manner similar to fracture stabilization. Because length of fusion is a contributing factor, the need for dynamic stabilization becomes more crucial in multisegment degenerative disease requiring fusion. At the caudal end of fusion, it may be reasonable to use rigid instrumentation, with interbody fusion when indicated, to restore lordosis and sagittal alignment, which is another contributing factor causing adjacent segment disease. The most beneficial internal fixation would therefore constitute a rigid stabilization with or without an interbody cage at the caudal segments, and a dynamic stabilization at the cranial one or two segments, to prevent ASD. Because preexisting disc degeneration in the adjacent segment is another contributing factor, these cases are a stronger indication of dynamic stabilization at the cranial end of fusion segments.

The length of the spacer causes distraction and defines the unloading of the facet joint, whereas an active lordosis, produced at the junction cylinder and the screw head, ensures unloading of the disc. The third design perspective is the use of regular top-loading pedicle screws, which makes it easy to combine fusion at an adjacent segment.

The conventional fusion allows additional stiffness and stresses which causes ASD. The rationale of dynamic stabilization is that it may offer adequate stabilization to achieve fusion but may not have a stress-shielding effect and therefore may not contribute to ASD. The length of fusion is a factor causing ASD, the new technology needs dynamic stabilization at the cranial segment more than single-segment fusion. The caudal segment may still need conventional rigid instrumentation to achieve lordosis of the segment. Our investigation supports the view that a softer fusion may avoid ASD, and also that semi-rigid fixation devices may achieve a better fusion mass. The third-generation dynamic stabilization devices (Transitional) may better serve the purpose of soft fusion.

While the results reported and parameters evaluated in this dissertation work are encouraging for the continued utilization of flexible stabilization constructs in the treatment of spinal disorders, further investigations are warranted. These preservation systems was found to be able to preserve the normal kinematics at index and adjacent segments of spine, and preserved the regular quality of motion by having extension-to-flexion center of rotation close to that of intact.

Outlook

Our model is semi-manually generated using a very tiresome procedure. The Computer technology has improved tremendously, a future model could rely on MRI data in which soft tissues are better differentiated. More importantly, the next model should account more accurate properties. This model is expected to predict more realistic behavior.

Such generated FE models will be able to facilitate the prediction of the outcome of patient postoperative surgery. A future study that concentrates more on the aspect of a realistic patient-specific finite element model, would need further improvements of constitutive models. An improvement of the FE model of the FSU requires, a better understanding which parameter have an influence on the predictions of the model.

Currently, Patient-specific models occupy great potential in the field of orthopedics. These models could be created and positioned in a central database system. Then the surgeon would examine them and recommend certain implants for the patients. Similarly, for the case of flexible stabilization alone, it is recommended to repeat the biomechanical studies with a model with slightly-moderate-severe degenerated disc.

Appendix

A. Mooney Rivlin Material Properties UMAT

```
C-----------------------------------------------------------------------
      PARAMETER(ZERO=0.D0, ONE=1.D0, TWO=2.D0, THREE=3.D0,
1 FOUR=4.D0,SIX=6 .D0)
C -----------------------------------------------------------------------
C        UMAT FOR COMPRESSIBLE MOONEY RIVLIN HYPERELASTICITY
C               USED FOR L1/S1 FE MODEL VALIDATION
C -----------------------------------------------------------------------
C PROPS(1) - EMOD
C PROPS(2) - ENU
C -----------------------------------------------------------------------
C  ELASTIC PROPERTIES
C-----------------------------------------------------------------------
EMOD=PROPS(1)
ENU=PROPS(2)
C10=EMOD/(FOUR*(ONE+ENU))
C01=ONE/(FOUR*C10)
D1=SIX*(ONE-TWO*ENU)/EMOD
EBULK =TWO/D1
C-----------------------------------------------------------------------
REAL EMOD, ENU, C10, C01, D1
C-----------------------------------------------------------------------
C  SPECIFY MATERIAL PROPERTIES
C-----------------------------------------------------------------------
EMOD=4.2
ENU=0.45
C10=0.56
C01=0.14
D1 =14.285e-2
EBULK =14
C -----------------------------------------------------------------------
```

B. Mooney Rivlin Model UHYPEROUTINE (uhyperoutine.for)

```
C ------------------------------------------------------------------- C
|              8-----------7     8-Noded Hybrid Hexahedral Element     |
|             /|          /|               -O- C3D8H -O-               |
|            / |         / |      zeta                                 |
|           5-----------6  |       |   eta                             |
|           |  |        |  |       |   /                               |
|           |  |        |  |       |  /                                |
|           |  4--------|--3       | /                                 |
|           | /         | /        |/                                  |
|           |/          |/         O--------- xi                       |
|           1-----------2      origin at cube center                   |
C ------------------------------------------------------------------- C
| MESBAH Moustafa. PhD                                                |
| Faculty of Sciences and Technology FST                              |
| University Abd El Hamid Ibn Badis. Mostaganem                       |
| Laboratory of Numerical and Experimental Modeling of Mechanical     |
```

```
| Phenomena LMNEPM                                                    |
C --------------------------------------------------------------------- C

       SUBROUTINE UHYPER(BI1,BI2,AJ,U,UI1,UI2,UI3,TEMP,
      1 NOEL, CMNAME,INCMPFLAG,NUMSTATEV,STATEV,NUMFIELDV,
      2 FIELDV,FIELDVINC,NUMPROPS,PROPS)

       DIMENSION UI1(3),UI2(6),UI3(6),STATEV(*),FIELDV(*),
      1 FIELDVINC(*),PROPS(*)

C
      INCLUDE 'ABA_PARAM.INC'
C
      CHARACTER*80 CMNAME
C
      PARAMETER (ZERO=0.0D0,ONE=1.0D0, TWO=2.0D0, THREE=3.0D0)
C
C ---------------------------------------------------------------------
|           UMAT FOR COMPRESSIBLE MOONEY-RIVLIN MODEL
|                HYBRID ELEMENTS SHOULD BE USED
|             W = C10(I-3)+C01(I-3)+((J-1)**2)/D1
C ---------------------------------------------------------------------
C ELASTIC PROPERTIES
C ---------------------------------------------------------------------

     C10= PROPS(1)
     C01= PROPS(2)
     D1= PROPS(3)

C
     U=C10*(BI1-THREE)+C01*(BI2-THREE) + ((AJ-ONE)**2)/D1
     UI1(1)=C10
     UI1(2)=C01
     UI1(3)=TWO*(AJ-ONE)/D1
     UI2(1)=ZERO
     UI2(2)=ZERO
     UI2(3)=TWO/D1
     UI2(4)=ZERO
     UI2(5)=ZERO
     UI2(6)=ZERO
     UI3(1)=ZERO
     UI3(2)=ZERO
     UI3(3)=ZERO
     UI3(4)=ZERO
     UI3(5)=ZERO
     UI3(6)=ZERO
     RETURN
     END
```

C. Mooney Rivlin Model UMAT (Morimodel.for)

```
       SUBROUTINE UMAT(STRESS,STATEV,DDSDDE,SSE,SPD,SCD,
      1 RPL,DDSDDT,DRPLDE,DRPLDT,
      2 STRAN,DSTRAN,TIME,DTIME,TEMP,DTEMP,PREDEF,DPRED,CMNAME,
      3 NDI,NSHR,NTENS,NSTATEV,PROPS,NPROPS,COORDS,DROT,PNEWDT,
      4 CELENT,DFGRD0,DFGRD1,NOEL,NPT,LAYER,KSPT,KSTEP,KINC)
```

```
C
C        INCLUDE 'ABA_PARAM.INC'
C
      CHARACTER*8 CMNAME
      DIMENSION STRESS(NTENS),STATEV(NSTATEV),
     1 DDSDDE(NTENS,NTENS),DDSDDT(NTENS),DRPLDE(NTENS),
     2 STRAN(NTENS),DSTRAN(NTENS),TIME(2),PREDEF(1),DPRED(1),
     3 PROPS(NPROPS),COORDS(3),DROT(3,3),DFGRD0(3,3),DFGRD1(3,3),
     4 Et(3),Stress_Max(3,3),EkEk(1),DFGRDM1_INV(3,3),En(3),
     5 TEMP(1),DTEMP(1),DFGRDP(3),DFGRDM1(3, 3),DFGRDM0(3, 3),
     6 CBAR(3,3),DDSDDE_Max(6,6) C
C
C    LOCAL ARRAYS
C ----------------------------------------------------------------
C    BBAR   - DEVIATORIC RIGHT CAUCHY-GREEN TENSOR
C    DISTGR - DEVIATORIC DEFORMATION GRADIENT (DISTORTION TENSOR)
C ----------------------------------------------------------------
C
      DIMENSION BBAR(6),DISTGR(3,3),BBARBBAR(6)
C
      PARAMETER(ZERO=0.D0, ONE=1.D0, TWO=2.D0, THREE=3.D0, FOUR=4.D0,
     1          FIVE=5.D0, SIX=6.D0, SEVEN=7.D0, EIGHT=8.D0)
C


C-----------------------------------------------------------------
|           UMAT FOR COMPRESSIBLE MOONEY-RIVLIN MODEL
|                HYBRID ELEMENTS SHOULD BE USED
|              W = C10(I-3)+C01(I-3)+((J-1)**2)/D1
C ----------------------------------------------------------------
C    PROPS(1) - C10      C1
C    PROPS(2) - C01      C2
C    PROPS(3) - D1       Bulk modulus
C    PROPS(4) - E1       E-field in X direction
C    PROPS(5) - E2       E-field in Y direction
C    PROPS(6) - E3       E-field in Z direction
C ----------------------------------------------------------------

C   Read Material PROPERTIES
C
      C10=PROPS(1)
      C01=PROPS(2)
      D1 =PROPS(3)
C
C    JACOBIAN AND DISTORTION TENSOR
C
      DET=DFGRD1(1, 1)*DFGRD1(2, 2)*DFGRD1(3, 3)
     1         -DFGRD1(1, 2)*DFGRD1(2, 1)*DFGRD1(3, 3)
      IF(NSHR.EQ.3) THEN
        DET=DET+DFGRD1(1, 2)*DFGRD1(2, 3)*DFGRD1(3, 1)
     1         +DFGRD1(1, 3)*DFGRD1(3, 2)*DFGRD1(2, 1)
     2         -DFGRD1(1, 3)*DFGRD1(3, 1)*DFGRD1(2, 2)
     3         -DFGRD1(2, 3)*DFGRD1(3, 2)*DFGRD1(1, 1)
      END IF
      SCALE=DET**(-ONE/THREE)
        DO K1=1, 3
          DO K2=1, 3
      DISTGR(K2, K1)=SCALE*DFGRD1(K2, K1)
```

```
          END DO
        END DO
C
C     CALCULATE LEFT CAUCHY-GREEN TENSOR (B=F.Ft)
C
       BBAR(1)=DISTGR(1, 1)**2+DISTGR(1, 2)**2+DISTGR(1, 3)**2
       BBAR(2)=DISTGR(2, 1)**2+DISTGR(2, 2)**2+DISTGR(2, 3)**2
       BBAR(3)=DISTGR(3, 3)**2+DISTGR(3, 1)**2+DISTGR(3, 2)**2
       BBAR(4)=DISTGR(1, 1)*DISTGR(2, 1)+DISTGR(1, 2)*DISTGR(2, 2)
      1         +DISTGR(1, 3)*DISTGR(2, 3)
       IF(NSHR.EQ.3) THEN
         BBAR(5)=DISTGR(1, 1)*DISTGR(3, 1)+DISTGR(1, 2)*DISTGR(3, 2)
      1         +DISTGR(1, 3)*DISTGR(3, 3)
         BBAR(6)=DISTGR(2, 1)*DISTGR(3, 1)+DISTGR(2, 2)*DISTGR(3, 2)
      1         +DISTGR(2, 3)*DISTGR(3, 3)
       END IF
C
C     CALCULATAE (B.Bt)
C
       BBARBBAR(1)=BBAR(1)*BBAR(1)+BBAR(4)*BBAR(4)+BBAR(5)*BBAR(5)
       BBARBBAR(2)=BBAR(4)*BBAR(4)+BBAR(2)*BBAR(2)+BBAR(6)*BBAR(6)
       BBARBBAR(3)=BBAR(5)*BBAR(5)+BBAR(6)*BBAR(6)+BBAR(3)*BBAR(3)
       BBARBBAR(4)=BBAR(1)*BBAR(4)+BBAR(4)*BBAR(2)+BBAR(5)*BBAR(6)
       BBARBBAR(5)=BBAR(1)*BBAR(5)+BBAR(4)*BBAR(6)+BBAR(5)*BBAR(3)
       BBARBBAR(6)=BBAR(4)*BBAR(5)+BBAR(2)*BBAR(6)+BBAR(6)*BBAR(3)
C
C     CALCULATE THE STRESS
C
       TRBBAR=(BBAR(1)+BBAR(2)+BBAR(3))
       TRBBAR1=(BBAR(1)+BBAR(2)+BBAR(3))/THREE
       TRBBAR2=(BBAR(1)**2+BBAR(2)**2+BBAR(3)**2)/THREE
       TRBBARBBAR=(BBARBBAR(1)+BBARBBAR(2)+BBARBBAR(3))/THREE
       EG1=TWO*C10/DET
       EG2=TWO*C01/DET
       EK=TWO/D1*(TWO*DET-ONE)
       PR=TWO/D1*(DET-ONE)
       DO K1=1,NDI
         STRESS(K1)=EG1*(BBAR(K1)-TRBBAR1)+PR
      1         +EG2*(TRBBAR*BBAR(K1)-TRBBAR2-BBARBBAR(K1)
      2         +TRBBARBBAR)
       END DO

       DO K1=NDI+1,NDI+NSHR
         STRESS(K1)=EG1*BBAR(K1)
      1         +EG2*(TRBBAR*BBAR(K1)-BBARBBAR(K1))
       END DO
C
      STRESS(NTENS+2)=EK
      STRESS(NTENS+3)=ZERO

C
C     CALCULATE THE STIFFNESS
C
       EG23=EG1*TWO/THREE
       EG24=EG2*TWO/THREE

       DDSDDE(1, 1)= EG23*(BBAR(1)+TRBBAR1)+EK
      1         +EG24*(-(BBAR(1)*(3*BBAR(1)+5*(BBAR(2)+BBAR(3))))/2
```

```
2          +BBAR(4)**2+BBAR(5)**2))
 DDSDDE(2, 2)= EG23*(BBAR(2)+TRBBAR1)+EK
1          +EG24*(-(BBAR(2)*(5*BBAR(1)+3*BBAR(2)+5*BBAR(3)))/2
2          +BBAR(4)**2+BBAR(6)**2)
 DDSDDE(3, 3)= EG23*(BBAR(3)+TRBBAR1)+EK
1          +EG24*(-(BBAR(3)*(5*(BBAR(1)+BBAR(2))+3*BBAR(3)))/2
2          +BBAR(5)**2+BBAR(6)**2)
 DDSDDE(1, 2)=-EG23*(BBAR(1)+BBAR(2)-TRBBAR1)+EK
1          +EG24*((3*(2*BBAR(1)*BBAR(2)-(4*(BBAR(1)+BBAR(2))
2          *(BBAR(1)+BBAR(2)+BBAR(3)))/3-2*BBAR(4)**2))/2)
 DDSDDE(1, 3)=-EG23*(BBAR(1)+BBAR(3)-TRBBAR1)+EK
1          +EG24*((3*(2*BBAR(1)*BBAR(3)-(4*(BBAR(1)+BBAR(3))
2          *(BBAR(1)+BBAR(2)+BBAR(3)))/3-2*BBAR(5)**2))/2)
 DDSDDE(2, 3)=-EG23*(BBAR(2)+BBAR(3)-TRBBAR1)+EK
1          +EG24*((3*(2*BBAR(2)*BBAR(3)-(4*(BBAR(2)+BBAR(3))
2          *(BBAR(1)+BBAR(2)+BBAR(3)))/3-2*BBAR(6)**2))/2)
 DDSDDE(1, 4)= EG23*BBAR(4)/TWO
1          +EG24*(-((3*(BBAR(1)+BBAR(2))+5*BBAR(3))*BBAR(4))/4
2          +(BBAR(5)*BBAR(6))/2)
 DDSDDE(2, 4)= EG23*BBAR(4)/TWO
1          +EG24*(-((3*(BBAR(1)+BBAR(2))+5*BBAR(3))*BBAR(4))/4
2          +(BBAR(5)*BBAR(6))/2)
 DDSDDE(3, 4)=-EG23*BBAR(4)
1          +EG24*((-2*(BBAR(1)+BBAR(2))+BBAR(3))*BBAR(4)
2          -3*BBAR(5)*BBAR(6))
 DDSDDE(4, 4)= EG1*(BBAR(1)+BBAR(2))
1          +EG24*((13*BBAR(1)**2-6*BBAR(1)*BBAR(2)+13*BBAR(2)**2
2          +3*(BBAR(1)+BBAR(2))*BBAR(3)+2*(16*BBAR(4)**2
3        +5*(BBAR(5)**2+BBAR(6)**2)))/8)
IF(NSHR.EQ.3) THEN
 DDSDDE(1, 5)= EG23*BBAR(5)/TWO
1          +EG24*(-((3*BBAR(1)+5*BBAR(2)+3*BBAR(3))*BBAR(5))/4
2          +(BBAR(4)*BBAR(6))/2)
 DDSDDE(2, 5)=-EG23*BBAR(5)
1          +EG24*((-2*BBAR(1)+BBAR(2)-2*BBAR(3))*BBAR(5)
2          -3*BBAR(4)*BBAR(6))
 DDSDDE(3, 5)= EG23*BBAR(5)/TWO
1          +EG24*(-((3*BBAR(1)+5*BBAR(2)+3*BBAR(3))*BBAR(5))/4
2          +(BBAR(4)*BBAR(6))/2)
 DDSDDE(1, 6)=-EG23*BBAR(6)
1          +EG24*(-3*BBAR(4)*BBAR(5)+(BBAR(1)-2*(BBAR(2)
2          +BBAR(3)))*BBAR(6))
 DDSDDE(2, 6)= EG23*BBAR(6)/TWO
1          +EG24*((2*BBAR(4)*BBAR(5)-(5*BBAR(1)+3*(BBAR(2)
2          +BBAR(3)))*BBAR(6))/4)
 DDSDDE(3, 6)= EG23*BBAR(6)/TWO
1          +EG24*((2*BBAR(4)*BBAR(5)-(5*BBAR(1)+3*(BBAR(2)
2          +BBAR(3)))*BBAR(6))/4)
 DDSDDE(5, 5)= EG1*(BBAR(1)+BBAR(3))/TWO
1          +EG24*((13*BBAR(1)**2+3*BBAR(1)*(BBAR(2)-2*BBAR(3))
2          +3*BBAR(2)*BBAR(3)+13*BBAR(3)**2+10*BBAR(4)**2
3          +32*BBAR(5)**2+10*BBAR(6)**2)/8)
 DDSDDE(6, 6)= EG1*(BBAR(2)+BBAR(3))/TWO
1          +EG24*((13*BBAR(2)**2-6*BBAR(2)*BBAR(3)
2          +13*BBAR(3)**2+3*BBAR(1)*(BBAR(2)+BBAR(3))
3          +10*(BBAR(4)**2+BBAR(5)**2)+32*BBAR(6)**2)/8)
 DDSDDE(4,5)= EG1*BBAR(6)/TWO
1          +EG24*((22*BBAR(4)*BBAR(5)+(-9*BBAR(1)+13*(BBAR(2)
```

```
     2          +BBAR(3)))*BBAR(6))/8)
               DDSDDE(4,6)= EG1*BBAR(5)/TWO
     1          +EG24*((-3*(BBAR(1)+3*BBAR(2)+BBAR(3))*BBAR(5))/8
     2          +(3*BBAR(4)*BBAR(6))/4)
      DDSDDE(5,6)= EG1*BBAR(4)/TWO
     1          +EG24*(((13*(BBAR(1)+BBAR(2))-9*BBAR(3))*BBAR(4)
     2          +22*BBAR(5)*BBAR(6))/8)
    END IF
     DO K1=1, NTENS
       DO K2=1, K1-1
     DDSDDE(K1, K2)=DDSDDE(K2, K1)
       END DO
     END DO
C
C     Calculate the inverse of deformation gradient
C
      DFGRDM1_INV(1,1)=DFGRD1(2,2)*DFGRD1(3,3)
     1          -DFGRD1(2,3)*DFGRD1(3,2) DFGRDM1_INV(1,2)=-
     DFGRD1(1,2)*DFGRD1(3,3)
     1          +DFGRD1(1,3)*DFGRD1(3,2)
      DFGRDM1_INV(1,3)=DFGRD1(1,2)*DFGRD1(2,3)
     1          -DFGRD1(1,3)*DFGRD1(2,2)
      DFGRDM1_INV(2,1)=-DFGRD1(2,1)*DFGRD1(3,3)
     1          +DFGRD1(2,3)*DFGRD1(3,1)
      DFGRDM1_INV(2,2)=DFGRD1(1,1)*DFGRD1(3,3)
     1          -DFGRD1(1,3)*DFGRD1(3,1)
      DFGRDM1_INV(2,3)=-DFGRD1(1,1)*DFGRD1(2,3)
     1          +DFGRD1(1,3)*DFGRD1(2,1)
      DFGRDM1_INV(3,1)=DFGRD1(2,1)*DFGRD1(3,2)
     1          -DFGRD1(2,2)*DFGRD1(3,1)
      DFGRDM1_INV(3,2)=-DFGRD1(1,1)*DFGRD1(3,2)
     1          +DFGRD1(1,2)*DFGRD1(3,1)
      DFGRDM1_INV(3,3)=DFGRD1(1,1)*DFGRD1(2,2)
     1 -DFGRD1(1,2)*DFGRD1(2,1)
      DO I=1,3
      DO J=1,3
      DFGRDM1_INV(I,J)=DFGRDM1_INV(I,J)/DET
      END DO
      END DO
      RETURN
      END
```

D. Hypoelastic Model for the ligaments (UHYPEL.for)

```
      SUBROUTINE UHYPEL (EMOD,ENU,STRAN,NDI,NSHR,EINV,COORDS,NOEL,
     1 TEMP,PREDEF,CMNAME,TEMP,DTEMP,PREDEF,DPRED,CMNAME,NTENS,
     2 NSTATV,PROPS,NPROPS)

C
      INCLUDE 'ABA_PARAM.INC'
C
      CHARACTER*80 CMNAME
C
       DIMENSION STRAN(NTENS),DSTRAN(NTENS),TIME(2),PREDEF(1),DPRED(1),
     1 PROPS(NPROPS),COORDS(3),DROT(3,3),DFGRD0(3,3),DFGRD1(3,3),
     2 DDSDDE(NTENS,NTENS)
C
C
```

```
      REAL*4 ZERO,EMOD1,EMOD1,ENU,EPS0,PSI,C(6),EINV(3).
C
      PARAMETER (ZERO=0.0D0, ONE=1.0D0, TWO=2.0D0, THREE=3.0D0)
C-----------------------------------------------------------------------C
|               2-Noded Linear 3-D Truss Hybrid Element                 |
|                          -O- T3D2H -O-                                |
|                        1 O————————O 2                                 |
C-----------------------------------------------------------------------C
| MESBAH Moustafa. PhD                                                  |
| Faculty of sciences and Technology FST                                |
| University Abd El Hamid Ibn Badis. Mostaganem                         |
C-----------------------------------------------------------------------C
C   ALL -            ! ANTERIOR LONGITUDINAL LIGAMENT
C   PROPS(1) - EMOD1 ! MAX YOUNG MODULUS OF THE 'ALL'
C   PROPS(2) - EMOD2 ! MIN YOUNG MODULUS OF THE 'ALL'
C   PROPS(3) - EPS0  ! STRAIN TRANSITION RATIO OF THE 'ALL'
C   ENU -            ! POISSON RATIO OF THE 'ALL'
C-----------------------------------------------------------------------
C   MATERIAL PROPERTIES
C-----------------------------------------------------------------------
EMOD1= PROPS(1)
EMOD2= PROPS(2)
EPS0= PROPS(3)
ENU= ZERO
C-----------------------------------------------------------------------
C   STRAIN VALUE UP TO THIS POINT:
C
      DO I=1,NTENS
          IF (STRAN(I).LE.EPS0 .AND. STRAN(I).GT.ZERO) THEN
            DO I=1,NSHR
DDSDDE(I,I) = EMOD1
            END DO
   PRINT *, 'INTER TO FIRST STRAIN ZONE'
   CALL XIT
          ELSE IF (STRAN(I).GT. EPS0) THEN
             DO I=1,NSHR
DDSDDE(I,I) = EMOD2
             END DO
          END IF
      END DO
      PRINT *, 'PASS TO SECOND STRAIN ZONE'
   CALL XIT

C
C  CALL THE STRAIN INVARIANTS ENV(*)
C
      DO
EINV(1)= ZERO
EINV(2)= THREE/FOUR*STRAN(I)**2
EINV(3)= ONE/FOUR*STRAN(I)**3
      END DO
C
C        COMPONENTS OF MATRIX STRAIN TENSOR
C
      DO I=1,3,NDI
         C(I) = STRAN(I,I)
      END DO
      C(4) = ZERO
      C(5) = ZERO
```

```
      C(6) = ZERO
C
C   STRESS VALUES
C
      DO I=1,NSHR
STRESS(I) = STRESS(I)+DDSDDE(I,I)*DSTRAN(I)
      END DO
C
RETURN
END
```

E. Anisotropic Holzapfel Model UMAT (AniHolzaModel.for)

```
C ------------------------------------------------------------------- C
|              8-----------7          8-Noded Hexahedral Element      |
|             /|          /|                 -O- C3D8 -O-             |
|            / |         / |       zeta                               |
|           5-----------6  |        |   eta                           |
|           |  |        |  |        |   /                             |
|           |  |        |  |        |  /                              |
|           |  4--------|--3        | /                               |
|           | /         | /         |/                                |
|           |/          |/          O--------- xi                     |
|           1-----------2       origin at cube center                 |
C ------------------------------------------------------------------- C
| MESBAH Moustafa. PhD                                                |
| Faculty of Sciences and Technology FST                              |
| University Abd El Hamid Ibn Badis. Mostaganem                       |
| Laboratory of Numerical and Experimental Modeling of Mechanical     |
| Phenomena LMNEPM                                                    |
C ------------------------------------------------------------------- C

       SUBROUTINE UMAT(STRESS,STATEV,DDSDDE,SSE,SPD,SCD,
      1 RPL,DDSDDT,DRPLDE,DRPLDT,
      2 STRAN,DSTRAN,TIME,DTIME,TEMP,DTEMP,PREDEF,DPRED,CMNAME,
      3 NDI,NSHR,NTENS,NSTATEV,PROPS,NPROPS,COORDS,DROT,PNEWDT,
      4 CELENT,DFGRD0,DFGRD1,NOEL,NPT,LAYER,KSPT,KSTEP,KINC)
 C
       INCLUDE 'ABA_PARAM.INC'
 C
       CHARACTER*8 CMNAME
       DIMENSION STRESS(NTENS),STATEV(NSTATEV),
      1 DDSDDE(NTENS,NTENS),DDSDDT(NTENS),DRPLDE(NTENS),
      2 STRAN(NTENS),DSTRAN(NTENS),TIME(2),PREDEF(1),DPRED(1),
      3 PROPS(NPROPS),COORDS(3),DROT(3,3),DFGRD0(3,3),DFGRD1(3,3),
      4 Et(3),Stress_Max(3,3),EkEk(1),DFGRDM1_INV(3,3),En(3),
      5 TEMP(1),DTEMP(1),DFGRDP(3),DFGRDM1(3, 3),DFGRDM0(3, 3),
      6 CBAR(3,3),DDSDDE_Max(6,6)
 C
       DIMENSION BBAR(6),DISTGR(3,3),BBARBBAR(6),MM(6),M(3),D(6),
      1 NN(6), N(3)
 C
       CONSTANT NUMBER (ZERO=0.D0, ONE=1.D0,TWO=2.D0,THREE=3.D0,
```

```
     2 FOUR=4.D0,FIVE=5.D0,SIX=6.D0,SEVEN=7.D0,EIGHT=8.D0)
C -------------------------------------------------------------------
|    UMAT FOR ANISOTROPIC INCOMPRESSIBLE HOLZAPFEL HYPERELASTICITY
|            MATRIX-FIBERS HOLZAPFEL STRAIN ENERGY FUNCTION
|    W=C10(I-3)+ D1(I-3)**2 + k1/2k2 exp[k2{(1-K)(I1-3)+K(I4i-1)}**2-1]
C  ------------------------------------------------------------------
-
C   PROPS(1) - C10
C   PROPS(2) - D1
C   PROPS(3) - k1
C   PROPS(4) - K2
C   PROPS(5) - k
C   PROPS(6) - cos (fiber angle1)
C   PROPS(7) - sin (fiber angle1)
C   PROPS(8) - cos (fiber angle2)
C   PROPS(9) - sin (fiber angle2)
C  ------------------------------------------------------------------
-

C     READ MATERIAL PROPERTIES
C
      C10 =PROPS(1)
      D1 =PROPS(2)
      P =PROPS(3)
      PP =PROPS(4)
      PK =PROPS(5)
      COS =PROPS(6)
      SIN =PROPS(7)
      Q =PROPS(8)
      QQ =PROPS(9)
      QK =PROPS(10)
      COSS =PROPS(11)
      SINN =PROPS(12)
C
C    JACOBIAN AND DISTORTION TENSOR
C
      DET=DFGRD1(1, 1)*DFGRD1(2, 2)*DFGRD1(3, 3)
     1   -DFGRD1(1, 2)*DFGRD1(2, 1)*DFGRD1(3, 3)
      IF(NSHR.EQ.3) THEN
        DET=DET+DFGRD1(1, 2)*DFGRD1(2, 3)*DFGRD1(3, 1)
     1         +DFGRD1(1, 3)*DFGRD1(3, 2)*DFGRD1(2, 1)
     2         -DFGRD1(1, 3)*DFGRD1(3, 1)*DFGRD1(2, 2)
     3         -DFGRD1(2, 3)*DFGRD1(3, 2)*DFGRD1(1, 1) END IF
      SCALE=DET**(ONE/THREE) DO K1=1, 3
        DO K2=1, 3
          DISTGR(K2, K1)=SCALE*DFGRD1(K2,K1)
        END DO END DO
C
C     CALCULATE LEFT CAUCHY-GREEN TENSOR (B=F.Ft)
C
      BBAR(1)=DISTGR(1, 1)**2+DISTGR(1, 2)**2+DISTGR(1, 3)**2
```

```
      BBAR(2)=DISTGR(2, 1)**2+DISTGR(2, 2)**2+DISTGR(2, 3)**2
      BBAR(3)=DISTGR(3, 3)**2+DISTGR(3, 1)**2+DISTGR(3, 2)**2
      BBAR(4)=DISTGR(1, 1)*DISTGR(2, 1)+DISTGR(1, 2)*DISTGR(2, 2)
     1       +DISTGR(1, 3)*DISTGR(2, 3) IF(NSHR.EQ.3) THEN
        BBAR(5)=DISTGR(1, 1)*DISTGR(3, 1)+DISTGR(1, 2)*DISTGR(3, 2)
     1         +DISTGR(1, 3)*DISTGR(3, 3)
        BBAR(6)=DISTGR(2, 1)*DISTGR(3, 1)+DISTGR(2, 2)*DISTGR(3, 2)
     1         +DISTGR(2, 3)*DISTGR(3, 3)
      END IF
C
C    CALCULATAE (B.Bt)
C
      BBARBBAR(1)=BBAR(1)*BBAR(1)+BBAR(4)*BBAR(4)+BBAR(5)*BBAR(5)
      BBARBBAR(2)=BBAR(4)*BBAR(4)+BBAR(2)*BBAR(2)+BBAR(6)*BBAR(6)
      BBARBBAR(3)=BBAR(5)*BBAR(5)+BBAR(6)*BBAR(6)+BBAR(3)*BBAR(3)
      BBARBBAR(4)=BBAR(1)*BBAR(4)+BBAR(4)*BBAR(2)+BBAR(5)*BBAR(6)
      BBARBBAR(5)=BBAR(1)*BBAR(5)+BBAR(4)*BBAR(6)+BBAR(5)*BBAR(3)
      BBARBBAR(6)=BBAR(4)*BBAR(5)+BBAR(2)*BBAR(6)+BBAR(6)*BBAR(3)
C
C    CALCULATE INVARIANT I1 I4
C
      TRBBAR=BBAR(1)+BBAR(2)+BBAR(3)
      M(1)=DISTGR(1,1)*COS+DISTGR(1,2)*SIN
      M(2)=DISTGR(2,1)*COS+DISTGR(2,2)*SIN
      M(3)=DISTGR(3,1)*COS+DISTGR(3,2)*SIN
      N(1)=DISTGR(1,1)*COSS+DISTGR(1,2)*SINN
      N(2)=DISTGR(2,1)*COSS+DISTGR(2,2)*SINN
      N(3)=DISTGR(3,1)*COSS+DISTGR(3,2)*SINN
      TRBBARR=M(1)**2+M(2)**2+M(3)**2
      TRBBARRR=N(1)**2+N(2)**2+N(3)**2
C
C   CALCULATE ORIENTATION mimj
C
      MM(1)=M(1)*M(1)   MM(2)=M(2)*M(2)   MM(3)=M(3)*M(3)   MM(4)=M(1)*M(2)
      MM(5)=M(1)*M(3)   MM(6)=M(2)*M(3)   NN(1)=N(1)*N(1)   NN(2)=N(2)*N(2)
      NN(3)=N(3)*N(3) NN(4)=N(1)*N(2) NN(5)=N(1)*N(3) NN(6)=N(2)*N(3)



C
C    CALCULATE DW/DI
C
      A=(-1+TRBBARR*(1-3*PK)+TRBBAR*PK) AA=PP*A**2
      B=(-1+TRBBARRR*(1-3*QK)+TRBBAR*QK)
      BB=QQ*B**2
      WO=C10+exp(AA)*PK*A*P+exp(BB)*QK*B*Q WFA=exp(AA)*(1-3*PK)*A*P
      WFB=exp(BB)*(1-3*QK)*B*Q
      WOO=(P*(2*exp(AA)*PK**2*PP+4*exp(AA)*PK**2*A**2*PP**2))/(2*PP)
     1  +(Q*(2*exp(BB)*QK**2*QQ+4*exp(BB)*QK**2*B**2*QQ**2))/(2*QQ)
     WFFA=(P*(2*exp(AA)*(1-3*PK)**2*PP+4*exp(AA)*(1-3*PK)**2*A**2
     1  *PP**2))/(2*PP)
      WFFB=(Q*(2*exp(BB)*(1-3*QK)**2*QQ+4*exp(BB)*(1-3*QK)**2*B**2
```

```
     1  *QQ**2))/(2*QQ)
        WOFA=exp(AA)*(1-3*PK)*PK*P+2*exp(AA)*(1-3*PK)*PK*A**2*P*PP
        WOFB=exp(BB)*(1-3*QK)*QK*Q+2*exp(QQ)*(1-3*QK)*QK*B**2*Q*QQ
C
C     CALCULATE THE STRESS
C
        TRBBART=TRBBAR/THREE TRBBARRT=TRBBARR/THREE
        TRBBARRRT=TRBBARRR/THREE EG=TWO/DET EK=TWO/D1*(TWO*DET-ONE)
        PR=TWO/D1*(DET-ONE)
        DO K1=1,NDI
          STRESS(K1)=EG*WO*(BBAR(K1)-TRBBART)+EG*WFA*(MM(K1)-TRBBARRT)
     1      +EG*WFB*(NN(K1)-TRBBARRRT)+PR
        END DO
        DO K1=NDI+1,NDI+NSHR
          STRESS(K1)=EG*WO*BBAR(K1)+EG*WFA*(MM(K1))+EG*WFB*(NN(K1)) END DO
C
C     CALCULATE THE STIFFNESS
C
          DDSDDE(1, 1)=(8*(2*TRBBAR*WO+2*TRBBARR*WFA+2*TRBBARRR*WFB))
     1           /(9*DET)-(2*(4*WO*BBAR(1)+4*WFA*(M(1))**2+4*WFB
     2           *(N(1))**2))/(3*DET)+(4*(WOO*(-TRBBART+BBAR(1))**2
     3           +2*WOFA*(-TRBBART+BBAR(1))*(-TRBBARRT+(M(1))**2)
     4           +2*WOFB*(-TRBBART+BBAR(1))*(-TRBBARRRT+(N(1))**2)
     5           +WFFA*(-TRBBARRT+(M(1))**2)**2)+WFFB*(-TRBBARRRT
     6           +(N(1))**2)**2)/DET+EK
          DDSDDE(2, 2)=(8*(2*TRBBAR*WO+2*TRBBARR*WFA++2*TRBBARRR*WFB))
     1           /(9*DET)-(2*(4*WO*BBAR(2)+4*WFA*(M(2))**2+4*WFB
     2           *(N(2))**2))/(3*DET)+(4*(WOO*(-TRBBART+BBAR(2))**2
     3          +2*WOFA*(-TRBBART+BBAR(2))*(-TRBBARRT+(M(2))**2)
     4          +2*WOFB*(-TRBBART+BBAR(2))*(-TRBBARRRT+(N(2))**2)
     5          +WFFA*(-TRBBARRT+(M(2))**2)**2)+WFFB*(-TRBBARRRT
     6          +(N(2))**2)**2)/DET+EK
          DDSDDE(3, 3)=(8*(2*TRBBAR*WO+2*TRBBARR*WFA++2*TRBBARRR*WFB))
     1          /(9*DET)-(2*(4*WO*BBAR(3)+4*WFA*(M(3))**2+4*WFB
     2          *(N(3))**2))/(3*DET)+(4*(WOO*(-TRBBART+BBAR(3))**2
     3          +2*WOFA*(-TRBBART+BBAR(3))*(-TRBBARRT+(M(3))**2)
     4          +2*WOFB*(-TRBBART+BBAR(3))*(-TRBBARRRT+(N(3))**2)
     5          +WFFA*(-TRBBARRT+(M(3))**2)**2)+WFFB*(-TRBBARRRT
     6          +(N(3))**2)**2)/DET+EK
          DDSDDE(1, 2)=(2*(2*TRBBAR*WO+2*TRBBARR*WFA+2*TRBBARRR*WFA))
     1          /(9*DET)-(2*(2*WO*BBAR(1)+2*WO*BBAR(2)+2*WFA*(M(1))**2
     2          +2*WFA*(M(2))**2+2*WFB*(N(1))**2+2*WFB*(N(2))**2))
     3          /(3*DET)+(4*(WOO*(-TRBBART+BBAR(1))*(-TRBBART+BBAR(2))
     4          +WFFA*(-TRBBARRT+(M(1))**2)*(-TRBBARRT+(M(2))**2)+WFFB
     5          *(-TRBBARRRT+(N(1))**2)*(-TRBBARRRT+(N(2))**2)+WOFA
     4          *((-TRBBART+BBAR(2))*(-TRBBARRT+(M(1))**2)+(-TRBBART
     5          +BBAR(1))*(-TRBBARRT+(M(2))**2))+WOFB*((-TRBBART
     6          +BBAR(2))*(-TRBBARRRT+(N(1))**2)+(-TRBBART+BBAR(1))
     7          *(-TRBBARRRT+(N(2))**2))))/DET+EK
          DDSDDE(1, 3)=(2*(2*TRBBAR*WO+2*TRBBARR*WFA+2*TRBBARRR*WFA))
     1          /(9*DET)-(2*(2*WO*BBAR(1)+2*WO*BBAR(3)+2*WFA*(M(1))**2
```

```
2          +2*WFA*(M(3))**2+2*WFB*(N(1))**2+2*WFB*(N(3))**2))
3          /(3*DET)+(4*(WOO*(-TRBBART+BBAR(1))*(-TRBBART+BBAR(3))
4          +WFFA*(-TRBBARRT+(M(1))**2)*(-TRBBARRT+(M(3))**2)+WFFB
5          *(-TRBBARRRT+(N(1))**2)*(-TRBBARRRT+(N(3))**2)+WOFA
4          *((-TRBBART+BBAR(3))*(-TRBBARRT+(M(1))**2)+(-TRBBART
5          +BBAR(1))*(-TRBBARRT+(M(3))**2))+WOFB*((-TRBBART
6          +BBAR(3))*(-TRBBARRRT+(N(1))**2)+(-TRBBART+BBAR(1))
7          *(-TRBBARRRT+(N(3))**2))))/DET+EK
   DDSDDE(2, 3)=(2*(2*TRBBAR*WO+2*TRBBARR*WFA+2*TRBBARRR*WFA))
1          /(9*DET)-(2*(2*WO*BBAR(2)+2*WO*BBAR(3)+2*WFA*(M(2))**2
2          +2*WFA*(M(3))**2+2*WFB*(N(2))**2+2*WFB*(N(3))**2))
3          /(3*DET)+(4*(WOO*(-TRBBART+BBAR(2))*(-TRBBART+BBAR(3))
4          +WFFA*(-TRBBARRT+(M(2))**2)*(-TRBBARRT+(M(3))**2)+WFFB
5          *(-TRBBARRRT+(N(2))**2)*(-TRBBARRRT+(N(3))**2)+WOFA
4          *((-TRBBART+BBAR(3))*(-TRBBARRT+(M(2))**2)+(-TRBBART
5          +BBAR(2))*(-TRBBARRT+(M(3))**2))+WOFB*((-TRBBART
6          +BBAR(3))*(-TRBBARRRT+(N(2))**2)+(-TRBBART+BBAR(2))
7          *(-TRBBARRRT+(N(3))**2))))/DET+EK
   DDSDDE(1, 4)=(-2*(2*WO*BBAR(4)+2*WFA*(M(1))*(M(2))+2*WFB*(N(1
1          *(N(2))))/(3*DET)+(4*(WOO*(-TRBBART+BBAR(1))*BBAR(4)
2          +WFFA*(M(1))*(-TRBBARRT+(M(1))**2)*(M(2))+WFFB*(N(1))
3          *(-TRBBARRRT+(N(1))**2)*(N(2))+WOFA*(BBAR(4)*(-TRBBARRT
4          +(M(1))**2)+(-TRBBART+BBAR(1))*(M(1))*(M(2)))+WOFB
5          *(BBAR(4)*(-TRBBARRRT+(N(1))**2)+(-TRBBART+BBAR(1))
6          *(N(1))*(N(2)))))/DET
   DDSDDE(2, 4)=(-2*(2*WO*BBAR(4)+2*WFA*(M(1))*(M(2))+2*WFB*(N(1))
1          *(N(2))))/(3*DET)+(4*(WOO*(-TRBBART+BBAR(2))*BBAR(4)
2          +WFFA*(M(1))*(M(2))*(-TRBBARRT+(M(2))**2)+WFFB*(N(1))
3          *(N(2))*(-TRBBARRRT+(N(2))**2)+WOFA*((-TRBBART+BBAR(2))
4          *(M(1))*(M(2))+BBAR(4)*(-TRBBARRT+(M(2))**2))+WOFB
5          *((-TRBBART+BBAR(2))*(N(1))*(N(2))+BBAR(4)*(-TRBBARRRT
6          +(N(2))**2))))/DET
   DDSDDE(3, 4)=(-2*(2*WO*BBAR(4)+2*WFA*(M(1))*(M(2))+2*WFB*(N(1))
1          *(N(2))))/(3*DET)+(4*(WOO*(-TRBBART+BBAR(3))*BBAR(4)
2          +WFFA*(M(1))*(M(2))*(-TRBBARRT+(M(3))**2)+WFFB*(N(1))
3          *(N(2))*(-TRBBARRT+(M(3))**2)+WOFA*((-TRBBART+BBAR(3))
4          *(M(1))*(M(2))+BBAR(4)*(-TRBBARRT+(M(3))**2))+WOFB
5          *((-TRBBART+BBAR(3))*(N(1))*(N(2))+BBAR(4)*(-TRBBARRRT
6          +(N(3))**2))))/DET
   DDSDDE(4, 4)=(2*TRBBAR*WO+2*TRBBARR*WFA+2*TRBBARRR*WFB)/(3*DET)
1          +(4*(WOO*BBAR(4)**2+2*WOFA*BBAR(4)*(M(1))*(M(2))+2*WOFB
2          *BBAR(4)*(N(1))*(N(2))+WFFA*(M(1))**2*(M(2))**2+WFFB
3          *(N(1))**2*(N(2))**2))/DET IF(NSHR.EQ.3) THEN
   DDSDDE(1, 5)=(-2*(2*WO*BBAR(5)+2*WFA*(M(1))*(M(3))+2*WFB
1          *(N(1))*(N(3))))/(3*DET)+(4*(WOO*(-TRBBART+BBAR(1))
2          *BBAR(5)+WFFA*(M(1))*(-TRBBARRT+(M(1))**2)*(M(3))+WFFB
3          *(N(1))*(-TRBBARRRT+(N(1))**2)*(N(3))+WOFA*(BBAR(5)
4          *(-TRBBARRT+(M(1))**2)+(-TRBBART+BBAR(1))*(M(1))*(M(3)))
5          +WOFB*(BBAR(5)*(-TRBBARRRT+(N(1))**2)+(-TRBBART+BBAR(1))
6          *(N(1))*(N(3)))))/DET
```

```
      DDSDDE(2, 5)=(-2*(2*WO*BBAR(5)+2*WFA*(M(1))*(M(3))+2*WFB
     1         *(N(1))*(N(3))))/(3*DET)+(4*(WOO*(-TRBBART+BBAR(2))
     2         *BBAR(5)+WFFA*(M(1))*(-TRBBARRT+(M(3))**2)*(M(3))+WFFB
     3         *(N(1))*(-TRBBARRRT+(N(3))**2)*(N(3))+WOFA*(BBAR(5)
     4         *(-TRBBARRT+(M(2))**2)+(-TRBBART+BBAR(2))*(M(1))*(M(3)))
     5         +WOFB*(BBAR(5)*(-TRBBARRRT+(N(2))**2)+(-TRBBART+BBAR(2))
     6         *(N(1))*(N(3)))))/DET
      DDSDDE(3, 5)=(-2*(2*WO*BBAR(5)+2*WFA*(M(1))*(M(3))+2*WFB
     1         *(N(1))*(N(3))))/(3*DET)+(4*(WOO*(-TRBBART+BBAR(3))
     2         *BBAR(5)+WFFA*(M(1))*(M(3))*(-TRBBARRT+(M(3))**2)+WFFB
     3         *(N(1))*(N(3))*(-TRBBARRRT+(N(3))**2)+WOFA*((-TRBBART
     4         +BBAR(3))*(M(1))*(M(3))+BBAR(5)*(-TRBBARRT+(M(3))**2))
     5         +WOFB*((-TRBBART+BBAR(3))*(N(1))*(N(3))+BBAR(5)
     6         *(-TRBBARRRT+(N(3))**2))))/DET
       DDSDDE(1, 6)=(-2*(2*WO*BBAR(6)+2*WFA*(M(2))*(M(3))+2*WFB
     1         *(N(2))*(N(3))))/(3*DET)+(4*(WOO*(-TRBBART+BBAR(1))*BBAR(6)
     2        +WFFA*(-TRBBARRT+(M(1))**2)*(M(2))*(M(3))+WFFB*(-TRBBARRRT
     3         +(N(1))**2)*(N(2))*(N(3))+WOFA*(BBAR(6)*(-TRBBARRT
     4                                                +(M(1))**2)+(-
TRBBART+BBAR(1))*(M(2))*(M(3)))+WOFB*(BBAR(6)
     5         *(-TRBBARRRT+(N(1))**2)+(-TRBBART+BBAR(1))*(N(2))
     6         *(N(3)))))/DET
      DDSDDE(2, 6)=(-2*(2*WO*BBAR(6)+2*WFA*(M(2))*(M(3))+2*WFB*(N(2))
     1         *(N(3))))/(3*DET)+(4*(WOO*(-TRBBART+BBAR(2))*BBAR(6)+WFFA
     2         *(M(2))*(-TRBBARRT+(M(2))**2)*(M(3))+WFFB*(N(2))
     3         *(-TRBBARRRT+(N(2))**2)*(N(3))+WOFA*(BBAR(6)*(-TRBBARRT
     4                                                +(M(2))**2)+(-
TRBBART+BBAR(2))*(M(2))*(M(3)))+WOFB*(BBAR(6)
     5         *(-TRBBARRRT+(N(2))**2)+(-TRBBART+BBAR(2))*(N(2))
     6         *(N(3)))))/DET
       DDSDDE(3, 6)=(-2*(2*WO*BBAR(6)+2*WFA*(M(2))*(M(3))+2*WFB*(N(2))
     1         *(N(3))))/(3*DET)+(4*(WOO*(-TRBBART+BBAR(3))*BBAR(6)+WFFA
     2         *(M(2))*(M(3))*(-TRBBARRT+(M(3))**2)+WFFB*(N(2))*(N(3))
     3         *(-TRBBARRRT+(N(3))**2)+WOFA*((-TRBBART+BBAR(3))*(M(2))
     4         *(M(3))+BBAR(6)*(-TRBBARRT+(M(3))**2))+WOFB*((-TRBBART
     5         +BBAR(3))*(N(2))*(N(3))+BBAR(6)*(-TRBBARRRT
     6         +(N(3))**2))))/DET
      DDSDDE(5, 5)=(2*TRBBAR*WO+2*TRBBARR*WFA+2*TRBBARRR*WFB)/(3*DET)
     1         +(4*(WOO*BBAR(5)**2+2*WOFA*BBAR(5)*(M(1))*(M(3))+2*WOFB
     2         *BBAR(5)*(N(1))*(N(3))+WFFA*(M(1))**2*(M(3))**2+WFFB
     3         *(N(1))**2*(N(3))**2))/DET
      DDSDDE(6, 6)=(2*TRBBAR*WO+2*TRBBARR*WFA+2*TRBBARRR*WFB)/(3*DET)
     1         +(4*(WOO*BBAR(6)**2+2*WOFA*BBAR(6)*(M(2))*(M(3))+2*WOFB
     2         *BBAR(6)*(N(2))*(N(3))+WFFA*(M(2))**2*(M(3))**2+WFFB
     3         *(N(2))**2*(N(3))**2))/DET
     DDSDDE(4,5)=(4*(WOO*BBAR(4)*BBAR(5)+WFFA*(M(1))**2*(M(2))*(M(3))
     1         +WFFB*(N(1))**2*(N(2))*(N(3))+WOFA*(BBAR(5)*(M(1))*(M(2))
     2
    +BBAR(4)*(M(1))*(M(3)))+WOFB*(BBAR(5)*(N(1))*(N(2))+BBAR(4)
     3         *(N(1))*(N(3)))))/DET
     DDSDDE(4,6)=(4*(WOO*BBAR(4)*BBAR(6)+WFFA*(M(1))*(M(2))**2*(M(3))
```

```
     1          +WFFB*(N(1))*(N(2))**2*(N(3))+WOFA*(BBAR(6)*(M(1))*(M(2))
     2
     +BBAR(4)*(M(2))*(M(3)))+WOFB*(BBAR(6)*(N(1))*(N(2))+BBAR(4)
     3          *(N(2))*(N(3)))))/DET
        DDSDDE(5,6)=(4*(WOO*BBAR(5)*BBAR(6)+WFFA*(M(1))*(M(2))*(M(3))**2
     1          +WFFB*(N(1))*(N(2))*(N(3))**2+WOFA*(BBAR(6)*(M(1))*(M(3))
     2
     +BBAR(5)*(M(2))*(M(3)))+WOFB*(BBAR(6)*(N(1))*(N(3))+BBAR(5)
     3          *(N(2))*(N(3)))))/DET
     END IF
    DO K1=1, NTENS
      DO K2=1, K1-1
        DDSDDE(K1, K2)=DDSDDE(K2, K1)
      END DO
    END DO
C
C     Calculate the inverse of deformation gradient
C
     DFGRDM1_INV(1,1)=DFGRD1(2,2)*DFGRD1(3,3)
    1          -DFGRD1(2,3)*DFGRD1(3,2)
     DFGRDM1_INV(1,2)=-DFGRD1(1,2)*DFGRD1(3,3)
    1          +DFGRD1(1,3)*DFGRD1(3,2)
     DFGRDM1_INV(1,3)=DFGRD1(1,2)*DFGRD1(2,3)
    1          -DFGRD1(1,3)*DFGRD1(2,2)
     DFGRDM1_INV(2,1)=-DFGRD1(2,1)*DFGRD1(3,3)
    1          +DFGRD1(2,3)*DFGRD1(3,1)
     DFGRDM1_INV(2,2)=DFGRD1(1,1)*DFGRD1(3,3)
    1          -DFGRD1(1,3)*DFGRD1(3,1)
     DFGRDM1_INV(2,3)=-DFGRD1(1,1)*DFGRD1(2,3)
    1          +DFGRD1(1,3)*DFGRD1(2,1)
     DFGRDM1_INV(3,1)=DFGRD1(2,1)*DFGRD1(3,2)
    1          -DFGRD1(2,2)*DFGRD1(3,1)
     DFGRDM1_INV(3,2)=-DFGRD1(1,1)*DFGRD1(3,2)
    1          +DFGRD1(1,2)*DFGRD1(3,1)
     DFGRDM1_INV(3,3)=DFGRD1(1,1)*DFGRD1(2,2)
    1          -DFGRD1(1,2)*DFGRD1(2,1)
    DO I=1,3
      DO J=1,3
        DFGRDM1_INV(I,J)=DFGRDM1_INV(I,J)/DET
      END DO
    END DO
    RETURN
    END
```

F. Nonlinear Seven Major Ligaments Model ALLIGAM (ALLIGAM.for)

```
      SUBROUTINE LIGAMENT(STRESS,STATEV,DDSDDE,SSE,SPD,SCD,
     1 RPL,DDSDDT, RPLDE,DRPLDT,STRAN,DSTRAN,TIME,DTIME,TEMP,
     2 DTEMP,PREDEF,DPRED,CMNAME,NDI,NSHR,NTENS,NSTATV,PROPS,
     3 NPROPS,COORDS,DROT,PNEWDT,CELENT,DFGRD0,DFGRD1,NOEL,
```

```
      4 NPT,LAYER,KSPT,KSTEP,KINC)

       DIMENSION STRESS(NTENS),STATEV(NSTATV),DDSDDE(NTENS,NTENS)
      1 DDSDDT(NTENS,DRPLDE(NTENS,STRAN(NTENS),DSTRAN(NTENS),TIME(2)
      2 PROPS(NPROPS),COORDS(3),DROT(3,3),DFGRD0(3,3),DFGRD1(3,3)
      3 C(6),STRAN(1),TEMP1(1,1),TEMP2(1,1),EINV(3)
C
      INCLUDE 'ABA_PARAM.INC'
C
      CHARACTER*80 CMNAME
C
      PARAMETER (ONE=1.0D0,TWO=2.0D0,THREE=3.0D0,SIX=6.0D0)

C ------------------------------------------------------------------------C
C           UMAT FOR UNIAXIAL TENSION ONLY TRUSS ELEMENT                  |
C                        O————————O   T3D2H                               |
C ------------------------------------------------------------------------C
C     MATERIAL PARAMETERS FOR ANTERIOR LONGITUDINAL LIGAMENT 'ALL'        |
C------------------------------------------------------------------------C
C     PROPS(1) – EMOD1 ! MAX YOUNG MODULUS OF THE 'ALL'
C     PROPS(2) – EMOD2 ! MIN YOUNG MODULUS OF THE 'ALL'
C     PROPS(3) – EPS0  ! STRAIN TRANSITION RATIO OF THE 'ALL'
C     PROPS(4) – PSI   ! STRAIN TRANSITION PARAMETER OF THE 'ALL'
C ------------------------------------------------------------------------
C                     CALL UMAT LIGAMENT
C ------------------------------------------------------------------------

     IF (NDI.NE.3) THEN
         WRITE(6,1)
 1       FORMAT(//,30X,'***ERROR - THIS UMAT MAY ONLY BE USED FOR ',
         1 'TRUSS ELEMENT)
      ENDIF
C
C     MATERIAL PROPERTY FOR “ALL”
C
      EMOD1 = PROPS(1)
      EMOD2 = PROPS(2)
      EPS0 = PROPS(3)
      PSI = PROPS(4)
      NU = ZERO

      IF   (CMNAME(1:4) .EQ. 'ALL') THEN
CALL ALLIGAM(STRESS,DDSDDE,STRAN,DSTRAN,EPS0,EMOD1,EMOD2,PSI)
      END IF
RETURN
END

C
C     CALL ANTERIOR LONGITUDINAL LIGAMENT 'ALL'
C
      SUBROUTINE ALLIGAM (STRESS,DDSDDE,STRAN,DSTRAN,EPS0,
     1 EMOD1,EMOD2,PSI)
C
      INCLUDE 'ABA_PARAM.INC'
C
      REAL EPS0,EMOD1,EMOD2,PSI
C
```

```
C     ELASTIC STIFFNESS
C
       DO I=1,NTENS
            DDSDDE(I,I)= ZERO
       ENDDO
C
C      CALCULATE STRESS FROM ELASTIC STRAINS
C
       DO I=1,NTENS
           IF(STRAN(I) .GT. ZERO) THEN
DDSDDE(I,I)=(ONE+TANH(PSI*(STRAN(I)-EPS0)))*(EMOD2-EMOD1)/TWO+ EMOD1
STRESS(I)=STRESS(I)+DDSDDE(I,I)*DSTRAN(I)
           ELSE
STRESS(I)= ZERO
           END IF
       ENDDO
RETURN
END
```

G. Validation Process of the Finite element model L1-S1 (Validation_process.py)

```
#-------------------------------------------------------------
# Load code/Rotation_angle.py
# MESBAH Moustafa. PhD
# University Abd El Hamid Ibn Badis. Mostaganem
# Faculty of Sciences and Technology FST
# Laboratory of Numerical and Experimental Modeling of
# Mechanical Phenomena LMNEPM
# Abaqus Scripting.
#-------------------------------------------------------------

# Import and Run abaqus modules

from abaqus import *
from abaqusConstants import *
from caeModules import *
import __main__

# Mosta python tools

def ValidationProcess(MaterType,MostaModel):

# ELEMENT TYPETO BE USED

    elemTypeH = mesh.ElemType(elemCode=C3D8H, elemLibrary=STANDARD)
    elemType = mesh.ElemType(elemCode=C3D8, elemLibrary=STANDARD)
p = [MostaModel.parts[partName] for partName in MostaModel.parts.keys()
if 'IVD' in partName]
    for IVDPart in p:
        IVDPart.setElementType(regions=IVDPart.sets['ANNULUS'],
elemTypes=(elemTypeH, ))
        IVDPart.setElementType(regions=IVDPart.sets['NUCLEUS'],
elemTypes=(elemType, ))

# MATERIALS

    for Mater in MostaModel.materials.keys():
        MostaMater = MostaModel.materials[Mater]
        if 'ANNULUS' in Mater:
            p = [MostaModel.parts[partName] for partName in
```

```
MostaModel.parts.keys() if 'IVD' in partName]
if MaterialType == 'Elastic':
MostaMater.Elastic(table=((4.2, 0.45), ))
for IVDPart in p:
IVDPart.setElementType(regions=IVDPart.sets['ANNULUS'],
elemTypes=(elemType, ))
elif MaterialType == 'NEO_HOOKean':
MostaMater.Hyperelastic(materialType=ISOTROPIC, testData=OFF,
type=NEO_HOOKE, table=((0.3, 0.2, 1), ))
for IVDPart in p:
IVDPart.setElementType(regions=IVDPart.sets['ANNULUS'],
elemTypes=(elemTypeH, ))
else:
del Mater.hyperelastic
for IVDPart in p:
                IVDPart.setElementType(regions=IVDPart.sets['ANNULUS'],
elemTypes=(elemTypeH, ))
MaterialType == 'MOONEY_RIVLIN':
MostaMater.HyperelasticHyperelastic(materialType=ISOTROPIC, testData=OFF,
type=MOONEY_RIVLIN, volumetricResponse=VOLUMETRIC_DATA, table=((0.56,
0.14, 0.14), ))
```

```
# Continuum Nucleus Elements
```

```
         elif 'NUCLEUS' in mater:
             p = [MostaModel.parts[partName] for partName in
MostaModel.parts.keys() if 'IVD' in partName]
             if MaterialType == 'Elastic':
                MostaMater.Elastic(table=((0.2, 0.4999), ))
                for IVDPart in p:

IVDPart.setElementType(regions=IVDPart.sets['NUCLEUS'],
elemTypes=(elemType, ))
                try:del MostaMater.Elastic
                except:pass
```

```
# Fluid Filled Cavity Elements
```

```
            elif MaterialType == 'Incompressible'
            n = p.nodes
            nodes = (NucleusNodes)
            p.deleteNode(nodes=nodes)
            MostaModel = mdb.Model(name=name).parts(name=name)
            del MostaModel.sets['NUCLEUS']
            del MostaModel.sectionAssignments['NUCLEUS']
            del MostaModel.sections['NUCLEUS']
            del MostaModel.materials['NUCLEUS']
            p.Surface(faceElements=faceElements, name='FLUID')
            a = MostaModel.rootAssembly
            for i in xrange(1, 5):
            ni = a.instances['partName'].nodes
            a.DatumPointByOffset(point=ni[nodesLabels], vector=(x,y,z))
            di = a.datums
            a.ReferencePoint(point=di[point_label])
            MostaModel.FluidCavityProperty(name='INCOMFLUID',
fluidDensity=1.36e-06)
            ri = a.referencePoints
            refPointsi=(ri[ref_label], )
            region1=a.Set(referencePoints=refPointsi,
name='FLUID_CHAMBER')
            a = MostaModel.rootAssembly
```

```
            region2=a.instances['partName'].surfaces['FLUID']
            a.FluidCavity(name='FLUID_NUC', createStepName='Initial',
            cavityPoint=region1, cavitySurface=region2,
            interactionProperty='INCOMFLUID', ambientPressure=0.1)

if __name__ == '__main__':
    try:
        extToKeep.extend(['cae','odb'])
    except:
        extToKeep = ['cae','odb']
    for Lumbar in LumbarToRun:
        caeFileName = 'Lumbar%i.cae'%Lumbosac
        for modelType in materialModels:
                mdb = openMdb(caeFileName)
                job = createModelCopy(modelType,'Lumbar%i'%Lumbosac)
                try:
                    job.submit()
                    job.waitForCompletion()
                except:
                    pass
                mdb.saveAs(caeFileName)
                cleanFiles(Lumbar)
                try:
                    odbFileName = job.name+".odb"
                    postPro(odbFileName)
                    mdb.close()
                except:
                    mdb.close()
                    continue
```

G. Generating the Intersegmental Rotation in degree (Python code: rotation_angle.py)

```
# Python Coding:

# Import Abaqus Modules

from abaqus import *
from abaqusConstants import *
import visualization
import odbAccess
# Opene odb File
odb = session.openOdb('L4-L5.odb')

# Specify Frame-Field Outputs

frame1 = odb.steps['Rotations'].frames[-1]
fo = frame1.fieldOutputs
rotation1  = fo['UR']

# Define Field Outputs Data

Pi = 3.14159
rotation2 = rotation1*180/Pi

# Execute Graphics Startup

vp = session.viewports['Viewport: 1']
vp.setValues(displayedObject=odb)
session.graphicsOptions.setValues(backgroundColor='#FFFFFF',backgroundSty
le=SOLID)
```

```
# Plot Output Variables
UR = frame1.FieldOutput(name='rotation2',description='angle',
type=SCALAR)
vp.odbDisplay.setPrimaryVariable(field=rotation2, outputPosition=NODAL,
refinement=(INVARIANT, 'Magnitude'))
vp.odbDisplay.display.setValues(plotState=(CONTOURS_ON_DEF,))
vp.view.fitView()
session.printToFile(fileName='Angle', format=PNG,  canvasObjects=(vp,))

# Define the Parameters for Field Outputs
rot = session.scratchOdbs['L4-L5.odb'].steps['Session
Step'].frames[0].fieldOutputs['UR * 180 / 3.14159']
tmpField = rot
sessionFrame = session.scratchOdbs['L4-L5.odb'].steps['Session Step'].
frames[0]
sessionField = sessionFrame.FieldOutput(name='Angle',
description='s3f0_UR180314159', field=tmpField)
# Saving and Closing the odb
odb.save()
odb.close()

if __name__ == '__main__':
# Get command line arguments.
        usage = "usage: abaqus python Rotation_Angle.py <L4-L5>"
        optlist, args = getopt.getopt(sys.argv[1:],'')
        JobID = args[0]
        odbPath = JobID + '.odb'
        print JobID
        print odbPath
        if not odbPath:
                print usage
                sys.exit(0)
        if not os.path.exists(odbPath):
                print "odb %s does not exist!" % odbPath
                sys.exit(0)
        odb L4-L5(JobID)
```

H. Creating the Facets Cartilage Component (Python code: Facet_Cartilage.py)

```
#-------------------------------------------------------------------#
#                       Facets Mesh Extrusion                       #
#-------------------------------------------------------------------#
from abaqus import *
from abaqusConstants import *
import __main__
def Facets():
import section
import regionToolset
import displayGroupMdbToolset as dgm
import part
import material
import assembly
```

```
import optimization
import step
import interaction
import load
import mesh
import job
import sketch
import visualization
import xyPlot
import displayGroupOdbToolset as dgo
import connectorBehavior
p = mdb.models['L4-L5'].parts['FSU45']
f = p.elements
# Defining Material orientation Axis
region = (part.Facet_cartilage, )
normalAxisRegion = part.surfaces['Facets']
primaryAxisRegion = p.sets['Set-edge']
p.MaterialOrientation(region=region,
orientationType=DISCRETE, axis=AXIS_1, normalAxisDefinition=SURFACE,
normalAxisRegion=normalAxisRegion, flipNormalDirection=False,
normalAxisDirection=AXIS_3, primaryAxisDefinition=EDGE,
primaryAxisRegion=primaryAxisRegion, primaryAxisDirection=AXIS_1,
flipPrimaryDirection=False, additionalRotationType=ROTATION_NONE,
angle=0.0, additionalRotationField='Field', stackDirection=STACK_3)
#Generating the Facet cartilage layers
mdb.meshEditOptions.setValues(enableUndo=True, maxUndoCacheElements=0.5)
p = mdb.models['L4-L5'].parts['FSU45']
f = p.elements
p.generateMeshByOffset(region=regionToolset.Region(
face2Elements=face2Elements,
face3Elements=face3Elements, face6Elements=face6Elements),
meshType=SOLID, totalThickness=0.4, numLayers=2,
constantThicknessCorners=True, shareNodes=True)
p = mdb.models['L4-L5'].parts['FSU45']
e = p.elements
elements = e.getSequenceFromMask(mask=(
'[#0:1173 #fffffe00 #ffffffff:13 #1fffffff ]', ), )
p.Set(elements=elements, name='Facets')
session.viewports['Viewport: 1'].enableMultipleColors()
session.viewports['Viewport: 1'].setColor(initialColor='#BDBDBD')
cmap = session.viewports['Viewport: 1'].colorMappings['Set']
cmap.updateOverrides(overrides={'Facets2':(True, '#FFFF00',
'Default', '#FFFF00')})
session.viewports['Viewport: 1'].setColor(colorMapping=cmap)
session.viewports['Viewport: 1'].disableMultipleColors()
```

H. Generating the Facets Cartilage Thickness (Python code: Facets.py)

```
from FSU45.inp
import Mesh, Nodes
mesh = Mesh('FSU45')
nodes = mesh.nodes
elements = mesh.element
p = mdb.models['L4-L5'].parts['FSU45']
# Get the Nodes from on the previously defined surface:
node_objects = p.surfaces['Facets'].nodes
```

```
# Same from the Facets set:
node_objects = p.sets['Cartilage'].nodes
# Get the labels for Facets Nodes:
node_labels = [node.label for node in node_objects]
p = mdb.models['L4-L5'].parts['FSU45']
surf_nodes = [nodes]

for face in p.elementFaces():
if len(face.getElements()) == 1:
# Get the nodes on the Facets Element Faces:
Faces=mdb.models['FSU45'].rootAssembly.instances['L4-L5'].elementFaces
SurfaceNodeLabels=get_Surface_Nodes(Labels)

#~~~~~~~~~~~~~~~~~~~~~~~~~~~~~~~~~~~~~~~~~~~#
#    Adding nodes Labels and coordinates    #
#~~~~~~~~~~~~~~~~~~~~~~~~~~~~~~~~~~~~~~~~~~~#

Part: FSU45, Modeling space: 3D,   Type: C3D8 Deformable
# FSU45 Part is an Orphan Mesh. Linear hexahedron element C3D8
labels = range(151290:151723) # 135 nodes
x = labels
y = labels
z = labels
[0. for i in x]
nodes = Nodes(label=label, x=x, y=y, z=z)
nodes.add_node(label=label, x=x, y=y, z=z)
# Define Facets nodes
nodes.add_set('Facets',[151290,151723])
# Adding nodes Labels and coordinates
  Nodes class instance:
  nodes.label:

  Labels        x             y              z
  151290    191.849289    199.178162    -493.372375
  151291    193.406158    197.84407     -495.250977
  151292    188.511581    199.231003    -488.438293
  151293    190.08136     199.509415    -491.034241
  151296    191.242828    187.475998    -487.916443
                       .
                       .
                       .
                       .
  151719    190.043488    198.673126    -490.713959
  151720    190.960007    199.419632    -492.245331
  151721    190.916687    198.601257    -491.897522
  151722    187.621521    198.713257    -486.96814
  151723    187.712158    198.065567    -486.858734
  Sets:
  myset     nodes()
print mesh.nodes[151290:151723] # requesting 135 nodes
# Adding Facets Elements
elements = elements(label=label, x=x, y=y, z=z)
elements.add_element(label=label, x=x, y=y, z=z)
mesh.add_element(label=label, connectivity= [1L,2L,3L,4L], space=space,
name=name)
Mesh class instance:
Elements:
Label     Connectivity                      Space    Name
109134    [151705, 151706, 151334, 151707]    3D     QUAD4
```

```
109136    [151655, 151358, 151657, 151656]    3D    QUAD4
109137    [151659, 151660, 151358, 151655]    3D    QUAD4
109138    [151700, 151701, 151345, 151658]    3D    QUAD4
109139    [151699, 151346, 151701, 151700]    3D    QUAD4
                          .
                          .
                          .
                          .
109239    [151293, 151719, 151721, 151720]    3D    QUAD4
109240    [151717, 151718, 151719, 151293]    3D    QUAD4
109241    [151292, 151716, 151718, 151717]    3D    QUAD4
109242    [151722, 151723, 151716, 151292]    3D    QUAD4
# Adding sets
mesh.add_set(label = 'Facets', elements = [109134,109242])
print mesh.element()
# Define the facets thikness to be applied along isoparametric y(2) axis=
= fthikness = float(l)/N
inodes = facet.nodes
omesh = Mesh(nodes=facet.nodes)
tempmesh = Mesh(nodes)
# Selection of QUAD Element
    for i in xrange(len(labels)):
      label = labels[i]
      [1L,2L,3L,4L] = connectivity
      connectivity = connectivity[i]
      space = space[i]
      name = name[i]

      if space == 3:
        if quad == False:
          if len(connectivity) in [3,4]:
tempmesh.add_element(Label = Label, connectivity = connectivity, space =
space, name = name)
    for sk in facet.sets.keys():
      tempmesh.add_set(sk,facet.sets[sk])

nNodes, nElements = len(tempmesh.nodes.labels), len(tempmesh.labels)
    nmax, emax = max(facet.nodes.labels), max(facet.labels)
# Creating New Nodes and Elements
    if quad == False:
      for i in xrange(N):
# New Generated Mesh Nodes
        tn =  tempmesh.nodes
        te =  tempmesh
        tns = tempmesh.nodes.sets
        tes = tempmesh.sets
        for nn in xrange(len(tn.labels)):
          oldLabel = tn.labels[nn]
          label = oldLabel + (i+1) * nmax
          x = tn.x[nn]
          y = tn.y[nn]
          z = tn.z[nn] + fthikness * (i+1)
          omesh.nodes.add_node(label,x,y,z)
# Extrude Facets Elements : QUAD To HEXAHEDRAL
        for ne in xrange(len(te.labels)):
          oldLabel = te.labels[ne]
```

```
          label = oldLabel + i * emax
          connectivity  = te.connectivity[ne]
connectivity = [c + (i) * nmax  for c in [L1,L2,L3,L4] + [c + (i+1) *
nmax  for c in [L1,L2,L3,L4]]
          name  = te.name[ne]
          if name in mapping.keys():
             name = mapping[name]
          else:
            name = 'C3D8'.format(len([1L,2L,3L,4L]))
          omesh.add_element(label = label,connectivity=
[1L,2L,3L,4L],space = 3,name = name)
          for sk in tes.keys():
            s = tes[sk]
            if oldLabel in s:
              omesh.add_set(sk,label)
# Create Cartilage Layers using predefined Surface sets or Create element
faces
# Managing sets
    if quad == False:
      ins = facet.nodes.sets
      onodes = omesh.nodes
      ies = facet.sets
      omesh = omesh
      for k in ins.keys():
        s = ins[k]
        os = []
        for i in xrange(1, N+1):
          os += [ l + i * nmax for l in s]
        onodes.add_set(k, facet(os))
        for k in ies.keys():
        s = ies[k]
        os = []
        for i in xrange(N):
          os += [ l + i * emax for l in s]
        omesh.add_set(k, facet(os))
# Managing Facet surfaces
    set_pattern = '{0}_f{1}_{2}'
    if quad == False:
      isurf = facet.surfaces
      for k in isurf.keys():
        s = isurf[k]
        elems, faces, etype = [], [], []
        for couple in s:
          labels = facet.sets[couple[0]]
          face = couple[1]
          for l in labels:
            elems.append(l)
            faces.append(face)
            i = facet.labels.index(l)
            etype.append(len(facet.connectivity[i]))
        F = {1:[],i:[]}
        for i in xrange(len(elems)):
          l = elems[i]
          f = faces[i]
          t = etype[i]
          F[f+2] += [l + emax * layer for layer in xrange(N)]
        surf = []
        for i in xrange(3,7):
          j = 0
```

```
            set_label = set_pattern.format(k,i,j)
            while set_label in facet.sets.keys():
              j += 1
              set_label = set_pattern.format(k,i,j)
            if F[i] != []:
              omesh.add_set(set_label, F[i])
              surf.append((set_label, i))
          omesh.add_surface(k, surf)
# Create surface element set: 'Cartilage'
Cartilage.surfaces = []
Cartilage.surfaces.append(element.label)
Cartilage.Set = Cartilage.ElementSetFromElementLabels(name = 'cartilage',
elementLabels = facetelementtList)
previousElmtLbl = -1

# Get nodes composing the element face on the surface
enodes = np.array(element.connectivity)
fnodes = enodes[dfaceNodes[str(Faces[i])]]
# Create two vectors on the face
# Compute normal vector to face and face area
Cart1=facet.nodes[fnodes[1]-1].coordinates-facets.nodes[fNodes[0]-
1].coordinates
Cart2=facet.nodes[fnodes[2]-1].coordinates-facets.nodes[fnodes[0]-
1].coordinates

# Define Material orientation Axis
orthogonalVect = np.cross(No,Cart1)
area = 0.5*np.linalg.norm(orthogonalVect)
normal =
orthogonalVect/np.linalg.norm(orthogonalVect)*dFaceSigns[str(Faces[i])]

# Define Specified Faces
mdb.models['L4-L5'].parts['FSU45'].allSurfaces['Cartilage'].sides[0]=
FACE1
# Element based surfaces are defined using the following commands:
p = mdb.models['L4-L5'].parts['FSU45']
f = p.elements
face1Elements = f[:]
          .
          .
          .
faceiElements = f[:]
p.Surface(face1Elements=face1Elements,, faceiElements=faceiElements,
name='Cartilage')
# The surface 'Cartilage' has been created (i mesh faces)
m = omesh()
m = m.extrude(l = l3, N = N3 )
vectorField = m.nodes.eval_vectorFunction(function)
m.nodes.apply_displacement(vectorField)
# Extrude the Quad Elements Mesh
m = omesh()
m.add_set('Cartilage',[i,i+1])
m.add_surface('Cartilage',[( 'Cartilage',i), ])
m2 = m.extrude(l = .4, N = 2)
x,y,z = m.get_edges()
xi,yi,zi = mi.get_edges()
return omesh
```